# Droughts and heatwaves in the Western Mediterranean, impact on ozone pollution

Antoine Guion

## To cite this version:

Antoine Guion. Droughts and heatwaves in the Western Mediterranean, impact on ozone pollution. Earth Sciences. Sorbonne Université, 2022. English. NNT : 2022SORUS056 . tel-03709085

**HAL Id: tel-03709085**

**https://theses.hal.science/tel-03709085**

Submitted on 29 Jun 2022

Sorbonne Université

École doctorale des sciences de l'environnement d'Ile de France (ED129)
*Laboratoire de Météorologie Dynamique / Équipe Interfaces et Troposphère*

# Droughts and heatwaves in the Western Mediterranean, impact on ozone pollution

Par Antoine Guion
Thèse de doctorat en sciences du climat et de l'atmosphère

Présentée et soutenue publiquement le 25 février 2022

Devant un jury composé de :

| | | | | |
|---|---|---|---|---|
| Francois Ravetta | - | Professeur SU (LATMOS) | - | Président |
| Jean-François Müller | - | Directeur de département IASB-BIRA | - | Rapporteur |
| Jean-Christophe Calvet | - | Météorologue Météo-France (CNRM) | - | Rapporteur |
| Juliette Lathière | - | Chargée de recherche CNRS (LSCE) | - | Examinatrice |
| Samira Khodayar Pardo | - | Directrice de département CEAM | - | Examinatrice |
| Solène Turquety | - | Professeure SU (LMD) | - | Directrice de thèse |
| Jan Polcher | - | Directeur de recherche CNRS (LMD) | - | Co-Directeur de thèse |

"I have noticed even people who claim everything is predestined, and that we can do nothing to change it, look before they cross the road."

**Stephen Hawking,**
*Black Holes and Baby Universes and Other Essays*, 1993

# Abstract

In line with what is expected in a context of global warming, droughts and heatwaves have increased both in frequency and severity over the last century in the Mediterranean area. Both direct and indirect adverse effects induced by droughts and heatwaves can lead to critical economic, social and environmental damages. In particular, such extreme weather events can significantly impact the vegetation state as well as atmospheric chemistry, through biosphere-troposphere interactions.

The objective of this thesis is to analyze the interactions between the biosphere and the troposphere during droughts and heatwaves and more specifically, to assess the impact of such extreme weather events on the biomass, fire activity and ground-level ozone ($O_3$) in the Western Mediterranean. This work is mainly based on three dimensional numerical modeling of the land surface and atmosphere (meteorology and atmospheric chemistry) at region scale, supported by different data sets of observations (both in-situ and satellite-based).

Firstly, a simulation by the RegIPSL coupled regional model (ORCHIDEE-WRF) over the 1979-2016 period is used to identify extreme weather events. Two methods are applied: the Standardized Precipitation Evapotranspiration Index (SPEI) for meteorological droughts and the Percentile Limit Anomalies (PLA) on the 2m temperature for heatwaves and on the soil dryness for agricultural droughts. Even if agricultural droughts affect fewer summers (33%) than heatwaves (97%), they last almost four times longer (mean summer duration of 22 days versus 6 days). The co-variability between droughts and heatwaves in the Mediterranean is another important feature. A cluster analysis of isolated and combined extreme events is therefore used to assess respective effects.

Secondly, the impact on biomass and fire characteristics is analyzed by combining simulated droughts and heatwaves with satellite observations of wildfires and vegetation from the MODIS instrument. Due to water stress, droughts lead to significant biomass decrease ($-10\%$ LAI on average) whose magnitude varies in function of the biome and the plant functional type. Through synergistic effects, simultaneous droughts and heatwaves increase burned area and the fire intensity by 2.1 and 2.9 times respectively, compared to normal conditions.

Finally, atmospheric chemistry is simulated using the CHIMERE chemistry-transport model (CTM) with meteorological fields from the WRF model over summers 2012, 2013 and 2014.

A complete sensitivity analysis of the biogenic emissions, the $O_3$ dry deposition velocity and the surface $O_3$ concentration to soil dryness and biomass decrease is performed. Our results show that soil dryness is a key factor during drought events, decreasing considerably the $C_5H_8$ emissions and $O_3$ dry deposition velocity. This effect has a larger impact than the biomass decrease. However, the net impact of this specific parameter on surface $O_3$ remains limited.

Observed $O_3$ concentration is on average significantly higher during heatwaves ($+18\mu g/m^3$ in daily maximum) and droughts ($+9\mu g/m^3$) compared to normal conditions. From the conducted simulations, this would be explained by an overall $O_3$ precursor emission enhancement (in agreement with $HCHO$ observations), $O_3$ dry deposition decrease and favourable weather conditions. Furthermore, almost half of summer days exceeding the EU target (of $O_3$) in the Mediterranean occurs during droughts or heatwaves. Heatwaves are the events characterized by the largest fraction of exceedance days (34%) and highest concentrations ($+24\mu g/m^3$ above the threshold).

I emphasize the need for a more dynamical representation of interactions between vegetation, hydrology, meteorology and atmospheric chemistry in models in order to improve the simulation of summer $O_3$.

**Keywords**: droughts, heatwaves, biogenic emissions, gas dry deposition, ozone pollution, regional modeling, CHIMERE, ORCHIDEE, WRF, in-situ and satellite observations, Mediterranean.

# Résumé

Conformément à ce qui est envisagé dans un contexte de réchauffement climatique, les sécheresses et les vagues de chaleur ont augmenté à la fois en fréquence et en intensité au cours du siècle dernier dans la région méditerranéenne. Les effets négatifs directs et indirects induits par les sécheresses et les vagues de chaleur peuvent entraîner des dommages économiques, sociaux et environnementaux critiques. Plus particulièrement, ces événements météorologiques extrêmes peuvent avoir un impact significatif sur l'état de la végétation ainsi que sur la chimie de l'atmosphère, par le biais des interactions biosphère-troposphère.

L'objectif de cette thèse est d'analyser les interactions entre la biosphère et la troposphère pendant les sécheresses et vagues de chaleur et, plus spécifiquement, d'évaluer l'impact de ces événements extrêmes sur la biomasse, l'activité des feux et l'ozone troposphérique ($O_3$) en Méditerranée occidentale. Ce travail est principalement basé sur une modélisation numérique tridimensionnelle de la surface terrestre et de l'atmosphère (météorologie et chimie atmosphérique) à l'échelle régionale, soutenue par différents ensembles de données d'observations (in-situ et satellitaires).

Tout d'abord, une simulation issue du modèle régional couplé RegIPSL (ORCHIDEE-WRF) sur la période 1979-2016 est utilisée pour identifier les événements météorologiques extrêmes. Deux méthodes sont appliquées: la méthode du "Standardized Precipitation Evapotranspiration Index" (SPEI) pour les sécheresses météorologiques et celle du "Percentile Limit Anomalies" (PLA) sur la température à 2m pour les vagues de chaleur et sur l'aridité du sol pour les sécheresses agricoles. Même si les sécheresses agricoles touchent moins d'étés (33%) que les vagues de chaleur (97%), elles durent presque quatre fois plus longtemps (durée moyenne estivale de 22,3 jours contre 5,8 jours). La co-variabilité entre les sécheresses et vagues de chaleur en Méditerranée est une autre caractéristique importante. Une analyse en "clusters" des événements extrêmes isolés et combinés est donc utilisée pour évaluer leurs effets respectifs.

Deuxièmement, l'impact sur la biomasse et les caractéristiques des incendies est analysé en combinant les sécheresses et vagues de chaleur simulées avec les observations satellitaires de la végétation et des feux par l'instrument MODIS. A cause du stress hydrique, les sécheresses entraînent une diminution significative de la biomasse (-10% du LAI en moyenne) dont l'ampleur varie en fonction du biome et du type de plante (PFTs). Par effet synergique, les sécheresses et vagues de chaleur simultanées augmentent la surface brûlée et l'intensité du feu de respectivement 2,1 et 2,9 fois, par rapport aux conditions normales.

Enfin, la chimie atmosphérique est simulée à l'aide du modèle de chimie-transport CHIMERE (CTM) avec les champs météorologiques du modèle WRF sur les étés 2012, 2013 et 2014. Une analyse de sensibilité complète des émissions biogéniques, de la vitesse de dépôt sec de l'$O_3$ et de la concentration de surface en $O_3$ aux paramètres de l'aridité du sol et de la diminution de la biomasse est réalisée. Nos résultats montrent que l'aridité du sol est un facteur clé pendant les événements de sécheresse, diminuant considérablement les émissions de $C_5H_8$ et la vitesse de dépôt sec de l'$O_3$. Cet effet a un impact plus important que la diminution de la biomasse. Cependant, son impact net sur la concentration de surface en $O_3$ reste limité.

La concentration observée en $O_3$ est en moyenne significativement plus élevée pendant les vagues de chaleur ($+18\mu g/m^3$ en maximum journalier) et les sécheresses ($+9\mu g/m^3$) par rapport aux conditions normales. D'après les simulations réalisées, cela s'explique par une augmentation générale des émissions de précurseurs d'$O_3$ (en accord avec les observations de $HCHO$), une diminution du dépôt sec d'$O_3$ et des conditions météorologiques favorables. Par ailleurs, près de la moitié des jours d'été dépassant l'objectif de la qualité de l'air (pour l'$O_3$) fixé par l'Union Européenne se produit pendant les sécheresses ou vagues de chaleur. Les vagues de chaleur sont les événements caractérisés par la plus grande fraction de jours de dépassement (34%) et les concentrations les plus élevées ($+24\mu g/m^3$ au-dessus du seuil). Je souligne la nécessité d'une représentation plus dynamique des interactions entre la végétation, l'hydrologie, la météorologie et la chimie atmosphérique dans les modèles, afin d'améliorer la simulation de l'$O_3$ en été.

**Mots clés**: sécheresses, vagues de chaleur, émissions biogéniques, dépôt sec des gaz, pollution à l'ozone, modélisation régionale, CHIMERE, ORCHIDEE, WRF, observations in-situ et satellites, Méditerranée.

# Remerciements

Ce manuscrit conclut trois années de doctorat passées au Laboratoire de Météorologie Dynamique. Si je devais décrire l'évolution de mon ressenti par rapport à mon sujet de thèse, je m'appuierais sur l'effet Dunning-Kruger qui est applicable, je pense, à une grande majorité de thésards.
Dans un repère orthogonal avec le niveau de compétence en abscisse et le niveau de confiance en ordonnée, l'arrivant thésard peut faire preuve d'une légère « surconfiance » par rapport à son expérience. Culminant sur la dénommée (injustement?) « montagne de la stupidité », le thésard y séjourne quelques temps, et très rapidement se rend compte de la complexité du sujet à étudier. Alors, il descend, que dis-je, il dégringole pour se retrouver dans la « vallée de l'humilité », lieu bien moins gratifiant; le niveau de confiance y est plutôt bas et le temps y est long. A son heureuse surprise, il peut compter sur ses pairs (qui sont nombreux) et le « syndrôme de l'imposteur » dont il pourrait souffrir s'éloigne. C'est dans cette « vallée de l'humilité » que le niveau de compétence augmente graduellement mois après mois. Sur les derniers temps, le thésard aperçoit au loin un léger relief annonciateur d'un rehaussement de confiance mais cette fois-ci en accord avec son réel niveau de compétence. Au bout de la promenade doctorale, le thésard peut enfin gravir les premières marches du « plateau de la consolidation ».

Plus sérieusement, bien que le doctorat demande beaucoup d'efforts, paradoxalement il apporte énormément de plaisirs et de satisfactions. Qui plus est, je suis convaincu qu'il est générateur de souvenirs inoubliables. Pour conclure cette thèse, et avant d'entamer la lecture de ce manuscrit, j'aimerais remercier de nombreuses personnes qui ont rendu ce projet à la fois agréable et enrichissant.
Je commencerais tout d'abord par ceux qui m'ont assisté et dirigé cette thèse: mes encadrants. Toujours disponibles et à l'écoute, ils ont prodigué de bons conseils et ont fait preuve de tolérance à mes approximations répetées.
Merci Solène pour la confiance que tu m'as accordée depuis le début, pour ta pédagogie et ton exigence quant à la démarche scientifique.
Merci Jan pour ton enthousiasme, ton sens critique et ta curiosité scientifique.

Merci à Jean-François Müller, Jean-Christophe Calvet, Juliette Lathière, Samira Khodayar Pardo et François Ravetta pour avoir accepté de faire partie de mon jury de thèse.

Merci à Juliette (de nouveau) et Augustin, membres de mon comité de suivi, qui ont permis d'orienter et d'affiner mon projet de recherche.

Ensuite, j'aimerais remercier toutes les personnes rencontrées qui ont égayé cette aventure doctorale. Ces rencontres, qu'elles aient été de longue ou de courte durée, ont été bénéfiques. Elles se sont passées dans des cadres multiples. Je citerais bien évidemment le laboratoire et l'école doctorale, mais également le club sportif de l'X, l'association des doctorants Doc'Up, la coloc et le Palais de la Découverte. Comme il est de coutume, il me faut à présent faire face à la liste de prénoms. Merci Aurore (x2), J-B, Lulu, Alexis, Rémy, Mathieu, Maureen, Olivier (x2), Bastien, Nicolas, Léo, Isa, Djamila, Laura, Guigui, Sylvain, Marco, J-F, Laurent, Arnaud, Vincent, Anthony, Antoine, Assia, Milena, Doug, Arineh, Alessandro, Fanny, Jérémie, Isabella, Joan, ... Ne me tenez par rigueur de tous ceux que, malencontreusement, j'aurais oubliés.

Finalement, merci à ma famille et à mes amis de Belgique et d'ailleurs pour leur soutien au quotidien.

# Contents

# List of acronyms and abbreviations

| | |
|---|---|
| AET | Actual evapotranspiration |
| APIFLAME | Analysis and prediction of the impact of fires on air quality modeling |
| AR | Assessment report |
| AQ | Air quality |
| BA | Burned area |
| CDI | Climate driver index |
| CORDEX | Coordinated regional climate downscaling experiment |
| CRU | Climate Research Unit |
| CTM | Chemistry-transport model |
| DGVM | Dynamic global vegetation model |
| DMS | Dimethyl sulfide |
| EEA | European Environment Agency |
| EF | Emission factor |
| EFFIS | European Forest Fires Information System |
| EMEP | European Monitoring and Evaluation Programme |
| ET | Evapotranspiration |
| EU | European Union |
| FD | Fire duration |
| FRP | Fire radiative power |
| GHG | Greenhouse gases |
| GPP | Gross primary productivity |
| HTAP | Hemispheric transport of air pollution |
| HyMeX | Hydrological cycle in the Mediterranean experiment |
| IGBP | International Geosphere–Biosphere Programme |
| IPPC | Intergovernmental Panel on Cimate Change |
| IR | Infraread |
| LAI | Leaf area index |
| LMD | Laboratoire de Météorologie Dynamique |
| Med-CORDEX | CORDEX for the Mediterranean |

| | |
|---|---|
| MEGAN | Model of emissions of gases and aerosols from nature |
| MODIS | Moderate-resolution imaging spectroradiometer |
| NEMO | Nucleus for european modelling of the ocean |
| NDD | Number of dry days |
| NDVI | Normalized difference vegetation index |
| NHD | Number of hot days |
| NRC | National Research Council |
| OMI | Ozone monitoring instrument |
| ORCHIDEE | Organising carbon and hydrology in dynamic ecosystems |
| PBL | Planetary boundary layer |
| PDSI | Palmer drought severity index |
| PET | Potential evapotranspiration |
| PLA | Percentile limit anomalies |
| PM | Particulate matter |
| PPB | Parts per billion |
| PPM | Parts per million |
| PPFD | Photosynthetic photon flux density |
| RCP | Representative concentration pathway |
| RegIPSL | Regional earth system model of the Institut Pierre Simon Laplace |
| sc-PDSI | self-calibrated PDSI |
| SM | Soil moisture |
| SOA | Secondary organic aerosol |
| SPI | Standardized precipitation index |
| SPEI | Standardized precipitation evapotranspiration index |
| SWI | Soil wetness index |
| SWS | Soil water stress |
| TOAR | Tropospheric ozone assessment report |
| UV | Ultraviolet |
| VOC | Volatile organic compound |
| AVOC | Anthopogenic VOC |
| BVOC | Biogenic VOC |
| NMVOC | Non-methane VOC |
| WHO | World Health Organization |
| WRF | Weather research and forecasting |

# Chapter 1

# Introduction

There are strong interactions between meteorological conditions, hydrological conditions, vegetation and atmospheric chemistry. Meteorological conditions are key to understand the variability of many surface atmospheric pollutants and of the vegetation state. The latter acts as a major source and sink for several atmospheric chemical species.

Droughts and heatwaves are extreme weather events that perturb considerably the biosphere, and modify atmospheric chemistry. There is a strong need to better characterize such extreme events and their effects, especially agricultural droughts for which knowledge remains limited. In this work, I will focus more specifically on their impact on surface ozone ($O_3$). As one of the main oxidants in the troposphere, it plays a key role in the equilibrium of its composition. However, at high concentrations, it is also harmful to human health and vegetation and is therefore one of the main pollutants monitored for air quality control. Although the co-variability between heatwaves and $O_3$ peaks is identified, such relationship is less certain for droughts. The variability of $O_3$ concentration is generally well represented in chemistry-transport models (CTM) compared to observations, but the amplitude of the variations is more difficult to simulate (peaks and minima). One factor that has been identified as a possible cause of these uncertainties is the lack of interactions between the biosphere and the atmosphere. This is for instance the case of the CHIMERE model that is largely used for both research and operational air quality monitoring and forecasting.

Meeting an identified need from the scientific literature, the research area of this PhD is about the interactions between the vegetation and the atmospheric chemistry during extreme weather events. More specifically, it focuses on the impact of agricultural droughts and heatwaves on $O_3$ pollution, through stressed vegetation.

The study area is delimited to the Mediterranean region, and more specifically to its western part for three main reasons: the diversity and abundance of vegetation, the availability of scientific observations used for this thesis and the large vulnerability to climate change.

## Contents

## 1.1 The Mediterranean

### 1.1.1 Climate variability

The Mediterranean climate is generally described as mild and wet in winter, and warm and dry in summer. It is highly variable, both spatially and temporally.

The Mediterranean region has specific spatial characteristics. It extends over the latitudinal band 30-46°N, covering a transitional area between arid and temperate climates characterized by a strong latitudinal temperature gradient. Based on in-situ observations, the summer mean air temperature (at 2m above surface) can vary up to 15°C depending on the latitude (Panthou et al., 2018). While the Southern Mediterranean is affected by sinking air (hot and dry) from the descending branch of the Hadley cell (especially in summer), the northern part is under the influence of the mid-latitude westerlies coming from the North Atlantic ocean (fresher and wetter air) (Jansa et al., 2017). Moreover, several pressure systems (anticyclone and depression) can evolve and converge over this large area (Cassou et al., 2005).

The Mediterranean sea plays an important role in the regional climate. Connected to the Atlantic Ocean by the Strait of Gibraltar, it is an enclosed basin that acts as moisture reservoir in the hydrological cycle (Moatti et al., 2018). More locally, moisture can be transported by sea-breeze when thermal difference between sea and land is significant. In daytime and from spring to fall, moisture can be advected from the sea up to 150km inland (Drobinski et al., 2018).

The complex morphology of the Mediterranean basin (Fig. 1.1) is another key feature explaining the spatial variability of climate variables (Lionello et al., 2006). The topography is varied, ranging from mountain chains (e.g. Alps, Pyrenees) to plains (e.g. Pô Valley). The coastline is very sinuous, with peninsulas (e.g. Iberia), gulfs (e.g. Lyon) and islands of different sizes (e.g. Corsica, Balears). Those characteristics induce complex temperature, precipitation and wind distribution. Figure 1.2 maps the spatial distribution of total precipitation between October and March, averaged over the 1951-2009 period. With an underlying south-north gradient, precipitation distribution follows mainly relief patterns, with values ranging from 150mm (e.g. Morocco) up to 1400mm (e.g. the Alps) (Philandras et al., 2011).

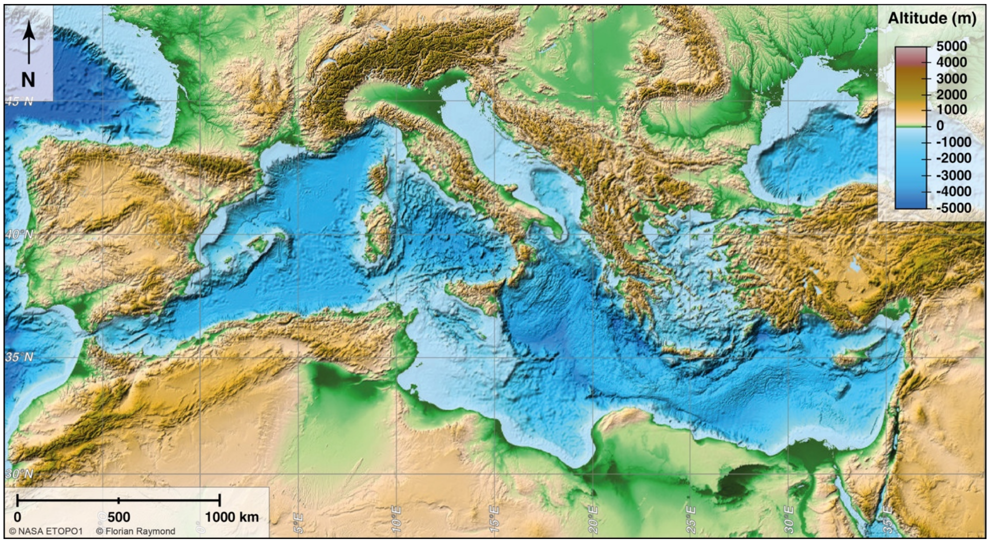

Figure 1.1: Figure from Raymond et al. (2018a), based on the Digital Elevation Model NASA ETOPO1 (Amante and Eakins, 2009). Topography and bathymetry of the Mediterranean basin.

The Mediterranean climate varies at both seasonal and annual scale. During a typical year, around 50% of the annual precipitation occur during the wet season which runs from October to March (Philandras et al., 2011). This percentage can vary across the region; it is generally higher (∼80%) in the Eastern Mediterranean (Xoplaki et al., 2004). Precipitation during fall and winter are critical for the water balance of the summer season, though sparse storms and local convective systems can occur in summer (Kelley et al., 2012). Regarding the temperature, the seasonal amplitude can range from ∼12°C in winter to ∼25°C in summer on average (Panthou et al., 2018).

Inter-annual variability of summer climate in the Mediterranean is also explained by the distribution of latent and sensible heat. Stéfanon et al. (2014) highlight the importance of the soil moisture-temperature feedback during summer. A dry soil cannot provide latent heat cooling by evapotranspiration and, therefore, contributes to the warming of temperature (Khodayar et al., 2015). In addition, dry convection increases the height of the planetary boundary layer (PBL) leading to the development of upper anticyclonic conditions (Zampieri et al., 2009). Finally, an atmosphere with lower humidity is less favourable for cloud formation, resulting in enhanced solar radiation (Liu et al., 2020).

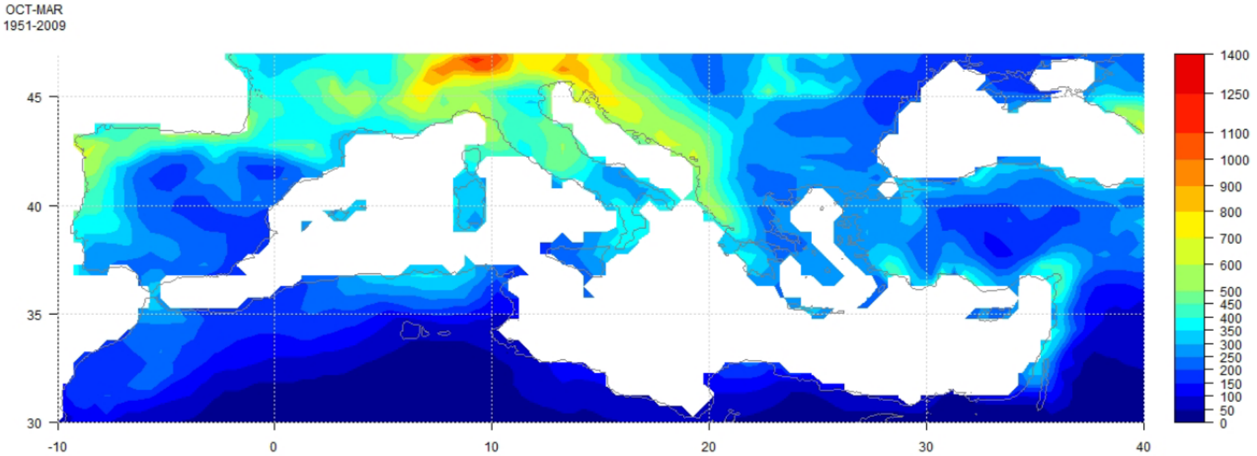

Figure 1.2: Figure from Philandras et al. (2011), based on CRU TS 3.1 data (Harris et al., 2014). Spatial distribution of mean precipitation for the rain season (October–March) over 1951–2009.

### 1.1.2 Climate change hotspot

Emissions of greenhouse gases (GHG) from human activities have increased exponentially since the industrial era, i.e. from 1850 until now (period defined in climatology field). For instance, $CO_2$ concentration has increased from 282 parts per million (ppm) to 417 ppm over this period in Mauna Loa site (Hawaii). Contributing to a net positive radiative forcing, GHG emission increase has induced climate warming at global scale (IPCC, 2021). The Mediterranean region has been for several years and is still identified as a climate change hotspot according to the 6th and last Assessment Report (AR) of the Intergovernmental Panel on Climate Change (IPCC), where warming and drying there are higher than the global average. The map in Figure 1.3 (high left panel) displays the trend of summer air temperature over the 1980-2014 period, based on extensive networks of weather station observations (CRU v4.04 database (Harris et al., 2020)). The temperature increased all over the Mediterranean varying between 0.20°C/decade (e.g. Portugal) and 0.75°C/decade (e.g. Greece) (Cos et al., 2021). This regional warming trend is expected to pursue according to recent climate projections (Fig. 1.3, high right panel).

Such warming trend has led to an increase in both duration and intensity of extreme hot periods over the last decades. 6 over the 11 record-breaking heatwaves during the period 1950-2014 over Europe occurred after 2000 (Russo et al., 2015). Extraordinary heatwaves that led recently to all-time temperature records (e.g. 46°C in metropolitan France during June 2019 (Vautard et al., 2020)) are projected to become normal heatwaves by the end of the 21st century (Molina et al., 2020).

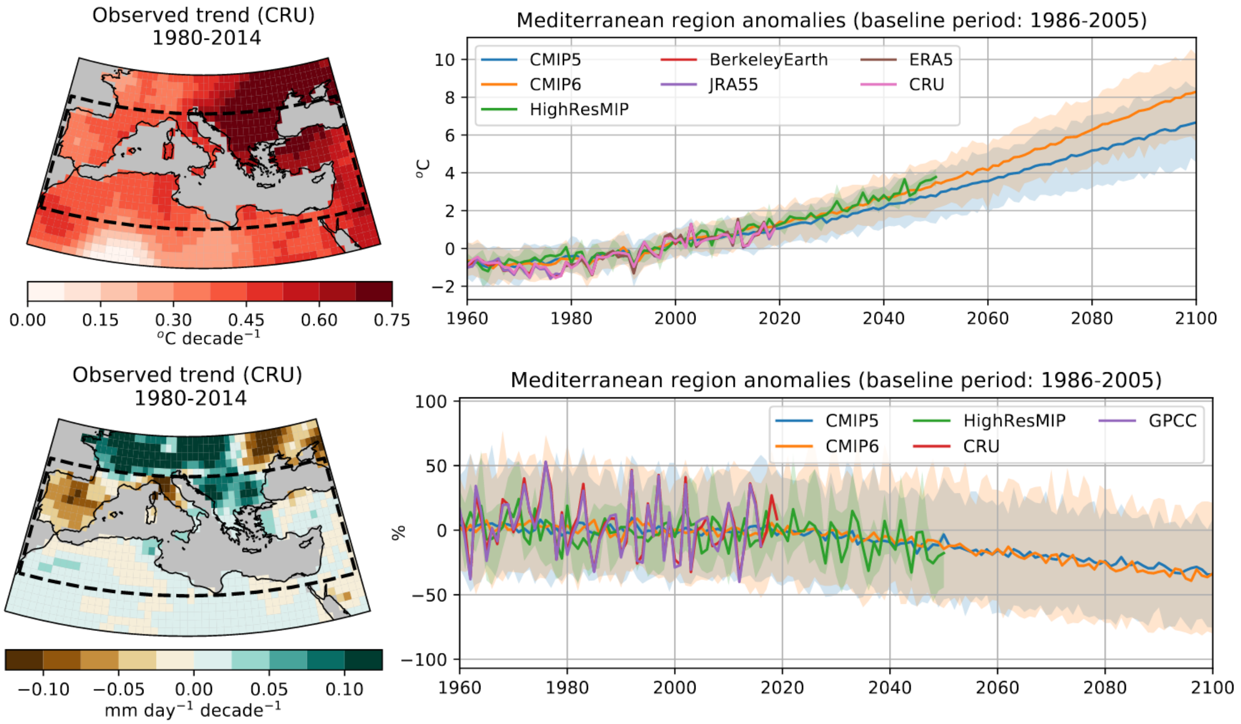

Figure 1.3: Figure from Cos et al. (2021). The map (top left panel) shows the trend of near-surface air temperature over the period 1980-2014, based on CRU (v4.04) observations. The time series plot (top right panel) shows the anomalies in the Mediterranean region with respect to the period 1986-2005 for the multi-model ensembles and the observational references. The low panels show the same for summer precipitation rate.

Regarding precipitation, trends are more heterogeneous, varying both spatially and seasonally. For rain season, Philandras et al. (2011) compute a significant decrease of precipitation during the 1951-2009 period over the whole Mediterranean except for Southern Italy, Northern Portugal, Turkey and Libya. For the summer season, trend (1980-2015) is negative over the Western Mediterranean (between -0.05 and -0.10mm/decade) and positive over the Eastern part (between +0.02 and +0.08mm/decade) (Fig. 1.3, low left panel). Recent climate projections simulate a reduction of summer rainfall by ∼20% at regional scale for the 2041-2060 period, compared to 1986-2005 (Cos et al., 2021).

In agreement with those precipitation trends, the driest periods observed over 1950-2012 occurred from the early 1990s in the Western Mediterranean (Spinoni et al., 2015). Furthermore, summer meteorological droughts are expected to be more severe in the Mediterranean with the current trends of GHG emissions (e.g. Tramblay et al., 2020; Drobinski et al., 2020). Definitions of the different types of droughts are given in the following section (see Sect. 1.2).

Finally, both meteorological droughts and heatwaves in the Mediterranean represent a real threat to the 520 millions of inhabitants living in this area (Anastasiou et al., 2021). Impacts can affect diverse activity sectors; the environment (e.g. increasing risk of fires (Moriondo et al., 2006)), the economy (e.g. reduced crop yield (Abd-Elmabod et al., 2020)) and the public health (e.g. death peaks during heatwaves (Vandentorren et al., 2006)). Moreover, meteorological droughts worsen the situation of water scarcity which is already alarming for some countries of the Mediterranean basin (Moatti et al., 2018; Cherif et al., 2020).

## 1.2 Droughts and heatwaves

### 1.2.1 Definitions

The definition of an extreme weather event is a critical step in the conducted research. In most cases, heatwaves are based on temperature only. They are described as a period of several days during which temperature is above a given threshold (Stéfanon et al., 2012a).

Droughts are more complex as they can be defined at different steps of the hydrological cycle. They are generally described by a prolonged period of water shortage. Rivoire et al. (2019) demonstrate that the chosen variable(s) for the dry day definition can impact considerably the analysis findings. However, the adequate definition depends on the drought type; as the timescale and nature of the processes involved are type specific (Svoboda and Fuchs, 2016). Droughts can be divided into three types:

- meteorological, defined by precipitation deficit or excess of evapotranspiration;
- agricultural, defined by the soil dryness limiting the water supply for plant growth;
- hydrological, defined by the limited soil water reservoir for underground and/or surface flows.

Prolonged meteorological droughts can lead to agricultural and hydrological droughts. In the latter two types, land surface and underground processes are directly involved, for which human activities can interfere with. Figure 1.4, from Van Loon et al. (2016), illustrates the propagation from meteorological droughts to agricultural and hydrological droughts initiated by both climatic and human drivers. For instance, land management through irrigation can attenuate and even prevent the propagation of a meteorological drought to an agricultural one (at local scale). Nevertheless, this activity being water-demanding can shift the stress on the aquifers from which water is extracted, and therefore induces a hydrological drought. More generally, ecological and socio-economic impacts due to droughts provoke responses which in turn, can influence the human activities and on longer term, the climate variability. In conclusion, Van Loon et al. (2016) emphasize the need to consider human inflows, outflows and storage changes for future researches about droughts. This highlighted guideline represents a real challenge for land surface and hydrological models (e.g. Garrigues et al., 2015).

For the impact analysis on the biosphere (see Chap. 5) and the ozone pollution (see Chap. 6), this thesis will be mainly focused on agricultural droughts.

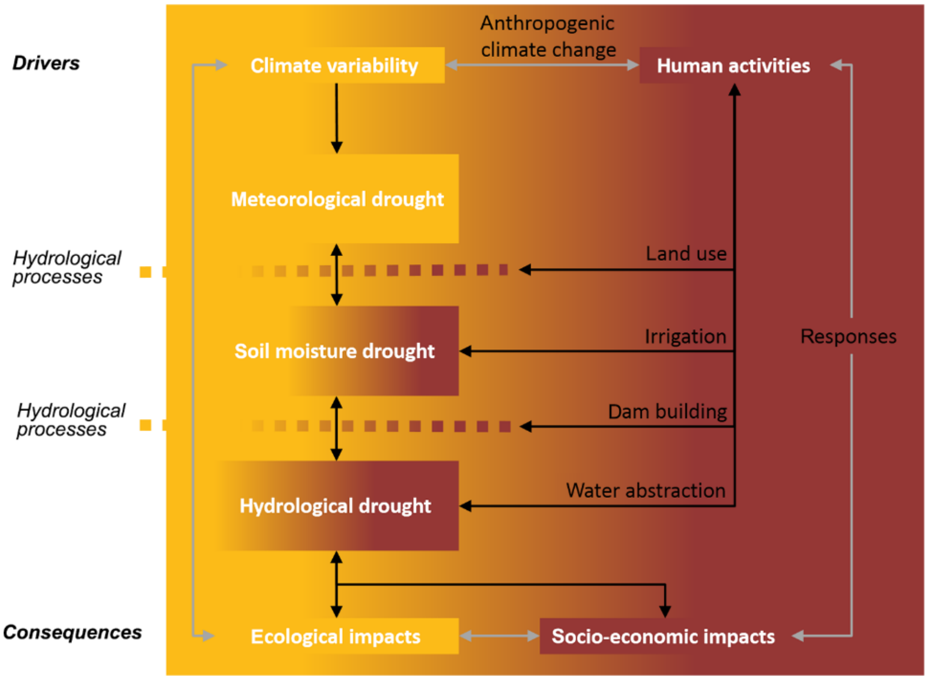

Figure 1.4: Figure from Van Loon et al. (2016). The propagation from meteorological drought to soil moisture and hydrological drought (vertical black arrows) is initiated by climatic (left; yellow) and human (right; red-brown) drivers. Drought is modified by hydrological catchment processes (dotted lines) that are altered by human activities (horizontal black arrows).

### 1.2.2 General overview of identification methods

There are many methods to quantify the severity (i.e. information about intensity, temporal and spatial extent) of heatwaves and droughts. The choice of method depends on the subject and objectives of the conducted research. Methods can be divided into two groups: indicators and indices (Svoboda and Fuchs, 2016). While indicators are directly using variables or parameters (e.g. temperature, precipitation), indices are the result of a calculation using environmental inputs (that can also include indicators) in order to summarize severity information. Furthermore, drought and heatwave severity can be assessed through their ecological and socio-economic impacts.

It must be emphasized that the overview of identification methods presented in this subsection covers only a limited part of the methods. This is the result of a state of the art study performed in the framework of this research project. The focus on some methods (e.g. SPEI) is arbitrary, but justified by the content of this thesis.

#### Threshold anomalies as indicator

A simple method to highlight dry or hot conditions is to compute deviation time series from a long term seasonal average for a considered variable (e.g. Hoerling et al., 2012). For instance, positive (negative) anomalies of temperature (rainfall) correspond to hotter (drier) conditions than the normal. However, this is not sufficient to detect extreme events.

Many studies normalize the anomaly distribution with a probability density function and establish a high percentile (e.g. 80th) as a threshold (e.g. Stéfanon et al., 2012a). As explored in Rivoire et al. (2019), the threshold can be either fixed or time-varying in order to take into account the long-term positive trend of temperature due to global warming. Another possibility is to detrend linearly the temperature anomalies distribution (e.g. Vautard et al., 2007).

Supplementary criteria on the spatial and temporal extension may be added in order to better assess the severity of the event. Several consecutive days are generally required to avoid any short-term high anomalies. In the same way, the spatial extent needs to reach a given surface or fraction area (e.g. Lhotka and Kyselý, 2015).

Furthermore, threshold can be applied on the spatial and/or temporal criteria. For instance, Raymond et al. (2016) fixed a percentile threshold (80th) on the winter dry spell duration in the Mediterranean. A dry spell is simply considered as a period of at least two consecutive days with less than 1mm of precipitation. The events shorter than the 20th percentile of dry spell duration are grouped into the "very short dry spells" category and those longer than the 80th into the "very long dry spells" category.

### Drought indices

Even if indices can be used for heatwave detection (e.g. Molina et al., 2020), they are more commonly used for droughts. They allow to sum up the complex processes involved in drought development. The following content presents a few drought indices present in the scientific literature that are mentioned or calculated in this thesis.

- The Palmer Drought Severity Index (PDSI) (Palmer, 1965) was developed some time ago but is still used (e.g. Vicente-Serrano et al., 2012). It computes water balance by including precipitation, water demand and soil storage (empirically derived). The water demand is computed from potential evapotranspiration (PET) and the soil storage from potential soil moisture capacity. PET is based on the simple calculation of Thornthwaite (1948) requiring only the temperature, latitude and month.
The initial parameters used in the PDSI were empirically developed from measurements in regions located in the United States. It has been improved into the self-calibrated PDSI (sc-PDSI) (Wells et al., 2004) by integrating a dynamical computation of the parameters on the chosen study area. As a consequence, the sc-PDSI allows spatial comparisons (e.g. Cook et al., 2016).
Although this index is able to identify meteorological droughts, it shows limited performance for agricultural droughts (e.g. Vicente-Serrano et al., 2012), due to a lack of representation of hydrological processes.

- Largely used, the Standardized Precipitation Index (SPI) (McKee et al., 1993) is appreciated for its simplicity and versatility. Its computation depends on precipitation only (at monthly time step). Standard deviations from a long term mean are standardized and converted into a probability function.
Unlike the sc-PDSI, the SPI is a multi-scalar index allowing to identify droughts at different time and spatial scales (thanks to its computation method). Moreover, the SPI can be computed by accumulating monthly precipitation over different duration. The SPI is suited for meteorological droughts. Nevertheless, agricultural droughts could be deducted from long-term precipitation deficit (between 4 and 24 months) according to Vicente-Serrano et al. (2012), but without providing accurate assessment.
The main weakness of the SPI is the absence of information related to temperature, especially since the influence of warming conditions on soil dryness has been clearly demonstrated (soil moisture-temperature feedback (e.g. Stéfanon et al., 2014)). Moreover, the SPI is highly dependent on the robustness of the precipitation data series.

- Vicente-Serrano et al. (2010) have improved this index by taking into account the temperature variability with the inclusion of the atmospheric evaporation demand. The Standardized Precipitation Evapotranspiration Index (SPEI) is also a multi-scalar drought index. It gives an estimate of the quantity of water in the ground available after evapotranspiration, taking into account the meteorological conditions of the previous period. SPEI has shown good performance (Vicente-Serrano et al., 2012) and is largely used. Since this index will be used in this thesis, the calculation method is developed here.

The water balance is calculated as the difference between the accumulated monthly precipitation ($P_m$) and the potential evapotranspiration ($PET_m$, from Thornthwaite (1948)):

$$D_m = P_m - PET_m \tag{1.1}$$

When $D_m$ is positive, the excess water (called useful water) can allow water runoff and infiltration in the soil and is assumed as available for plants. When $D_m$ is negative, the considered month is in a deficit. The $D_m$ series need to be normalized using a log-logistic distribution, which adjusts to the extreme values:

$$F(D_m) = \left[1 + \left(\frac{\alpha}{x - \gamma}\right)^{\beta}\right]^{-1} \tag{1.2}$$

where $\alpha$ is the parameter of scale, $\beta$ of shape and $\gamma$ of origin used for the the distribution of $D$ series. Vicente-Serrano et al. (2010) show that this function with empirical values from Singh et al. (1993) provides a good representation of the $D_m$ series in various locations and climates. Once the distribution function $F$ adjusted, the SPEI for month $m$ is derived from the standardized value of $F(D_m)$ following the approximation of Abramowitz et al. (1965) :

$$SPEI = W - \frac{C_0 + C_1 W + C_2 W^2}{1 + d_1 W + d_2 W^2 + d_3 W^3} \tag{1.3}$$

where

$$W = \sqrt{-2ln\left(P\right)}\ \ for\ \ P \leq 0.5 \tag{1.4}$$

and

$$P = 1 - F(x) \tag{1.5}$$

with the constants $C_0$ = 2.515517, $C_1$ = 0.802853, $C_3$= 0.010328, $D_1$ = 1.432788, $D_2$ = 0.189269, $D_3$ = 0.001308. If $P > 0.5$, $P$ is replaced by 1-$P$ and the sign of SPEI is reversed. An index of 0 represents normal conditions (average value of SPEI). A negative (positive) index means that the studied period is drier (wetter) than normal conditions. The standard deviation is 1. The SPEI gives information on the drought severity through its intensity and duration if the index is below -1 on consecutive months.
However, it has to be interpreted carefully since PET can be largely different from the actual evapotranspiration (AET). The PET calculation (based on temperature) assumes no water limit, whereas in some regions like (semi-)arid environments, the lack of soil water availability is the limiting factor.

- Both SPEI and sc-PDSI approximate the soil water availability using simplified methods of atmospheric evaporative demand. Nevertheless, the soil water content is more complex to compute as it depends on the soil type and structure that determine the water holding capacity, but also on the vegetation type and species that have different water demand (Bittelli, 2011).
Such complex processes need to be resolved dynamically using a land surface and vegetation model (e.g. ORCHIDEE (Maignan et al., 2011)) from which the soil wetness at each soil layer can be derived. The Soil Wetness Index (SWI) is equal to the ratio between the ground water content and the accessible water content. Such kind of index is convenient for identifying agricultural droughts, especially in ecologically heterogeneous regions. In this thesis, SWI is used for drought detection and compared to the SPEI (see Chap. 4).

## 1.3 Tropospheric ozone

### 1.3.1 Global budget

Composed of three oxygen atoms (O), ozone ($O_3$) is a highly reactive gas both anthropogenic and naturally produced (secondary species). It is important in environmental sciences because it (i) is an important GHG to consider in the radiation balance of the Earth, (ii) contributes largely to the oxidizing power of the atmosphere and finally, (iii) is harmful to vegetation and human health at high concentration (Jacob, 1999).

As illustrated in Figure 1.5, $O_3$ is mostly present in the stratosphere (from ∼15km to ∼50km in altitude), forming the $O_3$ layer (90% of total $O_3$). The stratopsheric $O_3$ layer protects humans and ecosystems by filtering the Ultraviolet (UV) radiation from the sun. The last fraction of $O_3$ is found in the troposphere, and comes from two sources: stratosphere-troposphere exchanges and chemical production. In the low troposphere and more specifically within the Planetary Boundary Layer (PBL), ozone can be produced in large quantities from highly non linear chemical reactions involving primary pollutants emitted by human activities and natural sources. This thesis focuses on the surface concentration of $O_3$ because the exposure of humans and vegetation to such pollution occurs at this level.

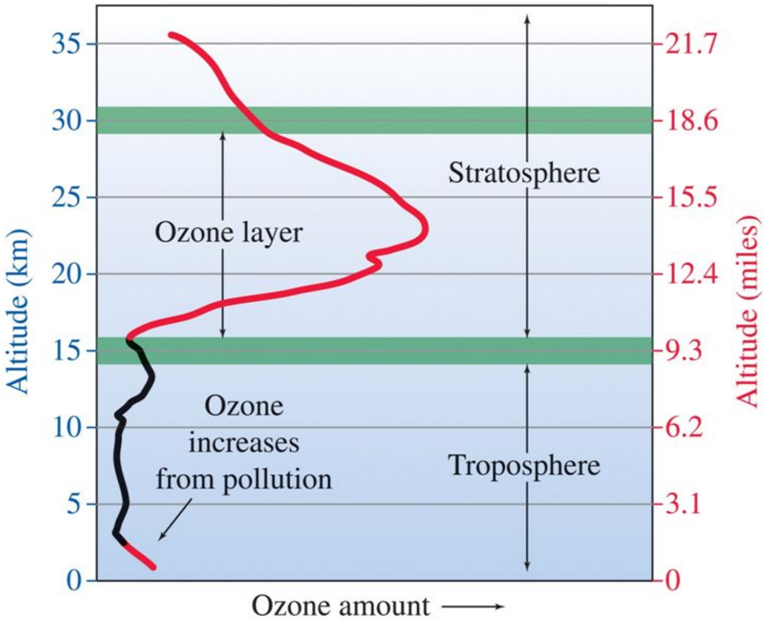

Figure 1.5: Vertical distribution of ozone in the atmosphere. ©McGraw-Hill Companies, Inc.

An example of global budget simulated by the GEOS-Chem chemistry-transport model (CTM) is shown in Table 1.1 (Hu et al., 2017). Influx from the stratosphere account for ∼6% of the sinks. This value is slightly lower than other studies (e.g. ∼10% in the IPCC-AR5).

The main source of $O_3$ (∼94%) is by chemical production. $O_3$ is a secondary air pollutant, formed from a chain of photochemical reactions with precursors. The most abundant $O_3$ precursors are nitrogen oxides ($NO_X$, where $NO_X = NO + NO_2$) and volatile organic compounds ($VOCs$). $VOCs$ are chemical compounds of various structures made of at least one carbon atom (C) and found in a gaseous state in the atmosphere. They can contain diverse compounds such as hydrogen, oxygen, nitrogen or silicon, resulting in a huge variety of VOC species (Koppmann, 2008). Methane ($CH_4$) is the most abundant VOC in the atmosphere and is generally distinguished from the others, under the designation non-methane $VOCs$ ($NMVOCs$). VOCs can be emitted from natural (e.g. wildfires, vegetation) and human sources. VOC species emitted by plants or microorganisms are referred to as biogenic VOCs (BVOCs). Anthropogenic VOCs (AVOCs) are emitted by human activities such as the production of solvents and fossil fuel use. The lifetime of VOCs varies a lot; from a few hours to several days. In addition to be ozone precursors, VOCs are an important source of Secondary Organic Aerosols (SOA).

$NO_X$ are highly reactive trace gases emitted from natural (e.g. lightning, soil) and anthropogenic sources (combustion processes from vehicles and power plants) (Atkinson, 2000). They count among the main pollutants in urban centers. The lifetime of $NO_X$ in the atmosphere is estimated at several hours.

The $O_3$ chemical production and loss processes will be briefly described in the next subsection (see Sect. 1.3.2).

$O_3$ can be removed from the troposphere by two processess: deposition (∼18%) and chemical loss (∼82%). These values are calculated on a global scale, i.e. without taking into account the transport. A differentiation is made between wet and dry deposition. Wet deposition (∼1%) occurs by precipitation scavenging while dry deposition (∼17%) is due to stomatal (through plant stomata) and non-stomatal uptake (leaf cuticles, soil or any other materials).

Table 1.1: Global budget of tropospheric ozone in a year [Tg/a] calculated using the GEOS-Chem model. Table is from Hu et al. (2017).

| | |
|---|---|
| **Sources [Tg/a]** | |
| Chemical production | 4960 |
| Stratosphere-troposphere exchange | 325 |
| Total | 5285 |
| **Sinks [Tg/a]** | |
| Chemical loss | 4360 |
| Dry deposition | 908 |
| Wet deposition | 17 |
| Total | 5285 |
| **Burden [Tg]** | 351 |
| **Lifetime [d]** | 24.2 |

At regional scale, the impact of transport needs to be considered for both $O_3$ sources and sinks. Due to its relatively long lifetime, from days to weeks, long-range transport can contribute to $O_3$ variation. Based on satellite measurements, Safieddine et al. (2014) demonstrated that transport contributes significantly to the tropospheric $O_3$ budget above 4km in the Eastern Mediterranean (e.g. pollution from Asia, stratosphere-troposphere exchange).

Transport can also occur at lower altitude. For instance, land transport of emitted $O_3$ precusors would have contributed to about 25% of extreme $O_3$ values (99th percentile) in the Pô Valley (2008-2010 time period), based on the estimations of Mertens et al. (2020).

### 1.3.2 Tropospheric $O_3$ chemical production

Under non-polluted conditions, a dynamic equilibrium between $O_3$, $NO$ and $NO_2$ species can be established in the troposphere (Jenkin and Clemitshaw, 2000). $NO_2$ produced from the reaction between $NO$ and $O_2$ (Eq. 1.6), can loose one atom of oxigen ($O$) by photo-dissociation (Eq. 1.7). Such photolysis occurs with photons in the wavelength range of 295-445nm. $O$ that is highly reactive, reacts quickly with $O_2$ (abundant in the troposphere) to produce $O_3$ (Eq. 1.8). $O_3$ is then depleted by $NO$ (titration process) to produce $NO_2$ and $O_2$ (Eq. 1.9). Such equilibrium occurs during the day with time scales of a few minutes.

$$2NO + O_2 \longrightarrow 2NO_2 \tag{1.6}$$

$$NO_2 + hv \longrightarrow NO + O \tag{1.7}$$

$$O + O_2 \longrightarrow O_3 \tag{1.8}$$

$$NO + O_3 \longrightarrow NO_2 + O_2 \tag{1.9}$$

This simple cycle does not lead to a net production of $O_3$. The equilibrium between $O_3$, $NO$ and $NO_2$ can be disturbed in presence of other precursors, whether at background or pollution levels. Precursors like $NMVOCs$, $CH_4$ or carbon monoxide ($CO$) are oxidized by the hydroxyl radical ($OH$). This radical comes from the reaction of water vapor ($H_2O$) and an excited oxygen atom ($O(^1D)$) (Eq. 1.11) that is produced by photolysis of $O_3$ (wavelength below 310nm) (Eq. 1.10). $OH$ is therefore present mainly during the day.

$$O_3 + hv \longrightarrow O_2 + O(^1D) \tag{1.10}$$

$$O(^1D) + H_2O \longrightarrow 2OH \tag{1.11}$$

The oxydation of these precursors (e.g. $NMVOCs$, $CH_4$) by the $OH$ radical leads to the production of hydroperoxyl ($HO_2$) and peroxyl ($RO_2$) radicals. $HO_2$ and $RO_2$ react therefore with $NO$ to form $NO_2$ (Eq. 1.12 & 1.13). However, this $NO_2$ formation happens without consuming $O_3$, leading to an increase of $O_3$.

$$HO_2 + NO \longrightarrow NO_2 + OH \tag{1.12}$$

$$RO_2 + NO \longrightarrow NO_2 + RO \tag{1.13}$$

Indeed, such reactions engage a competition with $O_3$ loss processes (Eq. 1.14 & 1.15).

$$HO_2 + O_3 \longrightarrow 2O_2 + OH \tag{1.14}$$

$$RO_2 + O_3 \longrightarrow 2O_2 + RO \tag{1.15}$$

Those additional processes, with different possible reaction chains, make the tropospheric $O_3$ cycle very complex and highly nonlinear in relation to precursor concentrations. A detailed explanation of the processes regulating the $O_3$ cycle in the PBL, including the oxidizing reactions of each $O_3$ precursor is given by Jenkin and Clemitshaw (2000). Nevertheless, it should be noted here that the oxidation cycle of $VOCs$ is much shorter than that of $CO$ and $CH_4$. As previously indicated, chemical loss of $O_3$ in the troposphere occurs either by photodissociation or by photochemical reactions (e.g. with $NO_X$, $OH$, $HO_2$ species).

Two chemical regimes depending on $NO_X$ and $VOCs$ relative concentrations can be described to understand how $O_3$ varies as a function of those precursors (NRC, 1992). Figure 1.6 shows an isopleth diagram illustrating the $O_3$ variation as a function of $NO_X/VOC$ ratio and highlighting the $VOC$ limited regime and $NO_X$ limited regime. The $VOC$ limited regime (from a $VOC/NO_X$ ratio of 4) describes an area where $NO_X$ concentration is high and $VOC$ low, such as in urban centers. In such regime ($NO_X$ in excess), $O_3$ increases when $VOC$ increases, but decreases when $NO_X$ increases. On the opposite, a $NO_X$ limited regime (from a $VOC/NO_X$ ratio of 15) is characterized by low $NO_X$ and high $VOC$. In such regime, $O_3$ increases with $NO_X$ independently of $VOC$ concentration. This regime can be found in rural area, away from major anthropogenic sources. In an intermediary regime, $O_3$ depends on both precursors.

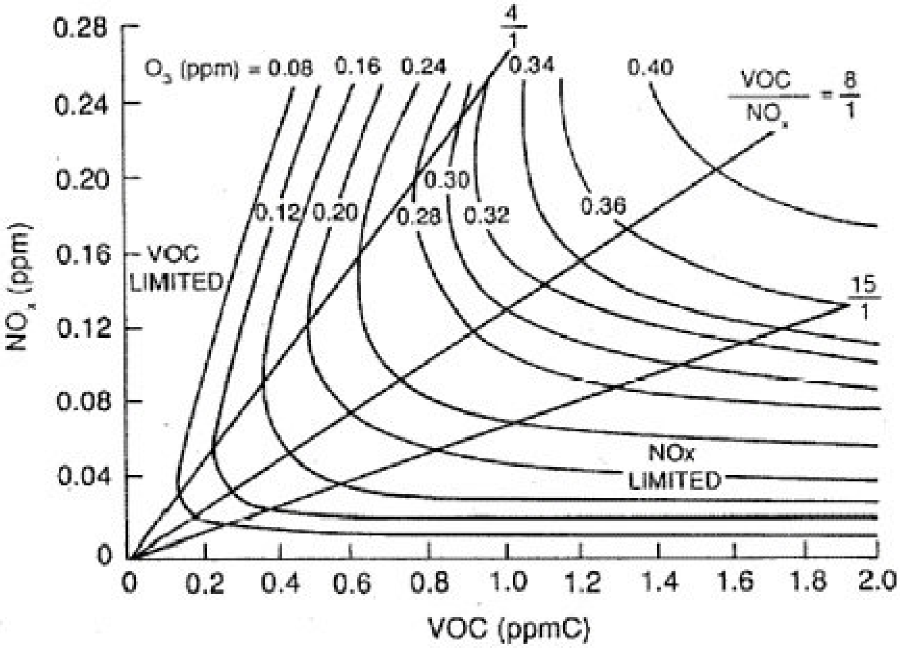

Figure 1.6: Figure from Jenkin and Clemitshaw (2000), based on NRC (1992). Example of an isopleth diagram illustrating calculated peak $O_3$ concentrations [ppm] generated from various initial concentrations of $NO_X$ and $VOCs$. For $O_3$, 1 ppm (= 1000 ppb) is almost equivalent to $2000\mu g/m^3$.

In addition to the availability of precursors, $O_3$ formation in the troposphere depends on weather conditions. High temperature and light enhance the rate of chemical reactions but also increase the emissions of precursors such as the biogenic VOCs. As a result, the variation of $O_3$ mixing ratio follows a diurnal cycle; with a maximum during the afternoon (photolysis and accumulation effect) and a minimum during the night (unfavorable weather and $O_3$ sinks still active) (Strode et al., 2019).

### 1.3.3 Threshold level exceedance and impact of high surface $O_3$ concentration

Based on toxicological studies assessing ozone exposure-response functions, concentration values not to exceed are set. They consequently define pollution levels. While European Union (EU) values are standards to respect for all Member States (according to the Ambient Air Quality Directive 2008/50/CE), World Health Organization (WHO) values are guidelines to follow. WHO values are more restrictive (i.e. with lower values). Table 1.2 presents the thresholds from the EU and the WHO. In 2018, 34% of the urban population (EU-28) have been exposed to $O_3$ concentrations above EU standards (EEA, 2020).

Table 1.2: Air quality standards for protecting human health from $O_3$, according to EU and WHO. Table adapted from EEA (2020). Symbol (*) means that this target value can not be exceeded on more than 25 days/year, averaged over three years.

| | Averaging period | Standard type and concentration |
|---|---|---|
| EU | Maximum daily 8-hour mean | Target value*: $120\mu g/m^3$ |
| | | Long-term objective: $120\mu g/m^3$ |
| | 1 hour | Information threshold: $180\mu g/m^3$ |
| | | Alert threshold: $240\mu g/m^3$ |
| WHO | Maximum daily 8-hour mean | Guidelines: $100\mu g/m^3$ |

Gathering the data from the HTAP (Hemispheric Transport of Air Pollution) and TOAR (Tropospheric Ozone Assessment Report) programmes, Parrish et al. (2021) show that the annual background level of near-surface $O_3$ increased by a factor two in Europe (e.g. from 50 to $100\mu g/m^3$ in the European Alpine) during the second part of the 21st century (1950-2000). This is mainly attributed to an increase of anthropogenic $O_3$ precursor emissions. Thanks to EU legislation, primary emissions have strongly decreased for many precursors (e.g. $NO_X$) since 2000, so that the annual background $O_3$ level has stabilised.

However, the trend signal is less clear during summer over the Mediterranean. Both negative and positive $O_3$ trends (2000-2014) were recorded (TOAR programme) with high spatial variability (Chang et al., 2017). There are substantial uncertainties about the explanatory processes. The background $O_3$ trend is the result of a complex combination of long-term evolution of biogenic and anthropogenic precursors, meteorological conditions and long range transport.

The Mediterranean is a favorable region for the formation of $O_3$ peaks; with warm and sunny weather with the presence of many precursor sources. Indeed, high values of $O_3$ concentrations (both hourly peaks and averaged days) are recorded, with a maximum in summer (generally July) (Safieddine et al., 2014). Figure 1.7 shows the maximum $O_3$ values recorded in 2018 at air quality measurement stations from the EEA (AQ e-Reporting database). Over the Mediterranean, highest values are observed in Northern Italy (Pô valley), Southeastern France and Eastern Spain, but also around urbanized areas (e.g. Madrid, Naples). Over Europe, 41% of the total stations recorded concentrations above the EU target.

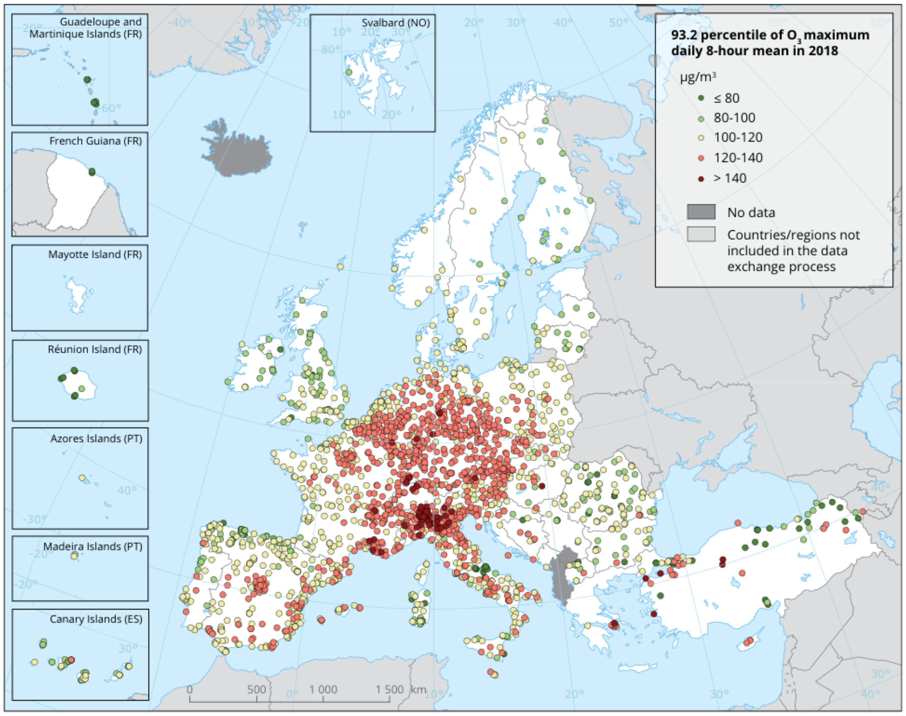

Reference data: ©ESRI | ©EuroGeographics

Figure 1.7: Figure from EEA (2020). Observed concentrations of $O_3$ in 2018. The map shows the 93.2 percentile of the $O_3$ maximum daily 8-hour mean, representing the 26th highest value in a complete series. Sites marked with dots in the last two colour categories indicate an exceedance of the target value threshold.

Over the last ten years (2009-2018), no clear tendency in extreme $O_3$ concentrations was observed at regional scale (EEA, 2020). Significant positive and negative trends were recorded at local scale with an important spatial variability. However, Sicard et al. (2013) found different results for the previous period (2000-2010): for more than 75% of the stations (AQ e-Reporting), daily peaks decreased with an averaged value of 0.76%/year, regardless the station type. It may be explained by the reduction of daily peaks in $NO_X$ and $VOCs$ emissions induced by EU regulation since the early 1990s.

At high concentrations, $O_3$ causes damages on human health, buildings and ecosystems being a highly oxidizing gas. $O_3$ effects on the human body are variable, depending on the concentration level and the exposure duration. However, it has been demonstrated that $O_3$ exposure at both short and long-term can cause eye, nose and throat tract irritation. It is also associated with an increasing risk of morbidity and mortality related to the disturbance of the respiratory (e.g. asthma attack) and cardiovascular system (Jerrett et al., 2009; Nuvolone et al., 2018). Such effects represent a significant economic cost. Im et al. (2018) assessed at 414 000 the total number of premature deaths due to air pollution (acute and chronic) in Europe for the year 2010, for a cost of 300 billion euro in the health sector. Those economic impacts also include life expectancy decreasing and working days lost for medical reasons.

As already introduced, $O_3$ is absorbed by vegetation through stomata and reacts with internal plant tissues and fluids. Even if considerable uncertainties remain about the whole physiological processes affected, clear evidences show that internal and external tissues (for non-stomatal uptake) can be oxidized and the photosynthesis inhibited (Grulke and Heath, 2020). Leaf effects are visible, as shown in Figure 1.8 with the burning marks. However, damages on vegetation should depend on the plant species and the biome. Based on satellite data, Anand et al. (2021) computed a Gross Primary Productivity (GPP) reduction induced by $O_3$ ranging from 0.36 to 9.55% over the European forests. It can also affect agricultural crop (Van Dingenen et al., 2009). Tai et al. (2014) estimate that ozone pollution enhanced by global warming (RCP8.5) could lead to a global crop yield reduction by 3.6% for 2050.

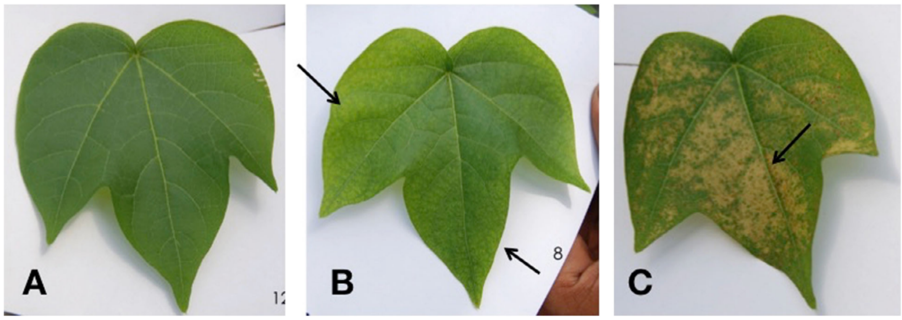

Figure 1.8: Figure from Grulke and Heath (2020). Examples of no to extreme $O_3$ exposure effects in primary cotton leaves. (A) No exposure; (B) 15-min exposure to 1200 ppb ($\approx 2400 \mu g/m^3$); (C) 15-min exposure to 2400ppb ($\approx 4800 \mu g/m^3$). Arrows in (B) indicate leaf margin "burn" while the arrow in (C) indicates lack of necrosis near the vein (photograph by D.A. Grantz).

## 1.4 Surface $O_3$ during droughts and heatwaves

As introduced previously, $O_3$ concentration depends on four main processes: emissions, chemistry, transport, and deposition (Jacob, 1999). Those processes as well as their possible evolution in a context of climate warming are schematically represented in Figure 1.9, from Lu et al. (2019). We will focus on each of those processes and the way they vary during droughts and heatwaves, based on the current literature. Being the main subject of this thesis, those processes will be further explored in the result chapters 4, 5 & 6.

### 1.4.1 Natural emissions

Based on simulations from the TOMCAT global model, Richards et al. (2013) show that the largest sensitivity of near-surface $O_3$ in the Mediterranean is, firstly, to local anthropogenic $NO_X$ emissions and, secondly, $BVOCs$ emissions. This reflects a general $NO_X$-limited ozone production regime for rural areas. Through variation of natural emissions (BVOCs and fires), droughts and heatwaves can modify considerably $O_3$ concentration.

The production of BVOCs is involved in plant development, reproduction and defence. Although BVOCs can be emitted on any surface of the plant, the major amount comes from the leaves. BVOCs production is directly related to enzymatic activity, so that abiotic stresses (e.g. light, temperature, water) can modify their emission rates (Lantz et al., 2019). Therefore, heatwaves, characterized by conditions of high temperature and intense solar radiation from a clear sky, are favorable to $BVOCs$ emissions.

However, large uncertainties remain regarding drought effects. Plant response to water stress is $BVOC$ (e.g. Bonn et al., 2019) and context specific (e.g. Genard-Zielinski et al., 2018); depending on the drought severity, the plant species and type, the soil structure and texture and the biome. Soil dryness may lead to a decrease of isoprene emissions, the dominant $BVOC$, due to limited water availability for enzyme isoprene synthase (Guenther et al., 2006, 2012). However, the amplitude of the decrease depends a lot on the chosen algorithm and its parameter. For now, the parameter generally used is the wilting point (i.e. level from which plants could not extract water from the soil). Another hypothesis involves a plant response in two phases (Potosnak et al., 2014). The primary effect (when the drought is moderate) would be an increase of $BVOC$ emissions due to a stimulation of the metabolism (increased leaf temperature). It would be followed (when the drought is severe) by an emission inhibition as explained just before. These processes are still subject to large uncertainty.

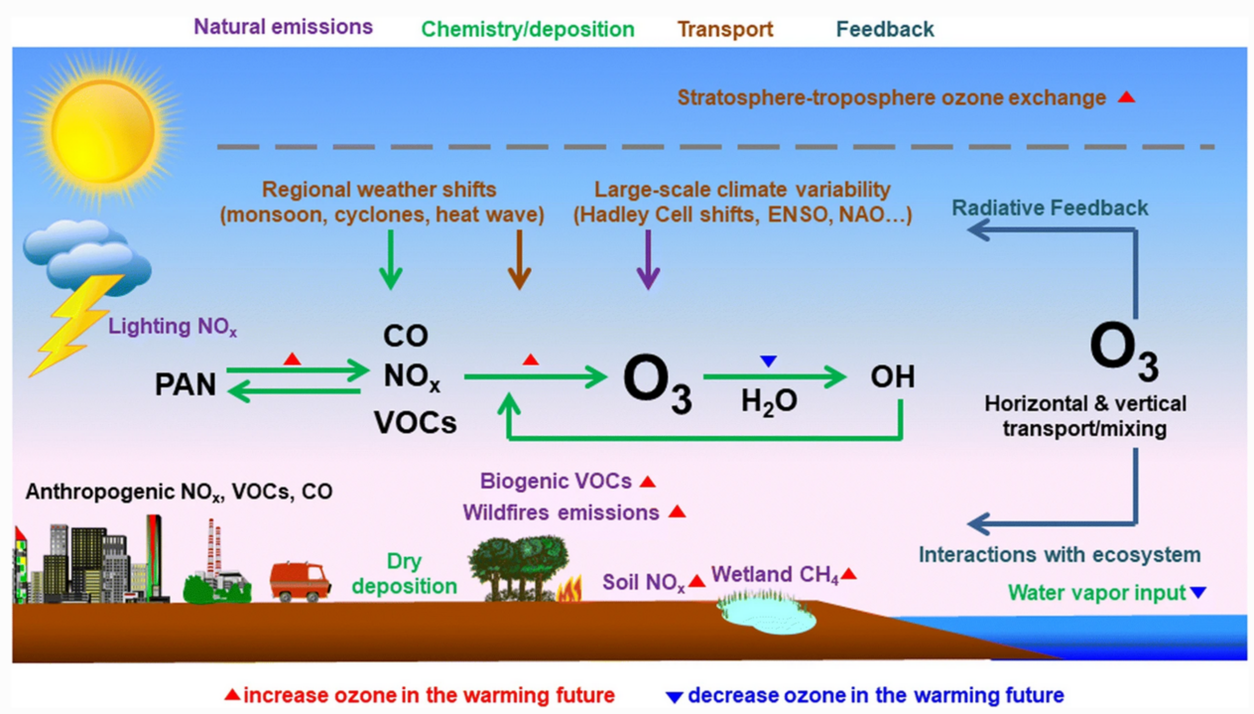

Figure 1.9: Figure from Lu et al. (2019). Pathways of interaction between meteorology/climate change and tropospheric ozone. The triangles represent the sign of future $O_3$ evolution under climate change based on current understanding. Blue triangles correspond to a decrease, red ones to an increase.

The risk of wildfires increases during hot and dry conditions (Moriondo et al., 2006). Wildfires can emit a large amount of $O_3$ precursors (e.g. $VOCs$, $CO$) in the troposphere (e.g. Majdi et al., 2019). Such events can lead to $O_3$ pollution peaks (such as in summer 2007 over Greece (Hodnebrog et al., 2012)). More information on this subject can be found in the science outreach article (Appendix A) I wrote and published in Découverte journal (available here: `https://www.palais-decouverte.fr/fr/lascienceestla/revue-decouverte/n-435-octobre-decembre-2021/articles/#item-grid-121854`). It describes the processes by which fires can impact air quality.

### 1.4.2 Photochemistry and transport

Characterized by elevated temperature and intense downward solar radiation allowing long photochemical episodes, heatwaves are often associated with $O_3$ peaks (e.g. Hertig et al., 2020). Moreover, heatwaves can occur in presence of blocked anticyclones. Such atmospheric conditions of stagnation lead to low diffusion and accumulation of $O_3$ in the troposphere (Vautard et al., 2005). Transport of $O_3$ and its precursors is therefore limited. Otero et al. (2021) computed that blocking systems increase, on average, the probability of ozone exceedances by 30 % over Europe.

Even if the relationship between heatwaves and $O_3$ peaks is identified as strong, there are still many uncertainties about the dominance between the involved mechanisms (e.g. chemical regimes, reaction rates), being complex and nonlinear (Porter and Heald, 2019).

Weather conditions associated with droughts can also, in a lower extent, be favorable to $O_3$ formation (Wang et al., 2017) due to low or absence of precipitation and cloud cover.

### 1.4.3 Dry deposition

Droughts and heatwaves can disturb considerably the stomatal uptake, having therefore an effect on $O_3$ dry deposition. Dry deposition decreases with the relative humidity of the air (Kavassalis and Murphy, 2017). This is represented by a leaf-to-air vapour pressure deficit (i.e. the difference between the amount of moisture in the air and the plant) that regulates exchanges through stomata.

Moreover, from a signal sent by its roots in conditions of soil dryness, the plant can close its stomata in order to protect itself from water loss. However, considerable uncertainties remain regarding the stress level at which this occurs (Simpson et al., 2012). Extreme hot conditions can also lead to stomatal closure to reduce transpiration. Those processes lead to $O_3$ accumulation (Lin et al., 2020).

Near plant tissues, $O_3$, as an oxidant, can alter its metabolic activity (Grulke and Heath, 2020). $O_3$-induced inhibition of stomatal uptake can then exacerbate ozone air pollution. Gong et al. (2020) estimated that inhibition of stomatal conductance can increase surface $O_3$ between 2.0 and $2.6 \mu g/m^3$ on average over the Western Europe.

## 1.5 Thesis objectives and outline

This research project aims at better understanding and assessing the impact of droughts and heatwaves on ground-level ozone pollution in the Western Mediterranean, through wildfires and vegetation activity variation.

Regional modeling has been chosen as main approach for studying this topic. This is an appropriate scientific tool, allowing to isolate, analyze and understand all the natural processes involved in this complex system. Both in-situ and satellite observations will be used to validate simulated environmental variables but also perform impact assessment.

This manuscript begins with the presentations of the material used: the models in Chapter 2 and the observations in Chapter 3. The analysis and results are then organized based on the three following scientific questions, one by chapter :

1. **What are the variations and characteristics of heatwaves, meteorological and agricultural droughts in the Western Mediterranean over the last decades (1979-2016)?**

   Chapter 4 is focused on the identification of droughts and heatwaves using the RegIPSL model, which couples the dynamical land surface and vegetation model ORCHIDEE and the atmospheric model WRF. The model performance is evaluated against surface observations of temperature and precipitation over the Western Mediterranean. Two methods of drought detection, one adapted for meteorological droughts and the other for agricultural ones, are computed and compared. Finally, the spatio-temporal variability of droughts and heatwaves is analyzed over the 1979-2016 period.

2. **What is the impact of agricultural droughts and heatwaves on the biomass and wildfire activity?**

   In Chapter 5, simulated indicators of extreme events are combined with observed characteristics of vegetation and wildfires from the MODIS satellite instrument. The isolated and combined impacts of agricultural droughts and heatwaves are statistically quantified using both correlation and cluster analysis. Moreover, observed biomass variation is compared to the simulated one by RegIPSL. Lastly, the relation between weather conditions and fuel load as drivers of the wildfire activity is discussed. An analysis of the fire weather risk during droughts and heatwaves is also provided.

3. **How do surface $O_3$ concentrations, and more specifically $O_3$ peaks, vary due to vegetation under abiotic stresses?**

   The chapter 6 assesses the effects of droughts and heatwaves on the ground level $O_3$ concentration from both observations and model. $O_3$ observations are from the European surface network AQ e-Reporting and atmospheric chemistry is simulated using the CHIMERE regional chemistry transport model with meteorological fields from the WRF model. Sensitivity analysis of biogenic emissions (computed online with the MEGAN model) to soil dryness and biomass decrease are performed. I also adapted the gas dry deposition scheme of CHIMERE to account for those drought effects, allowing to assess the contribution of both biogenic emissions and dry deposition to the variations of ozone during summer extremes.

Finally, conclusions and perspectives are presented in the last Chapter (n°7).

# Chapter 2

# Regional modeling using the RegIPSL and CHIMERE models

To analyze the impact of droughts and heatwaves on the biosphere and ozone pollution in the Western Mediterranean, five different numerical models are used at regional scale. With the benefit of a rather fine spatial resolution (~20km), the bio-climatic diversity over the Western Mediterranean is represented.
Each model covers a specific component of the Earth system relevant for this thesis :

- Land surface hydrology and vegetation dynamics are simulated by ORCHIDEE ;
- Regional meteorology is simulated by WRF, coupled or not with ORCHIDEE ;
- Regional chemistry-transport is simulated by CHIMERE, driven by the WRF meteorology ;
- Biogenic emissions are calculated online with CHIMERE using the MEGAN model ;
- Biomass burning emissions are calculated based on satellite observations of fire activity using the APIFLAME model.

This chapter introduces each of those models, and finally summarizes the interactions between them.

**Contents**

## 2.1 RegIPSL model

The Regional Earth system model of the Institut Pierre Simon Laplace (RegIPSL), an improved version of the MORCE-MED platform (Drobinski et al., 2012), couples the land surface model ORCHIDEE (ORganising Carbon and Hydrology In Dynamic EcosystEms), the atmospheric model WRF (Weather Research and Forecasting), and the ocean model NEMO (Nucleus for European Modelling of the Ocean). The RegIPSL version used in this thesis does not use the interactive oceanic component. The two main components used here, ORCHIDEE and WRF, are presented in Figure 2.1 and will be briefly described in the following subsections.

An original feature of this regional Earth system model is that the land surface model, ORCHIDEE, is coupled to the atmosphere (WRF) through the OASIS coupler (Craig et al., 2017) using the methodology described in Polcher et al. (1998). Because of the fast processes involved in this coupling, the same spatial grid and time step are used for the atmospheric and land surface components.

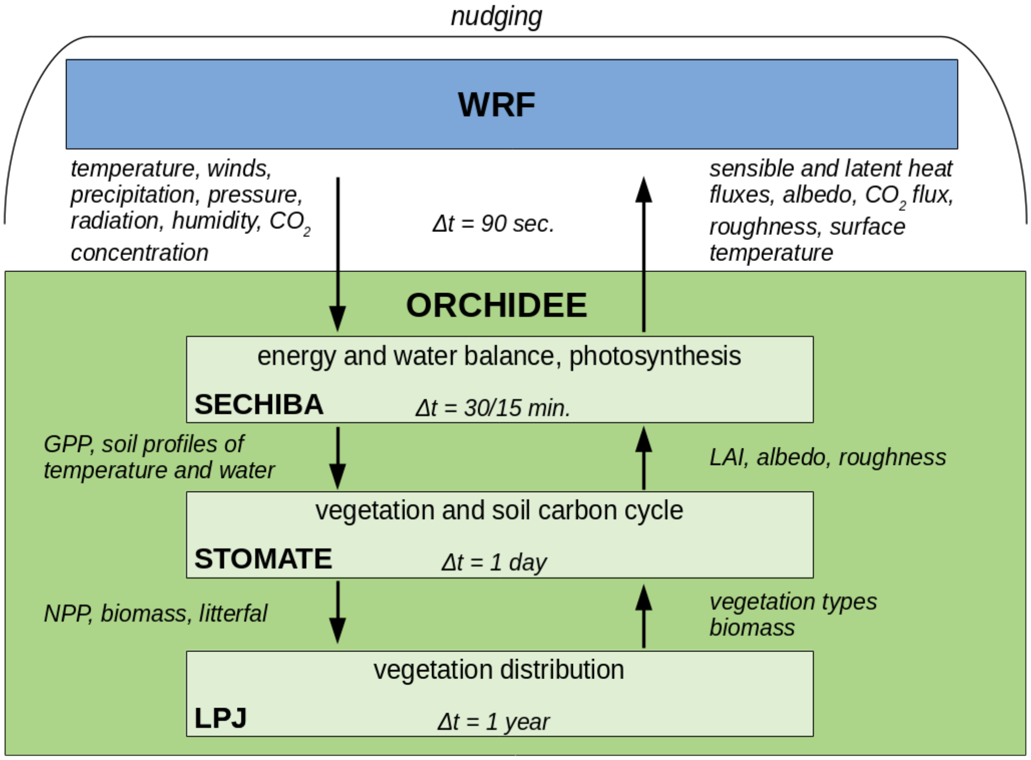

Figure 2.1: The RegIPSL coupling flow chart. This figure is inspired by the IPSL online documentation (`https://orchidee.ipsl.fr/`)

### 2.1.1 ORCHIDEE land surface and vegetation model

ORCHIDEE is a Dynamic Global Vegetation Model (DGVM) developed at IPSL and also used in the global Earth system model of the Institute (Krinner et al., 2005; Maignan et al., 2011). It includes three different modules (SECHIBA, STOMATE and LPJ) which resolve, respectively, the processes of the energy and water cycle, the carbon cycle and the evolution of the vegetation.

ORCHIDEE can run at global or regional scales and can be used ”off-line” or coupled with an atmospheric model. In all cases its spatial resolution is given by the atmospheric information provided.

### SECHIBA module

SECHIBA solves the surface energy balance equation (Eq. 2.1) for which it has to compute the various exchanges of water and energy between the biosphere and the atmosphere. It is the component through which the interactions with the atmosphere occur.

Considering an horizontal unit of the upper surface layer, the evolution of the total amount of energy stored in it ($Q$ $[W/m^2]$) can be determined by the following balance:

$$\frac{dQ}{dt} = R_n - G - H - \lambda ET \tag{2.1}$$

where $R_n$ is the net surface irradiance resulting from downward shortwave radiation (visible), upward and downward longwave radiation (infrared), $G$ the ground heat flux that represents the loss of energy by heat conduction through the lower soil layer, $H$ the sensible heat flux (heat transfer to the atmosphere), $\lambda ET$ the specific latent heat of vaporization ($\lambda$) and evapotranspiration rate ($ET$) from ground and plants.

However, including a multi-layer canopy, the energy budget in ORCHIDEE is calculated at each level considering a resistance of the leaf surface to the sensible and latent heat flux (Ryder et al., 2016).

SECHIBA also computes the soil water budget (De Rosnay and Polcher, 1998)(Eq. 2.2). The change in soil moisture storage per time step ($dW/dt$) on a unit area is defined by precipitation reaching the ground ($P$), the evapotranspiration ($ET$), the drainage ($D$) towards lower layers and the runoff water ($R$) which does not infiltrate.

$$\frac{dW}{dt} = P - ET - D - R \tag{2.2}$$

Based on the soil moisture computed at each soil layer, ORCHIDEE provides the Soil Wetness Index (SWI) integrating information from all levels. This index that is largely used in this thesis, is defined as follows:

$$SWI = \frac{W_c}{W_a} \tag{2.3}$$

$$W_a = C - \theta \tag{2.4}$$

where $W_c$ is the ground water content (i.e. the soil moisture), $W_a$ the accessible water content, $C$ the field capacity and $\theta$ the wilting point.

### STOMATE module

STOMATE is the biophysical component of the model. It simulates the carbon exchanges over the continent by computing sub-seasonal dynamics and phenology (budburst, senescence, and vernalisation) of the vegetation.

Carbon input from the atmosphere allows to compute the photosynthetic process from which organic matter is then allocated to biomass components (stems, reserve, roots and leaves). In addition to light, photosynthesis is limited by water supply. Water stress can modify the photosynthetic capacity, that is represented in the model by the $V_{cmax}$ parameter (Krinner et al., 2005). $V_{cmax}$ is the maximum rate of $RuBP$ (ribulose-1,5-bisphosphate) carboxylation. It also varies as a function of the leaf age.

Finally, the dynamic biomass provides information about the leaf area and the ground fraction covered by vegetation from which Leaf Area Index (LAI) can be computed. Being largely used in this thesis, the LAI will be properly defined in Chapter 3 (see Sect. 3.2). Biomass removal occurs by senescence and mortality, supplying the litter. From decomposition, carbon is transferred to soil stock. The soil is composed of 11 layers (De Rosnay et al., 2002). Soil organic matter, minerals, and water can be transferred to the underlying layers.

### LPJ module and Plant Functional Types

LPJ is the dynamic module of the vegetation. It describes the competition between the different Plant Functional Types (PFTs) at a temporal resolution of 1 year. The LPJ module is not activated in this thesis.

ORCHIDEE categorizes vegetation in 13 PFTs, the distribution of which is derived from the ESA-CCI (European Space Agency-Climate Change Initiative) database (ESA, 2017). Biophysical and biochemical variables are computed for each PFT. PFTs are distributed within a same grid cell by a percentage of vegetation cover. Many parameters attributed to the vegetation are PFT-specific (e.g. $V_{cmax}$). Table 2.1 summarizes basic PFT parameters used in ORCHIDEE. Within a same region such as the Mediterranean, vegetation characteristics (e.g. the canopy height ($h$), the maximum LAI ($LAI_{max}$)) between short (grass and agriculture) and long root systems plants (temperate forests) are relatively different.

Table 2.1: Table of the basic PFT parameters used in ORCHIDEE, inspired from Krinner et al. (2005) with updated values. $V_{cmax,fixed}$ is the fixed rubisco-limited potential photosynthetic capacity $[\mu mol/m^2.s]$ when STOMATE is not activated, $T_{max}$ the maximum photosynthesis temperature [°C], $LAI_{max}$ the maximum LAI, $Z_{root}$ the exponential factor for root density as a function of depth when maximum soil depth is 4m and 2m, $\alpha_{leaf}$ the prescribed leaf albedo in the near infrared, $h$ the prescribed height [m], $A_C$ the critical leaf age for leaf senescence [days] and $SM_S$ the critical relative moisture availability for senescence. The abbreviations used for PFT forests are the following: "Tr" for tropical, "Temp" temperate, "Bo" boreal, "B" broadleaf, "N" needleleaf, "E" evergreen and "S" summergreen.

| PFT | $V_{cmax,fixed}$ | $T_{max}$ | $LAI_{max}$ | $Z_{root,4m}/Z_{root,2m}$ | $\alpha_{leaf}$ | $h$ | $A_C$ | $SM_S$ |
|---|---|---|---|---|---|---|---|---|
| TrBE | 40 | 55 | 8.0 | 0.4/0.8 | 0.23 | 30 | 730 | - |
| TrBR | 50 | 55 | 8.0 | 0.4/0.8 | 0.18 | 30 | 180 | 0.3 |
| TempNE | 30 | 55 | 4.0 | 1.0/1.0 | 0.18 | 20 | 910 | - |
| TempBE | 35 | 55 | 4.5 | 0.8/0.8 | 0.20 | 20 | 730 | - |
| TempBS | 40 | 55 | 4.5 | 0.8/0.8 | 0.24 | 20 | 160 | - |
| BoNE | 30 | 55 | 4.0 | 1.0/1.0 | 0.15 | 15 | 910 | - |
| BoBS | 40 | 55 | 4.5 | 1.0/1.0 | 0.26 | 15 | 220 | - |
| BoNS | 35 | 55 | 4.0 | 0.8/0.8 | 0.20 | 15 | 120 | - |
| C3 grass | 60 | 55 | 2.0 | 4.0/4.0 | 0.24 | 0.5 | 80 | 0.2 |
| C4 grass | 60 | 55 | 2.0 | 1.0/4.0 | 0.27 | 0.6 | 120 | 0.2 |
| C3 agriculture | 70 | 55 | 2.0 | 4.0/4.0 | 0.28 | 1.0 | 90 | 0.3 |
| C4 agriculture | 70 | 55 | 2.0 | 1.0/4.0 | 0.26 | 1.0 | 90 | 0.2 |

### 2.1.2 WRF atmospheric model

The WRF model is used for operational forecasting as well as climate research (Skamarock et al., 2008, 2019). It is an atmospheric numerical model co-developed at the National Center for Atmospheric Research (NCAR), the National Oceanic and Atmospheric Administration (NOAA), the Department of Defense's Air Force Weather Agency (AFWA) and Naval Research Laboratory (NRL), the University of Oklahoma and the Federal Aviation Administration (FAA). It simulates physics and dynamics of the atmosphere; representing in three dimensions essential processes such as turbulence, diffusion or convection.

As shown in Figure 2.2, the WRF software framework includes a dynamical core that solves Eulerian nonhydrostatic equations, a physics interface for the surface (bottom boundary layer) and finally, a digital filtering initialization that connects inputs (e.g. analyses, observations) with the dynamical core. The digital filter allows to remove noise from initial conditions.

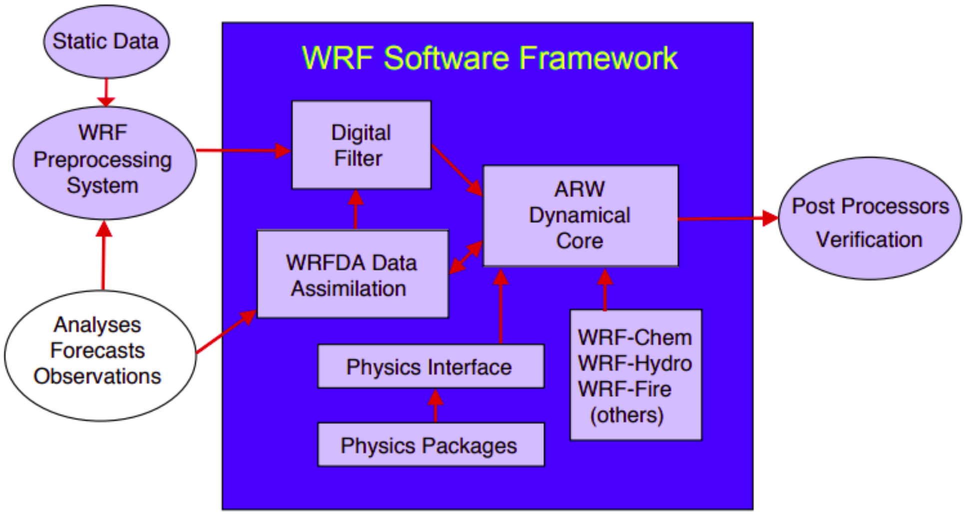

Figure 2.2: Figure from Skamarock et al. (2019). WRF system components.

RegIPSL uses WRF v3.7.1 with the following configuration. The ARW (Advanced Research WRF) non-hydrostatic dynamical core is selected together with a set of physics packages appropriate for regional resolutions (e.g. 20km). These include in particular the single-moment 5 class microphysics scheme (Hong et al., 2004), which produces the clouds and their properties in interaction with the radiation scheme developed by Iacono et al. (2008). Convection is parametrized at these resolutions with the Kain-Fritsch scheme (Kain, 2004) and the shallow convection scheme proposed by Park and Bretherton (2009). The interaction with the surface occurs through the Mellor-Yamada Level-3 representation of boundary layer turbulence, developed by Nakanishi and Niino (2009). These are standard parametrizations within WRF and were thoroughly tested over the Mediterranean region by Di Luca et al. (2014).

WRF (a version not coupled with ORCHIDEE) is also used to drive CHIMERE simulations, as described in the next section (see Sect. 2.2).

## 2.2 CHIMERE chemistry-transport model

### 2.2.1 General description of an Eulerian 3-dimensional regional CTM

Atmospheric chemistry and transport are simulated in this thesis using the CHIMERE v2020r1 regional chemistry-transport model (Menut et al., 2013; Mailler et al., 2017; Menut et al., 2021).

The CHIMERE model has been developed since 1999 in the Interfaces and Troposphere team (InTro) at the Laboratoire de Météorologie Dynamique (LMD), in collaboration with the Institut national de l'environnement industriel et des risques (INERIS) and the Laboratoire Inter-Universitaire des Systèmes Atmosphériques (LISA). CHIMERE, as a modeling tool of regional atmospheric pollution, is used in three types of activities. Firstly, it is used for research to study and better understand physico-chemical processes controlling the concentration of trace gases and aerosols in the atmosphere and their links to meteorology. Secondly, it is used for impact and risk assessment that can be provided as decision support for policies. Finally, it performs operational forecasting of air quality at regional (e.g. Airparif), national (e.g. PREV'AIR) and european scales (e.g. MACC project from Copernicus).

Unlike global CTM (e.g. LMDZ-INCA (Hauglustaine et al., 2004; Hourdin et al., 2006)), CHIMERE does not cover the whole globe, but is focused on adaptive regions: from the urban scale to the hemispheric one. Trace gas and aerosol concentrations at larger scale are prescribed as input for initial and boundary conditions. The detailed configuration used to perform the CHIMERE simulations in this thesis will be given in Chapter 6.

CHIMERE is an Eulerian 3-dimensional CTM. Dividing the atmosphere into grid cells along three axes (meridional $x$, zonal $y$ and vertical $z$), it computes surface emissions, gas-phase chemistry, aerosols formation, transport and deposition in each cell, as represented in the one-box model of Figure 2.3 (left panel). The concentration of a species $X$ is therefore known and assumed to be well mixed in the considered cell. To account for the exchange of mass and transport within the atmosphere, a 3-dimensional multi-box model needs to be considered (Fig. 2.3, right panel). The evolution of concentrations is calculated based on the continuity equation. In a fixed coordinate system (i.e. the Eulerian form), the temporal change of number density ($\delta n/\delta t$) for a species inside a determined volume is computed as follow:

$$\frac{\delta n}{\delta t} = -\frac{\delta F_x}{\delta x} - \frac{\delta F_y}{\delta y} - \frac{\delta F_z}{\delta z} + P - L = -\nabla \cdot F + P - L \tag{2.5}$$

where $\nabla \cdot F$ is the flux divergence (flux out minus flux in). $P$ and $L$ are the chemical production and loss respectively. $\nabla \cdot F$ includes both advection and turbulence.

Several advection schemes are available in CHIMERE. For this thesis, both horizontal and vertical advection are based on the second-order Van Leer (1977) scheme. Due to its good numerical accuracy and smaller diffusion than the first-order upwind scheme, this scheme is considered as appropriate.

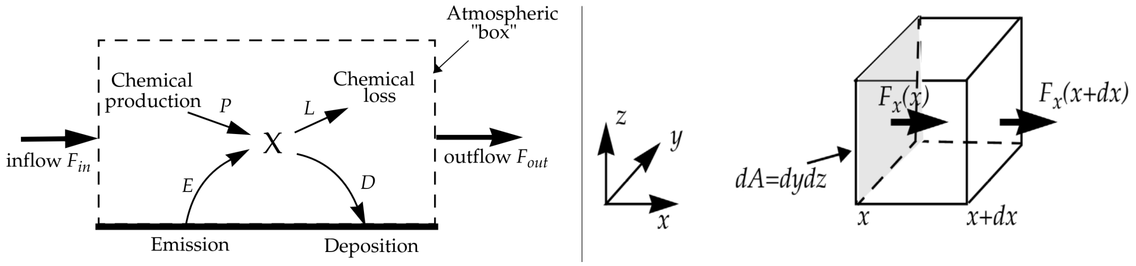

Figure 2.3: Figures from Jacob (1999). One-box model for an atmospheric species $X$ (left panel). Flux through an elemental volume (right panel).

Figure 2.4 shows the general structure of CHIMERE. To run a model simulation, users have to specify the domain (e.g. extent, resolution and land cover), the initial and boundary conditions, the surface emissions and the meteorology.
The key elements of CHIMERE are brielfy introduced in the following subsections, with a focus on those being the most relevant in this thesis. A full description of the CHIMERE model can be found in the peer-reviewed articles of Menut et al. (2013); Mailler et al. (2017); Menut et al. (2021) and from online documentation (`https://www.lmd.polytechnique.fr/chimere/`).

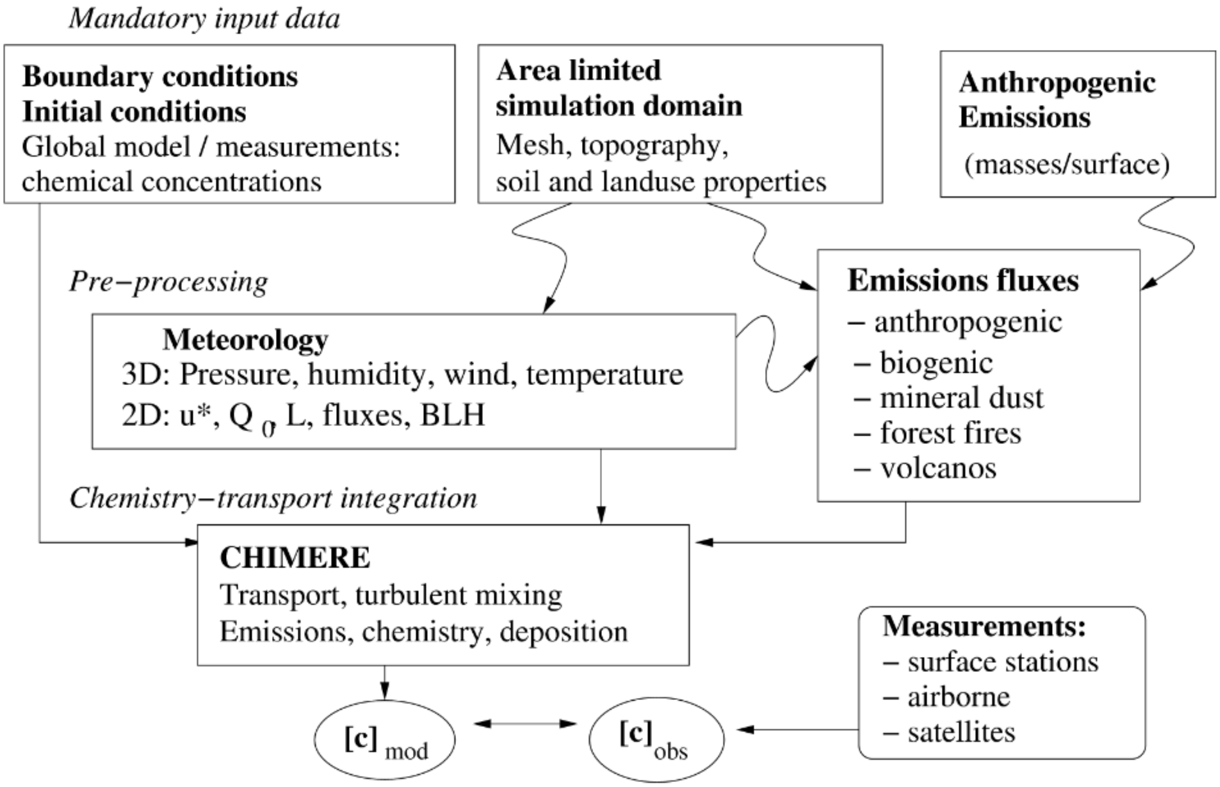

Figure 2.4: Figure from the CHIMERE documentation (`https://www.lmd.polytechnique.fr/chimere/`) showing the general principle of a chemistry-transport model such as CHIMERE. In the box "Meteorology", $u^*$ stands for the friction velocity, $Q_0$ the surface sensible heat flux, L the Monin–Obukhov length and BLH the boundary layer height. $c_{mod}$ and $c_{obs}$ are the modelled and the observed chemical concentrations fields, respectively.

### 2.2.2 Emissions

CHIMERE accounts for both anthropogenic and natural emissions, either prescribed or calculated online. Anthropogenic sources cover all emission sectors related to human activities (e.g. industrial, traffic, agriculture, housing).

For this thesis, the anthropogenic surface emissions are fixed (2014), from the EMEP database (`https://www.ceip.at`). EMEP inventory being limited to Europe, world emissions (2010) are from EDGARD-HTAP v2 data set (Janssens-Maenhout et al., 2015) (`https://edgar.jrc.ec.europa.eu`). Sea salts and dimethyl sulfide marine (DMS) are calculated online using the scheme of Monahan (1986) and Liss and Mervilat (1986) respectively. Mineral dust emissions are also calculated on-line (Marticorena and Bergametti, 1995; Alfaro and Gomes, 2001).

The calculation of biogenic and fire emissions will be developed in the next subsections (2.3 and 2.4), as they are central tools to meet the needs of this thesis.

### 2.2.3 Offline and online mode with the meteorology

CHIMERE needs to read meteorological fields (e.g. atmospheric pressure, precipitation, wind speed) in order to simulate atmospheric transport and chemistry. CHIMERE can be run using meteorological drivers in offline mode (e.g. outputs from regional meteorological model, global reanalysis, climate model projections).

It can also be used online with the WRF model (via the OASIS-MCT external coupler). It allows to take into account the direct and indirect effects of aerosols on meteorology. Figure 2.5 shows the variables exchanged.

Based on a performance assessment using surface observations of major pollutants, Menut et al. (2021) concluded that in spite of an improvement for modeling realistic physicochemical interactions, the coupling mode (i.e. with retroactions from CHIMERE to WRF) does not induce major changes for surface pollutant concentrations, compared to the offline mode.

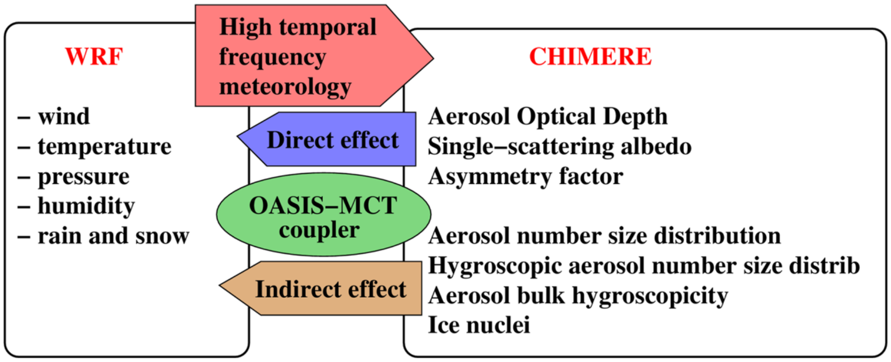

Figure 2.5: Figure from Menut et al. (2021). Main principle of the coupling between WRF and CHIMERE for the calculation of the direct and indirect effects of aerosols on meteorology.

### 2.2.4 Chemical mechanisms

Different gas-phase chemical mechanisms can be chosen in CHIMERE: the complete MELCHIOR mechanism (Lattuati, 1997), the reduced MELCHIOR2 mechanism (Derognat, 2003) and the SAPRC-07-A mechanism (Carter, 2010). From 300 reactions of 80 species, the complete MELCHIOR mechanism is reduced to 120 reactions of 40 species using chemical operators. To reduce the computing time and because the targeted species in this thesis are relatively common, the chosen mechanism is the reduced scheme MELCHIOR2. Menut et al. (2013) compared two CHIMERE simulations using the MELCHIOR2 and SAPRC-07-A

mechanism (275 reactions of 85 species) with EEA Airbase data for $NO_2$ and $O_3$ (Europe, summer 2005). Averaged scores are very similar, with an equal R coefficient (∼0.7) and a bias slightly lower for SAPRC-07-A (8.19 ppb against 9.29 ppb).
The aerosol module of CHIMERE includes aerosol microphysics, secondary aerosol formation mechanisms, aerosol thermodynamics, and deposition, as detailed in Couvidat et al. (2018). Aerosol chemistry is covered for several aerosol species types: mineral dust, anthropogenic primary particulate matter, anthropogenic and biogenic secondary organic aerosols, sulfates, nitrates, ammomium and water. The size distribution of aerosols depends on the distribution range and the number of aerosol size sections that can be chosen. Three processes involved in the aerosol life cycle are solved in CHIMERE, for each aerosol species and its own size distribution:

- The nucleation. It is designated as the transformation of gas-phase molecules into an aggregation of molecules. The creation of this aerosol core is favoured in a cold and wet atmosphere.
- The absorption (or condensation). Gas phase species condense on a pre-existing aerosol.
- The coagulation. It is defined as molecules merging by collision due to diffusion from thermal motion (Brownien motion). The number of particles decreases but the total mass stays constant.

Radiative transfer and photochemical rates are calculated online using the Fast-JX module version 7.0b (Bian and Prather, 2002). It takes into account three important effects on photolysis rates: the Mie diffusion by ice- and liquid-water, the absorption and Mie diffusion by aerosols and the absorption by ozone.

### 2.2.5 Deposition

#### Wet scavenging

Wet deposition of gases and particles in CHIMERE is taken into account by scavenging at two different levels, triggered in- and below-clouds. For in-clouds scavenging, particles are scavenged by coagulation with droplets or by precipitating drops, the deposition flux being proportional to the amount of water lost by precipitation. Gases are absorbed in clouds, dissolved and dropped off when precipitation occur. For below-clouds scavenging, gases and particles are scavenged by rain droplets and possibly by snowfall when conditions are met. Droplets properties (e.g. diameter, density) are taken into account in the calculation.

### Dry deposition

The deposition velocity for gases and aerosols is described through a resistance scheme (Wesely, 1989), as illustrated in Figure 2.6. Around 100m above the ground (surface layer), the aerodynamical resistance $R_a$ occurs. It depends on the turbulent diffusivity. Below, there is the laminar layer characterized by surface resistance $R_b$ (diffusitivity near the ground). Finally, there is the resistance at surface (vegetation level) only for gaseous species: the canopy resistance $R_c$.

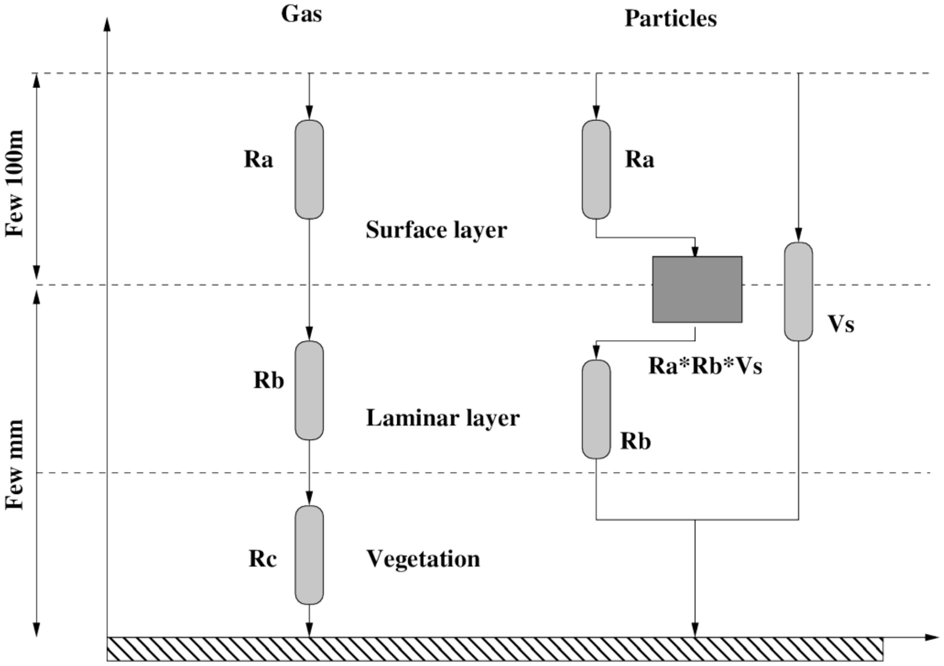

Figure 2.6: Figure from Menut et al. (2013) showing the general principle of dry deposition for trace gases and particles. For each model species, three resistances are estimated: deposition occurs if the sum of all these resistances is low. For particles, the settling velocity ($V_s$) is added.

To calculate $R_c$, CHIMERE follows the scheme of EMEP model (Emberson et al., 2000; Simpson et al., 2003, 2012), initially based on Erisman et al. (1994). The bulk canopy resistance is defined as the reverse of the bulk canopy conductance ($G_c$) (Eq. 2.6), that is computed from the stomatal conductance ($g_{sto}$) increasing proportionally with the LAI and complemented with the bulk non-stomatal conductance ($G_{ns}$) (Eq. 2.7). $g_{sto}$ is included between a maximum ($g_{max}$) and minimum ($g_{min}$) daytime stomatal conductance [mmol/$m^2.s$]. It varies in function of meteorological conditions represented by a series of factors of relative conductance ($f$) (Eq. 2.8). Parameters used to calculate those factors vary with land cover and the seasonality.

$$R_c = \frac{1}{G_c} \tag{2.6}$$

$$G_c = LAI \cdot g_{sto} + G_{ns} \tag{2.7}$$

$$g_{sto} = g_{max} \cdot f_{phen} \cdot f_{light} \cdot max(g_{min}, (f_{temp} \cdot f_{VPD} \cdot f_{SW})) \tag{2.8}$$

where $f$ are factors of relative conductance determined by the leaf/needle age ($phen$), irradiance ($light$), temperature ($temp$), leaf-to-air vapour pressure deficit ($VPD$) and the soil wetness ($SW$).

The sensitivity of those factors to environmental variables is shown in Figure 2.7. LAI and $f_{phen}$ are fixed and solely depend on the day of the year characterized by a growing season, with an overall maximum in June-July. However, they vary considerably between land cover classes. $f_{SW}$ equals to 1 and decreases when the soil moisture index is below 0.5. This factor will be further detailed in Sect. 6.3.3 (see Chap. 6). $f_{temp}$ is simply defined by a function including minimum, optimum and maximum temperatures at 2m above surface for each land cover. The optimum temperature for maximum conductance varies between 18°C and 28°C. The light parameter $f_{light}$ depends on solar elevation and irradiance. It increases logarithmically with the zenithal solar angle. Moreover, $f_{light}$ is composed of two elements: a factor under sun conditions and another one under shade light conditions representing diffuse radiation. The shade ligh factor varies in function of the LAI so that the $f_{light}$ also depends on the land cover. Finally, the leaf-to-air vapour pressure deficit (VPD) which represents the difference between the vapour pressure inside the leaf compared to that of the air, is based on both 2m temperature and relative humidity. Below a parameterized maximum VPD, $f_{VPD}$ decreases linearly until reaching a parameterized minimum VPD where $f_{VPD}$ is therefore fixed at 0.1.

Detailed description of the algorithms of activity factors can be found in Emberson et al. (2000); Simpson et al. (2003, 2012).

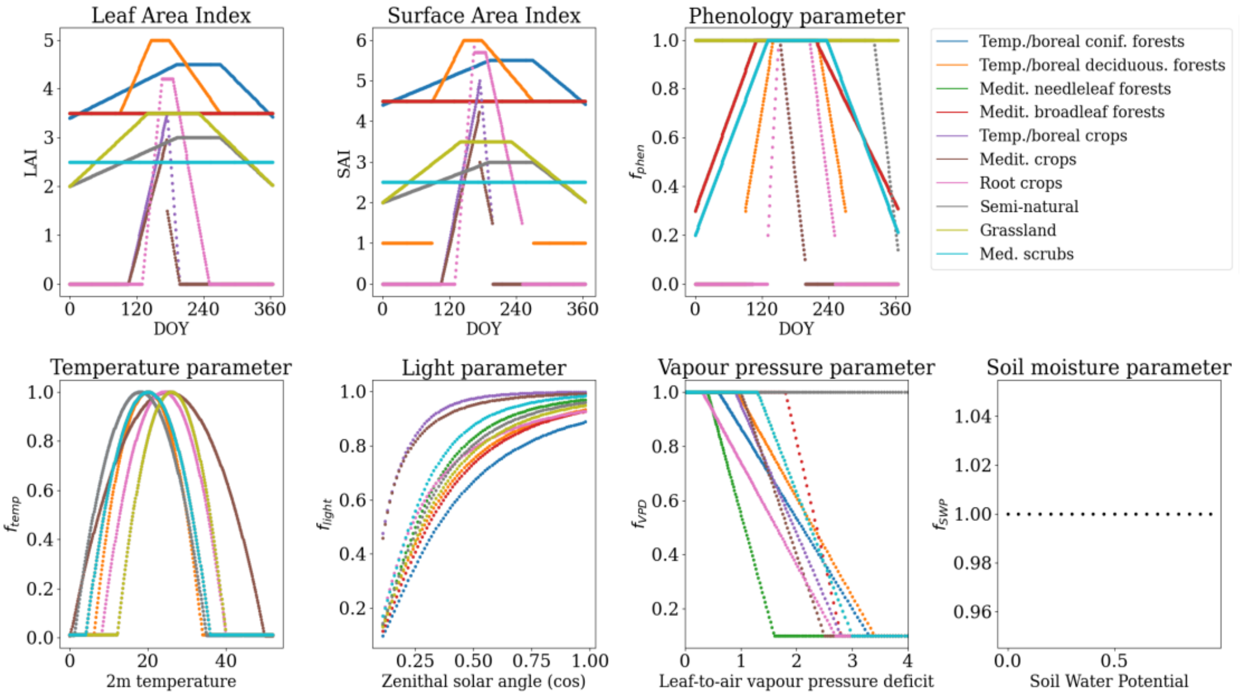

Figure 2.7: Sensitivity of the different $f$ factors used for the calculation of the stomatal conductance in CHIMERE (Emberson et al., 2000; Simpson et al., 2003, 2012). DOY stands for day of the year.

## 2.3 MEGAN biogenic emissions model

Biogenic emissions are computed using the Model of Emissions of Gases and Aerosols from Nature (MEGAN model) v2.04 (Guenther et al., 2006), including several updates from the version 2.1 (Guenther et al., 2012). Emission fluxes are calculated based on emission factors at canopy standard conditions for the following list of species: isoprene, $\alpha$-pinene, $\beta$-pinene, limonene, ocimene, humulene, nitrogen monoxide, carbon monoxide, methanol, ethylene, acetaldehyde, methyl ethyl ketone and unsaturated dicarbonyls. Canopy standard conditions are defined as $303K$ for the air temperature ($T$), 1500 $\mu mol/m^2.s$ for the photosynthetic photon flux density ($PPFD$) at the top of the canopy, 5 $m^2/m^2$ for the Leaf Area Index ($LAI$) and a one-layer canopy composed of 80% mature, 10% growing and 10% old foliage. As shown in Figure 2.8, environmental conditions are taken into account using activity factors ($\gamma$), that represent deviations from the canopy standard conditions. Hence, the emission rate ($ER$ $[\mu g/m^2.h]$) for a given species $i$ is calculated in each model grid cell as:

$$ER_i = EF_i \cdot \gamma_{LAI} \cdot \gamma_{PPFD,i} \cdot \gamma_{T,i} \cdot \gamma_{Age,i} \cdot \gamma_{SM,i} \cdot \gamma_{CO2,i} \cdot \rho_i \tag{2.9}$$

where $EF$ is the emission factor $[\mu g/m^2.h]$ provided by the MEGAN model and $\rho$ the production/loss term within canopy (being assumed equal to one). $EF$ values for the most common species are presented in Appendix B (Tab. B.1), showing the large variability between PFTs.

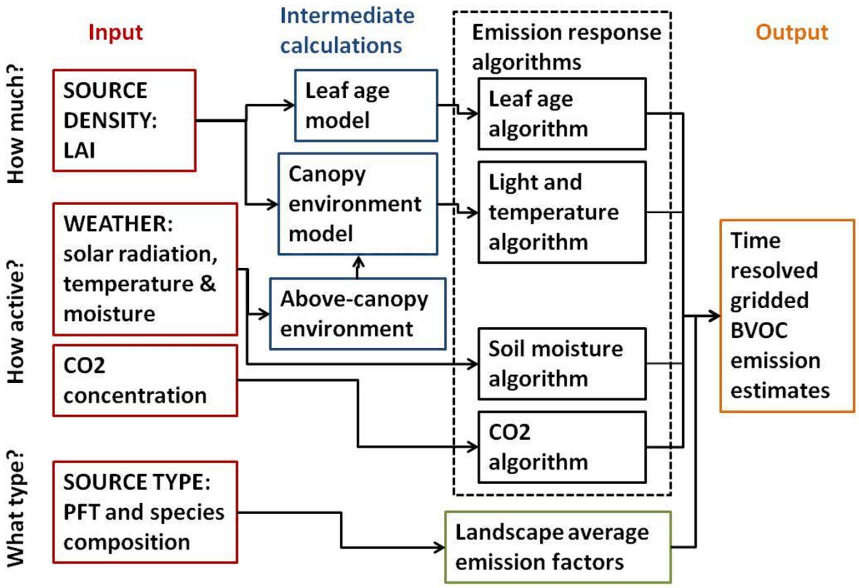

Figure 2.8: Figure from Guenther et al. (2012). Schematic of MEGAN2.1 model components and driving variables.

All the activity factors except the $\gamma_{LAI}$ that accounts for vegetation density, are species specific. Activity factors are derived from algorithms using meteorological variables and experimentally derived parameters. Parameters of each MEGAN species are shown in Appendix B (Tab. B.2). A full description of the MEGAN model can be found in the peer-reviewed articles of Guenther et al. (2006, 2012).

In order to perform sensitivity studies, an offline version of MEGAN was reproduced including spatial and BVOC species variability. Figure 2.9 and 2.10 present the sensitivity of the activity factors to environmental variables for isoprene and $\alpha$-pinene species. The activity factor $\gamma_{Age}$ represents the leaf age by dividing its life cycle into four states. For most of species, the emerging and growth state are optimal for the emission activity. $\gamma_T$ and $\gamma_{PPFD}$ account for the enzymatic activity and the electron transport, respectively enhanced by temperature and light (Guenther et al., 1991).

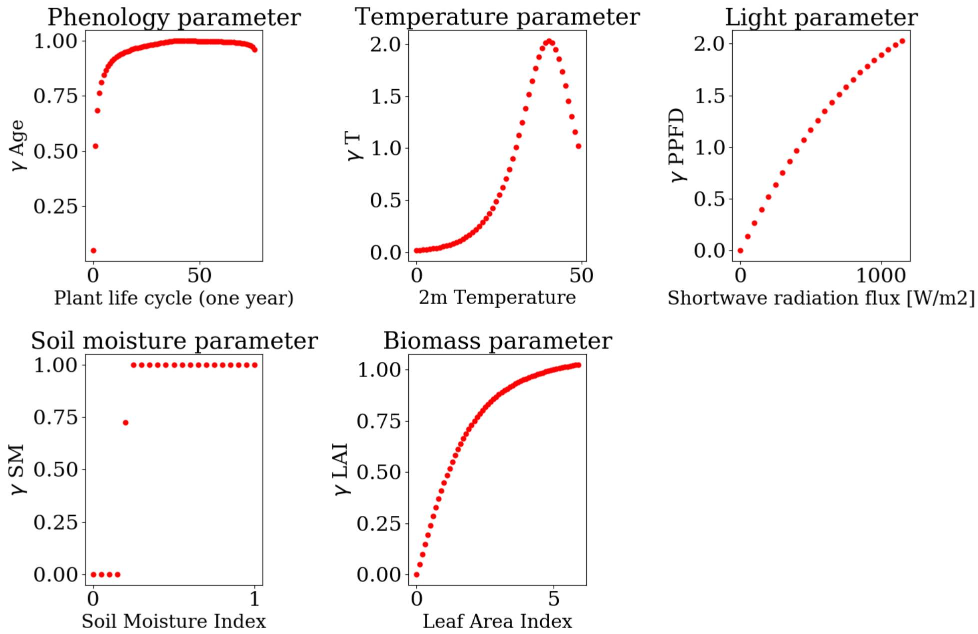

Figure 2.9: Sensitivity of the activity factors ($\gamma$) calculated in MEGAN (Guenther et al., 2006, 2012) to environmental variables for isoprene. For the sensitivity of the light parameter here, the day of the year has been set for July 15, 2015 and the cosine of solar zenith angle to 0.6.

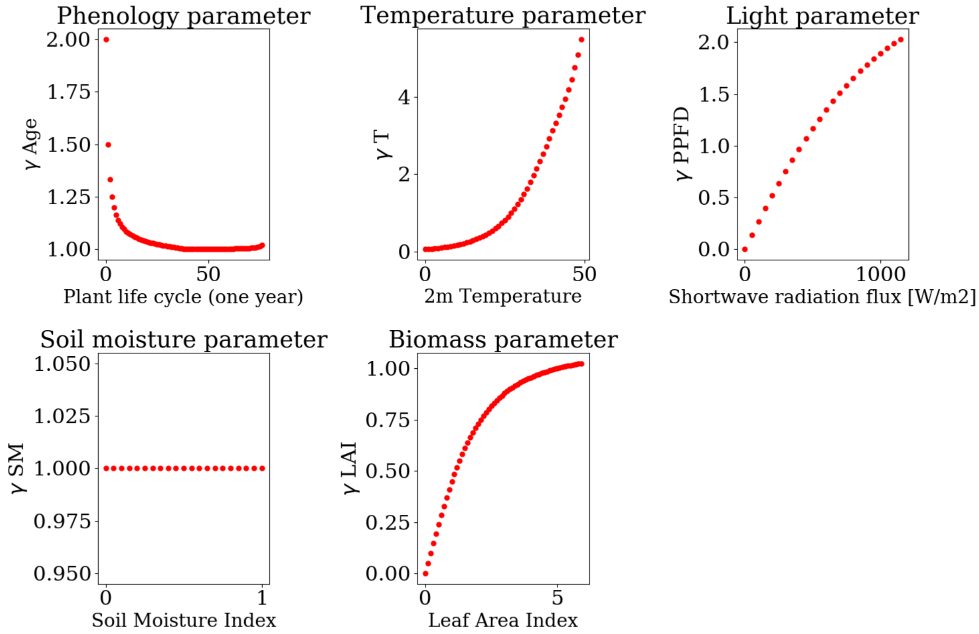

Figure 2.10: Same as Fig. 2.9 for $\alpha$-pinene species.

A distinction is made between light/temperature-dependent species (e.g. isoprene) and -independent species (e.g. monoterpenes). For dependent species, the sensitivity to light and temperature signal depends on the past weather conditions (Sharkey et al., 2000). Emissions are higher (lower) if the previous days were warm and sunny (cold and shady). Moreover, dependent species are characterized by an optimal temperature for emissions, unlike independent species for which the relationship with temperature is exponential (Guenther et al., 1993).

$\gamma_{SM}$ and $\gamma_{CO2}$ generally concern only isoprene species. $\gamma_{SM}$ leads to emissions reduction when soil moisture reaches the wilting point (i.e the minimal soil moisture the plant requires not to wilt). Below this limit, $\gamma_{SM}$ is equal to 0. $\gamma_{CO2}$ takes into account the isoprene emissions reduction with higher $CO_2$ atmospheric concentration (Heald et al., 2009). However, $\gamma_{CO2}$ is fixed here ($CO_2$ concentration at 395 ppm).

Biogenic emissions may vary considerably between models. The main factors explaining the divergence between emission models and so related to important uncertainties, are the emission factors, the land cover and vegetation species distribution and the vegetation density assessment (e.g. Messina et al., 2016).

MEGAN species are converted into CHIMERE species using an aggregation matrix (Appendix B: Tab. B.3) to be used on-line in CHIMERE at hourly time step. Meteorological fields are provided by the WRF model.

## 2.4 APIFLAME biomass burning emissions model

Based on a bottom-up approach, the APIFLAME (Analysis and Prediction of the Impact of Fires on Air quality ModEling) v2.0 model (Turquety et al., 2014, 2020) provides biomass burning emissions, usable as input files in CTM.

As schematized in Figure 2.11, APIFLAME firslty reads and maps MODIS satellite observations of Burned Area (BA, based on the MCD64 product) and Fire Radiative Power (FRP, based on the MOD14 and MYD14 products) onto a grid with specified domain and resolution. Vegetation type affected by fires is identified using the MODIS MCD12 product. APIFLAME includes a list of false detection. Thermal anomalies corresponding to power plants or active volcanoes that could be attributed to active fires, are filtered out.

Information about the fuel load, either from ORCHIDEE simulations (biomass density at monthly time-step) or from the literature, allows to calculate the amount of carbon consumed over the burned areas, that is vegetation specific. Finally, hourly emission fluxes are derived from emission factors listed by species. Inventory species from APFILAME are converted into the model species (CHIMERE in this case) using an aggregation matrix.

In addition to the the input uncertainties, the APIFLAME model is characterized by large uncertainties at each level of its scheme. Based on the different possible configurations in APIFLAME, an averaged dispersion of 80% was simulated, giving an estimate of uncertainty of emissions (Turquety et al., 2020). From a sensitivity analysis of CO emissions to model factors, they identified the choice of the emission factor database as the strongest effect. Vegetation cover also determines considerably the results (e.g. +17% of CO emitted when using Corine Land Cover database, instead of MODIS product). For the case study discussed in the Euro-Mediterranean area, the computed fuel consumption appears to be less critical.

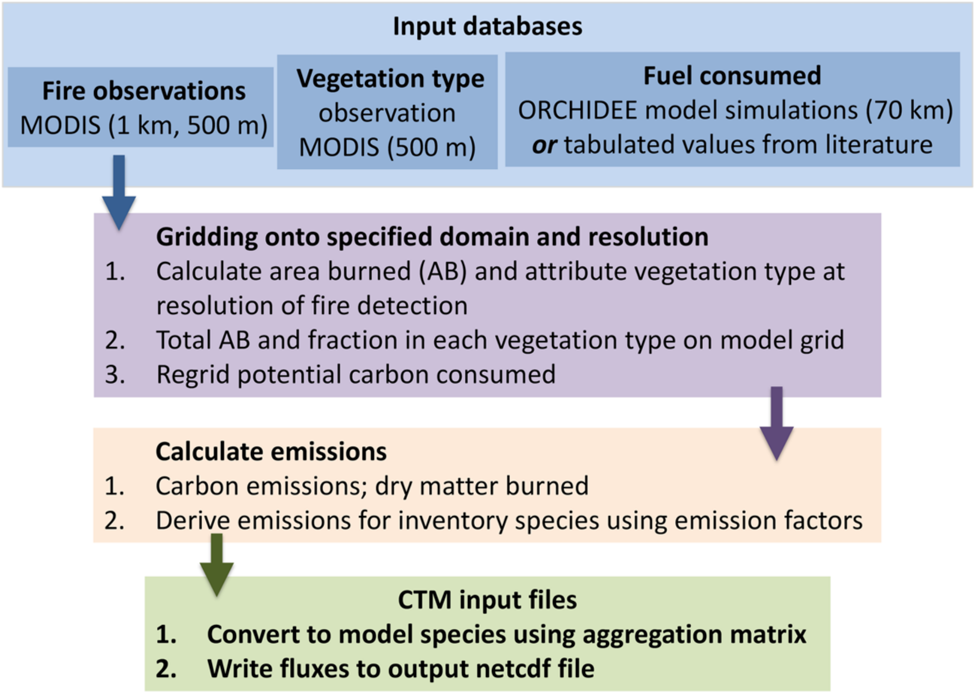

**Input databases**

**Fire observations**
MODIS (1 km, 500 m)

**Vegetation type**
observation
MODIS (500 m)

**Fuel consumed**
ORCHIDEE model simulations (70 km)
***or*** tabulated values from literature

**Gridding onto specified domain and resolution**

1. Calculate area burned (AB) and attribute vegetation type at resolution of fire detection
2. Total AB and fraction in each vegetation type on model grid
3. Regrid potential carbon consumed

**Calculate emissions**

1. Carbon emissions; dry matter burned
2. Derive emissions for inventory species using emission factors

**CTM input files**

1. **Convert to model species using aggregation matrix**
2. **Write fluxes to output netcdf file**

Figure 2.11: Figure from Turquety et al. (2020). Overview of the APIFLAME v2.0 emissions model.

## 2.5 Overview of interactions between models

The flow scheme in Figure 2.12 illustrates the interactions between the different models used for analyzing the impact of droughts and heatwaves on the biosphere and $O_3$ concentration. Droughts and heatwaves are identified using the RegIPSL coupled regional model (ORCHIDEE-WRF). Atmospheric chemistry and transport are simulated by the regional CHIMERE model using meteorological fields from the WRF model online, but not coupled with ORCHIDEE. The MEGAN and APIFLAME model provides respectively biogenic emissions and biomass burning emissions at high spatial and temporal resolution into the CHIMERE model. It must be emphasized it is not the MEGAN model itself but rather

a reproduction of the code ("big leaf" mode) in a CHIMERE module. MEGAN and APIFLAME use satellite observations from MODIS instrument to describe the vegetation state and wildfire activity. LAI from MODIS observations is only used for MEGAN while LAI is prescribed for the deposition scheme of CHIMERE.
Arrows in blue represent new interactions that have been developed and analyzed in the last chapter of results (see Chap. 6).

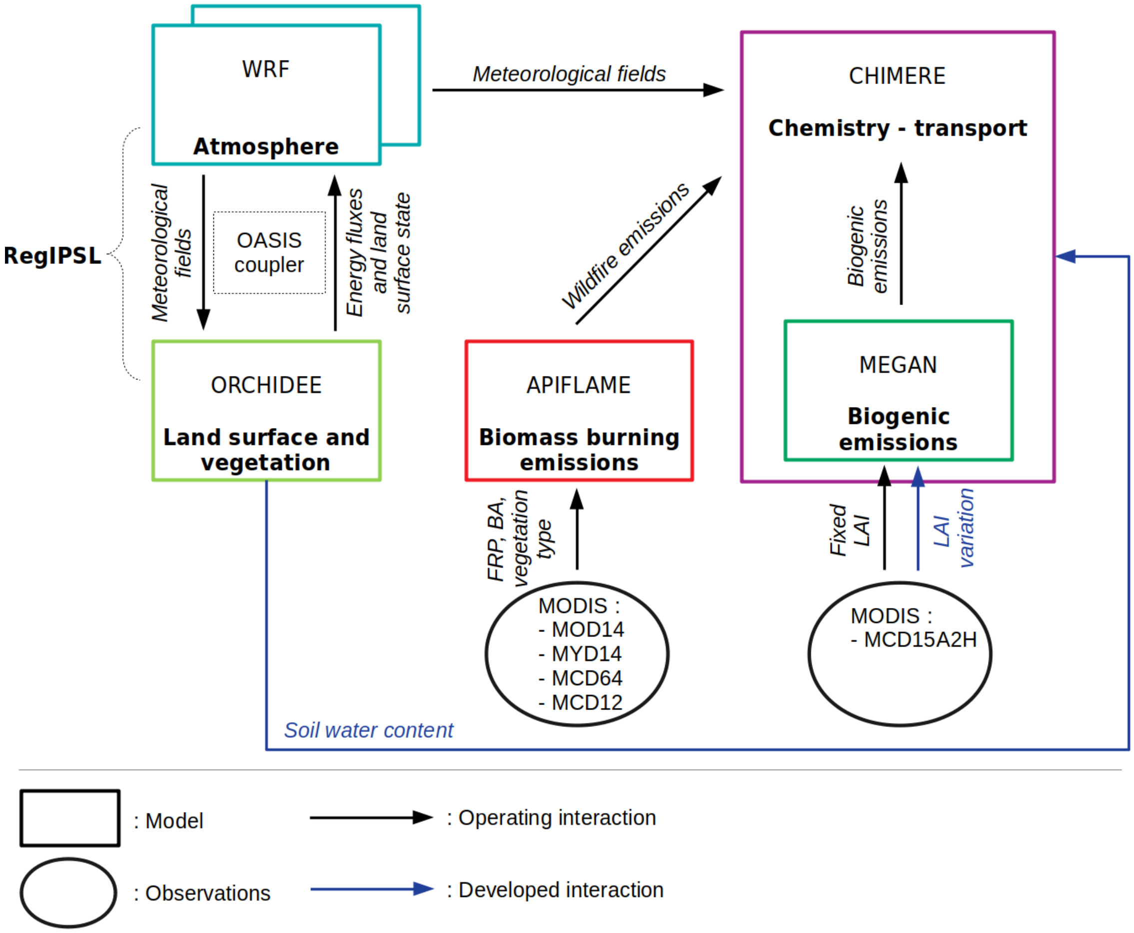

Figure 2.12: Flow scheme representing the interactions between the different models used in this thesis.

# Chapter 3

# Observations

This chapter introduces the different observational data sets used in this work, with three main objectives :

- Some observations are used as input to the models : fire characteristics for the APIFLAME model and vegetation (LAI) for the MEGAN model ;
- Observations are also essential to validate the behavior of the models and provide confidence in the results of the modeling study. Here I used the surface meteorology from E-OBS observations, surface ozone observations from the European Environment Agency, and formaldehyde observations from the satellite-based OMI instrument ;
- All observations are also directly used to analyze the variations of the surface and atmospheric properties according to the meteorological situation and thus to carry out impact studies.

The main characteristics of each data set are briefly described here, along with the associated uncertainty.

**Contents**

## 3.1 Surface meteorology from E-OBS

In-situ observations of surface meteorology from the ENSEMBLES data set E-OBS (Cornes et al., 2018) are used in this thesis. It is a daily gridded data set of standard meteorological observations constructed as part of the European Climate Assessment & Data set (ECA&D) project, covering the 1950-2018 period (version 16.0).

Variables used here are the air temperature at 2 meters above surface ($T_{2m}$) and precipitation. The station network covering the Europe and the northern limit of Africa (25°N-71.5°N × 25°W-45°E) is shown in Figure 3.1. In 2016, the network was composed of about 2000 stations. Temperature is generally measured between 1.25 and 2.0 meters high in a shelter, not exactly at the surface. Thermometers have to be protected from the solar and terrestrial radiation and from precipitation.

Data points from the network of measurement stations are interpolated onto a grid of resolution 0.25° × 0.25°, in three steps. First, thin-plate splines are applied over the monthly mean data in order to create a spatial trend. Then, the daily anomalies of the monthly mean are interpolated using a Kriging method. Finally, the daily and monthly data are combined (Haylock et al., 2008).

The uncertainty of the E-OBS data set can be considerable for some variables. Figure 3.1 shows that the percentage of data exceeding the 95% confidence interval can be high in the Mediterranean; ranging from 10 to 25% for the observed minimum 2m temperature and from 5 to 20% for the precipitation (Hofstra et al., 2009).

The two main sources of uncertainty are the stochastic method of interpolation and the spatial distribution of the measurement stations. Cornes et al. (2018) assessed the uncertainty between interpolated values and 100 reference stations of E-OBS over the 1950-2016 period. They computed an annual mean absolute error of 0.80°C, 1.22°C, 0.92°C respectively for the mean, minimum and maximum temperature and of 0.92mm/day for the rainfall rate. The Southern Mediterranean is not as well covered as other parts of the region. Hofstra et al.

(2009) compared the E-OBS precipitation data set with denser station network data sets of observations for Europe (ELDAS product) and, more specifically, over the Alps. The ELDAS precipitation product covers a relatively short period (2000-2001) in comparison to E-OBS. Even if they found good correlation between the different data sets (R coefficient between 0.85 and 0.88), considerable annual mean absolute errors were computed: 1.16mm/day over Europe and 2.25mm/day specifically over the Alps.

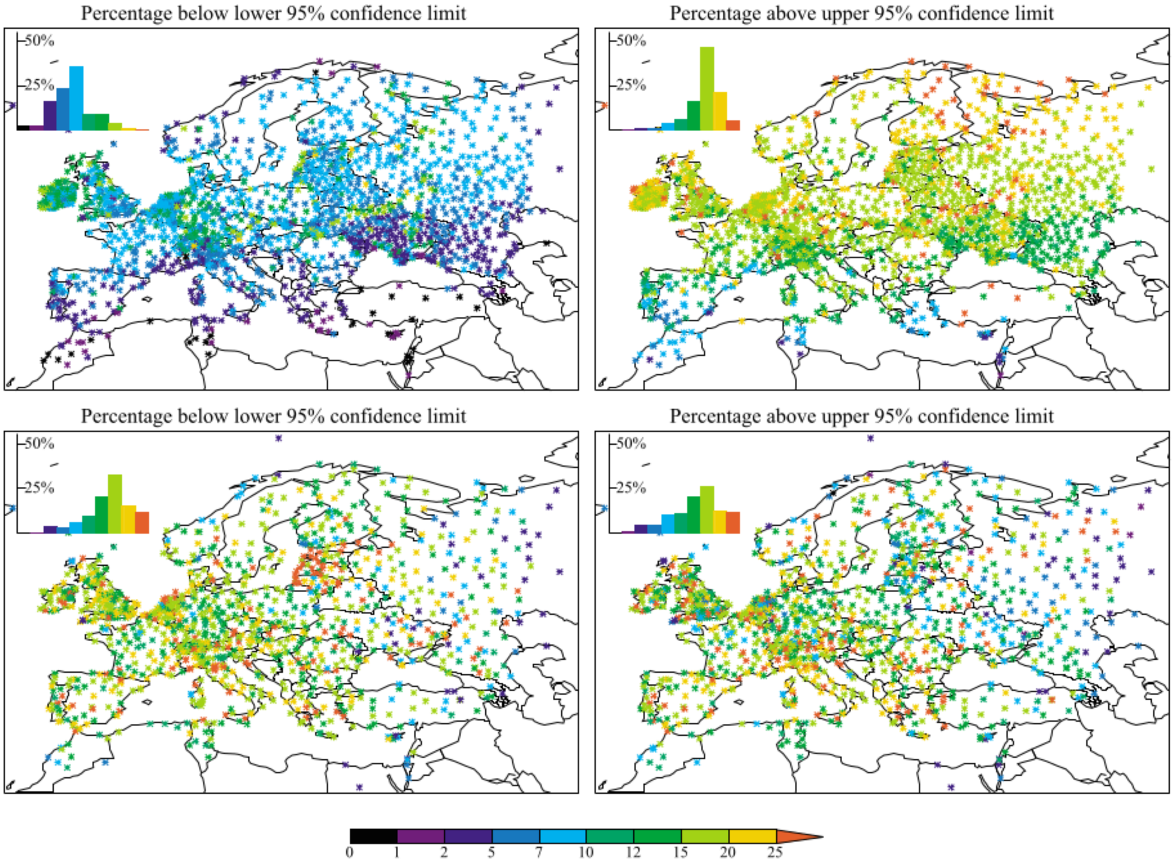

Figure 3.1: Figure from Hofstra et al. (2009). Spatial patterns of the percentage of interpolated data exceeding the lower (left) and upper (right) limits of the 95% confidence interval for precipitation (top) and minimum 2m temperature (bottom) for all stations. Insets display histograms of the frequency of the overestimation or underestimation of the stations.

Besides the heterogeneous spatial distribution of the stations, their total number varies over time. The mean standard error in spatial average is higher (0.72°C) at the beginning (1950-1960) than at the end (1990-2000) of the period (0.66°C), due to an increase in the number of stations. However, this error increased after 2000 due to a 20% decrease of the number stations. The error was estimated to be 0.70°C in 2008. Furthermore, uncertainty estimates

have seasonal variation: the standard error is higher in spring and lower in autumn, representing a difference of 0.4°C (Haylock et al., 2008).
In this thesis, the E-OBS data will be used to validate the simulated precipitation and temperature from the RegIPSL model.

## 3.2 Reconstructed LAI from MODIS

The MODIS (Moderate-Resolution Imaging Spectroradiometer) instrument is carried onboard both TERRA (launched in 1999) and AQUA (launched in 2002) polar orbiting satellites (Fig. 3.2). A complete screening of the globe is performed every two days. Their equatorial crossing time is at 10:30 a.m (TERRA) and at 01:30 p.m. (AQUA), ascending node. With an altitude of 705 km, the swath width (at nadir) is 2330 km. MODIS sensor absorbs in the visible and infrared (36 spectral bands, between 0.405 and 14.385 $\mu$m).

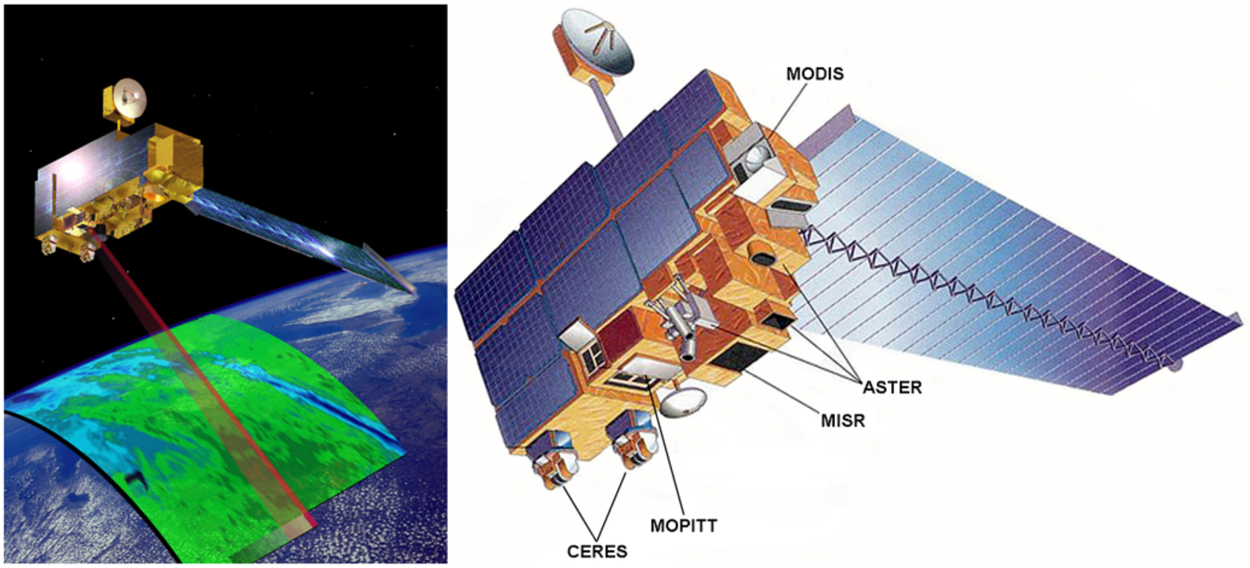

Figure 3.2: Figure from NASA website (`https://www.nasa.gov/directorates/heo/scan/services/missions/earth/Terra.html`). Illustration of Terra satellite carrying a payload of five remote sensors whose MODIS, designed to monitor the state of Earth's environment.

The Leaf Area Index (LAI) is commonly used to describe vegetation state. Mass and energy exchanges between the plant and the atmosphere occur through the leaves and more specifically through stomata (openings in the epidermis). The magnitude of such metabolic mechanisms (e.g. photosynthesis or transpiration) is proportional to the leaf surface. From a conceptual perspective, the LAI is a dimensionless quantity defined as the ratio between the total leaf area (one side) and the ground surface area (Eq. 3.1).

$$LAI = \frac{leaf\,area\,[m^2]}{ground\ area\,[m^2]} \tag{3.1}$$

There are many methods to compute the LAI. The LAI reconstructed from the MODIS instrument is used in this thesis to observe vegetation density variation. The MCD15A2H product (Myneni et al., 2015) provides the LAI with a 4 day temporal resolution and 500 meter horizontal resolution. LAI is computed from the Normalized Difference Vegetation Index (NDVI) by empirical relationships (Knyazikhin et al., 1998). The NDVI is derived from observations in the red channel (RED, 648nm) and the near infrared channel (NIR, 858nm) as follows:

$$NDVI = \frac{NIR - RED}{NIR + RED} \tag{3.2}$$

where the NIR channel is strongly reflected by the vegetation and the RED one strongly absorbed.

The uncertainty of the land surface bidirectional reflectance factor used for this calculation is estimated between 20% and 30% for the red channel and between 5% and 15% for the near infrared channel, depending on the vegetation type (Myneni et al., 2015). The NDVI can be limited in performance for sparsely vegetated areas where the photosynthetic activity is low. Cloud cover can also block NDVI measurement, resulting in missing data. Finally, even if inferring LAI from NDVI includes approximations (Yengoh et al., 2015), MODIS LAI remains a widely used vegetation index with satisfactory results (Yuan et al., 2011).

The estimated LAI from MODIS can show considerable differences with the LAI observed at the surface. Sprintsin et al. (2009) compared the MODIS LAI to ground-based measurements over a Mediterranean dryland forest over two years at monthly time steps. The summer MODIS LAI (0.6 $m^2/m^2$) was almost three times smaller than the LAI measurements (1.7). The monthly standard error of MODIS LAI was estimated at about 0.17.

Considerable differences in absolute values can be also found between the LAI from MODIS and the one from DGVM. With their own conceptual perspective, their calculation method are generally different (e.g. Maignan et al., 2011). However, their variation in relative values should be similar. To optimize the comparison, their values can be scaled to the same range of amplitude. This is what has been done in Chapter 4 with the LAI from ORCHIDEE (see Sect. 4.3.2).

## 3.3 Fire characteristics from MODIS

Three MODIS products are used to study the wildfire activity from satellite observations. Firstly, the MOD14/MYD14 product (from Terra and Aqua respectively) provides, at 1km resolution, the location of thermal anomalies in the spectral band 4$\mu$m (Giglio et al., 2006). Based on Kaufman et al. (1998), the Fire Radiative Power of active fires is computed as follows:

$$FRP = A_S\, \beta\, (T_f^8 - T_b^8) \tag{3.3}$$

where $A_S$ is the nominal MODIS pixel area evaluated at the scan angle, $\beta$ a coefficient (4.34 x $10^{-19}$ $Wm^{-2}K^{-8}$) specific to the MODIS 4$\mu$m spectral response, $T_f$ the 4$\mu$m brightness temperature of the fire pixel and $T_b$ the mean 4$\mu$m brightness temperature of the background window.

Secondly, the product MCD64 (Giglio et al., 2010) provides, at 500m resolution, the burning date based on burn scars defined by thresholds of surface reflectance imagery. Such thresholds are generated from a burn-sensitive vegetation index that discriminates burned pixels for different vegetation types. For each grid cell, the burning date is allocated to the nearest day. Burned area is estimated based on burned scars that are combined with the vegetation fraction in the considered area.

The uncertainty of fire and burn scar detection is mainly due to cloud cover, which prevents the observation of the surface properties. The estimated uncertainty of the burning date is about 2 days (Giglio et al., 2018). Dense aerosol plumes from wildfires may also attenuate the signal resulting in underestimated FRP. Finally, wildfires are dynamic events of varying duration for which satellites capture one or several instantaneous pictures, representative of limited periods of the event.

Lastly, the type of vegetation burned is identified using land cover classification from the MODIS MCD12 product (Friedl et al., 2010) at 500m spatial resolution. From cross-validation analysis, the classification performed by the product shows an accuracy of about 75%. Land cover classes used here are defined by the International Geosphere–Biosphere Programme (IGBP) (Loveland and Belward, 1997). The type of burned vegetation is converted into ORCHIDEE Plant Functional Types (see Chap. 5). The 16 MODIS classes as well as the aggregation matrix to ORCHIDEE PFTs can be found in Appendix B (Tab. B.4).

## 3.4 Atmospheric composition

### 3.4.1 European surface network of ozone concentration

The European Environment Agency (EEA) provides hourly concentrations of $O_3$ and other pollutants from in-situ measurements across Europe. The AQ e-Reporting project gathers air quality data provided by EEA member countries as well as european collaborating countries. Merging with the statistics of AirBase v8 project (2000-2012), AQ e-Reporting offers a multi-annual time series of air quality measurement data until 2019 (`https://www.eea.europa.eu/data-and-maps/data/aqereporting-9`, last access: 30 July 2021). Meta-information on the station network are also provided; specifying the station altitude, type (background, traffic or industrial) and zone (rural, suburban or urban).

$O_3$ concentration at field site is generally measured using an ozone analyzer, based on photometry (Thunis et al., 2013). Outdoor air is pumped into a chamber. An electromagnetic wave at 250 nm, in the $O_3$ absorption band, is sent through the sample. The measurement of the transmitted radiation ($l_t$) allows the derivation of the $O_3$ mixing ratio [$mol/mol$] based on the Beer-Lambert law :

$$O_3 = -\frac{RT}{\sigma N_A P L} ln \frac{l_t}{l_0} \tag{3.4}$$

where $R$ is the molar gas constant [J/mol.K], $T$ the temperature in the measuring chamber [K], $\sigma$ the absorption cross section [$m^2$], $N_A$ the Avogadro number, $P$ the pressure in the chamber [Pa], L the optical path length of the cell [m] and $l_t/l_0$ the transmittance (with $l_0$ the exciting energy [W] and $l_t$ the exciting energy minus the energy absorbed).

Uncertainties attributed to in-situ observations come mainly from measurement errors. Thunis et al. (2013) quantified the various uncertainty sources of $O_3$ measurements (e.g. linear calibration, UV photometry and sampling losses) to calculate a total uncertainty equal to 15%, regardless the concentration level. Based on 400 rural background stations from Airbase, Boynard et al. (2011) estimated the mean standard deviation of hourly $O_3$ concentrations at $8.8 \mu g/m^3$ (summer 2004 over the Central Europe). However, the same metric for an ensemble of CHIMERE simulations was two times larger.

Being point measurements, those data are limited in terms of representation, especially when they are compared to model grid cells. The spatial coverage of the network is heterogeneous, depending on the release of each country (e.g. Southeastern Europe less represented). The spatial distribution of all stations for 2018 is shown in Chap. 1 (Fig. 1.7). Classification of station types and zones can be prone to some approximations. Additionally, the continuity of measurements over years is variable. In 2003, the network included 1805 stations of $O_3$ measurements (30 reporting countries) against 2195 in 2018 (37 countries).

### 3.4.2 Formaldehyde total column from OMI

Formaldehyde ($HCHO$) is produced in high yield during the oxidation of hydrocarbons. The two main sinks of $HCHO$ are photolysis and OH reaction. It can be also removed by deposition (minor sink). As a consequence, its lifetime does not exceed a few hours during summertime. As an intermediate product of the oxidation of most VOCs and being characterized by a short-lifetime, $HCHO$ is used as a quantitative proxy of VOC emissions (e.g. Millet et al., 2008; Curci et al., 2010). However, there are considerable uncertainties concerning the relationship between $HCHO$ yield and VOC oxidation. Based on isoprene aircraft measurements over North America, Millet et al. (2006) estimated at ∼40% the uncertainty of inferring isoprene emissions from $HCHO$ satellite measurements.
The Ozone Monitoring Instrument (OMI) (Levelt et al., 2006, 2018) carried on NASA's Aura satellite, provides observations of $HCHO$ total column (Fig. 3.3). Launched in 2004, it is part of the Earth Observing System program aiming at studying the chemistry and dynamic of Earth's atmosphere. Aura is one of the seven satellites that compose the Afternoon Train (A-Train), a constellation of satellites (including Aqua) along the same or very similar orbit. Its equator crossing time is at 01:45 p.m on the ascending node. With about 14.5 revolutions per day and a swath width of 2600km, global coverage is performed every day. OMI measures backscattered solar radiation in the UV (270-314 and 306-380 nm) and visible (350-500 nm) bands.

Figure 3.3: NASA's Aura satellite carrying the OMI instrument. The figure is from online documentation of the Royal Netherlands Meteorological Institute (`https://www.knmiprojects.nl/projects/ozone-monitoring-instrument`).

$HCHO$ observations used in this thesis are from the OMHCHOd level 3 product (Chance, 2019). It provides daily measurements of $HCHO$ total column, globally with a spatial resolution of 0.1° × 0.1°. $HCHO$ is measured in the near-UV (between 306 and 360 nm). The seasonal cycle of $HCHO$ is observed by OMI over Europe with a maximum in summer and a minimum in winter. Curci et al. (2010) computed spatial correlations (R coefficient) over the continental Europe between observed (OMI) and simulated $HCHO$ columns (CHIMERE) of about 0.5-0.6 during summer 2005.

Uncertainties on the $HCHO$ retrieval is significant, varying between 30% (pixels with high concentrations) and 100% (with low concentrations), and mainly due to cloud and aerosol scattering along the field of view (González Abad et al., 2015). All satellite retrievals (e.g. OMI, GOME2A) of $HCHO$ products present a systematic low mean bias (20-51%) compared to aircraft observations (Zhu et al., 2016). However, the analysis using $HCHO$ total column from OMI presented in this thesis is mainly focused on the relative difference during droughts and heatwaves so that no correction factor has been applied.

# Chapter 4

# Identification and variability of droughts and heatwaves

This chapter aims at identifying droughts and heatwaves by using adapted methods in order to answer the following question: "What are the variations and characteristics of heatwaves, meteorological and agricultural droughts in the Western Mediterranean over the last decades (1979-2016) ?".

A simulation by the RegIPSL coupled regional model (ORCHIDEE-WRF) over the 1979-2016 period in the Western Mediterranean is used to identify heatwaves and droughts. After an evaluation of the model performance against observations of temperature, precipitation and vegetation, a spatio-temporal analysis is conducted using specific indicators of extreme events: the Standardized Precipitation Evapotranspiration Index (SPEI) and Percentile Limit Anomalies (PLA).

For the PLA method or similar, the chosen percentile is generally between 80 and 95 for the identification of extreme weather event (e.g. Stéfanon et al., 2012a). In this thesis, I applied the PLA on the percentile 75 for a larger statistical population. As a result, it must be emphasized that events detected here cover not only extreme events, but also periods that are significantly drier and warmer than normal conditions. Nevertheless, the PLA method has been tested on the percentile 90, presenting satisfying results. The PLA product (with both percentile 75 and 90) is freely available here: `https://thredds-x.ipsl.fr/thredds/catalog/HyMeX/medcordex/data/Droughts_Heatwaves_1979_2016/catalog.html`. All needed information about it can be found in the IPSL Data Catalog (`https://data.ipsl.fr/catalog/`, product name: "Agricultural droughts and heatwaves in the Euro-Mediterranean, daily indicator over the 1979-2016 period based on a coupled land surface and weather model (ORCHIDEE-WRF)").

The present and next chapter (5 - Isolated and combined effects of droughts and heatwaves on the biosphere) are from the article Guion et al. (2021) published in Climate Dynamics journal (freely available here: `https://doi.org/10.1007/s00382-021-05938-y`). The core of the text is the same as in the article. Some parts have been reorganized for the reader's convenience. Moreover, relevant elements of discussion with the reviewers have been added. A list of communications related to this PhD thesis is available in Appendix C.

## Contents

## 4.1 Introduction

In line with what is expected in a context of global warming, droughts and heatwaves have increased both in frequency and severity over the last century in the Mediterranean area. Half of the 10 strongest heatwaves during the 1950-2014 period occurred between 2003 and 2014 in Europe (Russo et al., 2015). The 1990s and 2000s are the decades with the highest drought frequency and intensity over the 1950-2012 period in the Mediterranean (Spinoni et al., 2015). This trend is expected to continue over the 21st century according to regional climate simulations from the EURO-CORDEX project (RCP4.5 and RCP8.5 scenarios) (Spinoni et al., 2018).

A heatwave is generally described as several days during which temperature is above seasonal average (e.g. Stéfanon et al., 2012a; Stegehuis et al., 2013). The definition of droughts is more complex and depends on the type of drought considered. There are meteorological, hydrological, and agricultural droughts with different related effects. These types of drought are manifested by, respectively, a rainfall deficit, a limited soil water reservoir for surface and underground flows, and a water shortage for plant growth (Vicente-Serrano et al., 2012; Svoboda and Fuchs, 2016).

The occurence of these extreme events over the Mediterranean is directly linked to weather regimes at the synoptic scale with, for instance, the Atlantic Low and the Blocking regime, which bring warm and dry air in summer over the Mediterranean (e.g. Cassou et al., 2005; Stéfanon et al., 2012a). Summer droughts also depend on the rainfall between October and March (between 50% and 80% of annual rainfall)(Philandras et al., 2011; Xoplaki et al., 2004). At the meso-scale, the development of droughts and heatwaves are linked, mainly through the soil moisture-temperature feedback. A dry soil cannot provide latent heat cooling by evapotranspiration and, therefore, contributes to the warming of temperatures (Stéfanon et al., 2014). In addition, the dry convection favoured by hot days increases the height of the planetary boundary layer (PBL), leading to the development of upper anticyclonic conditions and increasing atmospheric stability (Zampieri et al., 2009). Droughts in the Mediterranean can also lead to heatwaves in continental Europe induced by the northward transport of warm and dry air, with episodes of southerly winds (Vautard et al., 2007).

The variable chosen for the identification of drought is fundamental and may impact conclusions (Rivoire et al., 2019). Most studies use the Standardized Precipitation Evapotranspiration Index (SPEI). However, it contains limited information about the real soil water content and vegetation state (Svoboda and Fuchs, 2016). Gathering 117 sampling points across the world, Vicente-Serrano et al. (2012) computed the correlation between SPEI and soil moisture. The mean coefficient was around 0.45 in spring and 0.55 in summer with the highest values reaching 0.85. Moreover, information about water absorption by plant roots is missing in the SPEI. Even if this index, when compared to others, shows the best correlation with wheat yield over the Mediterranean, values ranged only from 0.2 to 0.6 (Vicente-Serrano et al., 2012). In this study, the coupled RegIPSL model, inherited from the MORCE-MED platform (Drobinski et al., 2012), is used in order to analyze both meteorological (temperature anomalies, SPEI) and hydrological variables (anomalies in soil dryness). The RegIPSL simulation has been performed for the 1979–2016 time period at 20 km spatial resolution, allowing an integration of the spatio-temporal dynamics of droughts, with inter-annual variability.

Finally, the RegIPSL simulation has been performed with interactive phenology which allows it to account for the soil moisture-temperature feedback. Stéfanon et al. (2014) emphasize the need to perform long term simulations integrating meso-scale surface atmosphere exchanges. According to Fischer et al. (2007), such interactions contribute to an increase of heatwave duration and account for 50-80% of the number of summer hot days. Furthermore, interactive phenology of the vegetation is important for the simulation of drought and heatwave processes. Water-stressed vegetation can amplify heatwaves by land surface heating. The opposite effect (heatwave dampening) is possible in situations of enhanced evapotranspiration and surface cooling. Stéfanon et al. (2012b) showed that dynamic vegetation can modify the 2003 summer heatwave assessment by ±1.5°C, i.e. 20% of its magnitude.

In the second section of this chapter, the chosen configuration for the regional coupled RegIPSL model is presented, and the simulation performed for the Western Mediterranean (Med-CORDEX) is evaluated against observations of temperature, precipitation (E-OBS data) and vegetation (MODIS) (see Sect. 4.3). After a presentation of the methods used for the identification of extreme events (see Sect. 4.4), the simulated spatio-temporal patterns of droughts and heatwaves are identified and then characterized both in frequency and intensity (see Sect. 4.5).

## 4.2 RegIPSL configuration

For the present study, a configuration of RegIPSL was chosen to comply with the recommendation of the Med-CORDEX initiative (Ruti et al., 2016), a contribution to CORDEX (Coordinated Regional Climate Downscaling Experiment). The domain covers the Euro-Mediterranean. The chosen resolution is 20km on a Lambert-conformal projection. For the vertical dimension, 46 levels were chosen with over half below 500hPa. The simulation covers the 1979-2016 period with the ERA-I reanalysis being used to drive the atmosphere at its lateral boundaries. In order to avoid too large of a divergence of the internal solution in the atmosphere and the boundaries, the wind and temperature at scales above 1200km, in the levels above the planetary boundary, were also nudged towards the ERA-I reanalysis. It was shown by Omrani et al. (2015) that this improves the quality of the simulation over the entire domain. To start the simulation with land surface state variables in equilibrium with the atmosphere, we have used the output of a long Med-CORDEX simulation as the initial conditions. This PhD is focused on the Western Mediterranean area. Figure 4.1 shows the dominant PFTs present in our study area. C3 agriculture is mainly located at low altitude over plains, while C3 grass and temperate forests are dominant on topographical features.

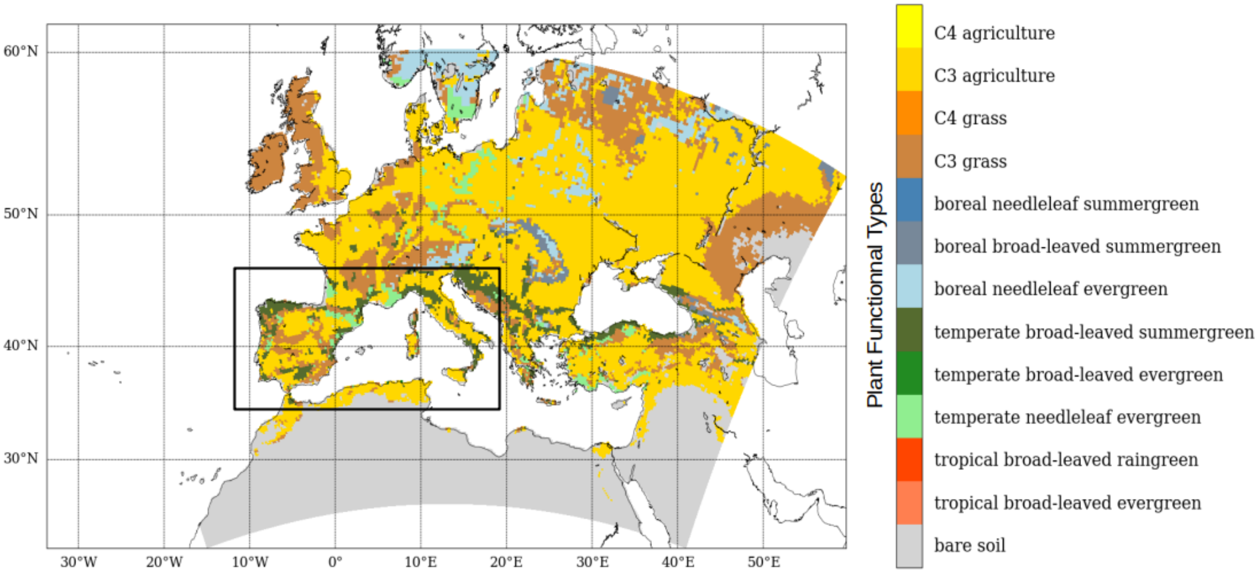

Figure 4.1: Dominant PFT vegetation over the domain of Med-CORDEX simulation. The Western Mediterranean region studied here is shown in black.

## 4.3 Validation of the Med-CORDEX simulation

### 4.3.1 Temperature and precipitation

The simulated temperature at 2m above surface ($T_{2m}$) is evaluated by comparisons with the E-OBS database. For the 1979-2016 period simulated here and during the summer (June-July-August), the average daily mean simulated $T_{2m}$ is overestimated by $\sim$2-3°C over most of the Western Mediterranean (Fig. 4.2). The bias is highest over the Southern Mediterranean (5-6°C) and negative over topographic relief (Alps and Pyrenees, -1 to -2°C), where the uncertainty on the gridded data set is higher (see Sect. 3.1). On average over the Western Mediterranean, the $T_{2m}$ time series (Fig. 4.3) show that the simulated daily mean $T_{2m}$ is overestimated by 1.75°C to 2.0°C (compared to observations), there is no bias on the daily maximum $T_{2m}$, and the daily minimum $T_{2m}$ is overestimated by 2.5°C–3.25°C. The correlation coefficient between observations and simulation is $\sim$0.96 for the minimum $T_{2m}$, and $\sim$0.98 for the mean and maximum $T_{2m}$.

During winter (December-January-February), the bias is less pronounced and more spatially heterogeneous. The time series show that the $T_{2m}$ bias is within the range of the E-OBS standard error ($\sim$0.7°C). The correlation coefficient is slightly lower in winter ($\sim$0.90) than in summer for the minimum $T_{2m}$. It is similar for the mean and maximum $T_{2m}$ ($\sim$0.98). The largest standard error of the bias is obtained for the minimum $T_{2m}$ (0.10°C in winter and 0.07°C in summer).

In order to understand the bias of $T_{2m}$, the seasonal distribution of the energy budget in Med-CORDEX was analyzed, as the seasonal temperature is mainly controlled by surface fluxes. Compared to the results presented by Pfeifroth et al. (2018), based on the SARAH-2 and CLARA-A2 satellite climate data sets and over the same time period (1992-2015), the average Med-CORDEX downward solar radiation reaching the surface is about 20W/m$^2$ higher over most of the domain (Appendix B: Fig. B.1). As shown by Chakroun et al. (2018), this overestimation could be due to a lack of low clouds, especially in summer. Low aerosol concentration may reinforce the bias. Bastin et al. (2018) found similar results for a regional WRF climate simulation over the Mediterranean when compared to ground-based observations (lidar station).

Compared to the E-OBS database, the simulated summer rainfall rate is, on average, slightly overestimated, from 0.1 up to 0.6 mm/day, depending on the year (Fig. 4.4). During winter, the average simulated precipitation in the area is underestimated. The bias decreases along the simulation period, from -0.4 mm/day in 1984 to -0.1 mm/day in 2015. Unlike summer, the winter bias pattern is heterogeneous (Fig. 4.5). The biggest bias is obtained over the Alps ($\sim$-5 mm/day). The correlation coefficients, 0.85 in summer and 0.9 in winter, show the ability of the model to capture the temporal variations.

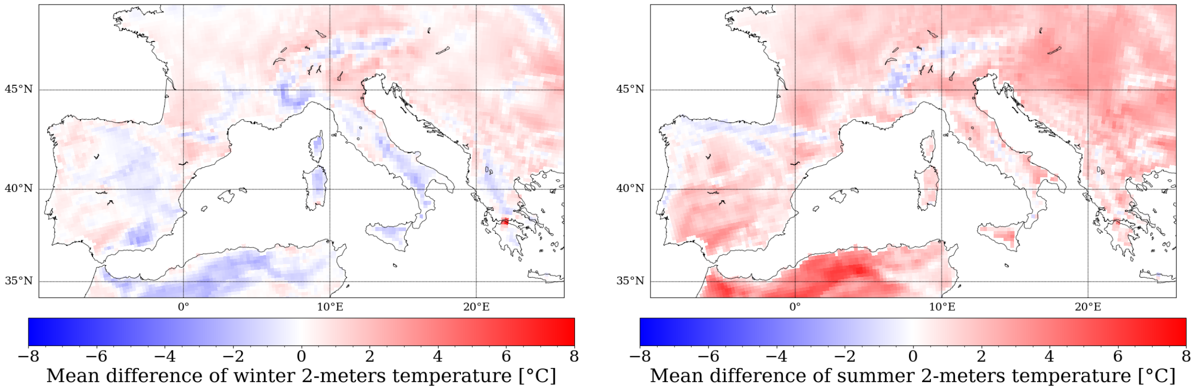

Figure 4.2: Spatial distribution of the daily mean temperature difference between Med-CORDEX simulation and E-OBS observations for winter DJF (left panel) and summer JJA seasons (right panel).

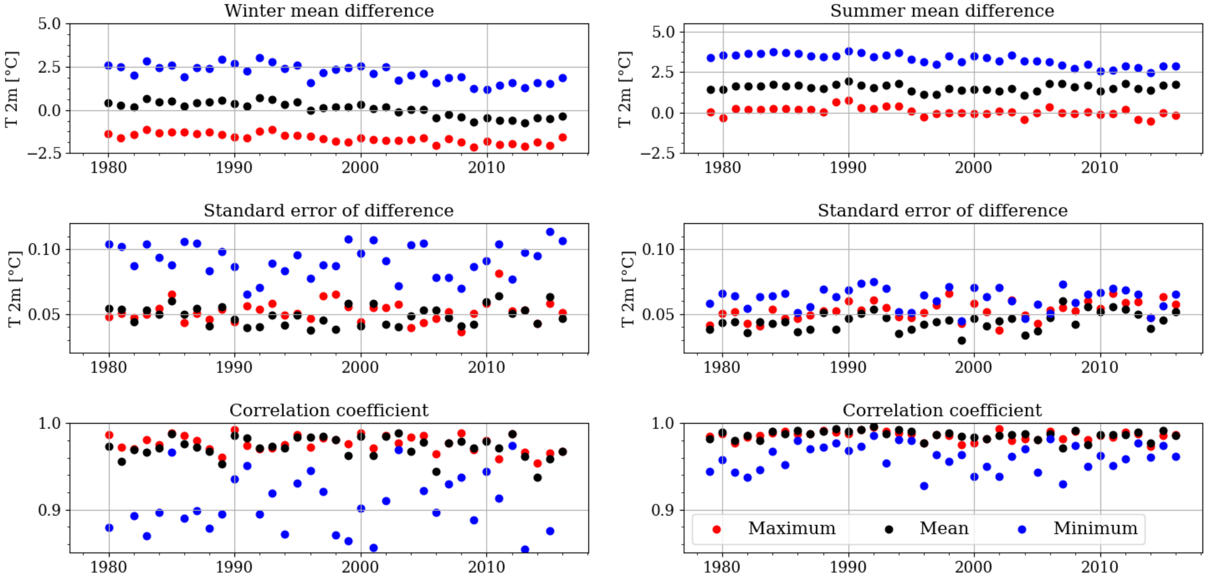

Figure 4.3: Mean difference of temperature (upper row), standard error of difference (middle row), and correlation coefficient of temperature (lower row) between the Med-CORDEX simulation and E-OBS observations spatially averaged for winter, DJF, (left column) and summer, JJA, seasons (right column). Times series cover the simulation period of 1979-2016. Maximum, mean and minimum temperature are, respectively, represented by red, black, and blue color. The standard error of the difference is computed as $\sigma/\sqrt{n}$, where $\sigma$ is the standard deviation of the bias and $n$ the sample size.

The rainfall rate bias obtained, with a low standard error (5 to 10%), is in the range of validation values from other analysis in the literature (see Sect. 3.1). The overestimated summer rainfall by WRF is also found by Herwehe et al. (2014) and Katragkou et al. (2015) for the United States and Europe. They suggest that the overestimated downward shortwave radiation implies an excess of latent heat flux which triggers an overestimate of the summertime convective precipitation through the Kain-Fristch convective scheme.

The simulated cloud cover fraction is close to 0.10 on average over the summer and 0.50 in winter (not shown). This seasonal variability in cloud cover is higher than that found by Ioannidis et al. (2018) using the NCEP/NCAR reanalysis for the period 1948-2014 (amplitude of $\sim$0.15 - 0.20, depending on the area). However, Chakroun et al. (2018) simulated with WRF a seasonal variability of cloud profiles over Europe, similar to space lidar observations (CALIPSO) for the period 2006-2011.

The simulated wind speed is also analyzed in this study for their role on wildfire activity (e.g. Beer, 1991; Duane and Brotons, 2018) (see Sect. 5.3). Since it is not central to this study, a full validation is not shown here. However, previous studies using the regional atmosphere/ocean coupled model WRF/NEMO-MED12, with similar configuration (HyMeX/MED-CORDEX simulations using ERA-Interim reanalysis), have demonstrated a satisfying reproduction of the intensity, direction and inland penetration of the sea breeze (mean accuracy of 5-20% for those characteristics) over the northwestern Mediterranean area (Drobinski et al., 2018).

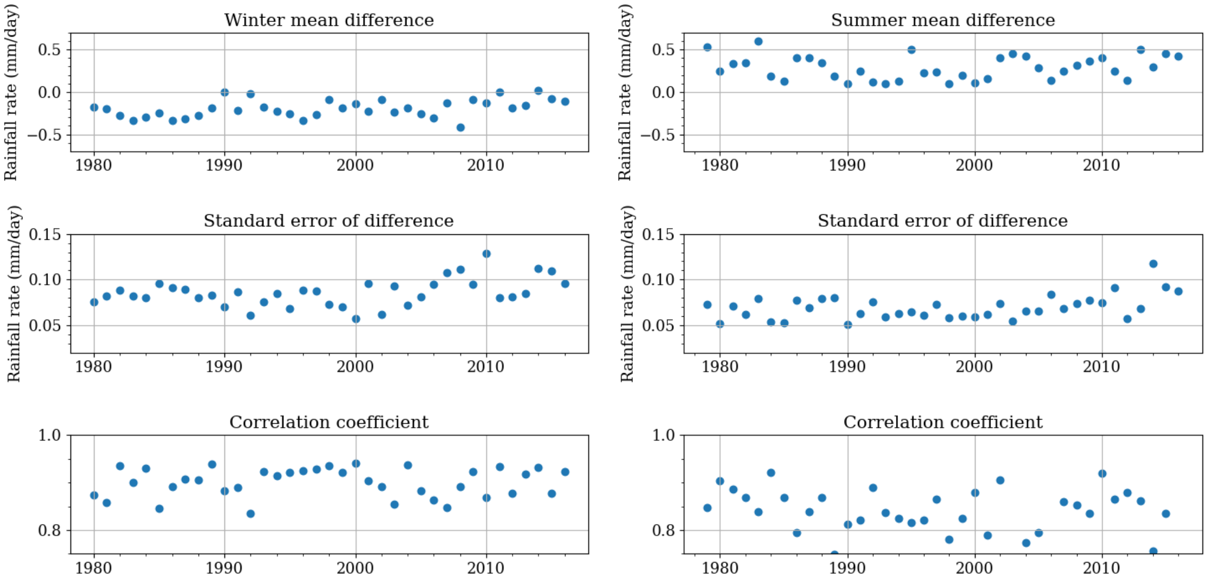

Figure 4.4: Mean difference of rainfall rate (upper row), standard error of difference (middle row), and correlation coefficient of rainfall rate (lower row) between the Med-CORDEX simulation and E-OBS observations spatially averaged for winter, DJF, (left column) and summer, JJA, seasons (right column). Times series cover the simulation period of 1979-2016. The standard error of the difference is computed as $\sigma/\sqrt{n}$, where $\sigma$ is the standard deviation of the bias and $n$ the sample size.

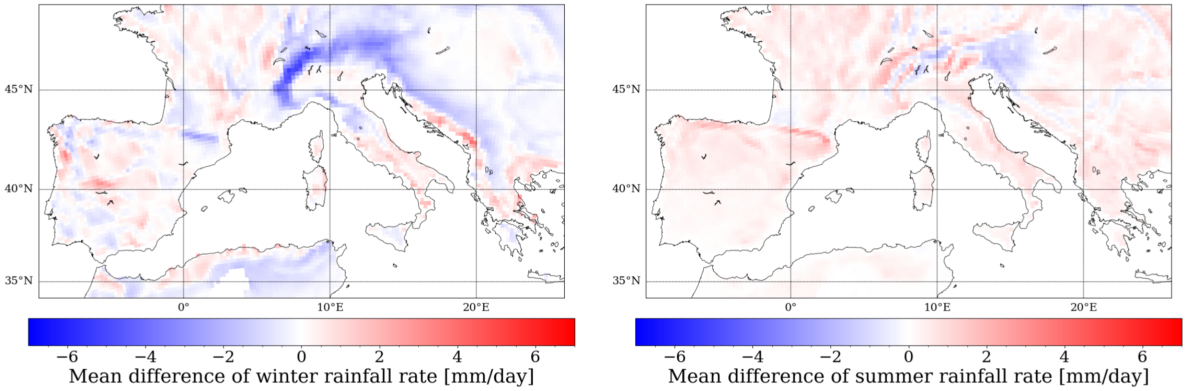

Figure 4.5: Spatial distribution of the rainfall rate mean difference between the Med-CORDEX simulation and E-OBS observations for winter, DJF, (left panel) and summer, JJA, seasons (right panel).

### 4.3.2 Leaf Area Index

The simulated LAI is evaluated by comparison with MODIS satellite observations of the 4-day mean LAI. The MODIS LAI was gridded over the Med-CORDEX domain and smoothed (Hanning window) to avoid any artificial variability that might be due to the representation of the data in grid cells. The simulated LAI was averaged over the 4-day observation periods, and only grid cells with coincident observations were considered.

Timeseries of 4-days LAI, averaged over the Western Mediterranean, are shown in Figure 4.6. Significant differences between simulated and observed LAI are obtained. In particular, the amplitude of the seasonal variation is larger in the simulation. On average, over the period, the Med-CORDEX LAI varies between 2.25 (summer) and 0.40 (winter) while the MODIS LAI varies between 1.25 (summer) and 0.60 (winter). The decrease of LAI from June to August is stronger in the simulation (-40.0%) than in the observations (-15.3%). As a result, the LAI bias decreases: +0.91 units on the 1st of June and +0.24 units on the 31st of August. The spatial distribution of the summer bias of LAI is homogeneous ($\sim 2.0$) over the Northern Mediterranean. It is much lower and more heterogeneous in semi-arid areas (between -0.5 and 0.5), like over Southern Spain or Maghreb (Fig. 4.7). Differences at the regional scale could be partly explained by the overestimated downward shortwave flux in RegIPSL during the summer, since exceeding solar energy can boost vegetation growth. It may also be due to different representations of phenology. However, the intra- and inter-annual variation are spatially and temporally similar. The temporal correlation between both LAI is high (between 0.5 and 0.8) over most of the Western Mediterranean as well as for the semi-arid regions (Appendix B: Fig. B.2).

Caldararu et al. (2014) found a similar seasonal amplitude of LAI with the MODIS instrument in the Mediterranean ($\sim 0.7$). Even if Chakroun et al. (2014) identified a low summer variation of the intra-annual MODIS LAI, they demonstrated that MODIS captures accurately the inter-annual variability of summer LAI response due to drought for most of the Mediterranean forests. However, Sprintsin et al. (2009) highlighted significant discrepancies between MODIS LAI and ground-based measurements for dry forests due to a lack of distinction at high resolution between land cover elements which can be highly heterogeneous and sparse over the semi-arid areas. In this case, the seasonal variation of MODIS LAI during the summer is too weak. Summer overestimation of simulated LAI from vegetation models in comparison to MODIS LAI was found in several previous studies; between 0.5 and 1 over the Mediterranean with ORCHIDEE (Demarty et al., 2007), and between 1 and 2 over the United States (Indiana) with the crop growth model CSM-CERES-Maize (Fang et al., 2011) as examples.

In order to compare the amplitude of the responses to heat and water stress both in absolute and relative values (see Chap. 5, Sect. 5.2), the amplitude of the simulated LAI has been scaled to that of the observations (Fig. 4.6).

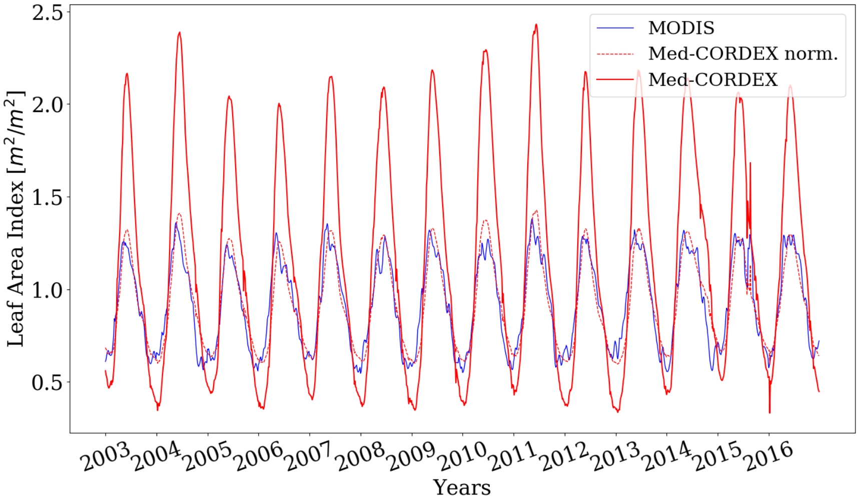

Figure 4.6: Leaf Area Index simulated by the RegIPSL model (Med-CORDEX) and estimated by the MODIS satellite instrument over the 2003-2016 period. The data are spatially averaged over the Western Mediterranean. The Med-CORDEX LAI has been normalized to the regional amplitude of the MODIS LAI (red dashed line).

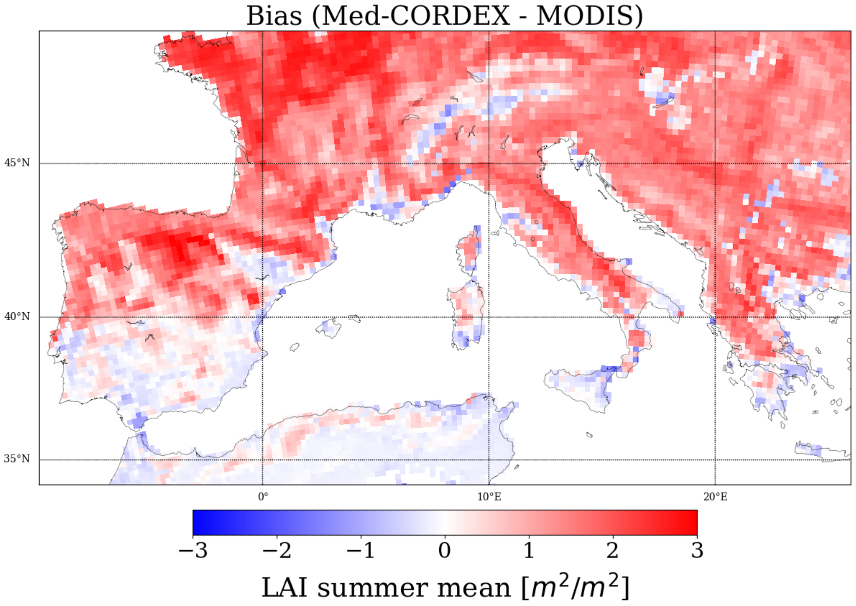

Figure 4.7: Summer mean bias of the Leaf Area Index between the Med-CORDEX and MODIS over the 2003-2016 period.

## 4.4 Indicators of extreme weather events

Several indicators have been calculated based on the RegIPSL simulation (and E-OBS data set for validation) in order to identify time periods affected by extreme events during the summer: heatwaves, droughts (and wind gusts, see Sect. 5.3).

Meteorological droughts may be identified using the Standardized Precipitation Evapotranspiration Index (SPEI method). Developed by Vicente-Serrano et al. (2010), it is based on the Standardized Precipitation Index (SPI) (McKee et al., 1993) but also includes temperature information through the potential evapotranspiration. For each region (or model grid cell) and for a given month $m$, the water balance is calculated as the difference between the accumulated monthly precipitation $P_m$ and the potential evapotranspiration $PET_m$:

$$D_m = P_m - PET_m \tag{4.1}$$

When $D_m$ is positive, the excess water (called useful water) can generate runoff and infiltration into the unsaturated soil and thus be available for plant transpiration. When $D_m$ is negative, the considered month is in a deficit. The water balance can be accumulated over several months, including a certain number of months before month $m$. Here $D_m$ is computed over periods of 3, 6 and 12 months. An index of 0 represents normal conditions (average value of SPEI). A negative (positive) index means that the studied period is dryer (wetter) than normal conditions. The standard deviation is 1. The SPEI gives information on the drought severity through its intensity and approximate duration if the index is below -1 for consecutive months. SPEI is commonly used to analyze the intensification of drought severity related to precipitation reduction in the context of climate change (Vicente-Serrano et al., 2010). However, it is less suitable in semi-arid conditions because the limiting factor is then water availability rather than energy, considered in $PET$.

Therefore, for agricultural drought detection, we chose to construct an indicator based on soil dryness using the Percentile Limit Anomalies ($PLA_{SD}$). The soil dryness is defined as the complement of the Soil Wetness Index (SWI) computed by ORCHIDEE:

$$SWI = \frac{W_c}{W_a} \tag{4.2}$$

where $W_c$ is the ground water content and $W_a$ the accessible water content. This index is convenient for ecologically heterogeneous regions. The water holding capacity of a soil depends largely on its composition. The Soil Dryness Index is then $SDI = 1 - SWI$ and varies between 0 (saturated) and 1 (totally dry).

The PLA method is also used for heatwave detection based on the 2m above surface temperature ($PLA_{T2m}$), and for wind gust detection based on the 10m above surface wind speed ($PLA_{w10}$). $T_{2m}$ has been detrended to detect the anomaly as extreme weather. For each cell of longitude ($i$) and latitude ($j$) in the considered area, the monthly distribution of the variable is normalized. For each month ($m$), the corresponding percentiles ($p$) are computed for the 1979-2016 period. Here $p$ is set at 0.75, to allow a large statistical population. Finally, the daily deviation ($dX_{i,j,d}$) between the 2m temperature/soil dryness/wind speed ($X_{i,j,d}$) and the monthly percentile ($X^p_{i,j,m}$) is computed cell by cell for the day ($d$) as follows:

$$dX_{i,j,d} = X_{i,j,d} - X^p_{i,j,m} \tag{4.3}$$

Equation 4.3 allows the analysis of spatial patterns and highlights local variability. If the spatial sum of $dX_{i,j,d}$ over the chosen area is positive, an extreme day is identified. An extreme event is defined as three consecutive extreme days (Fig.: 4.8). The intensity of the extreme event ($I$) is equal to the average of its anomalies :

$$I = \frac{\sum_{i,j} dX_{i,j,d}}{N} \tag{4.4}$$

where $N$ is the number of cells in the considered area.

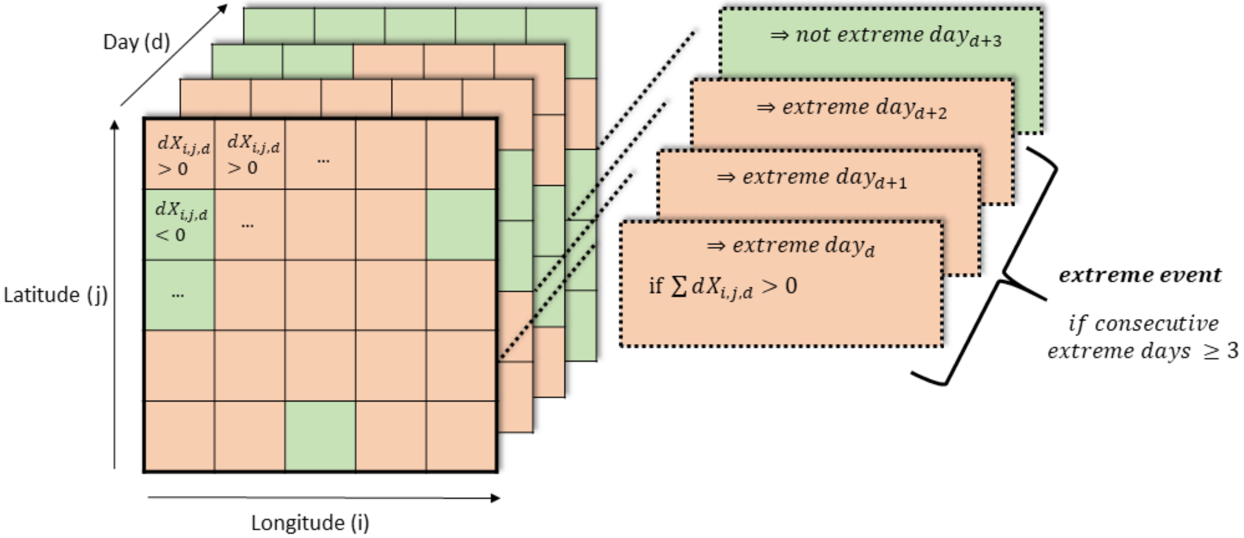

Figure 4.8: Diagram showing how the PLA is calculated. This figure is not included in the published article.

The value of the computed percentile depends on the distribution of the normalized range of values. This feature allows us to apply this method for different regions and is suitable for comparative studies as it accounts for local variability (Lhotka and Kyselý, 2015). Note that the higher the percentile that is established, the more extreme the event. To analyze the synergetic effects of heatwaves and droughts, soil dryness and temperature anomalies

($PLA_{SD}$ and $PLA_{T2m}$) can be combined ($PLA_{SD,T}$). Therefore, each anomaly distribution is standardized before being combined.

The indicators of extreme temperature and soil dryness are used to isolate events and analyze the spatial structures and temporal variations of drought and heatwave characteristics (intensity and frequency) in section 4.5, based on both the PLA and SPEI method. They are complementary methods and provide information on different drought types. SPEI is generally used to identify the meteorological droughts and $PLA_{SD}$ is more appropriate for agricultural droughts. The soil dryness in ORCHIDEE is directly computed from the soil water budget and therefore depends on the soil (water infiltration) and vegetation type (root absorption and plant transpiration) instead of the weather conditions. The spatial distribution of droughts identified by the SPEI is representative of different climate regions while drought patterns identified by $PLA_{SD}$ (more heterogeneous) provides information depending on the sub-regional vegetation and soil distribution, which can vary at local scale. Moreover, both methods represent different time scales: while the PLA method considers the inter-annual variability (conditions during one specific month are compared to the distribution of the same month during the full time-period), SPEI focuses on the intra-annual variability (from 3 to 12 months of accumulation in the considered year).

## 4.5 Frequency and intensity of droughts and heatwaves

### 4.5.1 Regional structures

Figure 4.9 shows the simulated spatial distribution of the mean percentile values ($T_{2m}$ and SD) during the summer (JJA), the mean intensity and the frequency (fraction of summer days) of intense heatwaves ($PLA_{T2m} > 1°C$) and droughts ($PLA_{SD} > 0.02$ of soil dryness). Heatwave and drought patterns are directly sensitive to the distribution of the 75th percentile value as background threshold.

Heatwaves are the most intense (+2°C above the 75th percentile value) and frequent (about 17% of of the summertime for events with $PLA_{T2m} > 1°C$) over the western part of the domain (Western Iberian Peninsula and Western France), North Africa (Northern Algeria and Tunisia) and the Pannonian Plain (mostly Hungary with Northern Serbia and Western Romania).

Droughts are more spatially heterogeneous than heatwaves because, beyond climatic forcing, vegetation and soil type also have an important influence. The Pannonian Plain is affected by intense (+5% of soil dryness) and frequent droughts (about 20% of the summertime for events with $PLA_{SD} > 2\%$). Northern Italy is also affected by intense droughts. Similar to heatwave patterns, drought patterns have to be analyzed in conjunction with the percentile values. For example, in Northern Africa, soil dryness percentile is high, which results in a low mean intensity and frequency of events.

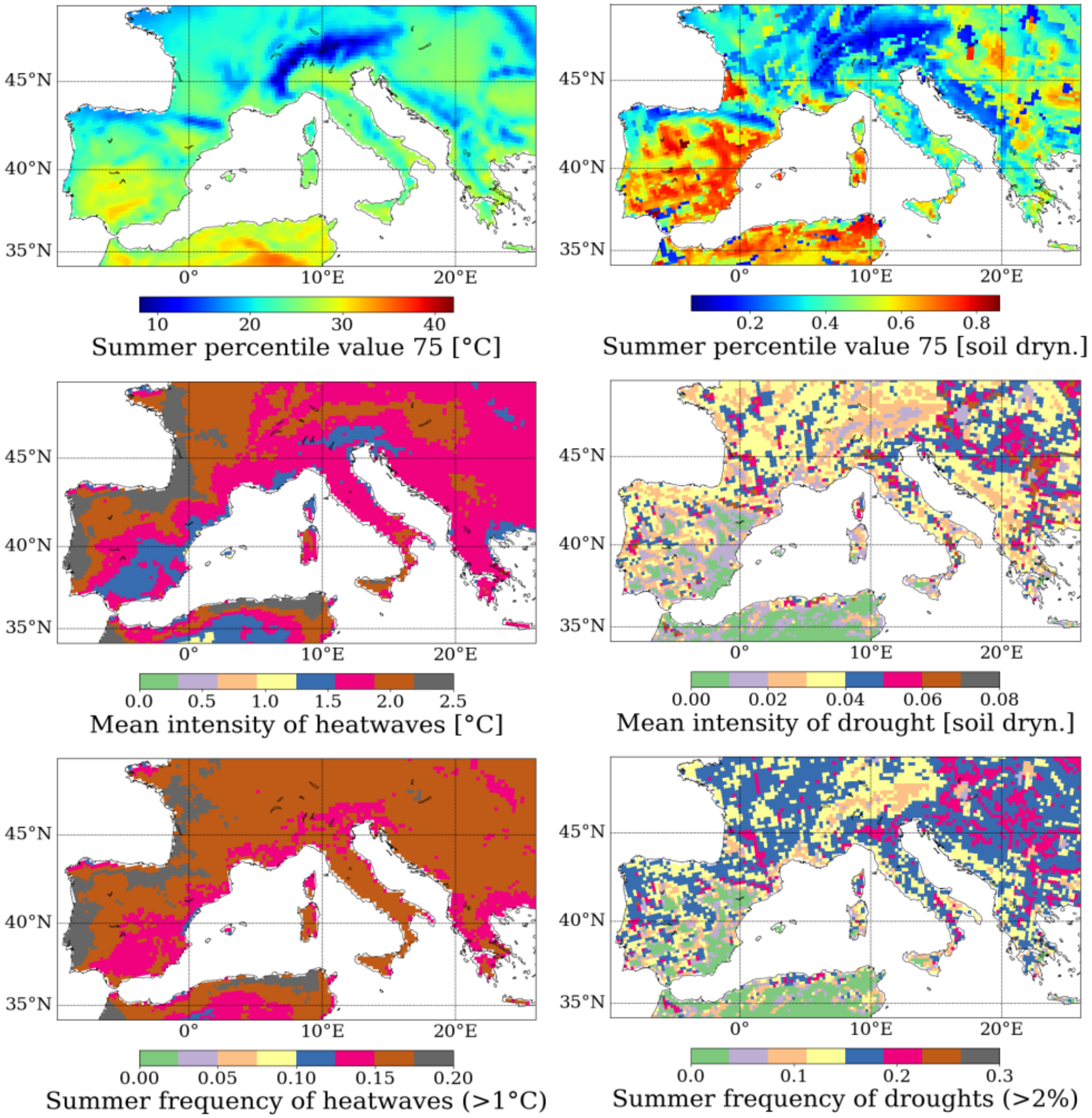

Figure 4.9: Heatwaves (left column) and droughts (right column) identified using the Percentile Limit Anomalies (PLA) method. The first row shows the $75^{th}$ percentile value during summer (JJA average), the second row shows the mean intensity of the extreme events, and the last row shows the frequency (over the total number of summer days) of intense events ($> 1$°C for heatwaves and $> 0.02$ of soil dryness for droughts).

Figure 4.10 shows the monthly frequency of low summer SPEI (< -1), calculated with 6 months of accumulation, characterizing meteorological droughts during the 1979-2016 period. Southern Spain and inland Algeria and Tunisia (with dominant bare soil) are the areas most affected by droughts (frequency of occurrence between 20% and 30% of summer months). Droughts are also very frequent over the Pannonian Plain, as obtained using the $PLA_{SD}$ method.

The spatial extent of droughts varies with the time scale and period of analysis (e.g. Vicente-Serrano et al., 2013; Gouveia et al., 2017). With 12 months of accumulation of water balance ($D_m$) in the calculation of the SPEI, clear distinction between semi-arid (Andalusia and Northern Africa) and temperate biomes (Northern Mediterranean) can be noticed (Appendix B: Fig. B.3). In the Northern Mediterranean, drought frequency decreases with increasing number of accumulated months: from 20% of summertime with 3 months to 10% with 12 months, because it covers the entire wet season. On the opposite side, semi-arid biomes can be affected by one-year-long droughts.

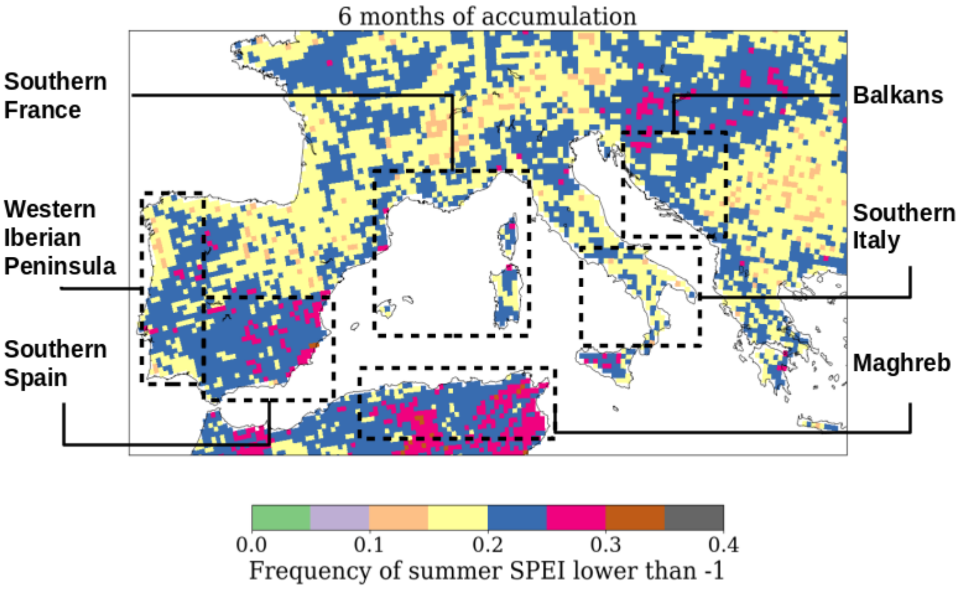

Figure 4.10: Spatial distribution of frequency of summer SPEI lower than -1 computed with 6 months of accumulation period. The frequency is expressed over the total number of summer months along the simulation period, namely 114 months. For diagnostic purposes, sub-regions are designated (dashed rectangles) within the Western Mediterranean region. The choice of those sub-regions is justified by both their high fire activity (see Sect. 5.3) and their representation of different biomes.

Raymond et al. (2016) also highlighted the Pannonian Plain as a cluster of drought occurrence. From 1957 to 2013, they identified 11 Very Long Dry Spells (designation for meteorological droughts based on wet season precipitation) with a mean duration of 62 day events. We found a good agreement on the periods identified.

The synoptic scale circulation in winter can cause a lack of precipitation and lead to the development of spring and summer droughts in the Euro-Mediterranean region. Raymond et al. (2018b) showed that the Blocking regime and the Atlantic Ridge can lead to long winter dry spells in the Mediterranean (and especially in the East) through the subsidence of cold and dry air coming from higher latitudes. Moreover, years with the winter positive phase of the North Atlantic Oscillation (NAO), inducing drier and colder winters than normal over the Mediterranean, can lead to dry springs and summers (Trigo et al., 2004; Bladé et al., 2012; Raymond et al., 2018b). We found a good agreement between positive values of the winter NAO index (Jones et al., 1997) and negative SPEI at the Western Mediterranean scale (not shown).

### 4.5.2 Temporal variability

The PLA method was also applied to the E-OBS $T_{2m}$ for validation. Observed heatwaves show similar regional structures to the simulated ones, especially concerning their frequency (Appendix B: Fig. B.4). Computing the mean bias of heatwave characteristics between Med-CORDEX and E-OBS, we found a bias of +0.16°C for the intensity, +0.07 for the fraction of days, and +0.03 days for the longest event. However, the intensity of observed heatwaves is, in general, slightly lower (Fig. 4.11). The temporal correlation coefficient between simulated and observed $PLA_{T2m}$ is around 0.9 over the study area, except over Northern Africa where it is lower (0.5) (not shown). In conclusion, despite the constant positive bias of simulated $T_{2m}$ (see Sect. 4.3.1), RegIPSL is suitable for simulating heatwaves since extreme conditions (peaks) are well represented.

The temporal variability of droughts and heatwaves has been analyzed for specific sub-regions, because averaged at the regional scale, the large variability of the Western Mediterranean is smoothed and the frequency of droughts and heatwaves is lower than for the sub-regions. Moreover, some events, especially droughts, occur only at sub-regional scale. The temporal variability of seasonal droughts and heatwaves identified for the sub-regions defined in Figure 4.10 are provided in Figure 4.12 & Appendix B: Figure B.5.

Over the set of sub-regions, heatwaves occur almost every summer (97% of summers) due to the low percentile value chosen for this study (0.75). Heatwaves affect 80% of summers considering the percentile of 0.85. Most of the spring and summer heatwaves are in the same range of intensity (between +1.0 and +3.0°C). The summer of 2003 is the season with the highest fraction of days marked as a heatwave for Southern Spain (0.46 during the period analyzed), Southern Italy (0.60) and Southern France (0.74). This record-breaking heatwave has been analyzed in numerous studies for its exceptional severity in Central Europe (e.g. Stéfanon et al., 2012b; Russo et al., 2015). The average duration of summer heatwaves is estimated to 5.8 days.

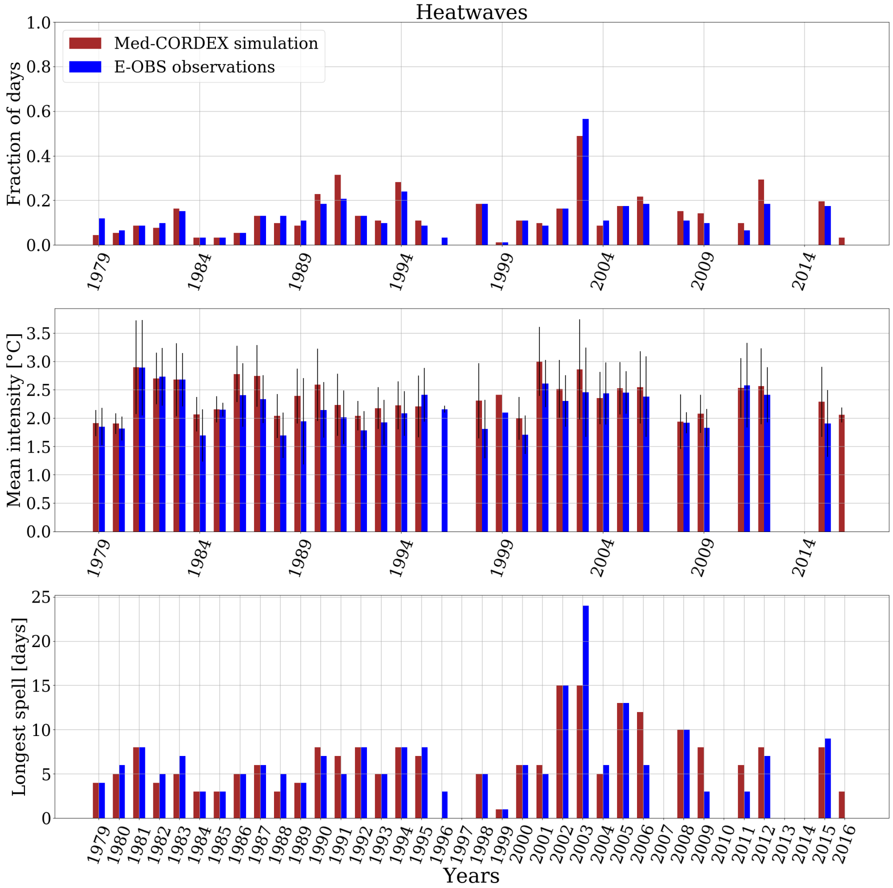

Figure 4.11: Temporal variation of summer (JJA) heatwaves over the Western Mediterranean region, using the $PLA_{T2m}$ method (on 2m temperature) from the Med-CORDEX simulation and E-OBS observations. Top panel: fraction of days affected. Middle panel: mean $PLA_{T2m}$ (intensity). Bottom panel: duration of the longest spell in the considered season.

Compared to heatwaves, droughts are less frequent. 33% of summers are affected by at least one drought event. The sub-regions Balkans, Maghreb, Southern Italy, Southern France and Western Iberian Peninsula are characterized by two clusters of intense summer droughts occurring at the beginning of the 1990s and 2000s. The average duration of summer droughts is 22.3 days.

The temporal distribution of spring (MAM) and summer (JJA) droughts are similar as they both depend on the variability of precipitation during the wet season (Fig. 4.12). On average, 90% of summer droughts are preceded by spring droughts. This shows the influence of spring precipitation and the temporal memory of the soil dryness for summer drought development (Vicente-Serrano et al., 2013). However, 23% of spring droughts are not followed by summer droughts, as in 1989, 1992, and 2008 for the entire Western Mediterranean region. This is due to periods of heavier rainfall in early summer (June-July) which can compensate for a water deficit. Spring droughts (between +3 and +8%) are generally more intense than summer droughts (between +2 and +5%) according to the $PLA_{SD}$ method. The inter-annual variability (and so extremes above the percentile) of precipitation is higher in spring than in summer.

The variation of the SPEI, also shown in Figure 4.12, is in good agreement with the $PLA_{SD}$ variation. Apart from few exceptions due to methodological differences (previously explained), positive anomalies of soil dryness from the 75th percentile are identified when SPEI values are lower than -1. The major drought periods identified are similar to reports from the literature in the Mediterranean region (e.g. Hoerling et al., 2012; Spinoni et al., 2015).

Droughts and heatwaves occurring simultaneously were also identified. On average over the set of sub-regions, 32.6% of dry days were also in a heatwave. The temporal correlation between $PLA_{SD}$ and $PLA_{T2m}$ can be considerable, especially in the Northern Mediterranean, as shown in Figure B.6 in Appendix B (e.g. coefficients of 0.4 and 0.5 over Southern France and the Balkans). With a mean increase of 18.5%, heatwaves are significantly more intense for Southern France, Southern Spain, and the Maghreb when they are accompanied by droughts (+2.3°C above the 75th percentile in comparison to +1.9°C). This highlights the importance of the soil moisture-temperature feedback system in heatwave severity. Droughts are also more intense (6.9%) when they occur simultaneously with heatwaves. However, the effect is non-significant, possibly because of the small sample size of droughts occurring alone.

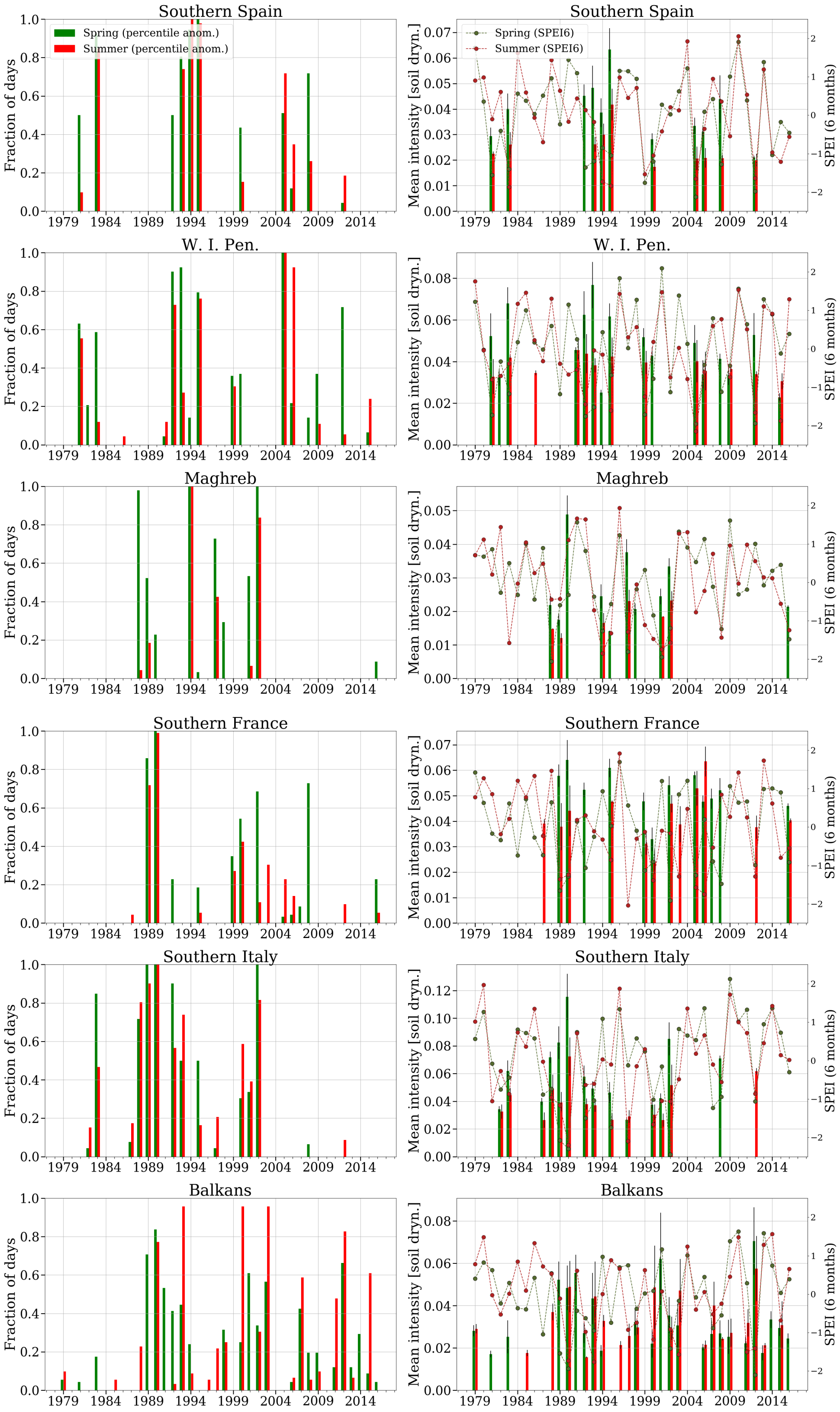

Figure 4.12: Temporal variation of spring (MAM) and summer (JJA) agricultural droughts for the sub-regions defined in Figure 4.10 using the $PLA_{SD}$ method (on soil dryness). Left column: fraction of days affected. Right column: mean $PLA_{SD}$ and SPEI (intensity).

## 4.6 Conclusions

The comparison of RegIPSL key simulated variables with observations demonstrates that the model is appropriate for research on droughts and heatwaves. While simulated summer mean 2m temperature and rainfall from Med-CORDEX show a constant daily overestimation compared to E-OBS, they are within its range of standard error. Extreme conditions are well represented.

Two methods have been used to identify extreme events: the SPEI for meteorological droughts, the percentile limit anomalies (PLA) on the 2m temperature for heatwaves, on the soil dryness for agricultural droughts, and on surface winds for strong wind events. Even if the temporal variability of major droughts detected using the SPEI is close to those detected using the $PLA_{SD}$, differences remain in their spatial distribution. Besides the weather conditions, the $PLA_{SD}$ method accounts for local heterogeneities of soil and vegetation type in the variability of the soil water content. Moreover, SPEI estimates the evapotranspiration from temperature, whereas the limiting factor in semi-arid biomes is often the soil water availability. The SPEI is relevant for detecting meteorological droughts, and the $PLA_{SD}$ method is more suitable for detecting agricultural droughts.

Heatwaves identified based on the E-OBS observations are slightly less intense than those identified based on the Med-CORDEX simulation (maximum difference of -0.5°C); they show similar variability. Moreover, spatio-temporal patterns of both heatwaves and droughts are in good agreement with similar studies found in the scientific literature (e.g. Russo et al., 2015; Raymond et al., 2016).

The most intense (2°C above the 75th percentile) and frequent (17% of the summertime events with $PLA_{T2m} > 1°C$) summer heatwaves occurred over the western part of the domain (Western Iberian Peninsula and Western France), Northern Africa, and the Pannonian Plain. The last is also affected by intense (+5% of soil dryness above the 75th percentile) and frequent (20% of the summertime events with $PLA_{SD} > 2\%$) agricultural droughts.

Even if agricultural droughts affect fewer summers (33%) than heatwaves (97%), they last almost four times longer (mean duration of 22.3 days versus 5.8 days). Moreover, 90% of summer droughts are preceded by spring droughts. This emphasizes how the temporal memory of weather conditions of the wet season determine agricultural drought development even during the summer season. We also highlighted the high co-variability between droughts and heatwaves over some areas (e.g. Balkans and Northern Italy). Heatwaves that occur at the same time as droughts are significantly more intense (+18.5% on average).

This work provides, to the best of our knowledge, the longest spatio-temporal database of agricultural droughts over the Mediterranean using a coupled surface atmosphere model. The method used for the identification of extreme events (PLA method) allows drought and heatwave phenomena to be related. This approach will allow for a more complete assessment of the various impacts of these extreme events (e.g. mitigation and prevention programs about loss of agricultural yield or forest ecosystems), especially in the context of climate change, with the increasing temperature and decreasing precipitation over the Mediterranean region.

# Chapter 5

# Isolated and combined effects of droughts and heatwaves on the biosphere

This chapter aims at analyzing the impact of agricultural droughts and heatwaves on the biosphere, and more specifically at answering the following question: "What is the impact of agricultural droughts and heatwaves on the biomass and wildfire activity ?". To achieve this, MODIS observations of Leaf Area Index (LAI), burned area (BA), and fire radiative power (FRP) are analyzed and clustered by simulated extreme weather events (PLA method).
The present chapter is from the article Guion et al. (2021) published in Climate Dynamics journal (freely available here: `https://doi.org/10.1007/s00382-021-05938-y`). The core of the text is the same as in the article. Some parts have been reorganized for the reader's convenience and relevant elements of discussion with the reviewers have been added.
Moreover, this chapter includes supplementary analysis on the fire weather risk in the Western Mediterranean (see Sect. 5.4) that is not part of the published article.

## Contents

## 5.1 Introduction

During droughts and heatwaves, vegetation is exposed to water and heat stresses. This can considerably affect plant development and vegetation activity, leading to a decrease of carbon uptake (e.g. Vicente-Serrano et al., 2013; Gouveia et al., 2017; Baumbach et al., 2017). For example, over the 1980-2010 period, 60% of the inter-annual variation of wheat production in Spain was attributed to these stresses (Zampieri et al., 2017). Severe wildfires can also result from extreme dry and hot weather conditions (e.g. Bowman et al., 2009; Turco et al., 2017; Duane and Brotons, 2018) with considerable economic, social, and environmental damage. For instance, more than 7000km$^2$ burned in Mediterranean Europe during the record-breaking heatwave in 2003, compared to the annual average of 4500km$^2$ (Russo et al., 2015; Turco et al., 2016). The present chapter aims at assessing the isolated and combined impacts of heatwaves and agricultural droughts on vegetation growth and wildfire activity in the Western Mediterranean region. Therefore, the simulated droughts and heatwave from the RegISPL model (see Chap. 4) are analyzed in conjunction with satellite observations of vegetation density and fire activity from the Moderate-Resolution Imaging Spectroradiometer (MODIS).

Quantifying the effect of droughts and heatwaves on vegetation is complex over the Mediterranean region since it depends on several parameters. The land cover with the associated vegetation type is one of them. Vicente-Serrano (2007) showed that irrigated croplands and deciduous forests with deep root systems are less affected by plant activity decline in comparison to shrubs and pasture-lands (on the basis of correlation analysis between drought and vegetation indicator). Moreover, each biome has its own sensitivity to the persistence of a water deficit. Being adapted to recurrent dry conditions, vegetation in semi-arid biomes (e.g. Morocco and Andalusia) responds quickly to water stress (short-term droughts of 3-6 months), whereas in temperate biomes (e.g. France) it is affected by larger droughts of 6-9 months (Vicente-Serrano et al., 2013). Although all Mediterranean biomes are susceptible to biomass reduction over several months (Guiot and Cramer, 2016), semi-arid and arid environments are more prone to plant mortality (Vicente-Serrano et al., 2013). The season, and more specifically, the month of drought occurrence is another important factor. Gouveia et al. (2017) found that the strongest influence of drought on semi-arid biomes occurs in May because plant greenness peaks in spring, whereas it occurs in June-July for temperate biomes (maximum greenness in summer). Heatwaves can also induce a shift in vegetation phenology whose effect can vary seasonally, especially over the Northern Mediterranean (Baumbach et al., 2017). Extreme high temperatures can lead to a slight increase of the vegetation development in March-April, while it induces a strong decrease later in spring and in summer. Topo-climatic conditions are also fundamental, as they modify considerably the temperature and precipitation distribution (Vicente-Serrano, 2007).

The impact of droughts and heatwaves on plant biomass is evaluated in Section 5.2, using the MODIS Leaf Area Index (LAI) primarily, but also from the Med-CORDEX LAI for comparison and to access PFT-dependant information.

In addition to the impact on vegetation, meteorological conditions play a major role on the intensity of wildfire events. Strong winds and hot days favour fire propagation. Duane and Brotons (2018) identified 3 out of the 6 weather regimes at the synoptic scale that control wildfire activity, driven by strong winds: the Scandinavian Low, the Atlantic Ridge, and the Atlantic Low, the last is also favorable for heatwaves (Cassou et al., 2005). Droughts can influence the wildfire activity through two factors: fuel availability and fuel dryness. On one hand, a precipitation deficit during the wet season (November-May) and early summer (June) inhibits vegetation growth and thereby reduces the fuel load (Sarris et al., 2014; Gouveia et al., 2016). On the other hand, droughts during the fire season (June-September) decrease the fuel moisture (Turco et al., 2017). The effect of drought on fuel dryness could be offset by a reduction in fuel availability leading to a limited fire intensity. However, there are many uncertainties as to which effect predominates (Turco et al., 2017).

Moreover, human influence can be considerable. Even if an increase in wildfire risk is simulated in response to climate change (Moriondo et al., 2006), trends of wildfire activity over the Mediterranean were negative in the past few decades, with a total decrease of 3020 km$^2$ burned area (i.e -66%) over the 1985-2011 period (Turco et al., 2016). This is mainly due to efforts in improving fire suppression (direct anthropogenic drivers), and fire management and prevention (indirect drivers). Nevertheless, human control over mega-fires is limited and these extreme fire events are mainly driven by weather conditions and fuel availability. In order to understand the dominant factors in the Western Mediterranean region, it is therefore important to take into account both meteorological conditions and the response of vegetation to extreme events.

In this chapter, the impact of heatwaves and droughts on wildfires (see Sect. 5.3) is analyzed using satellite fire activity observations from MODIS, combined with the identified extreme weather events from the PLA method (see Chap. 4). Supplementary analysis are provided in the last section (5.4) about the trend of the fire weather risk over the last decades but also its assessment against observed wildfires and simulated drought and heatwave indicators.

## 5.2 Vegetation biomass

### 5.2.1 LAI variations during droughts

The impact of droughts on vegetation is first assessed by comparing the LAI observed for different summers, chosen to represent different conditions: 2010 which was wetter than the 1979-2016 average, and 2012 which was drier on average over the study area ($PLA_{SD}$ of $\sim +4\%$ at the Western Mediterranean scale). Figure 5.1 shows the comparison ($\Delta LAI = LAI_{2012} - LAI_{2010}$) for the MODIS observations and the Med-CORDEX simulation (scaled to the MODIS amplitude, as explained in Sect. 4.3.2), as well as the difference in $\mathrm{PLA}_{SD}$ between both years (i.e. shift towards dry conditions), $\Delta\mathrm{PLA}_{SD}$. The patterns of positive difference in $\Delta\mathrm{PLA}_{SD}$ correspond to those of negative $\Delta$LAI for both MODIS and Med-CORDEX, showing that water stress leads to plant activity decline and biomass decrease. The LAI reduction in 2012 compared to 2010 can reach -1 unit over some areas (e.g. Central Spain). Conversely, areas of negative $\Delta\mathrm{PLA}_{SD}$ have positive $\Delta$LAI.

Even if the $\Delta$LAI from MODIS and Med-CORDEX have similar spatial distributions, differences can be more heterogeneous in the MODIS data, and lower (e.g. Pô valley), although the dynamical range of the RegIPSL LAI summer values has been normalized to that of MODIS. This may be explained by the fact that RegIPSL does not account for land use management while the reconstructed LAI from MODIS observations captures possible human effects. The impact of drought on LAI could be reduced by water supply from human intervention (irrigation). The Ebro valley and the Lombardia region are the largest irrigated cropland areas of the Western Mediterranean, according to the land cover classification from the European Space Agency (ESA, 2017). Considering an area of 10000 km$^2$ located close to the outlet of the Ebro catchment area (southeastern part: $\sim$ 42.0°N-0.1°W), MODIS LAI remains constant (0.64) during the entire wet summer of 2010 while the simulated LAI endures a seasonal decrease (continuous from 1.09 to 0.60). During the extreme dry summer of 2012, the MODIS LAI is slightly below 2010 (0.58) but remains constant during the entire summer suggesting that it is not affected by a water deficit. On the contrary, the simulated LAI decreases steeply as early as June (from 0.89 to 0.50) and the LAI remains low until the end of August.

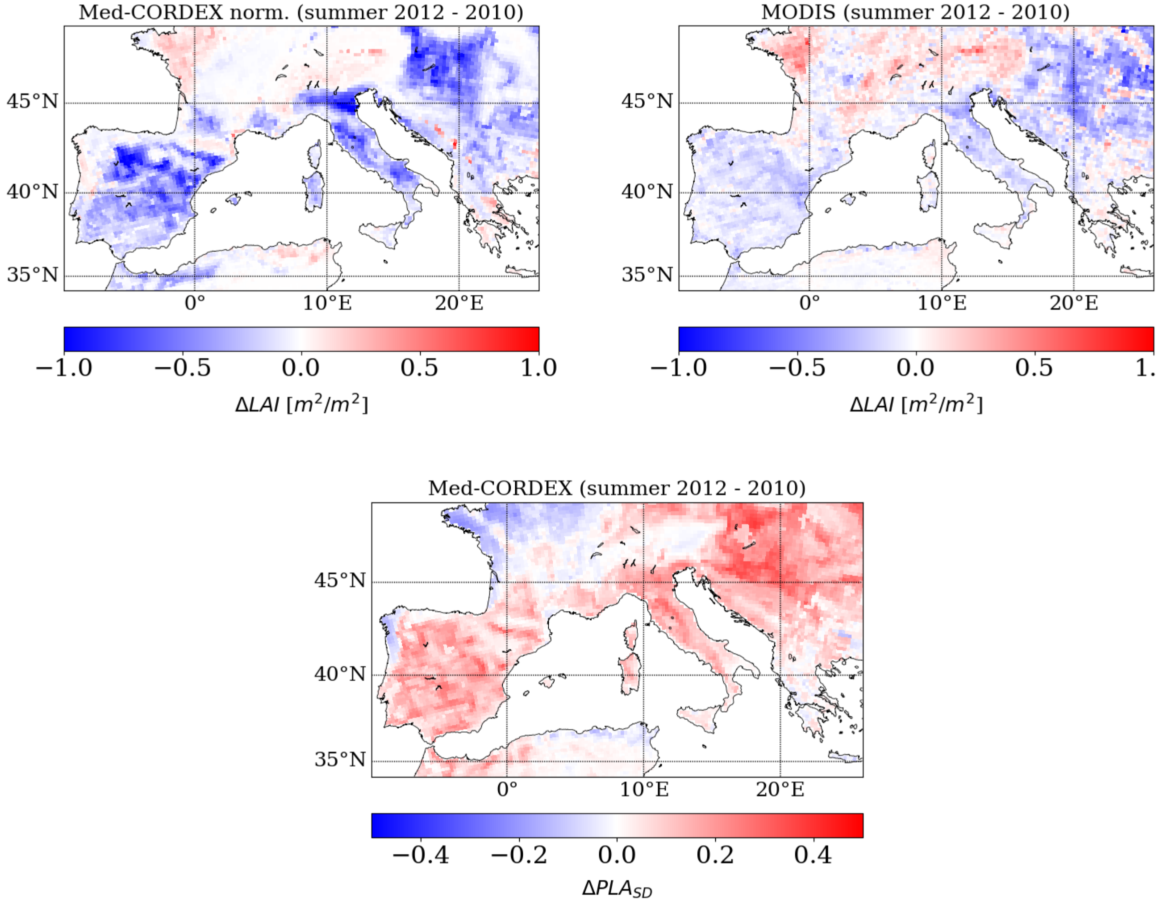

Figure 5.1: Spatial distribution of mean ΔLAI between the summer of 2012 and 2010 with the Med-CORDEX simulation normalized (upper left panel) and MODIS observations (upper right). Spatial distribution of the mean $\Delta\text{PLA}_{SD}$ with the Med-CORDEX simulation (lower).

The same analysis was performed for all dry years detected using the $PLA_{SD}$ method. Table 5.1 compares the observed and simulated summer ΔLAI averaged over some sub-regions (same as those defined in Chap. 4) for a reference wet summer (2010) and the dry summers (2005, 2006 and 2012). The spring drought of 2008, which was not followed by a summer drought, is also included. The ΔLAI was also calculated relative to another reference summer, 2007, which was close to normal conditions, neither wet nor dry. The results obtained are similar to those presented here, which are only for sub-regions that experienced more than 10% of dry days during the selected summers.

Observed and simulated ΔLAI are negative for all sub-regions, except the simulated "Balkans 2008". Within each sub-region, the difference in magnitude of ΔLAI between the years is linked with drought severity. The largest ΔLAI occurs in "Southern Spain 2005" with a value of -23% observed and -33% simulated caused by the longest drought (48% of dry days during the summer). "Balkans 2012" is not characterized by a high decrease of LAI (about -7%) whereas 45% of its summer days were in drought conditions. This further highlights a specific behaviour in this elevated and forested region.

The spring drought of 2008 led to a decrease in LAI that continued into the summer despite normal weather conditions (-6% observed and -16% simulated ΔLAI over the Western Mediterranean).

The observed ΔLAI is generally smaller than the simulated variation (both in absolute and relative values). We have shown that water supply by irrigation can explain part of the differences. The type of biome is also important. The largest discrepancies between observed and simulated ΔLAI occur in Southern Spain (semi-arid biomes) with 19% of difference in the summer of 2006. Maghreb presents also considerable differences (e.g. 2005 with 5%) where the dominant PFT is bare soil. As already mentioned, MODIS is less efficient for identifying drought effects on sparse vegetation (Chakroun et al., 2014). Results for these regions may therefore be less reliable. In other sub-regions, C3 agriculture and grass are the dominant PFTs affected.

Table 5.1: Mean ΔLAI in absolute and relative values between the reference wet summer (2010) and the dry summers (2005, 2006 and 2015) / spring (2008) for Med-CORDEX simulation (weighted sum of PFTs) and MODIS observations. ΔLAI is computed only for drought days. The percentage of dry days and simultaneous hot days for the considered summer is given in the fourth and fifth column. Only years with at least 10% of summer dry days are kept. The dominant PFT affected is given in the last column. The sub-regions are defined in Figure 5.4 which are the same as in Chap. 4 (Fig. 4.10).

| | ΔLAI obs. ($m^2/m^2$) | ΔLAI sim. ($m^2/m^2$) | Dry days (%) | Simult. hot days (%) | Dominant PFT |
|---|---|---|---|---|---|
| Balkans 2008 | -0.04 (-2%) | 0.04 (2%) | 16 | 4 | C3 agriculture |
| 2012 | -0.16 (-7%) | -0.14 (-7%) | 45 | 25 | C3 agriculture |
| Maghreb 2005 | -0.04 (-14%) | -0.12 (-19%) | 16 | 5 | bare soil / C3 agr. |
| 2008 | -0.04 (-13%) | -0.09 (-14%) | 15 | 3 | bare soil / C3 agr. |
| 2012 | -0.01 (-3%) | -0.04 (-7%) | 10 | 6 | bare soil / C3 agr. |
| W. I. Pen. 2005 | -0.22 (-16%) | -0.20 (-15%) | 37 | 14 | C3 agriculture |
| 2006 | -0.15 (-11%) | -0.24 (-17%) | 31 | 11 | C3 agriculture |
| 2008 | -0.03 (-3%) | -0.05 (-6%) | 10 | 2 | C3 grass |
| 2012 | -0.10 (-7%) | -0.14 (-11%) | 19 | 4 | C3 agriculture |
| S. France 2005 | -0.13 (-7%) | -0.21 (-12%) | 13 | 4 | C3 agriculture |
| 2006 | -0.21 (-11%) | -0.38 (-20%) | 12 | 7 | C3 agriculture |
| 2012 | -0.04 (-2%) | -0.16 (-10%) | 10 | 4 | C3 agriculture |
| S. Italy 2012 | -0.11 (-6%) | -0.27 (-14%) | 11 | 6 | C3 agriculture |
| S. Spain 2005 | -0.17 (-23%) | -0.35 (-33%) | 48 | 15 | C3 agriculture |
| 2006 | -0.11 (-15%) | -0.37 (-34%) | 34 | 11 | C3 grass |
| 2008 | -0.04 (-6%) | -0.20 (-21%) | 38 | 7 | C3 grass |
| 2012 | -0.14 (-18%) | -0.37 (-32%) | 35 | 12 | C3 agriculture |
| W. Medit. 2005 | -0.14 (-11%) | -0.24 (-17%) | 25 | 8 | C3 agriculture |
| 2006 | -0.14 (-9%) | -0.31 (-19%) | 19 | 8 | C3 agriculture |
| 2008 | -0.05 (-6%) | -0.18 (-16%) | 13 | 3 | C3 grass |
| 2012 | -0.11 (-8%) | -0.27 (-17%) | 20 | 8 | C3 grass |

The temporal correlation between daily LAI anomalies and PLA$_{SD}$ during the summer is mapped on Figure 5.2 based on the observations and Figure 5.3 based on the simulation. For MODIS, negative and significant correlations, ranging from -0.5 to -0.9, are obtained over almost the entire Western Mediterranean except the mountainous areas (e.g. Pyrenees). These areas are much less soil moisture limited (due to higher precipitation and lower evaporative demand). The simulated LAI (all PFTs) shows similar patterns. However, opposite correlations are obtained for the simulated LAI in the Western France, which may be explained by irrigated croplands not accounted for.

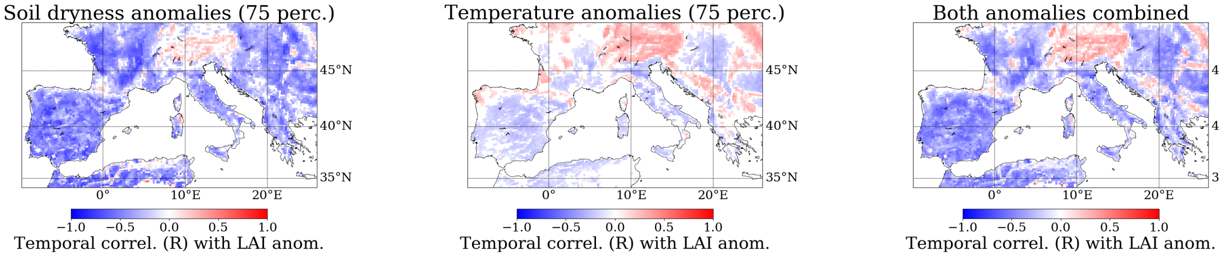

Figure 5.2: Spatial distribution of temporal correlation (R) during summers (2003-2016) between MODIS LAI anomalies and $PLA_{SD}$ (left), $PLA_{T2m}$ (middle) and combined $PLA_{SD,T}$ (right). White cells correspond to non-significant correlation coefficients (Spearman test p-value $> 0.1$). Each summer includes 24 days of observations (4 days average for the LAI), so that the final time series contain 336 values.

The effect of droughts on plant growth is expected to be very dependant on vegetation type and biome (e.g. Vicente-Serrano, 2007; Gouveia et al., 2017). To discuss this, the correlation between simulated LAI anomalies and $PLA_{SD}$ is calculated for each PFT and each summer month of the period 1979-2016 (not shown), as well as for the full summer (June-July-August) as shown on Figure 5.3. C3 grass and agriculture are highly correlated with $PLA_{SD}$ from June until August (between -0.5 and -0.9 depending on the sub-region). Plants with shallow root systems are sensitive to water shortages as soon as the early summer. On the opposite side, correlations for forests are low in June ($\sim$-0.1) and increase during the season ($\sim$-0.7 in August). Forests have longer resistance to droughts than grassland and agriculture due to their deeper root systems. In addition, the semi-arid biomes (Northern Africa and Andalusia) show a strong negative correlation throughout the summer. This type of biome may be exposed to a significant decrease in biomass from early to late summer, with possible plant mortality (Vicente-Serrano et al., 2013).

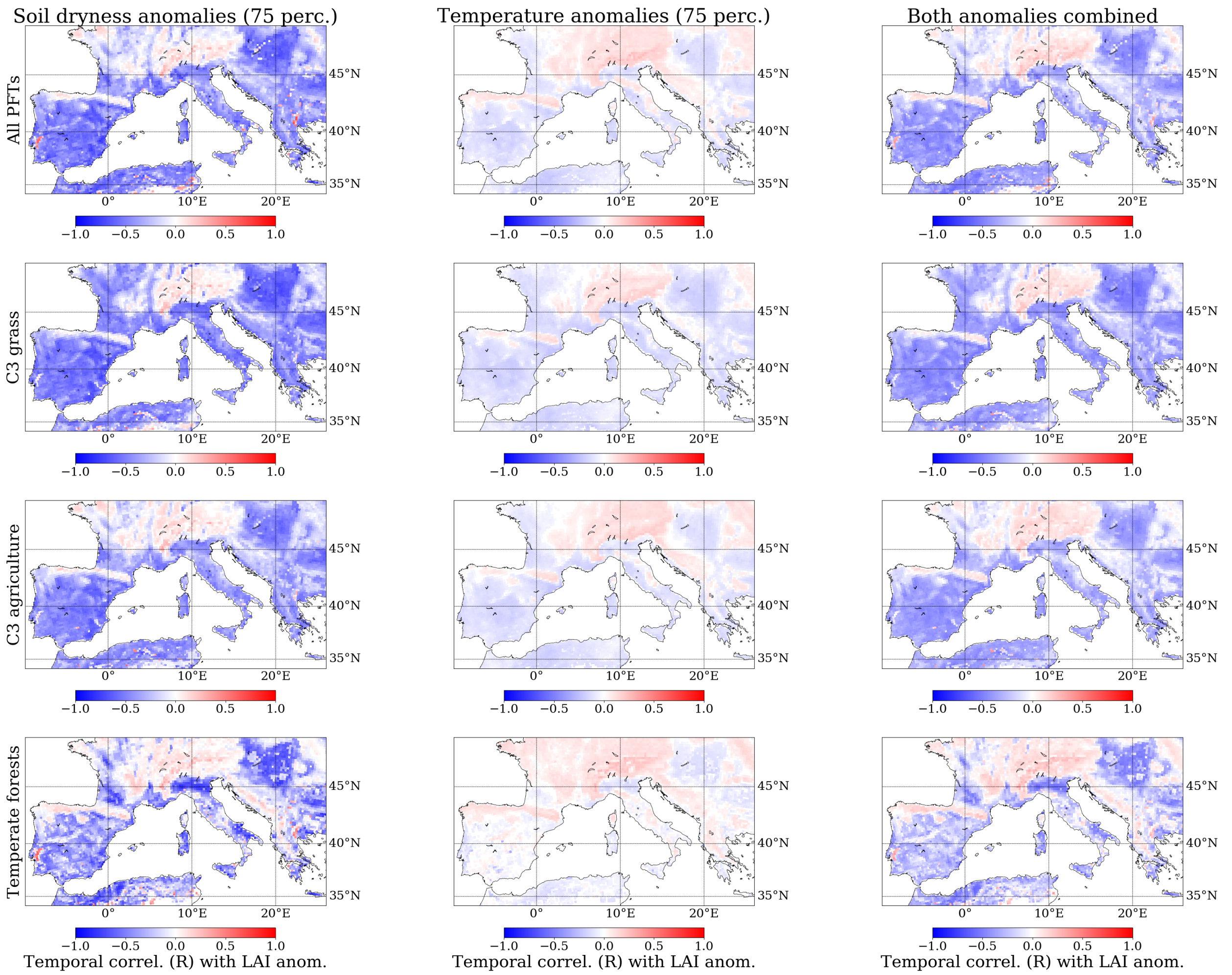

Figure 5.3: Spatial distribution of temporal correlation (R) during summers (1979-2016 period) between Med-CORDEX LAI anomalies and $PLA_{SD}$ (left), $PLA_{T2m}$ (middle) and combined $PLA_{SD,T}$ (right). White cells correspond to non-significant correlation coefficients (Spearman test p-value $>$ 0.1). Each row represents a selection of PFT. The needleleaf and broad-leaved forests are aggregated into a single class called "temperate forests".

### 5.2.2 LAI variations during heatwaves

Following the same method as with droughts, the LAI anomalies during heatwaves have been computed (Appendix B: Table B.5). The variation of LAI is computed as the difference between LAI during summer heatwaves not accompanied by durable droughts (2003, 2009, 2011 and 2016) and a reference summer without heatwaves (2014). The LAI decrease is considerably lower during heatwaves than during droughts, and sometimes even close to 0 (e.g. Southern Spain). However, some heatwaves can still cause important biomass decrease (for MODIS and Med-CORDEX). The intense summer heatwave of 2003 induced a LAI decrease of $\sim$14% in Southern Italy. This record-breaking heatwave affected also sub-regions located further north: $\sim$-8% of LAI in the Balkans and $\sim$-12% in Southern France.

The correlation between $PLA_{T2m}$ and LAI anomalies during summers from MODIS (resp. from Med-CORDEX) are shown in Figure 5.2 (resp. Fig. 5.3). They do not show a strong signal of co-variance. Correlations with MODIS LAI are overall slightly negative (between -0.2 and -0.4 with some non-significant values) but positive over the Northern Mediterranean, as well as the mountainous areas. The spatial distribution of correlation values with Med-CORDEX LAI is very similar, however, slightly lower (between -0.1 and -0.3).

### 5.2.3 Combined effect of droughts and heatwaves on LAI

Summer droughts are often characterized by simultaneous heatwaves of varying intensity: from 4% of summer days for "Western Iberian Peninsula 2012" to 25% for "Balkans 2005" (see Table 5.1 as example).

The $\Delta$LAI induced by droughts without heatwaves is similar to all droughts (with or without heatwaves) in all sub-regions. On average over the Western Mediterranean, the mean LAI decrease during droughts alone is reduced by 0.01 $m^2/m^2$ compared to the $\Delta$LAI for all droughts, whereas the number of dry days decreases by 8%. According to our results, a simultaneous heatwave during a drought does not induce cumulative biomass reduction and can even counterbalance the effect of the drought (e.g. Northern Mediterranean).

The synergetic effect of droughts and heatwaves is further characterised using correlations between LAI and $PLA_{SD,T}$ (right panels of Fig. 5.2 and 5.3). It is less anti-correlated with LAI than $PLA_{SD}$ because the higher temperature can have a compensating effect (mean difference of correlation of 0.08 for observed LAI and 0.10 for simulated LAI). Being combined, opposite signals of droughts and heatwaves, such as in the Balkans, can lead to an absence of correlation with LAI anomalies.

## 5.3 Fire activity

### 5.3.1 Spatial variability over the Western Mediterranean

MODIS products are used to analyzed the observed fire activity: MOD14 for the Fire Radiative Power, MCD64 for the Burned Area and MCD12 for the type of vegetation burned. Those MODIS data sets are processed using the APIFLAME model (Turquety et al., 2020) in order to derive daily BA and FRP distributions over the RegIPSL domain.

Figure 5.4 shows the spatial distribution of yearly summer burned area (JJA) during the 2003-2016 period, as well as the frequency of burning. The Western Iberian Peninsula, Maghreb, and Balkans sub-regions are characterized by a total yearly burned area higher than 20000ha, with at least half of the summers affected by wildfires during 2003-2016. All sub-regions together include about 82% of fires detected in the Western Mediterranean area. 36% of these fires are detected in Western Iberian Peninsula. The vegetation types most affected by fires in the Western Mediterranean are temperate forests (needleleaf and broad-leaved forests aggregated), grassland, and agriculture. For each sub-region, grasslands are the most affected (between 46% in the Balkans and 65% in Southern Spain). The largest percentage of temperate forests (28%) is found in the west of the Iberian Peninsula and the lowest in Southern Italy (6%). Burned agricultural areas vary considerably between sub-regions (by more than 35%).

The total annual burned area estimated from the MODIS product has been compared to that reported by the European Forest Fires Information System (EFFIS) program (San-Miguel-Ayanz et al., 2012) for the years of 2003-2016 (Appendix B: Fig. B.7). The difference is equal to 215km$^2$ on average over Southern Europe and can reach 270km$^2$ on average in Portugal (up to almost 2500km$^2$ in 2003). The MODIS burned area tends to be higher than the EFFIS burned area. However, the temporal correlation between both data sets is high ($\sim 0.9$) for each country. This is consistent with the analysis by Turco et al. (2019) who found temporal correlations of 0.95 for the annual total burned area (2001-2011 period) between MODIS and EFFIS for several countries of Southern Europe. In spite of the uncertainties, the inter-annual variability is thus well represented in the MODIS data.

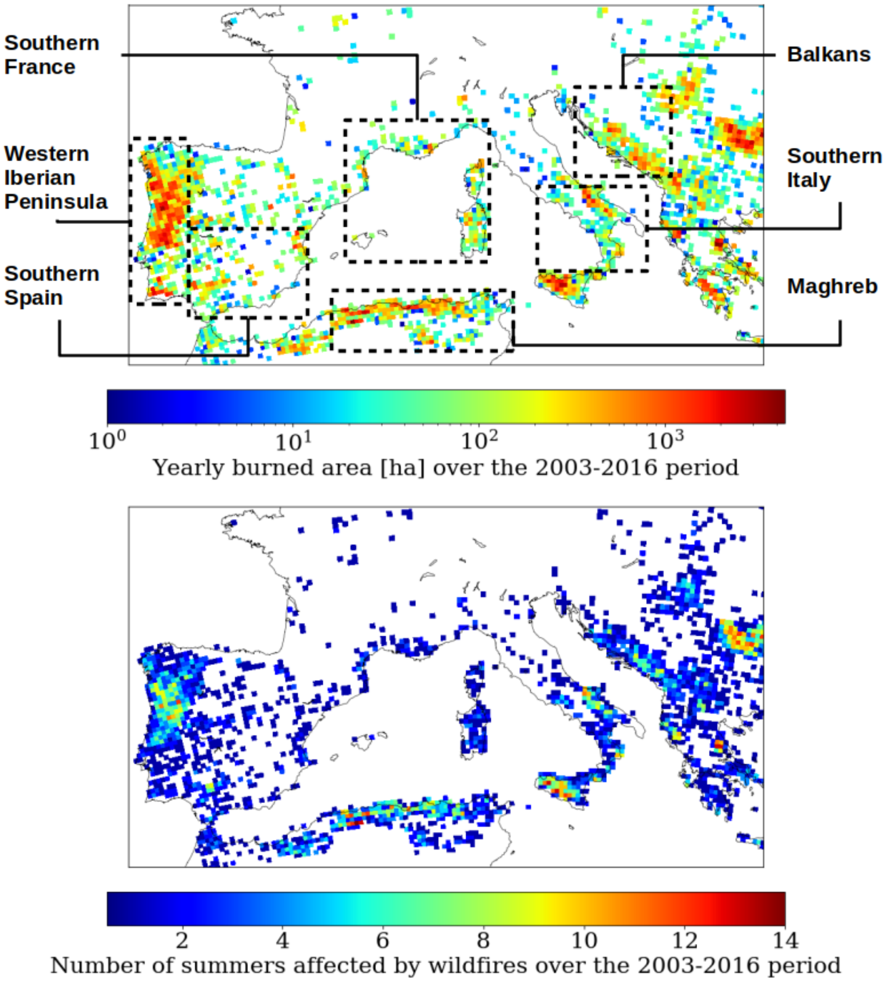

Figure 5.4: Total yearly summer burned area (JJA) above 1ha (top panel) and number of summers affected by wildfires (bottom panel). For diagnostic purposes, sub-regions are designated (dashed rectangles) within the Western Mediterranean region.

The effects of droughts, heatwaves, and wind gusts on wildfire activity are analyzed using the total BA, the maximum FRP as a surrogate for fire intensity and the mean Fire Duration (FD). In order to study the fire mainly driven by natural conditions, we exclude fires lasting less than one day and burned areas less than 1km$^2$. Moreover, at the scale considered, fires in adjacent grid cells and separated by less than two days are considered as one fire event.

### 5.3.2 Effect of heatwaves, droughts and wind gusts on large fires

Since wildfires are very sporadic in the region, a cluster approach was used to characterize the impact of extremes. Based on the indicator values (PLA method), the detected events were classified to construct samples corresponding to periods of heatwaves, droughts, and strong winds (isolated or combined). The definition of the clusters of extreme events (only for agricultural droughts and heatwaves) based on the PLA indicator is shown in Figure 5.5. These clusters are also largely used in the Chapter 6.

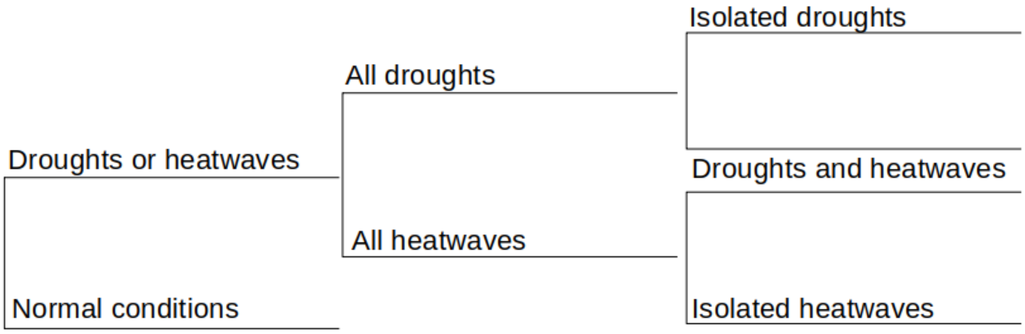

Figure 5.5: Definition of clusters for agricultural droughts and heatwaves based on the PLA indicator. This figure is not included in the published article.

Figure 5.6 presents the distribution of large fire characteristics (as defined in Sect. 5.3.1), for each cluster over the Western Mediterranean. The number of large fires varies considerably between clusters. The largest number of fires is found in the cluster "heatwave" with 509 events, highlighting the prevalent role of hot temperatures. 103 and 107 large fires occur, respectively, during droughts and wind gusts over the 2003-2016 period.

Compared to wildfires occurring during normal conditions (median FD of 4.0 days, BA of 3.6 km$^2$, and FRP of 102 MW), all the fire characteristics are significantly higher during agricultural droughts, heatwaves, or wind gusts (Mann Whitney U test p-value $< 0.01$). The three clusters have similar median distributions of FD (5 days). However, limiting the water availability for plants, agricultural droughts lead to a considerably larger median BA (7.1 km$^2$) and FRP (225 MW) than heatwaves (significant difference of $+1.2$ km$^2$ and $+84$ MW) and wind gusts (non significant difference of $+0.9$ km$^2$ and $+33$ MW). Those meteorological and hydrological conditions are major controlling factors of fire intensity and propagation over the Western Mediterranean. Hot and dry atmospheric conditions enhance the flammability with fire ignition and spread more likely to happen (Sarris et al., 2014). Agricultural droughts also decrease the fuel moisture (Turco et al., 2017). Strong winds also boost biomass burning, even with "cold" winds (Hernandez et al., 2015; Duane and Brotons, 2018).

The cluster analysis was also conducted for isolated and combined extreme events (Fig. 5.6). During wind gusts, the meteorological conditions can be very different from agricultural droughts and heatwaves, especially at the Western Mediterranean scale. The combined effects of heatwaves and/or droughts with wind gusts could not be analyzed due to the low number of fire events in this cluster (non significant results). Subsequently, the effects of droughts and heatwaves are studied independently of wind. The highest median BA (8.0 km$^2$) and FD (6.0 days) observed occur in the cluster of isolated droughts ("dr. and not hw." with only 43 large fires). Nevertheless, simultaneous droughts and heatwaves (cluster "hw. and dr.", 60 large fires) induce fire characteristics larger than each individual cluster ("heatwave" and "drought"): median BA of 7.5 km$^2$, FRP of 293 MW, and FD of 5.5 days, which represent, respectively, a multiplication factor of 2.1, 2.9, and 1.4 compared to normal conditions. These results suggest that their respective effects can be cumulative.

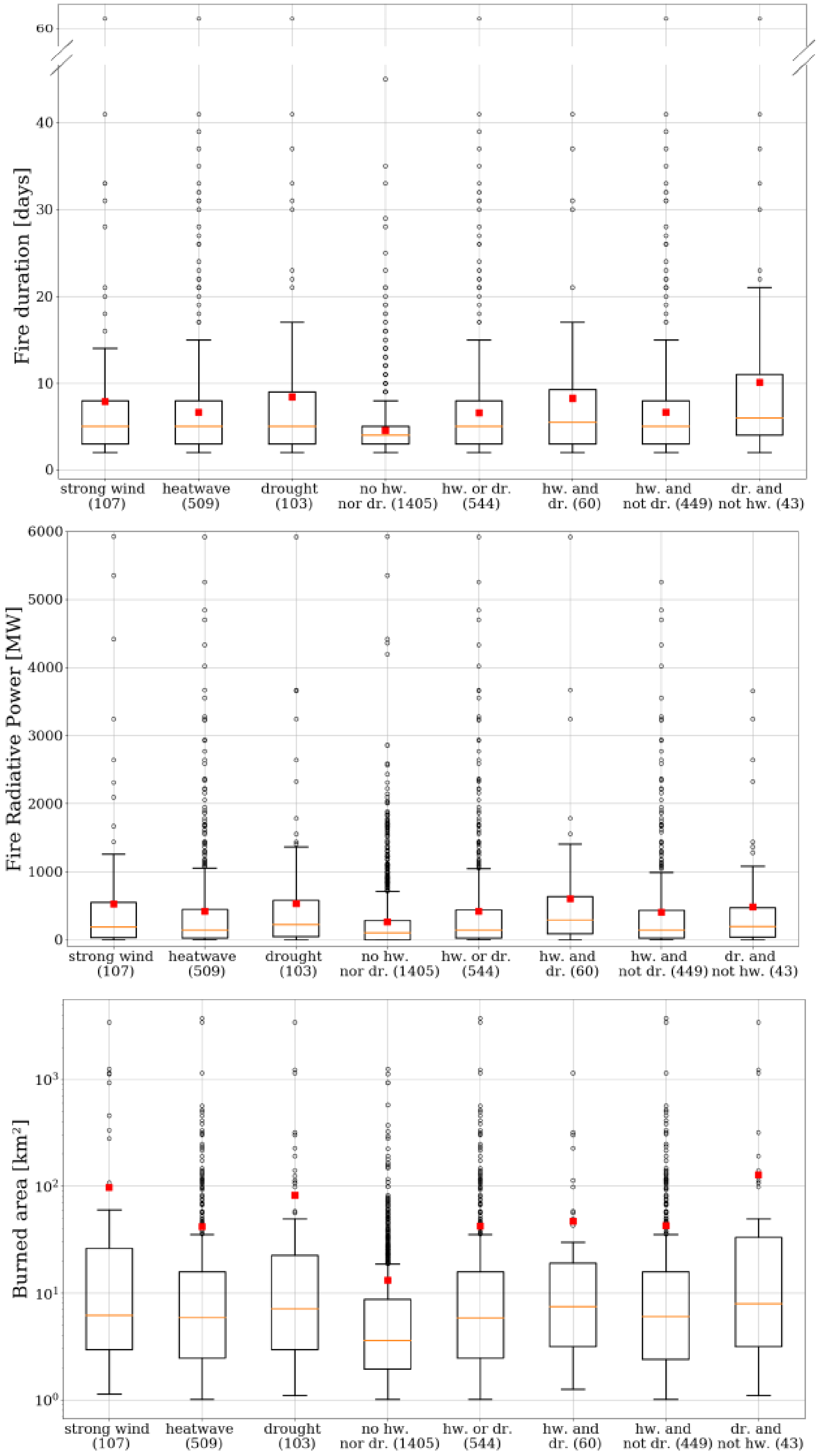

Figure 5.6: Summer BA (bottom panel on log scale), FRP (middle), and FD (top) of large fires from MODIS observations over the Western Mediterranean. Fires are clustered by extreme events using the PLA method: "windspells", "heatwaves", "droughts", "no heatwave nor drought", "heatwaves or droughts", "simultaneous droughts and heatwaves", "heatwaves without droughts" and "droughts without heatwaves" (from left to right). The number of fire events is between the parentheses. Red squares are the mean of the distribution and black circles the outliers. The box covers the InterQuartile Range (IQR) between Q1 (25th percentile) and Q3 (75th percentile). The lower whisker is limited to a statistical minimum (Q1-1.5*IQR) and the upper one to a maximum (Q3+1.5*IQR).

### 5.3.3 Impact of meteorological conditions or fuel availability

The cluster analysis showed that extremely dry and hot weather conditions exacerbate summer wildfire activity. However, the fire intensity could be limited by a reduced fuel availability following a dry pre-fire season. The relative importance of each of these factors has been then explored using correlation analysis.

Figure 5.7 (upper panels) maps the temporal correlations between the daily FRP (for large fires) and LAI from MODIS and Med-CORDEX during the summers of 2003-2016. The same analysis has been performed with the BA (Appendix B: Fig. B.8) and similar results were obtained. Since 90% of summer droughts are preceded by spring (MAM) droughts (see Sect. 4.5.2), the summer LAI metric includes the temporal memory of the soil dryness from the pre-fire season. Negative correlations mean that even with a decrease of the summer biomass density from one year to another due to an agricultural drought during the preceding spring, the summer FRP increases. On the contrary, positive correlations mean that FRP variations are driven by fuel availability.

Our results do not show a single major signal. For simulated and observed LAI, FRP-LAI correlations are significantly negative or positive for several sub-regions (Western Iberian Peninsula, Maghreb, Southern Italy, and Balkans). In summary, the fuel driver does not explain the inter-annual variability in a fully consistent way.

The correlations between the fire characteristics and the hydrological and meteorological conditions, using the Number of Dry Days (NDD) and Hot Days (NHD), have also been studied. Positive correlations are obtained all over the Western Mediterranean (R values between 0.5 and 0.9) (Appendix B: Fig. B.9). Correlations are higher with NDD, as we showed that droughts induce a larger enhancement of fire activity than heatwaves (see Fig. 5.6). However, NDD-FRP correlations are not significant in the Maghreb sub-region. Turco et al. (2017) show that the relationship between droughts and fire activity could be stronger in the Northern Mediterranean, where soil is initially wetter and vegetation more active than in the Southern Mediterranean, with semi-arid biomes.

The synergetic effect of meteorological conditions and fuel load are integrated in the Climate Driver Index, initially developed by Gouveia et al. (2016). Here, it is defined as the ratio between the NHD and the summer average LAI:

$$CDI = \frac{NHD}{LAI} \tag{5.1}$$

In order to evaluate if the fire regime is led by the climate driver (favourable warm and dry weather conditions) or the fuel driver (favourable biomass availability), the temporal correlation between the CDI and the FRP (as well as the BA) is analyzed (Fig. 5.7 - lower panels). The correlation is significantly positive (r values between 0.5 and 0.8) almost over all of the Western Mediterranean, suggesting that the pluri-annual fire regime is led by the climate driver. Short-term effects of favourable weather conditions for fire ignition and spread are sufficiently strong enough to dominate the longer effect of biomass availability.

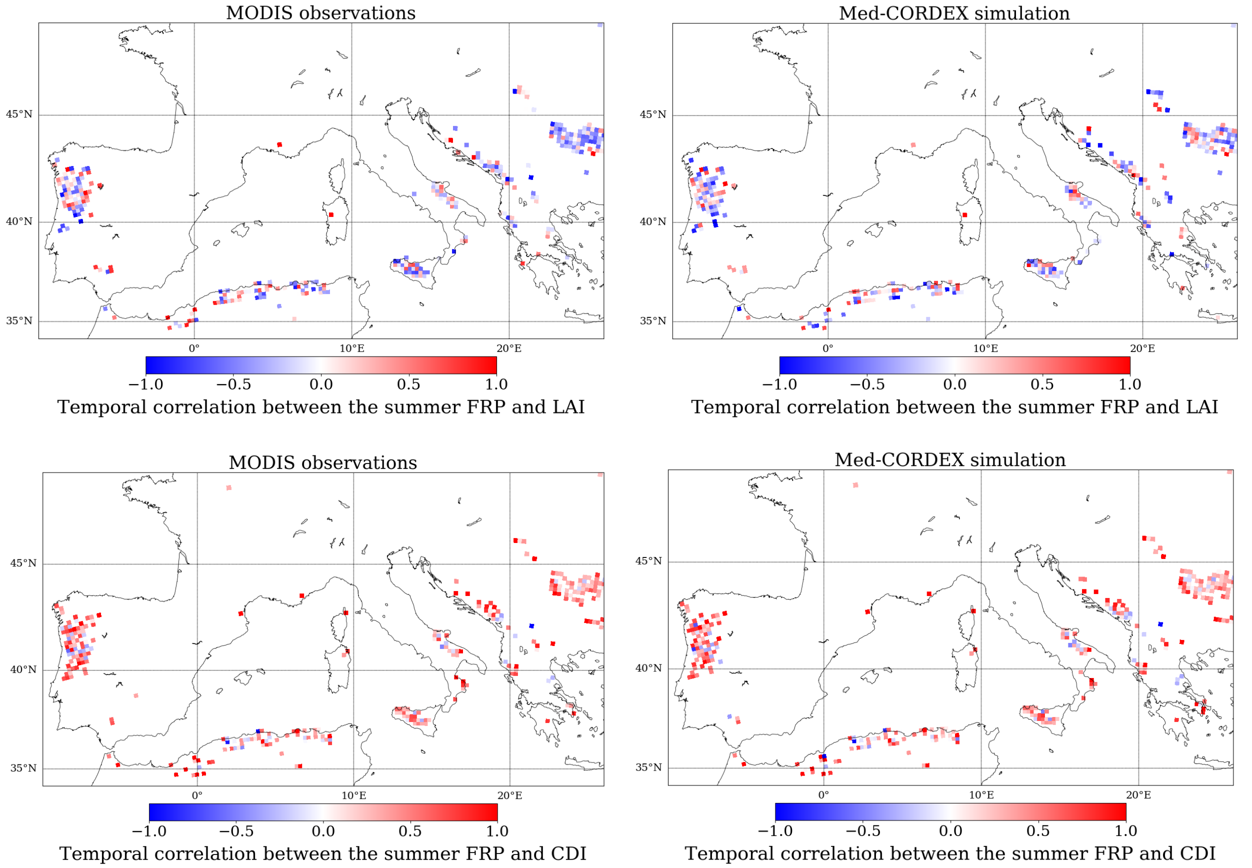

Figure 5.7: Spatial distribution of temporal correlation (R) between summer Fire Radiative Power (FRP) and Leaf Area Index (LAI) from MODIS (upper left panel) and from Med-CORDEX (upper right panel) for areas of high fire activity (pixels with at least 1km$^2$ of burned area for minimum 3 summers over 2003-2016). Same criteria of correlation are applied between FRP and CDI from MODIS (lower left panel) and from Med-CORDEX (lower right panel). Number of hot days (NHD) used for CDI is from Med-CORDEX ($PLA_{T2m}$) in both configurations. Only significant correlations (Spearman test with p-value $<$ 0.1) are shown.

Analyzing the fire season of 2007 in Southern Greece (Peloponnese Peninsula) which was characterized by two summer heatwaves and a drought, Gouveia et al. (2016) found that higher fire activity was located in areas of high accumulated precipitation (during September 2006 and August 2007). They suggested that large burned areas within the affected region can be more sensitive to vegetation density than to weather conditions. Considering the same study area and period, we also observed that fires with the highest BA ($> 80km^2$) occurred in areas of slightly positive anomalies of LAI from MODIS, for June (+0.1 in comparison to the 2003-2016 period) (not shown). However, we did not find any significant correlation over Southern Greece on the basis of our regional pluri-annual analysis.

## 5.4 Fire weather risk

### 5.4.1 The Canadian Fire Weather Index

The Canadian Fire Weather Index (FWI), initially developed by Turner and Lawson (1978) and adjusted for numerical computation by Van Wagner and Pickett (1985), is an index largely used, for different regions such as Australia (e.g. Dowdy et al., 2009) or the Mediterranean (e.g. San-Miguel-Ayanz et al., 2012). FWI is computed from empirical combination of two components: one describing the fuel moisture (fine fuel moisture, duff moisture and drought code) and the other one the fire behavior (initial spread and the buildup index). Those components are calculated based on the following meteorological variables: relative humidity, wind speed, temperature and precipitation. A diagram of the FWI code structure is represented in Figure 5.8.

The FWI has been computed from Med-CORDEX simulation on a daily time step over the 1979-2016 period. Figure 5.9 shows the linear trend of summer FWI for this period. The trend is positive over almost the entire Western Mediterranean ($\sim$+0.1 FWI/summer), except for some areas where the trend is either non-significant (e.g. a part of Sicily) or negative (e.g. Northern Africa, Alps). Accumulated over the full period, such positive trend can induce about +4 FWI units that represents an increase between 10 and 30% depending on the area. Figure B.10 in Appendix B shows how the mean summer FWI is higly variable over the Mediterranean region.

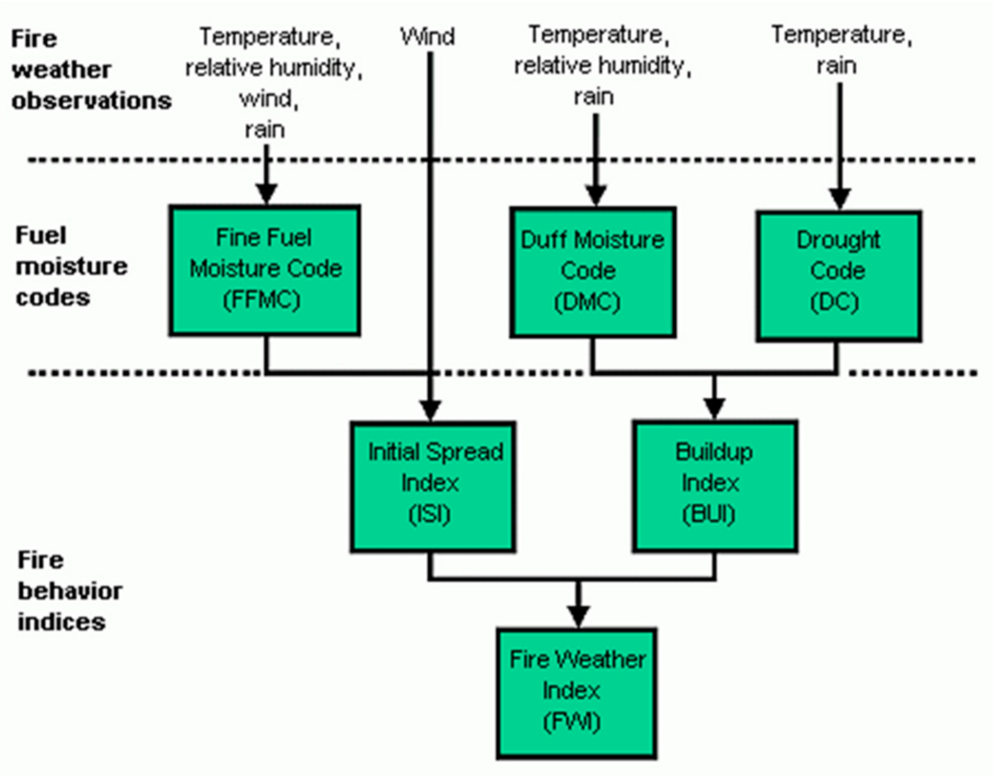

Figure 5.8: Structure components and flow diagram of FWI calculation process.

Spatial distribution of the summer FWI trend can be mainly explained by the trend of each meteorological variable used as input to the FWI code (Appendix B: Fig. B.11). The regional positive trend is induced by temperature increase that concerns the entire Western Mediterranean. Negative and non-significant FWI trends correspond to areas where precipitation and relative humidity trends are slightly positive. Finally, specific areas (e.g. Tuscany, Lisbon) are characterized by strong FWI trend (between +0.3 and +0.5 FWI/summer) due to an increasing wind speed on their coast.

The results of this trend analysis are consistent with those of Giannaros et al. (2021), both in terms of magnitude and spatial variability. They identified the Iberian Peninsula as the area with the highest positive trend of summmer maximum FWI (period 1987–2016). However, the FWI is an index of fire danger, only driven by meteorological variables. Its overall increasing trend is due to climate change. The observed evolution of fire activity over the last decades in Mediterranean is influenced by human intervention and does not follow the FWI trend (e.g. Turco et al., 2016) (see Sect. 5.1).

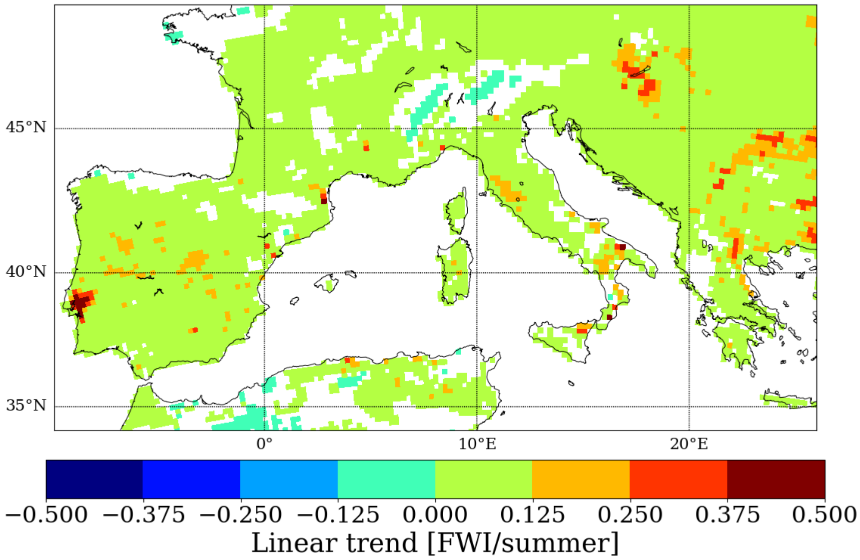

Figure 5.9: Spatial distribution of the summer FWI trend. The trend is computed over the period 1979-2016 with a daily time-step. White cells correspond to non-significant linear trend (p-value > 0.1).

### 5.4.2 Assessment against $PLA_{SD}$, $PLA_{T2m}$ and observed fires

The co-variability between FWI anomalies and indicators of extreme conditions ($PLA_{SD}$, $PLA_{T2m}$ and $PLA_{SD,T}$) was analyzed, as shown in Figure 5.10. Temporal correlation (1979-2016 period) between $PLA_{T2m}$ and FWI anomalies is high (R coefficient between 0.25 and 0.75). $PLA_{SD}$-FWI anomalies correlation is lower (between 0.10 and 0.50), although we have shown in the two last sections that dry conditions are important for explaining the wildfire severity. This result may highlight the limited ability of the FWI to represent agricultural drought conditions, especially since FWI is based on meteorological variables only (Dimitrakopoulos et al., 2011). However, the combination of $PLA_{SD}$ and $PLA_{T2m}$ ($PLA_{SD,T}$) induces a slight increase of the mean R coefficient (+0.05 in comparison to $PLA_{T2m}$-FWI correlation), assuming that cumulative effects of extreme soil dryness and hot conditions are taken into account in the FWI.

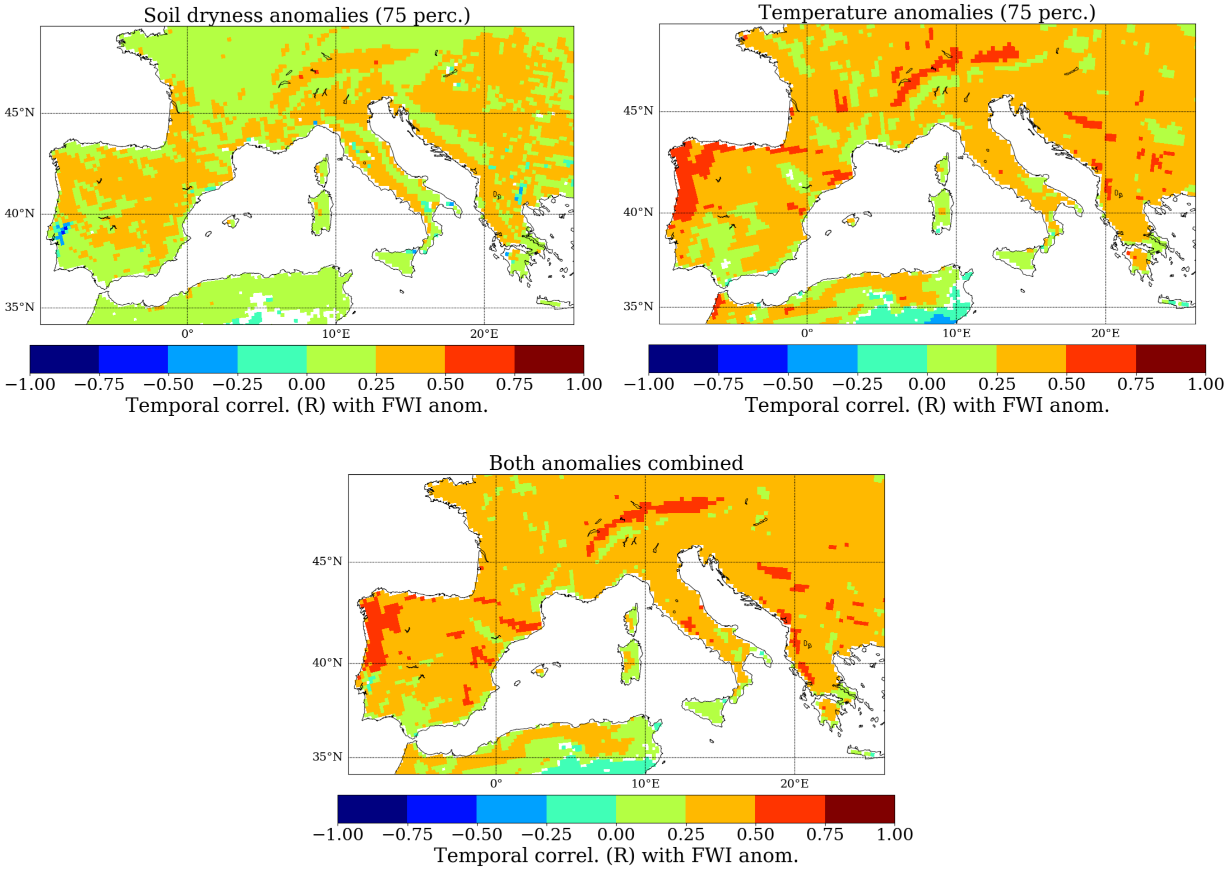

Figure 5.10: Spatial distribution of temporal correlation (R) during summers (1979-2016 period) between FWI anomalies and $PLA_{SD}$ (left), $PLA_{T2m}$ (right) and combined $PLA_{SD,T}$ (middle). White cells correspond to non-significant correlation coefficients (Spearman test p-value $> 0.1$).

The simulated FWI has also been assessed against observed fires from MODIS. As they are not controlled by natural conditions, small fires tend to be independent of FWI values. Figure 5.11 (top panels) classifies observed characteristics (total yearly BA and max FRP) of large summer fires into categories of fire danger described by the FWI. The FWI class with the largest total BA (884 $km^2$) is "21-30" (lower part of high danger). The maximum FRP observed (5920 MW) is within the class "31-40" (middle part of high danger). However, the class of extreme fire danger (FWI$>$50) is characterized by a low maximum BA (not shown, about 25 $km^2$) and FRP (1031 MW), being in the same range of values that the FWI classes low and moderate fire danger.

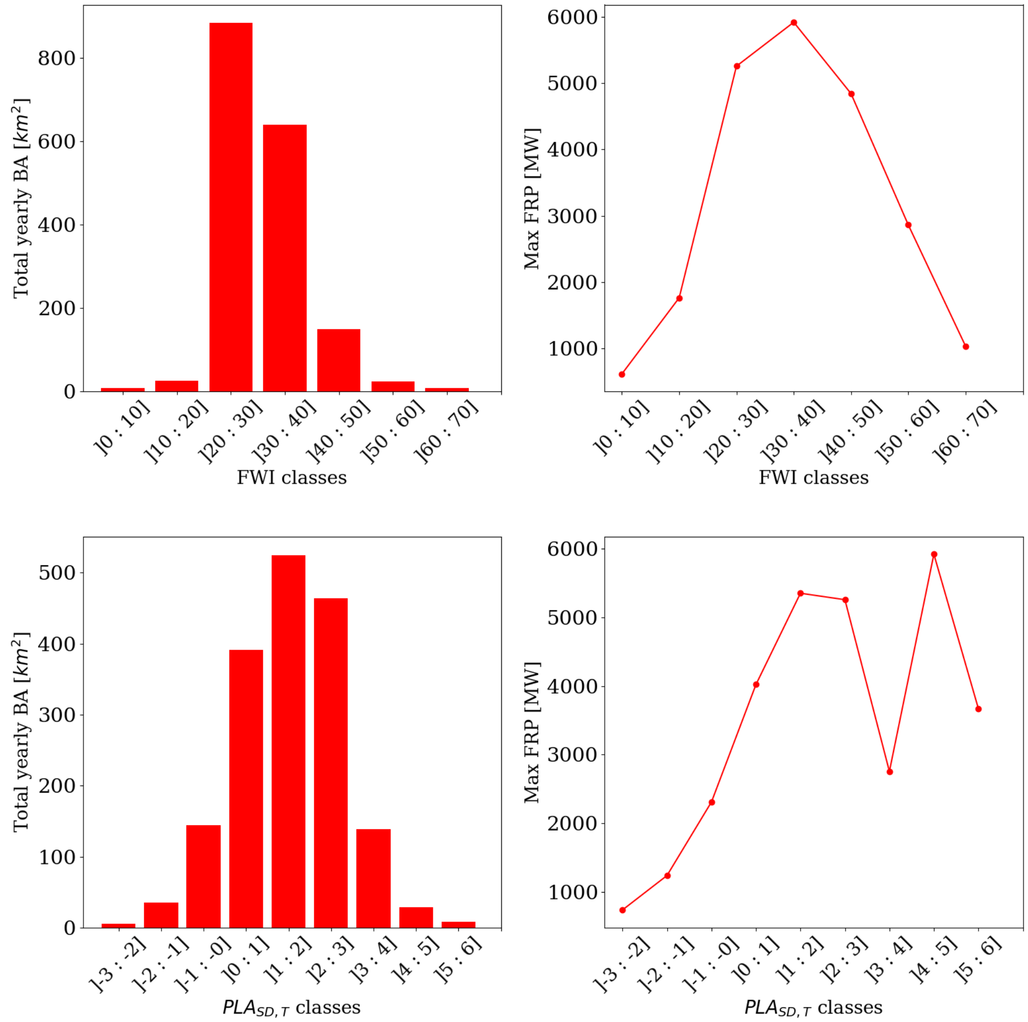

Figure 5.11: Observed fire characteristics (total yearly Burned Area and maximum Fire Radiative Power) during summers 2003-2016 from MODIS, categorized into classes of FWI from Med-CORDEX simulation (top panels) and into classes of $PLA_{SD,T}$ (bottom panels). Fires lasting less than one day and burning less than $1km^2$ are excluded. The assessment scale of FWI described by EFFIS is summarized here as: low fire danger (<=10), moderate (11-20), high (21-50) and extreme (>50).

Similar results of fire distribution have been found over the Mediterranean. For instance, San-Miguel-Ayanz et al. (2013) computed FWI values between 40 and 50 for numerous fires larger than 500ha, in Portugal during summer 2003 and 2005. Dimitrakopoulos et al. (2011) evaluated the FWI in the Mediterranean and highlighted a poor match with the burned area. Moreover, they found that the drought code was weakly correlated to soil moisture in the upper layer, from in-situ measurements in Greece. The same correlation has been computed with the soil moisture (upper layer) from Med-CORDEX simulation. The R coefficient is between 0.3 in Southern Mediterranean and 0.5 in the northern part. Chelli et al. (2015) proposed a calibration method for a better representation of the fuel moisture component in more arid environments such as the Mediterranean, since the FWI is initially suited for Canadian forests.

Figure 5.11 (bottom panels) presents the same analysis using categories based on the $PLA_{SD,T}$ indicator (combined heatwaves and agricultural droughts). The total yearly BA is normally distributed around the class "1-2" (presence of moderate droughts and heatwaves). Unlike the FWI, the maximum FRP observed is included in a class of high $PLA_{SD,T}$ values (4-5), with a general trend of linear variability between maximum FRP and $PLA_{SD,T}$ indicator.

## 5.5 Conclusions

The objective of this chapter was to quantify the isolated and combined impacts of heatwaves and droughts on vegetation and wildfires, using extreme events identified by regional land surface-atmosphere modeling and impacts observed by satellite observations of surface properties (MODIS).

Due to water stress, agricultural droughts lead to plant activity decline and a significant biomass decrease. This impact has been assessed using both observed and simulated LAI. We have shown that MODIS observations of LAI can capture some human effects that are not yet included in the simulations. Water supply by irrigation can reduce and even mask drought effects, as identified in the Ebro valley. Almost 30% of the croplands in the Mediterranean are irrigated, with the biggest areas in Spain, Northern Italy, and Morocco (Harmanny and Malek, 2019). Moreover, the limited ability of MODIS to evaluate accurately the LAI in sparse canopies, such as in semi-arid biomes, has been highlighted by Sprintsin et al. (2009). However, the general response to heat and water stress is well simulated.

Averaged over the Western Mediterranean, the LAI decrease between wet and dry summers is estimated at -10.0% (from MODIS observations) with some critical areas reaching -23.O%, such as in Southern Spain (during the summer of 2005). The simulated decrease of LAI by Med-CORDEX is larger (-17.7%), possibly because it does not include irrigation. However, both LAI have similar spatial patterns of biomass variation. The drought effect on biomass variation depends on the plant and biome type. This effect is weaker on vegetation with a deep root system (e.g. temperate forests), as well as for elevated or temperate regions with water reserves more often filled up than in semi-arid biomes.

Summer heatwaves, through thermal stress, can lead to biomass decrease, but to a much smaller extent than droughts. Averaged over the Western Mediterranean, we computed a mean observed and simulated LAI decrease of, respectively, 3.0% and 3.7%. We did not find significant cumulative effects of summer droughts and heatwaves on biomass reduction.

Heatwaves and droughts significantly promote summer wildfires. Through a synergistic effect, simultaneous droughts and heatwaves can worsen median BA by 3.9 $km^2$, FRP by 341 MW, and FD by 1.5 days, compared to normal conditions (2.1, 2.9, and 1.4 times more, respectively). Heatwaves and agricultural droughts contribute to an increased wildfire severity. Moreover, deficits in soil water content can begin in the spring and induce a decrease of the potentially combustible fuel measured here with the LAI. Using the CDI (positively correlated to BA and FRP), we have shown that the inter-annual variation of fire activity is not limited by the fuel availability; favourable extreme weather conditions have a dominant effect.

Based on the calculation of the FWI (from MED-CORDEX simulation) over the 1979-2016 period, the fire weather risk has increased almost everywhere in the Western Mediterranean (up to +30%), in line with global warming. Based on 14 years of fire observations, the FWI is able to identify periods of higher fire danger in the Mediterranean. However, it shows limited performance for describing conditions of high soil dryness, although they are, together with high temperatures, critical for assessing the fire severity.

In conclusion, even if agricultural droughts do not occur each summer, such extreme weather events can develop over long periods, inducing significant adverse effects on the biosphere. Firstly, persistent water stress leads to plant activity decline and biomass decrease. Secondly, droughts can worsen peaks of fire activity, mainly occurring during heatwaves. Isolated droughts are also favourable to intense fires.

# Chapter 6

# Surface ozone pollution induced by stressed vegetation

In the previous chapter, we demonstrated that droughts and heatwaves can affect the biosphere by enhancing wildfire activity and inducing considerable biomass variation. This chapter focuses on the possible variations of surface ozone triggered by the vegetation under abiotic stresses. A series of sensitivity tests performed off-line (see Chap. 2) with MEGAN model (BVOC emissions) and the gas dry deposition scheme of CHIMERE ($O_3$ dry deposition) have shown a strong influence of the activity factors to hydro-meteorological variables. Furthermore, several gaps for those algorithms were highlighted, especially about the soil dryness.

This chapter aims at (i) quantifying the impact of isolated and combined droughts and heatwaves on ozone in Southwestern Europe, and (ii) assessing the sensitivity of isoprene emissions, ozone dry deposition and ozone concentrations to drought effects (soil dryness and biomass decrease), being dismissed in many studies. In order to meet these objectives, developments that are recent and under current discussion within the scientific community, were conducted. Furthermore, they were new to our team. Shown in Figure 2.12 (see Chap. 2), this concerns firstly the inter-annual variability of the LAI in MEGAN that was initially fixed. Secondly, it is about the integration of soil moisture from the land surface and vegetation model ORCHIDEE into MEGAN-CHIMERE model (for both emissions and deposition in the canopy).

This chapter consists of a draft article that was submitted to the peer-reviewed journal Atmospheric Chemistry and Physics (https://www.atmospheric-chemistry-and-physics.net/), under the title “Interactions between the terrestrial biosphere and atmosphere during droughts and heatwaves: impact on surface ozone over Southwestern Europe”. Here is the co-author list : Solène Turquety, Arineh Cholakian, Jan Polcher, Antoine Ehret and Juliette

Lathière. The core of the text is the same as in the draft article. This version will probably have some modifications compared to the one supposedly published.

## Contents

## 6.1 Introduction

Tropospheric ozone ($O_3$) plays a critical role in maintaining the oxidative capacity of the troposphere. However, as a high oxidant, it also deteriorates air quality at high concentrations, inducing adverse effects on human and ecosystem health. Both short and long-term $O_3$ exposure significantly increases the risk of morbidity and mortality from cardiovascular or respiratory causes (e.g. Jerrett et al., 2009; Nuvolone et al., 2018). It also causes visible damage on plant epidermis as well as photosynthesis inhibition, seriously threatening vegetation growth (Anand et al., 2021) and crop yields (De Andrés et al., 2012). Tai et al. (2014) estimate that $O_3$ pollution enhanced by global warming (RCP8.5) could lead to a global crop yield reduction by 3.6% in 2050.

Tropospheric $O_3$ is a secondary air pollutant formed by photochemical reaction chains initiated by the oxidation of volatile organic compounds ($VOCs$) in the presence of nitrogen oxides ($NO_x$). $NO_x/VOC$ emission ratio determines the chemical regime of $O_3$ production at local scale in a highly nonlinear relationship (Jacob, 1999). Methane ($CH_4$) and carbon monoxide ($CO$) are also $O_3$ precursors in background conditions.

Meteorological conditions are a key driver for $O_3$ formation and transport (Mertens et al., 2020). Indeed, $O_3$ production is favoured by warm and sunny conditions, and $O_3$ peaks therefore occur mainly during summer. The overall objective of this paper is to quantify the variation of surface $O_3$ concentrations over the Euro-Mediterranean area during extreme weather events of heatwaves and droughts.

The Euro-Mediterranean region is often affected by both heatwaves (Russo et al., 2015) and droughts (Spinoni et al., 2015). The intensity and frequency of such events have increased over the last decades in the region. According to projections based on climate models, these trends could last and worsen over the 21st century (Perkins-Kirkpatrick and Gibson, 2017; Spinoni et al., 2018).

Heatwaves are often associated with high $O_3$ concentration. For example, Vautard et al. (2005) show that the persistent heatwave of August 2003 led to high $O_3$ concentration over the Western Europe for several days (daily maximum above $150\mu g/m^3$, spatially averaged). Jaén et al. (2021) report hourly values of $O_3$ exceeding $250\mu g/m^3$ during a shorter heatwave (28-29 June 2019) at local scale (Barcelona). These values are well above the European Union (EU) recommendation of a 8h-average maximum of $120\mu g/m^3$.

Porter and Heald (2019) highlighted that despite a strong correlation between surface temperature and $O_3$ concentration identified in Europe, this relationship is nonlinear and complex as it depends on several mechanisms including precursor emissions, reaction rates and lifetimes in the atmosphere. High temperatures favour emissions of biogenic $VOCs$ ($BVOCs$), which can induce an increased formation of $O_3$ in the case of a $NO_x$-limited regime as many areas in the Mediterranean basin (Richards et al., 2013). Persistent and intense solar radiation also allows long photochemical episodes (Jaén et al., 2021). Heatwaves in the Mediterranean being often related to a blocking situation of atmospheric systems, stagnant anticyclonic conditions lead to the accumulation of both precursors and $O_3$ (Otero et al., 2021). Moreover, extreme temperature and high $O_3$ concentration can cause stomatal closure reducing the dry deposition of $O_3$, as highlighted by Gong et al. (2020) with the $O_3$-vegetation feedback.

Droughts also significantly impact atmospheric chemistry through biosphere and atmospheric cycle perturbation (Wang et al., 2017). Drought impact on air pollutants and more specifically $O_3$ is difficult to investigate for several reasons. It is firstly related to the characterization of droughts. Due to its multiscalar character, drought events can last on timescales ranging from days to months, making their extent difficult to assess (Vicente-Serrano et al., 2010). Moreover, drought definition depends on the type considered (Svoboda and Fuchs, 2016). Meteorological droughts correspond to a rainfall deficit or an excess of evapotranspiration, agricultural ones to soil water shortage for plant growth, and hydrological ones to surface and/or underground flow decrease. Another difficulty is that droughts affect not only the atmosphere but also the land biosphere, and to a larger extent than heatwaves.

The variability of $O_3$ concentration is generally not well represented in chemistry-transport models (CTMs) compared to observations because of the lack of land-biosphere interactions in many models (Wang et al., 2017). Uncertainties related to $BVOC$ emission modeling could lead to a $BVOC$-derived $O_3$ uncertainty estimated at about 50% in Europe (Curci et al., 2010). Another major cause of uncertainties concerns the simulation of meteorological conditions.

Meteorological conditions specific to droughts are low relative humidity, low or absence of precipitation and cloud cover. The latter leads to an increase of downward solar radiation. Temperature can also be higher during droughts than during normal conditions. Wang et al. (2017) found that drought periods in the United States over 1990-2014 were characterized by temperatures up to 2°C hotter and radiation $12.4 W/m^2$ higher. Their analysis of surface measurements shows a mean enhancement in $O_3$ concentration of 3.5 ppbv (8%), explained by enhanced precursor emissions and photochemistry.

Through soil moisture deficit, droughts can induce considerable adverse effects on the biosphere, leading to a decrease of the overall biomass but also of the $BVOC$ emission activity. Guion et al. (2021) report a decrease of $\sim 10\%$ of Leaf Area Index (LAI) observed by satellite during droughts in Southern Europe. Areas of low altitude and vegetation with short root systems are more sensitive. Based on simulations from the Model of Emissions of Gases and Aerosols from Nature (MEGAN) (Guenther et al., 2006, 2012) and using MODIS LAI between 2003 and 2018, Cao et al. (2021) found that vegetation biomass variability in China is a major controlling factor of the interannual variation of $BVOC$ emissions.

Biogenic emission models such as the MEGAN model, consider an emission reduction when drought episodes occur only for isoprene ($C_5H_8$). Emmerson et al. (2019) simulated a reduction in $C_5H_8$ emissions of 24-52% over Southeastern Australia due to soil dryness in summer. However, there is a lot of uncertainty on how plant activity reacts to water stress. In the case of $C_5H_8$, the response to water stress could occur in two phases: a state of increasing emissions due to leaf temperature stimulation during the drought onset, followed by a state of isoprene synthase limitation (Potosnak et al., 2014). For monoterpenes, the response to water stress may be different depending on the species (Bonn et al., 2019). For instance, sabinene emissions (experimentally measured) from the European beech (*Fagus sylvatica*) decrease strongly with decreasing soil water availability while trans-$\beta$-ocimene emissions (from the same plant species) remain constant.

Dry deposition velocity directly depends on the stomatal conductance, which can be modified under hot and dry conditions (Lin et al., 2020). Stomatal conductance depends on several parameters. As identified by Kavassalis and Murphy (2017), the leaf-to-air vapor pressure deficit that depends on both temperature and relative humidity, is a key variable regulating the stomatal conductance. Extreme hot and dry conditions can cause stomatal closure to reduce transpiration. Moreover, lack of rainfall prevents wet deposition and plant water stress slows dry deposition. However, there are still large uncertainties about the relationship between the soil moisture and the dry deposition (Clifton et al., 2020).

Considering the difficulty for models to simulate accurately soil moisture (Cheng et al., 2017) and the uncertainties about plant and $BVOC$ species response to water stress (Bonn et al., 2019), the impact of soil moisture is often dismissed in biogenic emissions and dry deposition schemes used in CTMs. Therefore, knowledge about the respective effect on $O_3$ remains limited. To evaluate the effects of droughts and heatwaves on surface $O_3$ in Southwestern Europe, the variation of both $BVOC$ emissions and dry deposition as a function of meteorological and hydrological conditions are analyzed in this paper including the soil dryness effect.

Agricultural droughts and heatwaves are identified based on the coupled meteorological (WRF) and land surface vegetation (ORCHIDEE) regional model (RegIPSL) for the 1979-2016 period (Guion et al., 2021). Summers are less affected by drought events (33% of them) than by heatwaves (97%). Nevertheless, drought periods are generally much longer than heatwaves (22.3 days against 5.8). Those two types of extreme weather events can be highly correlated over the Western Mediterranean (temporal correlation R between 0.4 and 0.5).

Atmospheric chemistry is simulated using the regional CHIMERE CTM (Menut et al., 2021) over three selected summers (2012, 2013 and 2014), including the online calculation of biogenic emissions using the MEGAN model. Simulations are analyzed in conjunction with surface $O_3$ observations from the European surface network AQ e-Reporting (EEA, `https://www.eea.europa.eu/data-and-maps/data/aqereporting-9`, last access: 30 July 2021). Concentrations of formaldehyde ($HCHO$) are used as a proxy for $BVOC$ emissions. $HCHO$ is produced in high yield during the oxidation of hydrocarbons. As an intermediate product of the oxidation of most $VOC$ and being characterized by a short lifetime (about a few hours), $HCHO$ has been used in many studies to infer $VOC$ emissions (e.g. Millet et al., 2006, 2008; Curci et al., 2010). Observations of $HCHO$ total column by the Ozone Monitoring Instrument (OMI) onboard the Aura satellite (Levelt et al., 2006) are used.

The observations and models used for this research are presented in Sect. 6.2 and 6.3, respectively. The RegIPSL, CHIMERE and MEGAN models, as well as the different modeling experiments undertaken are detailed. Results (see Sect. 6.4) are divided into three parts. Firstly, the sensitivity of $C_5H_8$ emissions, $O_3$ dry deposition and surface $O_3$ concentration to drought effects (biomass decrease and soil dryness) is assessed (see Sect. 6.4.1). Secondly, the variation of observed and simulated $O_3$, integrating drought and heatwave effects, is analyzed with respect to the variation of troposphere-atmosphere interactions during extreme weather events (see Sect. 6.4.2). Finally, the number and distribution of days exceeding the EU air quality standard are presented (see Sect. 6.4.3).

## 6.2 Observations

### 6.2.1 European surface network of $O_3$ concentration

The in-situ measurements of surface $O_3$ provided by the European Environment Agency (EEA) are used. The Air Quality e-Reporting project gathers air quality data provided by EEA member countries as well as european collaborating countries. Merging with the statistics of AirBase v8 project (2000-2012), AQ e-Reporting offers a multi-annual time series of air quality measurement data until 2021, categorized by station types and zones across Europe.

Thunis et al. (2013) quantified the various sources of uncertainty for $O_3$ measurements (e.g. linear calibration and UV photometry) and estimated a total uncertainty of 15%, regardless of concentration level.

Only measurements from stations classified as background and rural are considered for this study. The number of stations taken into account is 167, 188 and 207 respectively for summer 2012, 2013 and 2014.

### 6.2.2 Satellite observations of formaldehyde total column

The $HCHO$ total column observations from the OMI/Aura instrument are used as a quantitative proxy of $BVOC$ emissions. OMI has an equator crossing time at 01:45 pm on the ascending node, about 14.5 revolutions per day and a swath width of 2600km, allowing daily global coverage (Levelt et al., 2006, 2018). The OMHCHOd level 3 product (Chance, 2019) is used for this research. It provides $HCHO$ total column with a spatial resolution of $0.1° \times 0.1°$, based on the backscatter solar radiation in the UV (306 and 360 nm). Uncertainties on the $HCHO$ retrieval is significant, varying between 30% (pixels with high concentrations) and 100% (with low concentrations), and mainly due to cloud and aerosol scattering along the field of view (González Abad et al., 2015). All satellite retrievals (e.g. OMI, GOME2A) of $HCHO$ products present a systematic low mean bias (20-51%) compared to aircraft observations (Zhu et al., 2016). However, the analysis using $HCHO$ total column from OMI presented in this study is mainly focused on the relative difference during droughts and heatwaves so that no correction factor has been applied.

Finally, only cloud free observations and pixels with a vertical column density within the range of -0.8e16 and 7.6e16 $mocelules/cm^2$ are selected in order to minimize OMI row anomalies, following Zhu et al. (2017). For a suitable comparison with model simulations, $HCHO$ data were regridded on the CTM grid.

### 6.2.3 In-situ observations of 2m temperature and $C_5H_8$ surface concentration

To validate our simulations in the most complete way, two data sets are added to our study but do no represent the main focus of the paper. Firstly, in-situ observations of temperature at 2 meters above the surface ($T_{2m}$) from the ENSEMBLES dataset E-OBS (Cornes et al., 2018) are used to validate the simulated temperature by the WRF weather model.
Secondly, simulated $C_5H_8$ concentrations from different experiments undertaken in this study are compared to in-situ observational data gathered by the EBAS infrastructure (`https://ebas.nilu.no/`). EBAS is handled by the Norwegian Institute for Air Research (NILU).

## 6.3 Models

### 6.3.1 WRF-ORCHIDEE

#### Model description

The regional WRF-ORCHIDEE model couples the land surface model ORCHIDEE (ORganising Carbon and Hydrology In Dynamic EcosystEms) (Maignan et al., 2011) and the meteorological model WRF (Weather Research and Forecasting) (Skamarock et al., 2008). ORCHIDEE is composed of three modules. SECHIBA simulates the water and energy cycle. STOMATE resolves the processes of the carbon cycle, allowing an interactive phenology. The dynamical module of the vegetation LPJ which is responsible for the competition between the Plant Functional Types (PFTs) in ORCHIDEE is not used for this research.
WRF-ORCHIDEE model has been used following the recommendation of the Med-CORDEX initiative (Ruti et al., 2016). On a Lambert-conformal projection, the domain covers the Euro-Mediterranean with a spatial resolution of 20km. There are 46 vertical levels, with over half below 500hPa. The lateral boundaries of the atmosphere were nudged towards the ERA-I reanalysis.
The performed Med-CORDEX simulations over the 1979-2016 period have been evaluated against surface observations of temperature and precipitation, demonstrating that it is suitable for research on droughts and heatwaves (Guion et al., 2021).

#### Indicators of droughts and heatwaves

Based on simulations performed by the coupled WRF-ORCHIDEE regional model, we identified heatwaves and agricultural droughts over the Euro-Mediterranean using indicators of extreme weather events, as described in Guion et al. (2021) (data access: `https://thredds-x.ipsl.fr/thredds/catalog/HyMeX/medcordex/data/Droughts_Heatwaves_1979_2016/catalog.html`).

Following the approach of Lhotka and Kyselý (2015), we computed the Percentile Limit Anomalies of 2m above surface temperature ($PLA_{T2m}$) for heatwave detection and of soil dryness ($PLA_{SD}$) for agricultural drought detection. The soil dryness is computed as the complement of the soil wetness index, which is described in ORCHIDEE as the ratio between the soil moisture and the accesible water content.

For each cell of longitude ($i$) and latitude ($j$) of the domain, the monthly distribution of the 2m temperature/soil dryness is normalized and the $75^{th}$ percentile is computed ($p = 0.75$). The daily $PLA_{T2m/SD}$ indicator is equal to the daily deviation ($dX_{i,j,d}$) between the reference variable ($X_{i,j,d}$) and the corresponding monthly percentile ($X^p_{i,j,m}$) (Equation 6.1). A heatwave/drought is identified when the daily $PLA_{T2m/SD}$ is positive for three consecutive days.

$$dX_{i,j,d} = X_{i,j,d} - X^p_{i,j,m} \tag{6.1}$$

The chosen percentile for the detection of extreme weather events is generally higher, between 80 and 95 (e.g. Stéfanon et al., 2012a). We chose the percentile 75 in this study for a larger population. As a result, events detected here cover not only extreme events, but also periods that are significantly drier and warmer than normal conditions.

### Soil water stress for plants

The Soil Water Stress ($SWS$) calculated by RegIPSL based on liquid water content in the soil is used to describe the water stress for plant transpiration and photosynthesis (De Rosnay et al., 2002). It is an index varying between 0 (plants fully stressed) and 1 (not stressed) that takes into account the water transfer between the soil layers along root profiles (11 layers in the version of ORCHIDEE used here). For each PFT ($p$), soil class ($s$) and soil layer ($v$), it is computed as follows:

$$SWS_{p,s} = \frac{SM_{p,s,v} - SMw_{p,s,v}}{SMnostress_{p,s,v} - SMw_{p,s,v}} \times nroot_{p,s,v} \tag{6.2}$$

where $SM$ is the soil moisture of each layer (liquid phase), $SMw$ the soil moisture of each layer at wilting point, $SMnostress$ the soil moisture of each layer at which $SWS$ reaches 1 and $nroot$ is the normalized root length fraction in each soil layer (between 0 and 1). There are three soil classes to avoid competition for water uptake: bare soil, short root systems and long root systems plants.

### 6.3.2 MEGAN and the soil moisture factor

Biogenic emissions of VOCs and NO were computed using the MEGAN model v2.04 (Guenther et al., 2006), including several updates from the version 2.1 (Guenther et al., 2012). It is used on-line in the CHIMERE model at hourly time step. Emission fluxes are calculated based on emission factors at canopy standard conditions that are defined as $303K$ for the air temperature ($T$), 1500 $\mu mol/m^2.s$ for the photosynthetic photon flux density ($PPFD$) at the top of the canopy, 5 $m^2/m^2$ for the $LAI$ and a canopy composed of 80% mature, 10% growing and 10% old foliage. Environmental conditions are taken into account using activity factors ($\gamma$) that represent deviations from the canopy standard conditions, so that the emission rate ($ER$ $[\mu g.m^{-2}.h^{-1}]$) for a given species $i$ is calculated in each model grid cell as:

$$ER_i = EF_i \cdot \gamma_{LAI} \cdot \gamma_{PPFD,i} \cdot \gamma_{T,i} \cdot \gamma_{Age,i} \cdot \gamma_{SM,i} \cdot \gamma_{CO2,i} \cdot \rho_i \tag{6.3}$$

where $EF$ is the emission factor $[\mu g.m^{-2}.h^{-1}]$ provided by the MEGAN model and $\rho$ the production/loss term within canopy that is assumed to be equal to one. $\gamma_{LAI}$ is the activity factor based on $LAI$ observations from the MODIS MOD15A2H product (Myneni et al., 2015) improved by Yuan et al. (2011) (`http://globalchange.bnu.edu.cn/research/lai`). This improvement is undertaken with a two-step integrated method: (1) the Modified Temporal Spatial Filter (mTSF) is used to fill the gaps and replace low quality data by consistent data; (2) the TIMESAT Salvitzky and Golay filter is applied to smooth the final product. The temporal resolution is 8 days.

$\gamma_{PPFD,i}$, $\gamma_{T,i}$ and $\gamma_{Age,i}$ are the activity factors accounting for light, temperature and leaf age respectively. They are calculated in MEGAN using meteorological variables from the WRF model. The activity factors accounting for the soil moisture ($\gamma_{SM}$) and $CO_2$ concentration ($\gamma_{CO2}$) are applied on $C_5H_8$ species only. $\gamma_{CO2}$ is fixed ($CO_2$ concentration at 395 ppm) and $\gamma_{SM}$ depends on the deviation between the soil wetness and a fixed wilting point, computed as follows:

$$\begin{cases} \gamma_{SM} = 1 & \text{if} \quad \theta > \theta_1 \\ \gamma_{SM} = \frac{(\theta - \theta_w)}{\Delta\theta_1} & \text{if} \quad \theta_w < \theta < \theta_1 \\ \gamma_{SM} = 0 & \text{if} \quad \theta < \theta_w \end{cases} \tag{6.4}$$

where $\theta$ is the soil wetness (volumetric water content in $m^3/m^3$), $\theta_w$ the wilting point (level from which plants can not extract water from the soil, in $m^3/m^3$), $\Delta\theta_1$ equal to 0.04 (empirical parameter) and $\theta_1$ the sum of $\theta_w$ and $\Delta\theta_1$. $\theta$ values (third layer, 60cm depth) are provided by the WRF-Noah land surface model (Ek et al., 2003; Greve et al., 2013). $\theta_w$ values are computed over the domain (Appendix B: Fig. B.12) using tabulated values from Chen and Dudhia (2001) that are soil type specific and parametrized on Noah soil wetness values.

However, emission response to drought is very sensitive to the wilting point (Müller et al., 2008). Wang et al. (2021b) computed a relative difference of biogenic emissions varying between 50 and 90% depending on the wilting point values.
Based on a comprehensive data set of in-situ measurements of $C_5H_8$ emissions, Bonn et al. (2019) computed an activity factor of soil moisture in function of the soil water availability. The fitted function is relatively in good agreement with the $\gamma_{SM}$ algorithm in MEGAN.
As an alternative, Jiang et al. (2018) propose to use an activity factor of soil moisture that integrates the soil water stress for plant photosynthesis. Below a critical value (fixed here at 0.5), the activity factor using SWS from RegIPSL decreases lineary as follows:

$$\begin{cases} \gamma_{SWS} = 2\,SWS & \text{if} \quad SWS \leq 0.5 \\ \gamma_{SWS} = 1 & \text{if} \quad SWS > 0.5 \end{cases} \tag{6.5}$$

The different soil wetness functions presented here will be subject to dedicated simulations for comparison.

### 6.3.3 CHIMERE

#### General description and configuration

The CHIMERE v2020r1 model (Menut et al., 2021) Eulerian 3-dimensional regional CTM computes gas-phase chemistry, aerosols formation, transport and deposition. It can be guided by pre-calculated meteorology (offline simulations) or used in an online simulation with the WRF regional meteorological model (Skamarock et al., 2008), including the direct and indirect effects of aerosols in option. In this study, we chose to use the online version of CHIMERE but without any aerosol effects in order to reduce the calculation time and to isolate possible feedbacks.
Here, the reduced scheme MELCHIOR2 (Derognat, 2003) is used for gas phase chemistry (44 species, almost 120 reactions). The aerosol module includes aerosol microphysics, secondary aerosol formation mechanisms, aerosol thermodynamics and deposition, as detailed in Couvidat et al. (2018); Menut et al. (2021). The photolysis rates are calculated online using the Fast-JX module version 7.0b (Bian and Prather, 2002) which accounts for the radiative impact of aerosols. Horizontal and vertical advection are based on the scheme of Van Leer (1977). The physical and chemical time steps are respectively 30 and 10 minutes. The simulations have been performed for June-July-August (with a 5 days spin-up) of years 2012, 2013, 2014, over two nested simulation domains (Fig. 6.1), and on 15 vertical layers, from 998hPa up to 300hPa. The large domain covers Northern Africa and Europe at 60km horizontal resolution (EUMED60, 164x120 cells) and the small domain is close to that of

Med-CORDEX although smaller; it covers the Western Mediterranean region at 20km horizontal resolution (Med-CORDEX, 222x93 cells). The area studied in more detail in the following is the Southwestern Europe (35-46°N, 10°W-20°E).

Boundary conditions for the larger domain are provided by a climatology from the global CTM LMDZ4-INCA3 (Hauglustaine et al., 2014) for trace gases and non-dust aerosols, and from the GOCART model (Chin et al., 2002) for dust.

The biogenic emissions are calculated online by the MEGAN model (see Sect. 6.3.2). Sea salts and dimethyl sulfide marine emissions are calculated online using the scheme of Monahan (1986) and Liss and Mervilat (1986), respectively. Mineral dust emissions are also calculated on-line (Marticorena and Bergametti, 1995; Alfaro and Gomes, 2001). Consistently with the WRF model, the land cover classification used for the calculation of biogenic emissions and dust emissions is from the USGS land cover database (`http://www.usgs.gov`).

The biomass burning emissions from the APIFLAME v2.0 model (Turquety et al., 2020) are used. The anthropogenic surface emissions are derived from the EMEP (European Monitoring and Evaluation Programme) database at 0.1°×0.1° resolution (`https://www.ceip.at/webdab-emission-database`) for the year 2014. The inventory was preprocessed by the emiSURF program in order to calculate hourly emissions fluxes on the CHIMERE grid and the period of simulation (`https://www.lmd.polytechnique.fr/chimere/formation_2021/emisurf.pdf`).

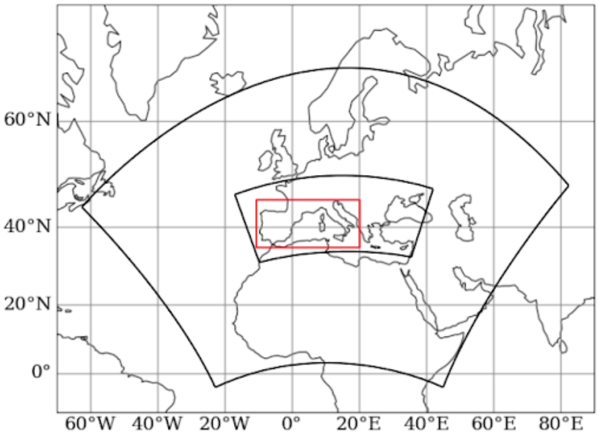

Figure 6.1: Domains used for the CHIMERE simulations: EUMED60 at 60km resolution is the large domain, the smaller nested domain is Med-CORDEX at 20km resolution. The Southwestern Europe region studied here is shown in red.

### Dry deposition scheme

Dry deposition in CHIMERE is resolved online using a canopy resistance approach, based on the scheme of the EMEP model (Wesely, 1989; Emberson et al., 2000; Simpson et al., 2003, 2012). Canopy resistance is calculated from stomatal conductance ($g_{sto}$) which increases proportionally with LAI, and the bulk non-stomatal conductance. $g_{sto}$ varies between a maximum ($g_{max}$) and minimum ($g_{min}$) daytime stomatal conductance [mmol $O_3/m^2.s$] depending on a series of meteorological conditions represented by factors of relative conductance ($f$) (Eq. 6.6). The parameters used to calculate these factors vary with land cover ($lc$) and the seasonality (Emberson et al., 2000). The land cover classes used in the dry deposition scheme being different from the one used in CHIMERE (USGS), a matrix of conversion is applied.

$$g_{sto} = g_{max,lc} \cdot f_{phen,lc} \cdot f_{light,lc} \cdot max(g_{min,lc}, (f_{temp,lc} \cdot f_{VPD,lc} \cdot f_{SWS,lc})) \tag{6.6}$$

where $f_X$ are factors of relative conductance determined by the leaf/needle age ($X = phen$), irradiance ($X = light$), temperature ($X = temp$), leaf-to-air vapour pressure deficit ($X = VPD$) and the soil moisture ($X = SWS$). Environmental variables required for $f_X$ factors are from the WRF model except for $f_{SWS}$ that is based on SWS from RegIPSL. $f_{SWS}$ for which the calculation is the same as $\gamma_{SWS}$, follows the parametrization suggested by Simpson et al. (2012) for the stomatal conductance.

### Experiments

The years 2012-2013-2014 were selected for the large diversity of hydro-climatic conditions and the availability of $O_3$ observations over the study area. During summer 2012, Southwestern Europe was affected by severe droughts ($PLA_{SD} > 0.1$ of soil dryness) and heatwaves ($PLA_{T2m} > 1.5$°C) (Appendix B: Fig. B.13). The summer 2013 was wet in the Iberian Peninsula, while the summer 2014 was wet in Italy and the Balkans. A few heatwaves occurred in summer 2013 over Southern France, Northern Italy and Northern Spain. Summer 2014 was colder ($PLA_{T2m}$ of -4.0°C) for the entire study area. The analysis method we propose here is divided into two steps.

Firstly, a focus is made on drought effects (biomass decrease and soil dryness) that are generally poorly represented in modeling experiments, over summer 2012. Several experiments are conducted on the Med-CORDEX domain in order to analyze the sensitivity of simulated biogenic emissions, dry deposition and surface $O_3$ to drought effects. Table 6.1 summarizes the CHIMERE simulations conducted. The "Reference" simulations include all the emissions as defined in Sect. 6.3.3 but without accounting for the soil moisture factor in the emission scheme of MEGAN and deposition one of CHIMERE. A simulation with no biogenic emissions is also performed ("NoBio-emiss") to estimate their relative contribution to

$O_3$ concentration.

The LAI used in the emission scheme of MEGAN is year dependant. To evaluate the effect of biomass decrease by droughts, a simulation with $LAI$ corresponding to a wet summer was used ("HighLAI-emiss"). Summer 2012 which was affected by an important biomass decrease over most of the study area (Appendix B: Fig. B.14), has been simulated with the LAI of the wet summer of 2014 (higher than the 2012-2014 mean).

The LAI database used in the dry deposition scheme in CHIMERE does not vary with the year, so that the biomass decrease during the summer 2012 is not reflected. In order to evaluate the importance of this effect, a simulation ("LAIdecr-dep") with a LAI decrease of 5% for forests and 20% for grass and crops (close to the variations observed in 2012 (Appendix B: Fig. B.14)) has been conducted.

The effect of soil dryness for the $BVOC$ emissions is evaluated using three different approaches:

- using $\gamma_{SM}$ from WRF-Noah in MEGAN ("$\gamma_{SM}$-emiss" experiment),
- using $\gamma_{SWS}$ from RegIPSL (WRF-ORCHIDEE) in MEGAN ("$\gamma_{SWS}$-emiss" experiment),
- using $\gamma_{SWSfit}$ from RegIPSL (WRF-ORCHIDEE) in MEGAN ("$\gamma_{SWSfit}$-emiss" experiment). The fitted function of Bonn et al. (2019) is applied on the SWS.

The soil dryness effect on the dry deposition is evaluated using the $f_{SWS}$ from ORCHIDEE in CHIMERE ("$f_{SWS}$-dep" experiment).

Secondly, based on a simulation configuration integrating all drought and heatwave effects ("$\gamma_{SWSfit}$-emiss & LAIdecr/$f_{SWS}$-dep" experiment, hereafter called "all-emiss-dep" experiment), the variation of $C_5H_8$ emissions, $O_3$ dry deposition velocity and surface $O_3$ concentration is analyzed over summers 2012, 2013 and 2014. In order to compare isolated and combined extreme events with normal conditions, we used a cluster approach based on the $PLA_{T2m}$ and $PLA_{SD}$ indicators.

Table 6.1: Name, description and aim of the simulations launched with the CHIMERE model on the nested Med-CORDEX domain for summers 2012, 2013 and 2014.

| Simulation name | Description | Aim |
|---|---|---|
| Reference (R.) | CHIMERE reference (v2020r1) | Default for dry and hot periods |
| | | *On biogenic emissions* |
| NoBio-emiss | R. without biogenic emissions | Contribution of biogenic emissions to $O_3$ |
| HighLAI-emiss | R. with wet summer LAI | Effect of biomass decrease |
| $\gamma_{SM}$-emiss | R. with $\gamma_{SM}$ factor from Noah | Effect of soil dryness |
| $\gamma_{SWS}$-emiss | R. with $\gamma_{SWS}$ factor from ORCHIDEE | Effect of soil dryness |
| $\gamma_{SWSfit}$-emiss | R. with $\gamma_{SWSfit}$ factor from ORCHIDEE | Effect of soil dryness |
| | | *On gas dry deposition* |
| LAIdecr-dep | R. with prescribed LAI reduction | Effect of biomass decrease |
| LAIdecr/$f_{SWS}$-dep | R. with prescribed LAI reduction and $f_{SWS}$ factor from ORCHIDEE | Effect of biomass decrease and soil dryness |

### Validation of surface $O_3$, $NO_2$ and 2m temperature

Simulated surface $O_3$ and $NO_2$ concentrations by CHIMERE were compared to the EEA observations while simulated temperature at 2m above the surface by WRF was compared to the E-OBS observations (Cornes et al., 2018). Table 6.2 presents the mean validation scores of the "Reference" simulations over Southwestern Europe for summer 2012. Validation scores of $O_3$ and $NO_2$ are very similar for summers 2013 and 2014.

The simulated surface $O_3$ is slightly higher than the observations for hourly and daily mean values (bias "observation - model" of -1.93 and -0.13$\mu g/m^3$) and lower for the daily maximum values (+10.94$\mu g/m^3$). The simulated diurnal cycle is lower than the observed one: CHIMERE overestimates the daily minimum and underestimates the maximum. The temporal correlation (R pearson coefficient) varies between a 0.53 in daily mean and 0.57 in hourly mean. The spatial distribution of bias and correlation scores of daily maximum values for each summer is shown in Appendix B (Fig. B.15). The highest bias ($> +25\mu g/m^3$) and lowest correlations (R of $\approx 0.2$) are obtained near large urban areas (e.g. Madrid, Milano) which may be less well represented in the model even if the stations are classified as rural background. There are substantial uncertainties related to the $NO_x/VOC$ emissions in (peri-)urban areas.

These $O_3$ scores show an overall agreement with those calculated by Gaubert et al. (2014) and Menut et al. (2021) over Europe. The averaged daily maximum bias and correlation coefficient computed are slightly higher and lower, respectively, in this study mainly because the area is limited to Southwestern Europe. Due to the multiple sources of $O_3$ precursors and favourable temperature and light conditions, the Mediterranean is identified as a region of important uncertainty for modeling $O_3$ concentration (Richards et al., 2013).

Validation scores are also computed for the surface $NO_2$ using the EEA observations, with a different distribution of stations than for ozone. In agreement with the results of Menut et al. (2021), CHIMERE underestimates $NO_2$ concentrations ($+4.95\mu g/m^3$ in daily mean and $+8.57\mu g/m^3$ in daily maximum) compared to EEA observations. Lamsal et al. (2008) emphasize that the chemiluminescence analyzer, the measurement technique primarily found in air quality stations, is subject to significant interference from other reactive species containing oxidized nitrogen (e.g. PAN, $HNO_3$). It may partly explain the constant underestimation compared to observations.

The mean temporal correlation coefficients do not exceed 0.4. These low validation scores may also be linked to the emission inventory used as well as meteorological conditions (boundary layer height representation in particular). As a major $O_3$ precursor, part of the uncertainty of this study is directly related to $NO_2$ emissions and concentrations.

Finally, as a critical variable for simulating diurnal and seasonal $O_3$ concentrations, temperatures at 2m above the surface ($T_{2m}$) have been compared to the E-OBS observations. Averaged over the Southwestern Europe, the bias is close to $0°C$ while the RMSE is significant ($8.19°C$ in daily mean and $12.63°C$ in daily maximum). The spatial distribution of the bias presents large variations (Appendix B: Fig. B.16). The daily maximum $T_{2m}$ is overestimated in the Southern Mediterranean (up to $5°C$) compared to observations while it is underestimated in the norhtern part (up to $5°C$). Nevertheless, the averaged scores of temporal correlation are high (around 0.75).

Even if such validation scores are close to those found in the scientific literature (e.g. Panthou et al., 2018), the temperature uncertainties significantly contribute to those of the $O_3$ simulated by CHIMERE.

Table 6.2: Comparisons between observed and simulated surface $O_3$ concentration, $NO_2$ concentration and 2m temperature, averaged over Southwestern Europe during summer 2012, for the "Reference" CHIMERE simulation.

| | Observations | Model | Bias (obs. - mod.) | RMSE | Pearson correl. (R) |
|---|---|---|---|---|---|
| $O_3$ | $[\mu g/m^3]$ | $[\mu g/m^3]$ | $[\mu g/m^3]$ | $[\mu g/m^3]$ | |
| Hourly | 83.21 | 85.14 | -1.93 | 20.45 | 0.57 |
| Daily mean | 83.93 | 84.06 | -0.13 | 14.31 | 0.53 |
| Daily max | 116.32 | 105.39 | 10.94 | 21.49 | 0.54 |
| $NO_2$ | $[\mu g/m^3]$ | $[\mu g/m^3]$ | $[\mu g/m^3]$ | $[\mu g/m^3]$ | |
| Hourly | 7.65 | 3.70 | 3.95 | 5.57 | 0.25 |
| Daily mean | 7.55 | 2.60 | 4.95 | 5.24 | 0.40 |
| Daily max | 14.65 | 6.08 | 8.57 | 9.87 | 0.37 |
| $T_{2m}$ | $[°C]$ | $[°C]$ | $[°C]$ | $[°C]$ | |
| Daily mean | 22.25 | 22.25 | -0.01 | 8.19 | 0.76 |
| Daily max | 23.13 | 28.34 | 0.56 | 12.63 | 0.75 |

## 6.4 Results

### 6.4.1 Sensitivity to soil dryness and biomass decrease effects

The sensitivity analysis to soil dryness and biomass decrease effects is focused on summer 2012 as droughts mainly occurred during this year (over the 2012-2014 period). Most of Southwestern Europe was affected by a biomass decrease in 2012 (compared to the wet summer 2014), except Eastern Spain. The LAI difference between summer 2012 and 2014 can reach -30% over central Italy (Appenines region) corresponding to a mean decrease of 0.5 $m^2/m^2$ (Appendix B: Fig. B.14).

$C_5H_8$ is the main contributor to the total mass of $BVOCs$ emitted (70%), followed by the model species APINEN (13%, including e.g. $\alpha$-pinene, sabinene).

#### $C_5H_8$ emissions

Figure 6.2 (lower panel) shows the daily mean $C_5H_8$ emissions in Southwestern Europe for summer 2012 simulated by the MEGAN model ("Reference" simulation). The spatial distribution of $C_5H_8$ over the Mediterranean is heterogeneous, ranging from areas of zero or low emissions ($\sim 1 \times 10^{-3} g.m^{-2}.h^{-1}$) to high emitting areas ($\sim 1.5 \times 10^{-3} g.m^{-2}.h^{-1}$) such as in the Balkans, Apennins, Sierra Morena, Sardinia and Central Portugal. Similar spatial distributions were found for APINEN. Differences in spatial patterns among species depend on the variation of emission factors over the land cover classes.

The effect biomass decrease and soil dryness on $C_5H_8$ emissions during the dry summer 2012 is also shown in Figure 6.2. The effect of biomass decrease averaged over June, July and August is characterized by negative differences over most of the southern part of the region, reaching -20% in Northern Spain and -25% in Northern Italy.

The impact of soil dryness is assessed with the "$\gamma_{SM}$-emiss", "$\gamma_{SWS}$-emiss" and "$\gamma_{SWSfit}$-emiss" MEGAN simulations. The quantified impact can vary considerably between them. In the "$\gamma_{SM}$-emiss" experience, $C_5H_8$ emissions stay constant as long as the soil moisture is above the wilting point. Once this point is reached (water is missing), it is assumed that plant can not synthesize $C_5H_8$ anymore and the emissions decrease steeply. The wilting point is constant and depends only on the soil type. For instance, silt soil is characterized by lower wilting point values than clay soil, so that $\theta_w$ is more quickly reached for the latter. Due to the high spatial variability of soil type, the difference induced by "$\gamma_{SM}$-emiss" is also characterized by large variability. Within a same region (e.g. Central Italy), the difference sharply varies between -50% and 0% while the region is all over affected by an agricultural drought according to the $PLA_{SD}$ indicator (Appendix B: Fig. B.13).

For the alternative approach based on the dynamical $SWS$ function, the relative difference of $C_5H_8$ emissions ("Reference" .vs. "$\gamma_{SWS}$-emiss" experiment) is more spatially homogeneous than "$\gamma_{SM}$-emiss", and the overall reduction is larger. The strongest stress values are located in plains and for plants with short-root systems, in agreement with the sensitivity analysis performed by Vicente-Serrano (2007) about drought effects on vegetation. Semi-arid regions (e.g. Andalusia) are strongly affected as the water budget is almost permanently in deficit (high solar radiation and low/no precipitation). Being adapted to recurrent droughts, some plant species (e.g. *Arundo donax* in a Moroccan ecotype) can reduce the isoprene synthesis as the result of pressure selection to preserve their viability (Haworth et al., 2017). However, the emission reduction could be overestimated as irrigation is largely used in many semi-arid areas (e.g. García-Vila et al., 2008). A specific analysis should be undertaken to cover the diversity of answers to drought stress in both natural and human influenced systems within such regions.

The third experiment "$\gamma_{SWSfit}$-emiss" presents the same areas of $C_5H_8$ decrease as "$\gamma_{SWS}$-emiss" but in a lower extent. $C_5H_8$ decreases when SWS values are the lowest. Semi-arid regions are also more affected (-50%) than others (e.g. -20% in Central Italy).

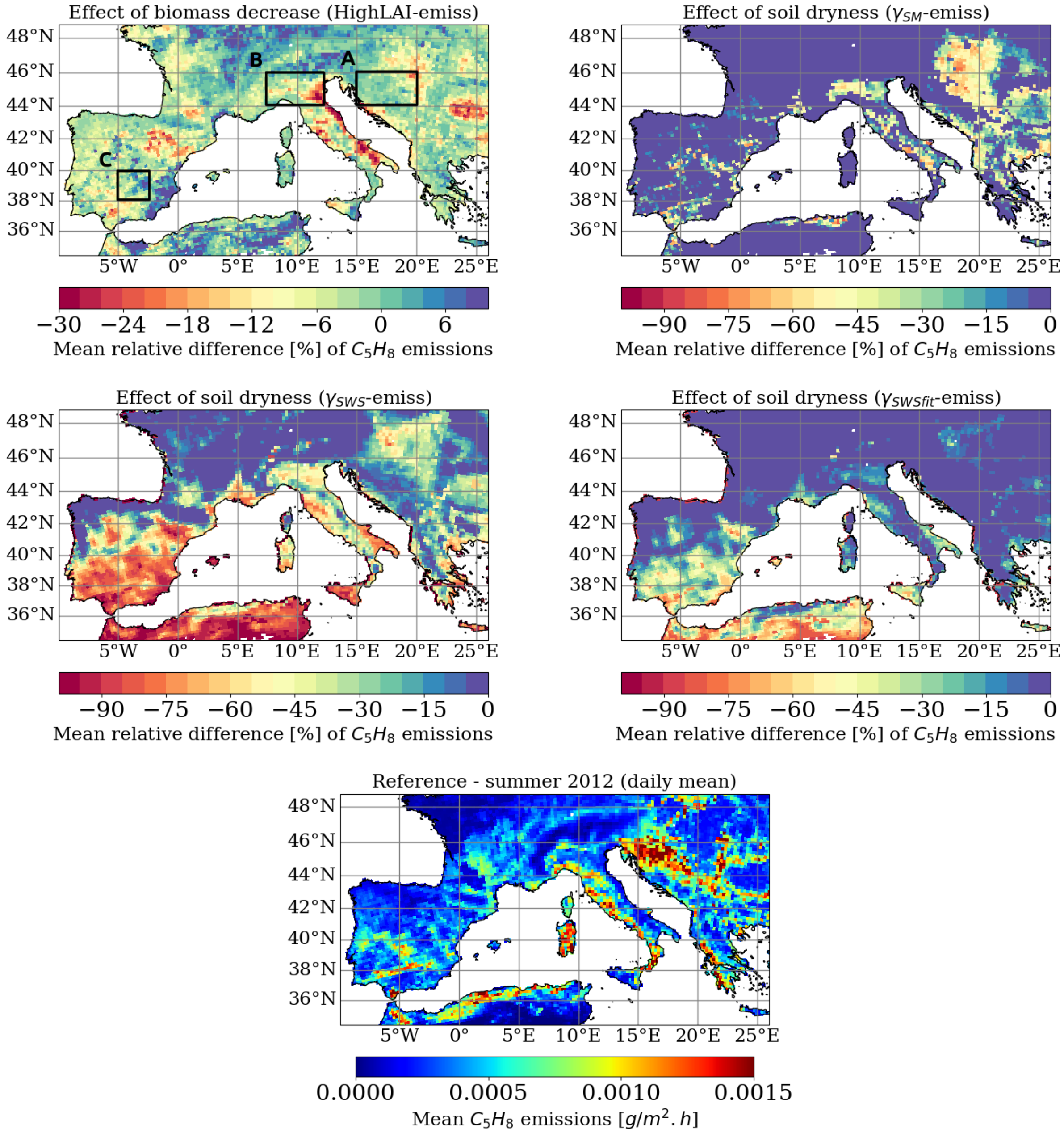

Figure 6.2: Summer mean (JJA) of daily mean isoprene emissions [$g.m^{-2}.h^{-1}$] for 2012 from the "Reference" simulation (lower panel). Mean relative difference [%] of $C_5H_8$ emissions due to biomass decrease and soil dryness. The relative difference is computed between the "Reference" and "HighLAI-emiss" simulation to quantify the biomass decrease effect (upper left panel), and "$\gamma_{SM}$-emiss"/"$\gamma_{SWS}$-emiss"/"$\gamma_{SWSfit}$-emiss" to quantify the soil dryness effect. For diagnostic purposes, areas of interest are designated within the dashed rectangles: here named as the "Balkans" (A), "Pô Valley" (B) and "Central Spain" (C).

Three areas of high emissions are analyzed more specifically (boxes in Fig. 6.2): the Balkans, the Pô Valley and Central Spain. The temporal evolution of $C_5H_8$ emissions during the summer 2012 for the different experiments is shown in Figure 6.3. Droughts and heatwaves occured over the three regions. Droughts do not negate the dependence on light and/or temperature, and emission peaks are driven by heatwaves with higher 2m temperature and solar radiation (Appendix B: Fig. B.17). However, the peak values are reduced if LAI decrease and soil dryness are accounted for. Averaged over the three regions, the biomass decrease induces a 3% decrease of the total summer amount of $C_5H_8$ emitted. The soil dryness parameter induces difference of -12% for "$\gamma_{SM}$-emiss", -39% for"$\gamma_{SWS}$-emiss" and -13% for "$\gamma_{SWSfit}$-emiss". Based on experimental measurements over three summers (2012, 2013 and 2014) in a Mediterranean environment (Observatoire de Haute Provence, *Quercus pubescens* plant species), Saunier et al. (2017) identified a 35% emission decrease due to severe droughts. Demetillo et al. (2019) measured in California a $C_5H_8$ concentration reduction of 50% during severe droughts (2014 and 2015). These values are close to and even in the range of the simulated experiments. "$\gamma_{SWS}$-emiss" experiment is considered here as the lower limit of the reduction range of $C_5H_8$ emissions due to dry conditions, $SWS$ being included in the calculation of the emissions rate as soon as soil water stress for plant stress is below 0.5.

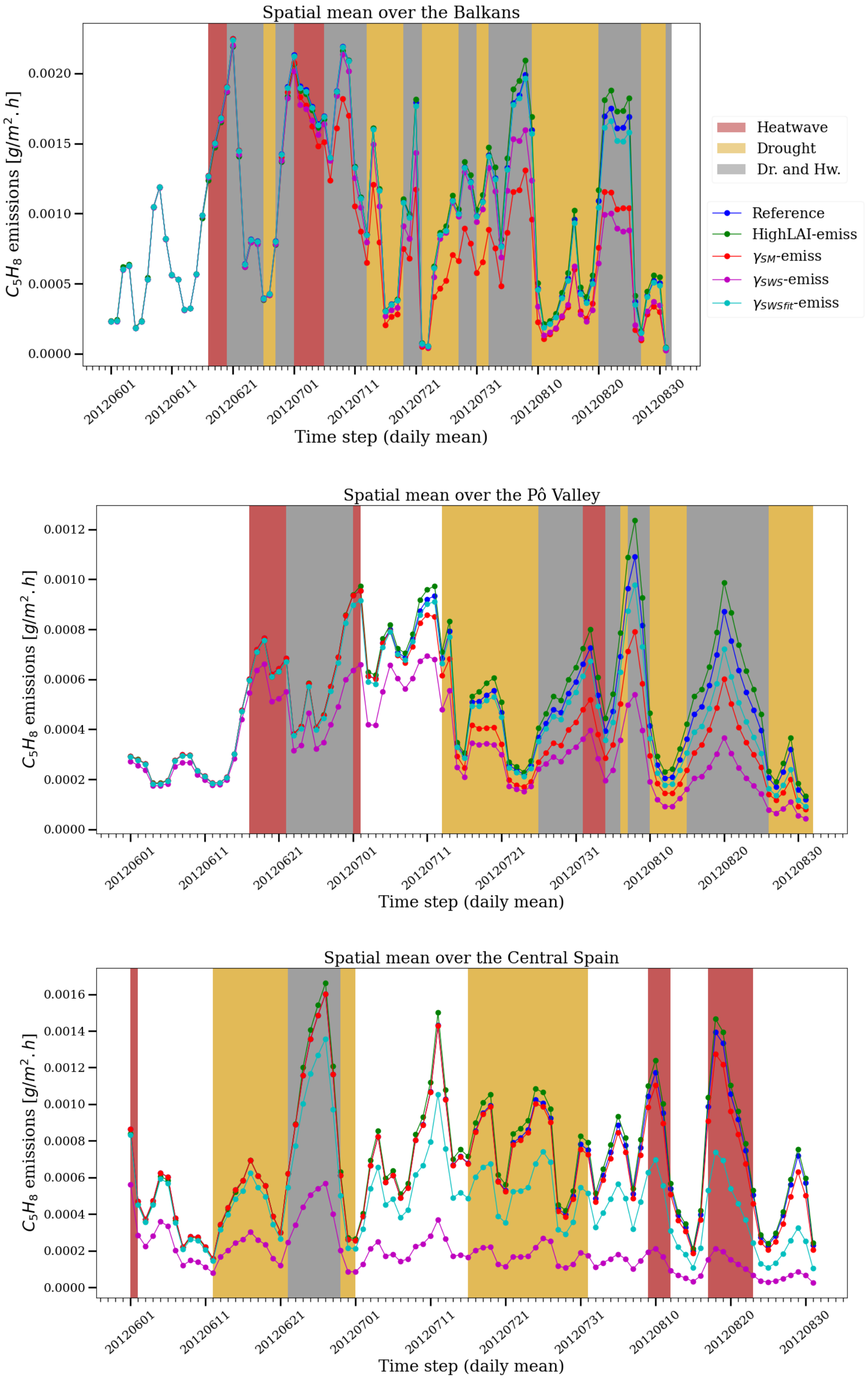

Figure 6.3: Daily mean $C_5H_8$ emissions $[g.m^{-2}.h^{-1}]$ during the summer 2012, spatially averaged over the Balkans (upper panel), Pô Valley (middle panel) and Central Spain (lower panel) for the different MEGAN experiments. The colored bands highlight periods of droughts and heatwaves.

Finally, the different simulated experiments from the MEGAN-CHIMERE model have been compared to observations of surface $C_5H_8$ concentrations from EBAS data set (Fig. 6.4). The Ersa station has an almost complete time series for summer 2012. Based on the $PLA$ indicator, Northern Corsica was affected by two heatwaves but no drought. However, we detected soil dryness conditions close to the drought limit (mean $PLA_{SD}$ of -0.09). The temporal correlation between the simulated and observed $C_5H_8$ concentration is similar for each experiment (R coefficient around 0.68). Averaged over the summer, the lowest mean bias with the observations is obtained with "$\gamma_{SWSfit}$-emiss" (-28 pmol/mol) and the largest one with "$\gamma_{SM}$-emiss" (-151 pmol/mol). However, over July and August, "$\gamma_{SWS}$-emiss" experiment presents the lowest mean bias (+56 pmol/mol). The "Reference" and "$\gamma_{SM}$-emiss" experiments have equal values as the soil wetness from WRF-Noah is above the local wilting point.

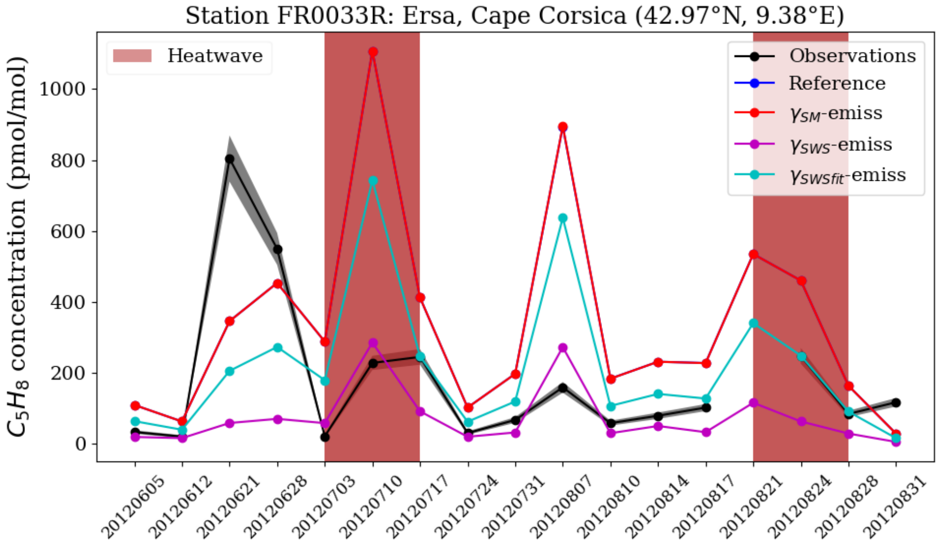

Figure 6.4: Observed surface $C_5H_8$ concentration $[pmol/mol]$ during the summer 2012 at the Ersa station (FR0033R, Cape Corsica) from the EBAS data set, compared to the different simulated experiments undertaken by the MEGAN-CHIMERE model. The shaded curve in black represents the precision range of the measurements. The "Reference" and "$\gamma_{SM}$-emiss" experiments here have equal values.

### $O_3$ dry depositon velocity

Figure 6.5 (upper left panel) presents daily mean dry deposition velocity values that range between 1.0 and 1.8cm/s within our areas of interest. The mean effect of biomass decrease (relative difference between the "Reference" and the "LAIdecr-dep" experiment, upper right panel) over the summer does not exceed -8%, and is lower over the forested areas (as prescribed in our experiment). The cumulative effects of biomass decrease and soil dryness is represented with the "LAIdecr-dep/$f_{SWS}$-dep" experiment (Fig. 6.5, lower pannel). The soil dryness effect is much larger than that of biomass decrease. Values range from 0 to -35%. Central Italy and the Iberian Peninsula are the most affected regions.

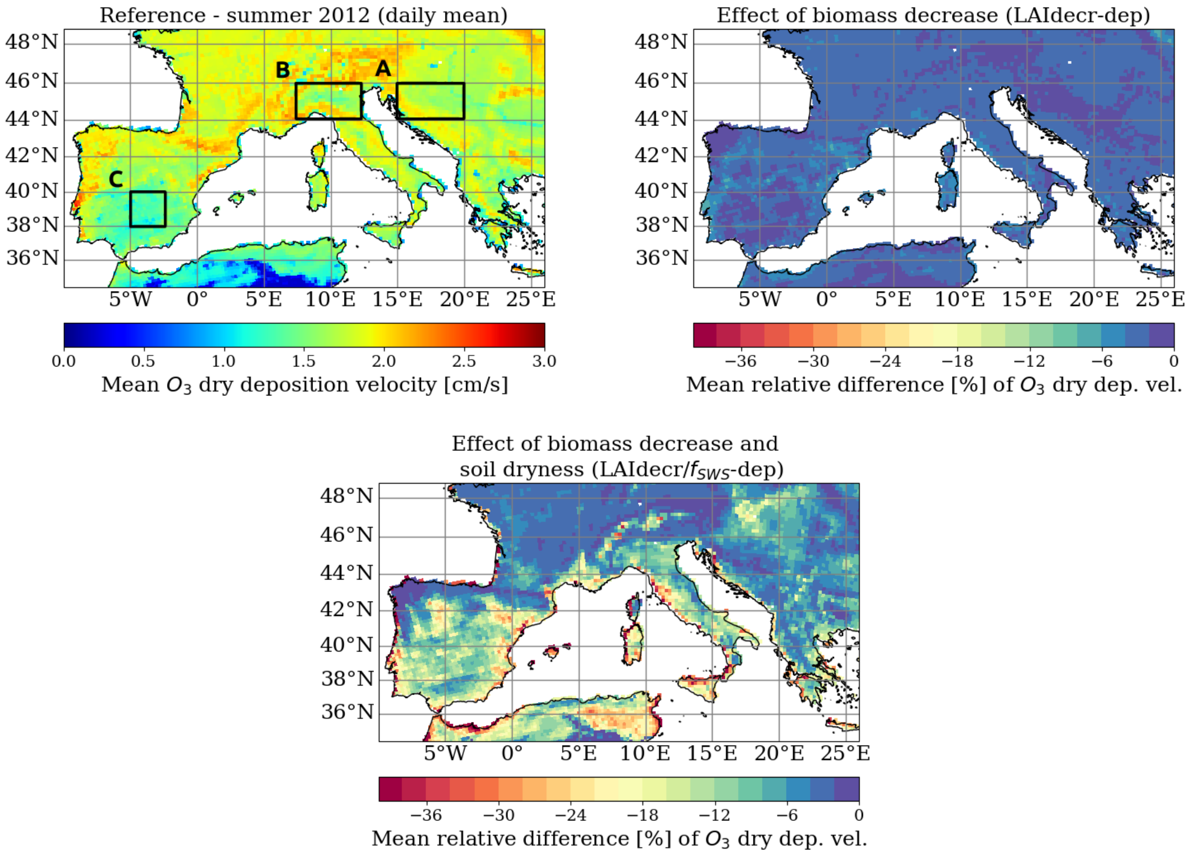

Figure 6.5: Summer mean (JJA) of daily mean $O_3$ dry deposition velocity $[cm/s]$ for 2012 from the "Reference" simulation (upper left panel). Mean relative difference [%] of $O_3$ dry deposition velocity due to biomass decrease and soil dryness. The relative difference is computed between the "Reference" and "LAIdecr-dep" simulation to quantify the biomass decrease effect (upper right panel) and "LAIdecr-dep/$f_{SWS}$-dep" to quantify combined biomass decrease and soil dryness effect (lower panel).

The temporal evolution of $O_3$ dry deposition velocity for the three areas of interest is shown in Figure 6.6. The biomass decrease effect is larger (e.g. -9% over the Pô Valley) during the first half of summer. It is close to -1% at the end of summer. This is explained by the LAI decrease prescribed from mid-July in the dry deposition scheme. In addition to that, the dry deposition velocity is characterized by a decreasing trend over summer imposed by the fixed phenology factor ($f_{phen}$).

Regarding the soil dryness, its effect (larger than the biomass decrease) is almost constant during summer (e.g. -12% over the Pô Valley). Based on measurements over Central Italy, Lin et al. (2020) computed a relative difference of about -50% between August 2004 (wet summer, ~0.8cm/s) and August 2003 (dry summer, ~0.4cm/s). However, summer 2003 was characterized by considerable heatwaves in Italy ($PLA_{T2m}$ positive) which might intensify the decrease. We emphasize that dry deposition velocity generally decreases during heatwaves (Fig. 6.6) as the near surface temperature is above the optimal temperature of stomatal conductance. In conclusion, both effects related to droughts and heatwaves (the most intense) lead to a reduction in $O_3$ deposition.

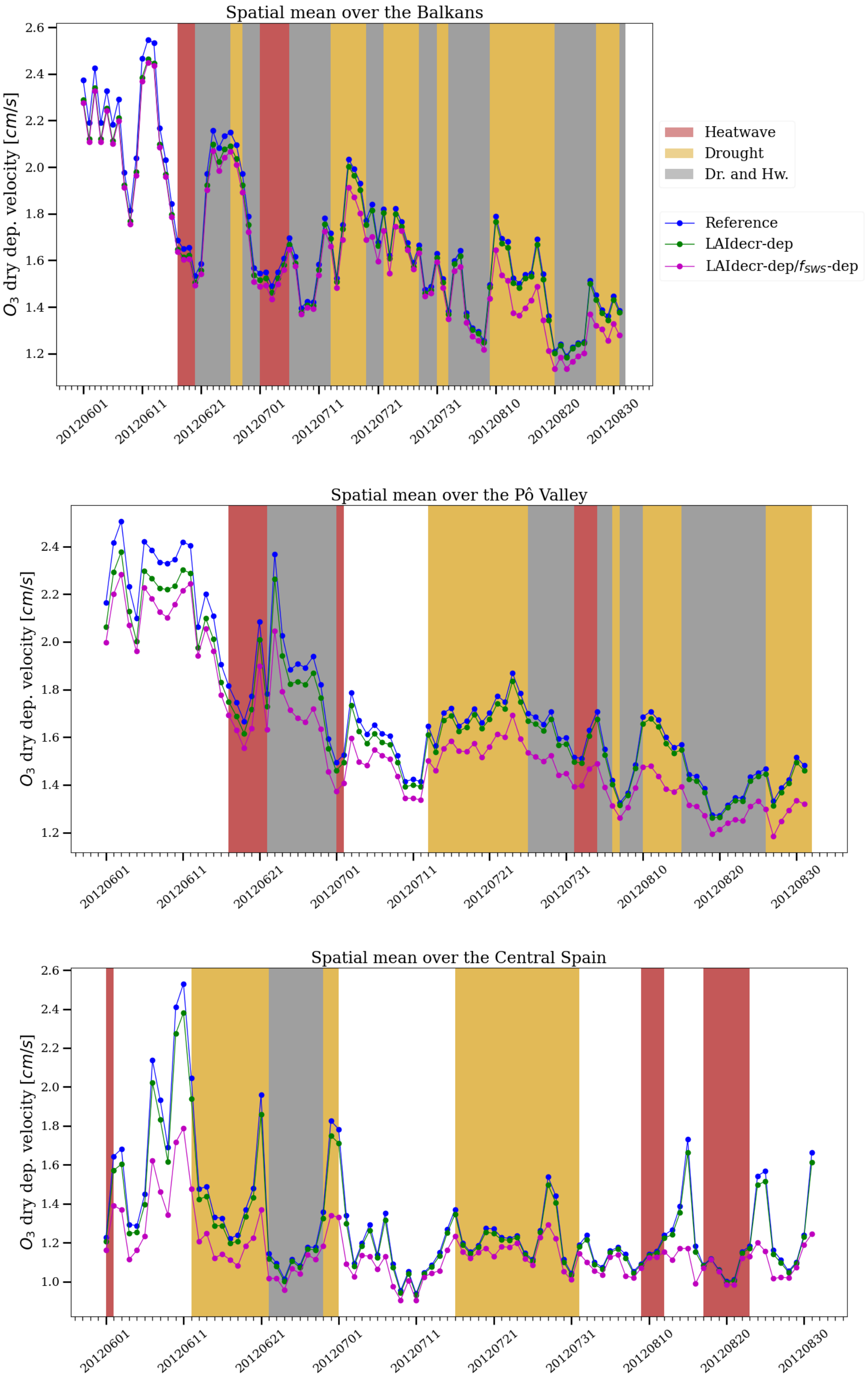

Figure 6.6: Daily mean $O_3$ dry deposition velocity [cm/s] during the summer 2012, spatially averaged over the Balkans (upper panel), Pô Valley (middle panel) and Central Spain (lower panel) for the different CHIMERE experiments.

### $O_3$ surface concentration

Figure 6.7 (upper left panel) maps the mean surface $O_3$ concentration simulated by CHIMERE ("Reference" experiment) over the summer 2012. High concentrations (between 100 and $110\mu g/m^3$) are located in the eastern part of the study area (e.g. the Balkans and Italy). The spatial distribution of mean surface $O_3$ shows similar patterns as the distribution of $PLA_{T2m}$ (Appendix B: Fig. B.13), highlighting the critical role of the temperature. Surface $O_3$ remains high above the sea due to transport and the absence of dry deposition (e.g. $120\mu g/m^3$ over the Adriatic sea). The contribution of $BVOC$ emissions on surface $O_3$ is also presented (upper right panel). It varies between 4% (e.g. Iberian Peninsula) and 22% (e.g. Northern Italy). $BVOC$ emissions are known to be significant precursors of $O_3$ production in the Mediterranean region, and in the same range of values (e.g. Mertens et al., 2020). Moreover, our areas of interest are located in rural regions, mostly characterized by a $NO_x$-limited regime (Appendix B: Fig. B.18).

A simulation including drought effects on both $C_5H_8$ emissions and $O_3$ dry deposition has been conducted with MEGAN-CHIMERE ("$\gamma_{SWS}$-emiss & LAIdecr/$f_{SWS}$-dep" experiment). The resulting effect on surface $O_3$ is shown in Figure 6.7 (lower panels). On average during the summer (lower left), $O_3$ concentration slightly increases over the continent (between +0.5% and +3.0%) due to the decrease of $O_3$ deposition as dominant effect, while it slightly decreases (between -1% and -1.5%) over the sea and ocean due to the lower transport of $O_3$ precursors, compared to the "Reference" experiment. However, the $O_3$ increase over the Iberian Peninsula may be overestimated as the LAI reduction we applied to the whole domain (e.g. -20% for grass PFTs) is larger compared to the variation of MODIS LAI in this specific region (Appendix B: Fig. B.14).

Drought effects on surface $O_3$ induced by $C_5H_8$ emission reduction is not constant. It is largest during combined heatwaves (i.e. when biogenic contribution is high). As a result, drought effects on $C_5H_8$ emissions can be dominant (compared to the effects on $O_3$ deposition) during simultaneous droughts and heatwaves, inducing a decrease of $O_3$ peaks by a few $\mu g/m^3$ both over continent and sea/ocean. The maximum absolute relative difference (Fig. 6.7, lower right panel) reaches -5% over the Pô Valley and -14% along the strait of Gibraltar. $O_3$ formation over the latter is favoured by large $NO_x$ shipping emissions.

Conducting a similar modeling experiment based on the $\gamma_{SM}$ from MEGANv3, Jiang et al. (2018) simulated for the dry summer 2010 a maximum absolute relative difference of surface $O_3$ in August of -4%. $O_3$ reduction (-10% on average) due to severe droughts was also measured in California over the period 2002-2015 (Demetillo et al., 2019). This was identified as being related to a steep decrease of $C_5H_8$ concentrations.

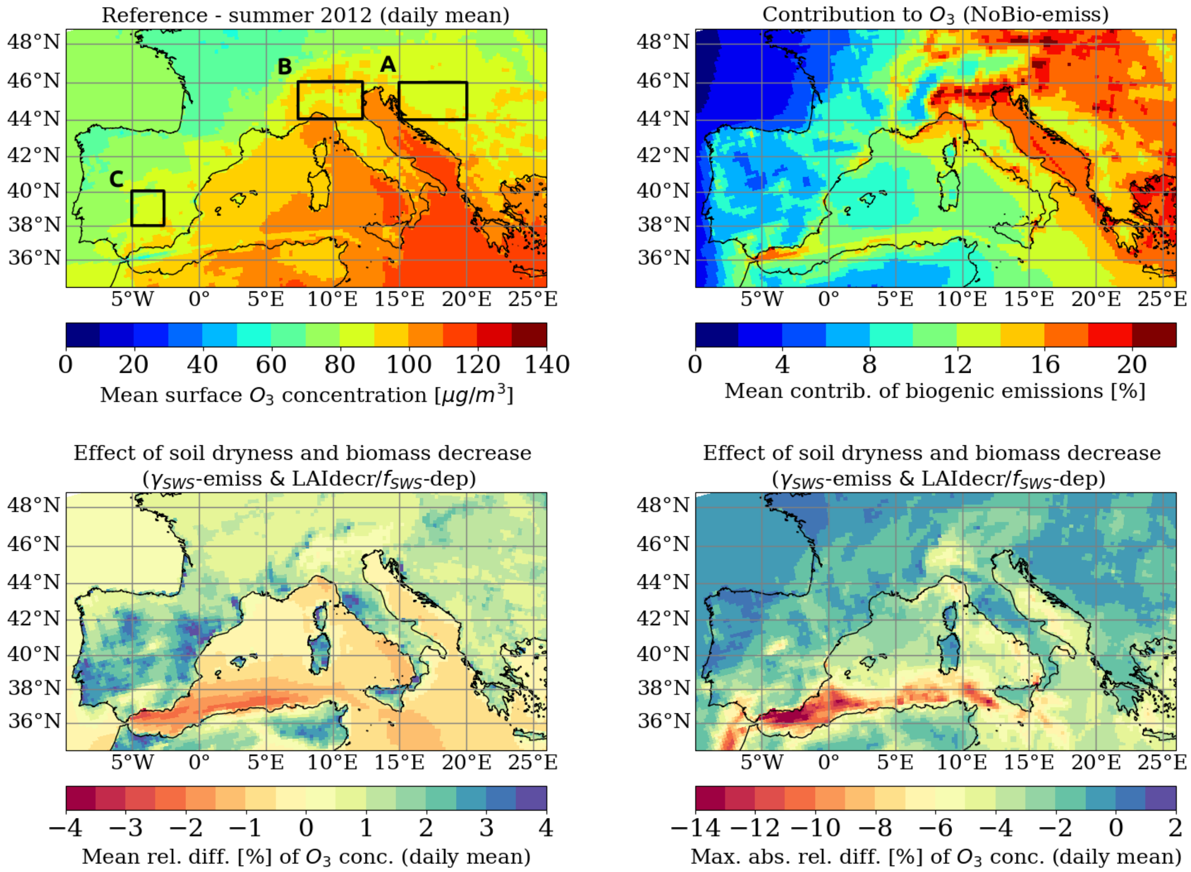

Figure 6.7: Summer mean (JJA) of daily mean $O_3$ surface concentration [$\mu g/m^3$] for 2012 from the "Reference" simulation (upper left panel). Mean contribution of biogenic emissions to $O_3$ surface concentration based on the "NoBio-emiss" experiment (upper right panel). Mean (lower left panel) and maximum absolute (lower right) relative difference [%] of $O_3$ surface concentration due to biomass decrease and soil dryness. The relative difference is computed between the "Reference" and "$\gamma_{SWS}$-emiss & LAIdecr-dep/$f_{SWS}$-dep" simulation from CHIMERE.

For each area of interest, the temporal evolution of surface $O_3$ based on the different CHIMERE experiments and the EEA observations (AQ e-Reporting) is presented (Fig. 6.8 for the Pô Valley and Fig. B.19 for the Balkans and Central Spain in Appendix B). Since the drought specific effects (both emissions and deposition variation) on surface $O_3$ are less than the bias between model and observations (see Sect. 6.3.3), no simulation can be designated with certainty as the best fit. Furthermore, we emphasize the need for more observational data, with the most complete spatial coverage.

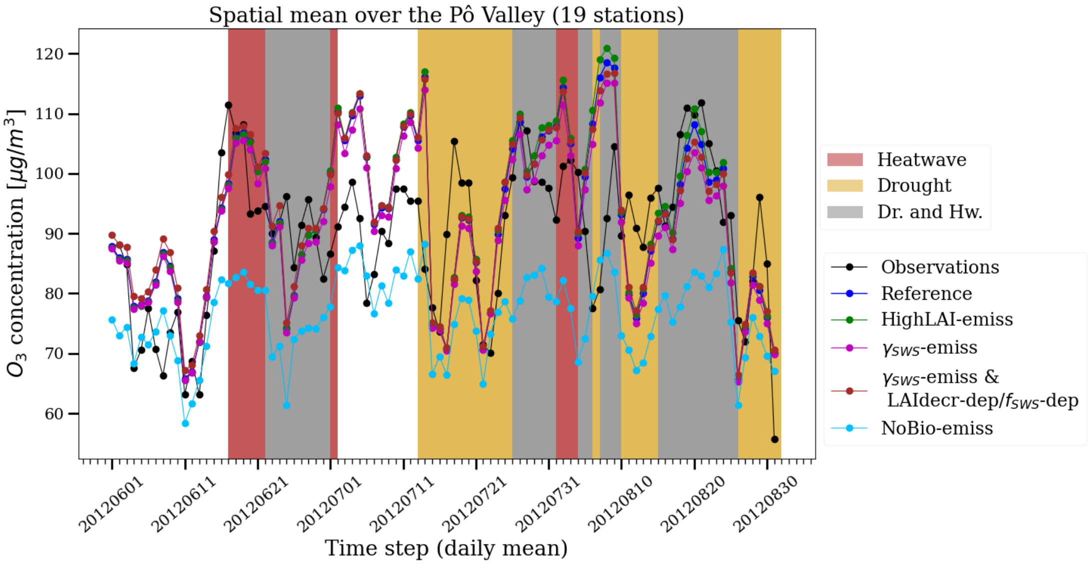

Figure 6.8: Daily mean $O_3$ surface concentration [$\mu g/m^3$] during summer 2012, spatially averaged over the Pô Valley from the EEA observations and the different CHIMERE experiments.

### 6.4.2 Statistical variation during droughts and heatwaves

In this result section, a statistical analysis is performed using observations and simulations of the summers 2012, 2013 and 2014. The "all-emiss-dep" experiment has been chosen because it includes drought and heatwave effects in the most comprehensive way. Moreover, the $C_5H_8$ emission approach ("$\gamma_{SWSfit}$-emiss") has shown good performance compared to observations (Fig. 6.4), remaining rather conservative, not in the lower limit of the $C_5H_8$ reduction range. Clusters of droughts and heatwaves (isolated or combined) are constructed based on the $PLA_{T2m}$ and $PLA_{SD}$ indicators and are used to represent the spatial distribution of $C_5H_8$ emissions, $O_3$ stomatal conductance and $O_3$ surface concentration during such events.

### $C_5H_8$ emissions

Figure 6.9 shows the distribution of $C_5H_8$ emission rates over the Southwestern Mediterranean for clusters of extreme weatger events. On average, the daily maximum $C_5H_8$ emission is significantly higher (t-test, $p < 0.01$) during isolated and combined heatwaves than normal conditions (no heatwaves nor droughts) with a mean value of $0.16 \times 10^{-2}$ against $0.12 \times 10^{-2} g.m^{-2}.h^{-1}$. However, emissions during droughts have the same mean value as in normal conditions. During isolated droughts (cluster "drought and not heatwave"), the mean daily maximum $C_5H_8$ emission rate is lower than normal conditions ($-0.02 \times 10^{-2} g.m^{-2}.h^{-1}$, non-significant difference).

The associated weather conditions are considerably different between droughts combined to heatwaves and isolated droughts (Appendix B: Fig. B.20). The combined (resp. isolated) droughts are characterized by a 2m temperature of 23.9°C (resp. 22.6°C), a shortwave radiation of $342.2 W/m^2$ (resp. $296.0 W/m^2$) and a cloud cover of 1.8% (resp. 3.1%). Those weather variables are used for the computation of the activity factors $\gamma_P$ and $\gamma_T$, thus directly affecting emissions. During isolated droughts, $\gamma_{LAI}$ (0.51) and $\gamma_{SWS}$ (0.89) are smaller than for normal conditions (0.48 and 0.76 respectively, significant difference for both). Nevertheless, this negative signal is not large enough for significant variation of the emission rates (compared to normal conditions).

Gathering worldwide data from experimental measurements of biogenic emissions under different climate drivers, the scientific review presented by Feng et al. (2019) (based on 74 articles) estimated to +53% the emission change of $C_5H_8$ during warm conditions and -15% during dry conditions. Those variations are close to what we simulated (+35% and -13% respectively).

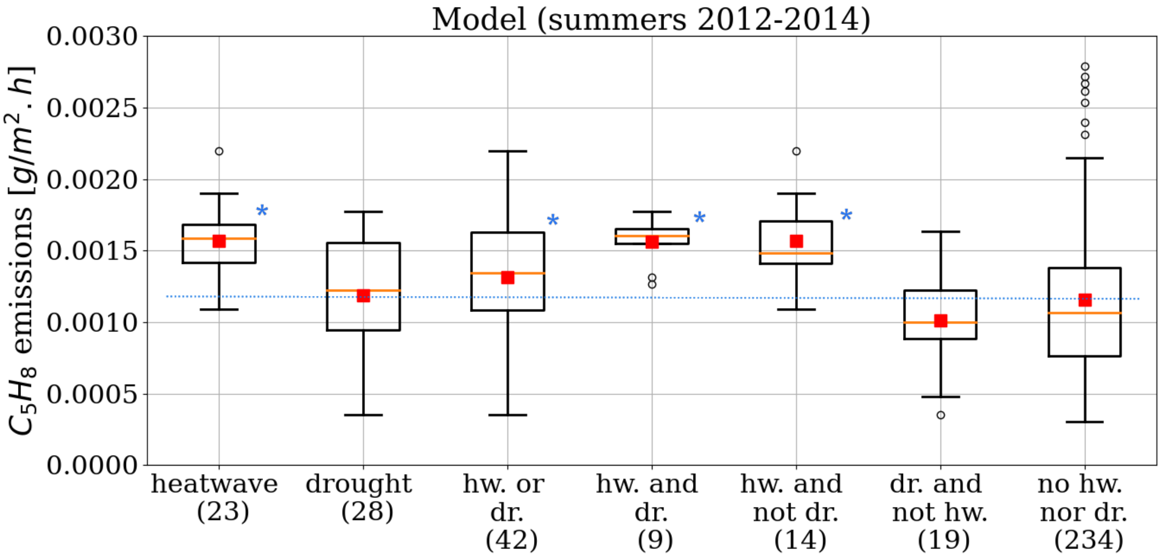

Figure 6.9: Daily maximum $C_5H_8$ emission rate $[g.m^{-2}.h^{-1}]$ simulated by the MEGAN model ("$\gamma_{SWSfit}$-emiss" experiment) over Southwestern Europe, clustered by identified extreme weather events ($PLA_{T2m}$ and $PLA_{SD}$ indicators from RegIPSL). The number of days is indicated in parentheses. The analyzed period is June-July-August 2012, 2013 and 2014, covering a total of 276 days. The red squares show the mean of the distribution and the black circles are the outliers. The blue dotted line indicates the mean value of the normal conditions ("no hw. nor dr." cluster) and the blue stars if the mean value of the considered cluster is significantly different (t-test, at least $p < 0.1$) from the normal conditions. The box covers the InterQuartile Range (IQR) between Q1 (25th percentile) and Q3 (75th percentile). The lower whisker is limited to a statistical minimum (Q1-1.5*IQR) and the upper one to a statistical maximum (Q3+1.5*IQR).

### $HCHO$ total column

According to the CHIMERE simulations "Reference" and "NoBio-emiss", biogenic emissions contribute between 60 and 80% of the $HCHO$ concentration over the whole region. Variations of $HCHO$ concentration may therefore be used as indicator of $BVOC$ emission variations during droughts and heatwaves. This allows us to use satellite observations of $HCHO$, which is particularly interesting due to the lack of in-situ data. Observations of the $HCHO$ total column from the OMI instrument are used.
Table 6.3 presents the average difference of $HCHO$ ($\Delta HCHO$) during extreme events compared to normal conditions (no heatwave nor drought). Over summers 2005 to 2016, $HCHO$ is significantly higher during heatwaves for the Balkans, Pô Valley and Central Spain (+15% on average). ΔHCHO is also positive during droughts but to a lesser extent (+3% on aver-

age, non-significant for Central Spain only). However, isolated droughts induce a significant decrease for the Balkans (-7%), Pô Valley (-6%) and Central Spain (-6%). Those results are consistent with the variation of $C_5H_8$ emissions simulated by MEGAN when a soil moisture parameter is taken into account (see Sect. 6.4.2). Wang et al. (2021a) also report a significant $HCHO$ column decrease (up to -30%) induced by a prolonged drought in a forested area in China.

The observed and simulated total $HCHO$ have been compared for the summer 2012, for the "$\gamma_{SWSfit}$-emiss" experiment. Time series showing $HCHO$ evolution for the three areas of interest are shown in Appendix B (Fig. B.21). The simulated $HCHO$ column is generally higher than the observations, especially for the Balkans. As mentioned in 6.2.2, uncertainty on the observations is large (between 30 and 100%) with large spatial variability (about a factor of two larger than in CHIMERE). HCHO products from OMI also present a systematic low mean bias (20-51%) (Zhu et al., 2016). However, the differences could be attributed to wrong specifications of land cover, and thus of the EF (e.g. Curci et al., 2010). Temperate tree PFTs are characterized by high $C_5H_8$ emission rates (respectively 10 000 and $600\mu g.m^{-2}.h^{-1}$ for broadleaf and needleleaf types), compared to grassland ($800\mu g.m^{-2}.h^{-1}$) or cropland ($1\mu g.m^{-2}.h^{-1}$) (Guenther et al., 2012). After aggregation of the USGS land cover classes, the vegetation type assumed in CHIMERE in the Balkans is 57% of forest cover, 9% grassland and 33% cropland. Using the MODIS MCD12 product (Friedl et al., 2010), we find a different distribution, with 30% of forest cover, 25% grassland and 31% cropland. Finally, $HCHO$ is a product of oxidation of $VOCs$, which were not compared, so that it is extremely difficult to pinpoint the main source of error on $HCHO$.

The comparison between CHIMERE and OMI of $HCHO$ total column variations during drought and heatwave days relies on very few cases. It is therefore difficult to support conclusions with a sufficient level of certainty. Nevertheless, CHIMERE simulations are more sensitive to temperature than OMI observations (+52.2% and +27.7% during heatwaves respectively, averaged over the three areas of interests). Since the summer 2012 was affected by long agricultural droughts, the inclusion of a soil dryness parameter in CHIMERE ("$\gamma_{SWSfit}$-emiss" experiment) reduces the simulated $HCHO$ peaks (Appendix B: Fig. B.21). However, the mean $\Delta HCHO$ during heatwaves and droughts in CHIMERE remain very similar with the "$\gamma_{SWSfit}$-emiss" experiment compared to the "Reference" one (decrease of -2% and -1% respectively). The temporal correlation does not vary significantly either (e.g. R coefficient around 0.5 for the Balkans).

Table 6.3: Variation of HCHO total atmospheric column [$molecules/cm^2$] ($\Delta$HCHO) due to heatwaves, droughts and isolated droughts in comparison to normal conditions (no heatwaves nor droughts) for summers (JJA) between 2005-2016 (measurements at 1pm). Summer 2012 is compared with CHIMERE simulations. Results are computed for each pixels and averaged over areas of interests: the Balkans, Central Italy and Central Spain. Stars mean that the difference with normal conditions is statistically significant (t-test, $p < 0.1$).

| | OMI (2005-16) | OMI (2012) | CHIMERE (2012) | |
|---|---|---|---|---|
| | | | Reference | $\gamma_{SWSfit}$-emiss |
| Balkans (norm. cdt.) | 5.74e15 $mol./cm^2$ | 4.02e15 $mol./cm^2$ | 7.64e15 $mol./cm^2$ | 7.62e15 $mol./cm^2$ |
| $\Delta$ with heatwaves | + 16.9 %* | + 64.1 %* | + 93.7 %* | + 92.2 %* |
| $\Delta$ with droughts | + 6.0 %* | + 54.3 %* | + 63.1 %* | + 61.9 %* |
| $\Delta$ with isolated droughts | - 6.9 %* | + 31.6 %* | + 10.0 %* | + 9.4 %* |
| Pô Valley (norm. cdt.) | 5.86e15 $mol./cm^2$ | 5.33e15 $mol./cm^2$ | 7.59e15 $mol./cm^2$ | 7.52e15 $mol./cm^2$ |
| $\Delta$ with heatwaves | + 16.0 %* | + 16.8 %* | + 35.6 %* | + 33.9 %* |
| $\Delta$ with droughts | + 2.3 %* | + 11.3 %* | + 23.9 %* | + 22.7 %* |
| $\Delta$ with isolated droughts | - 6.0 %* | - 0.9 % | - 2.6 %* | - 2.8 %* |
| Central Spain (norm. cdt.) | 5.22e15 $mol./cm^2$ | 4.83e15 $mol./cm^2$ | 6.13e15 $mol./cm^2$ | 5.76e15 $mol./cm^2$ |
| $\Delta$ with heatwaves | + 12.2 %* | + 2.2 % | + 28.2 %* | + 24.9 %* |
| $\Delta$ with droughts | + 0.4 % | - 6.7 %* | + 8.9 %* | + 7.8 %* |
| $\Delta$ with isolated droughts | - 6.1 %* | - 10.8 %* | - 2.7 %* | - 3.0 %* |

### $O_3$ stomatal conductance

Surface weather conditions are critical for the stomatal conductance and therefore influence the dry deposition velocity. Figure 6.10 shows the maximum daily stomatal conductance of $O_3$ ("LAIdecr/$f_{SWS}$-dep" CHIMERE experiment) clustered by simulated extreme weather events and averaged over the Western Mediterranean. The same analysis has been performed on the dry deposition velocity and signals induced by extreme weather events are similar.

Droughts and heatwaves (isolated or combined) induce a significant decrease of the $O_3$ stomatal conductance, quantified at -25% for heatwaves and -35% for droughts compared to normal conditions. The activity factors mainly affected by droughts and heatwaves are $f_{temp}$, $f_{VPD}$ and $f_{SWS}$.

The variation of $f_{temp}$ depends on the magnitude of heatwaves and so their location. Over the Pô Valley and Balkans for instance, most heatwaves are characterized by temperatures close to the optimal values of stomatal conductance that is fixed around 24°C (Appendix B:

Fig. B.17). However, for those occurring in Central Spain (between 30° and 32°C), $f_{temp}$ decreases by 7% compared to normal conditions. The temperature limit before complete stomatal closure is set at 40°C. Therefore exceptional heatwaves occurring in Southern Spain for instance could lead quickly to an accumulation of $O_3$ at the surface. $f_{VPD}$ that depends both on temperature and relative humidity significantly decreases during droughts and heatwaves (e.g. -6% averaged over the Southwestern Europe and -6% over the Pô Valley). Finally, $f_{SWS}$ is the factor dominating the signal of variation of the stomatal conductance. At the Southwestern Europe scale, this factor is the lower during isolated droughts with a mean decrease of -35%.

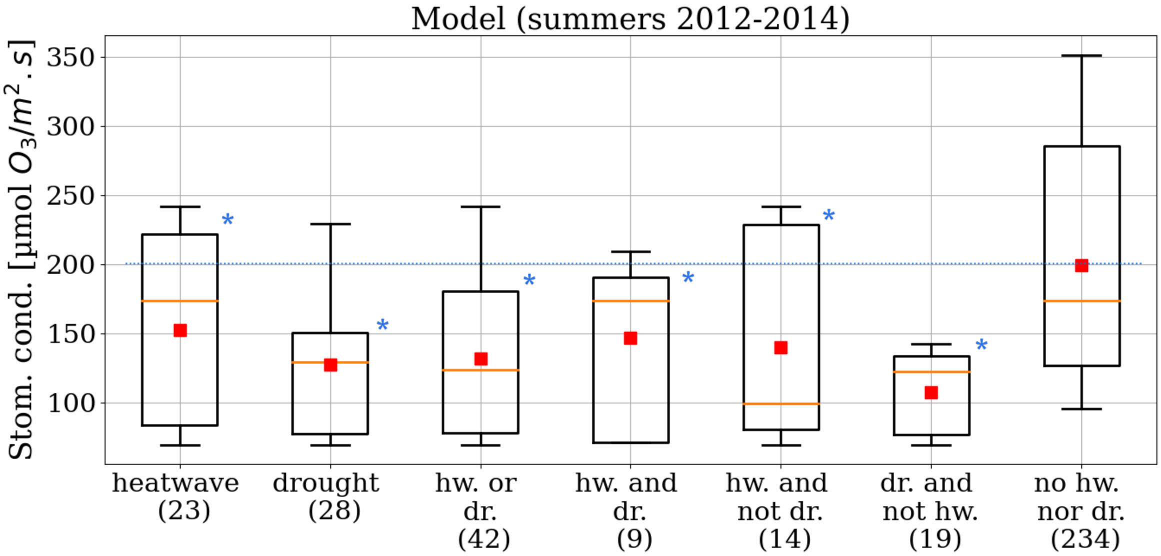

Figure 6.10: Same as Figure 6.9 with the simulated $O_3$ stomatal conductance [$\mu mol O_3.m^{-2}.s^{-1}$] by the CHIMERE model ("LAIdecr/$f_{SWS}$-dep" experiment).

### $O_3$ surface concentration

Figure 6.11 shows the distribution of the observed (2000-2016 and 2012-2014) and simulated (2012-2014) daily maximum surface $O_3$ concentrations over Southwestern Europe for each cluster of extreme events. Observed $O_3$ (upper panel) is significantly (t-test, $p < 0.01$) higher during heatwaves ($+18 \mu g/m^3$) and droughts ($+9 \mu g/m^3$) than during normal conditions. Considering all droughts over the United States of America, Wang et al. (2017) also computed a mean increase in surface $O_3$ (+17% compared to the average). During isolated droughts, daily maximum $O_3$ ($+4 \mu g/m^3$) is larger but the difference is non-significant.

The distribution of the simulated surface $O_3$ ("all-emiss-dep" experiment) by extreme events over the period 2012-2014 (lower panel) presents similar signals but of lower magnitude: $+9 \mu g/m^3$ during heatwaves, $+3 \mu g/m^3$ during droughts and non-significant difference during isolated droughts compared to normal conditions. Based on the results discussed above, the difference between the "heatwave" and "isolated drought" cluster could be explained by the different conditions of biogenic emissions, dry deposition, temperature and light. However, observations over the same period (middle panel) present a significant increase of the daily maximum $O_3$ during isolated droughts ($+9 \mu g/m^3$), unlike what we simulated. The $C_5H_8$ emission reduction effect during such extreme event could be counterbalanced in a larger extent by the $O_3$ dry deposition decrease. It could also be explained by an underestimated impact of the enhanced photochemistry in the simulations, as we simulated favourable weather conditions during both combined and isolated droughts.

In summary, the variation of canopy-troposphere interactions (biogenic emissions and dry deposition) simulated by the MEGAN and CHIMERE models during droughts and heatwaves presents a consistent signal with respect to ozone observations (except for the isolated droughts over summers 2012-2014). Meteorological conditions being critical for the $O_3$ budget especially during droughts and heatwaves, differences between observations and simulations may rely on uncertainties related to the weather, such as the diurnal cycle of temperature (see Sect. 6.3.3) or the planetary boundary layer height.

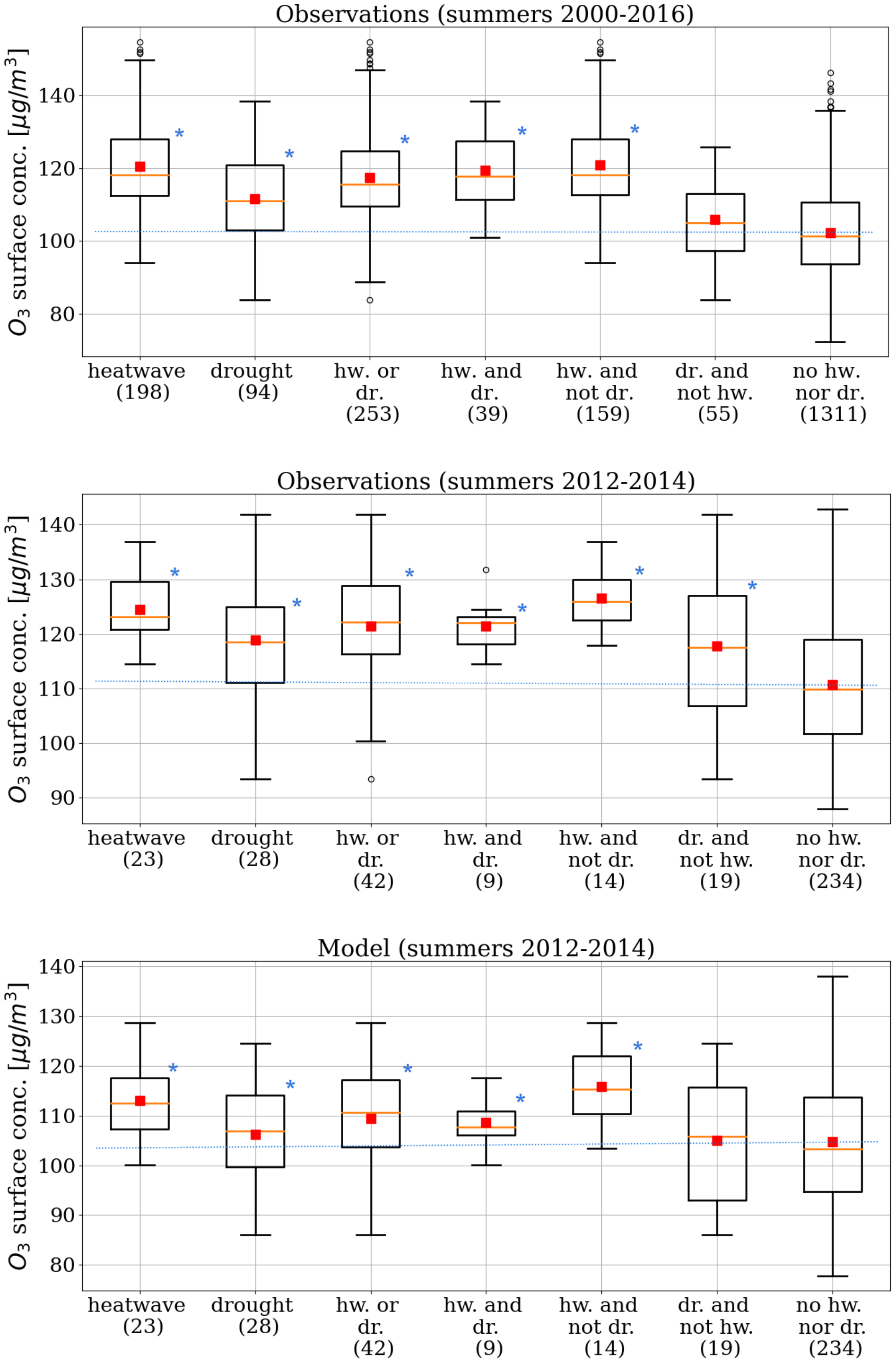
Observations (summers 2000-2016)

Observations (summers 2012-2014)

Model (summers 2012-2014)

Figure 6.11: Same as Figure 6.9 with the observed surface $O_3$ concentration $[\mu g/m^3]$ over the summers 2000-2016 (upper panel) and 2012-2014 (middle panel), and with the simulated surface $O_3$ ("all-emiss-dep" experiment) over the summers 2012-2014 (lower panel).

### 6.4.3 Threshold level exceedance of $O_3$

In the European Union, the air quality standard for $O_3$ exposure is set at a daily maximum concentration of 120 $\mu g/m^3$ (8h-average) (EEA, 2020). Figure 6.12 shows the number of days above this threshold based on the AQ e-Reporting observations and the CHIMERE "all-emiss-dep" simulations for summers 2012, 2013 and 2014. Summers 2012 and 2013 present a large number of days exceeding the standard concentration. Even if exceedances occur in similar regions for observations and simulations, the number of days is generally larger in the observations. This is due to the overall underestimated daily maximum in CHIMERE compared to observations (see Sect. 6.3.3). For instance, in the Pô Valley, the most affected region in Southwestern Europe, around 60 exceeding days were observed and 50 were simulated over summer 2012 (significantly more than half of the summer). This region is known for its highly polluted air ($O_3$ and other pollutants) due to high anthropogenic emissions and unfavourable topographic and meteorological conditions for pollutants dispersion (e.g. Bigi et al., 2012). Other regions affected by $O_3$ peaks can be highlighted: Southeastern France, central Spain and central Italy for both summers 2012 and 2013.

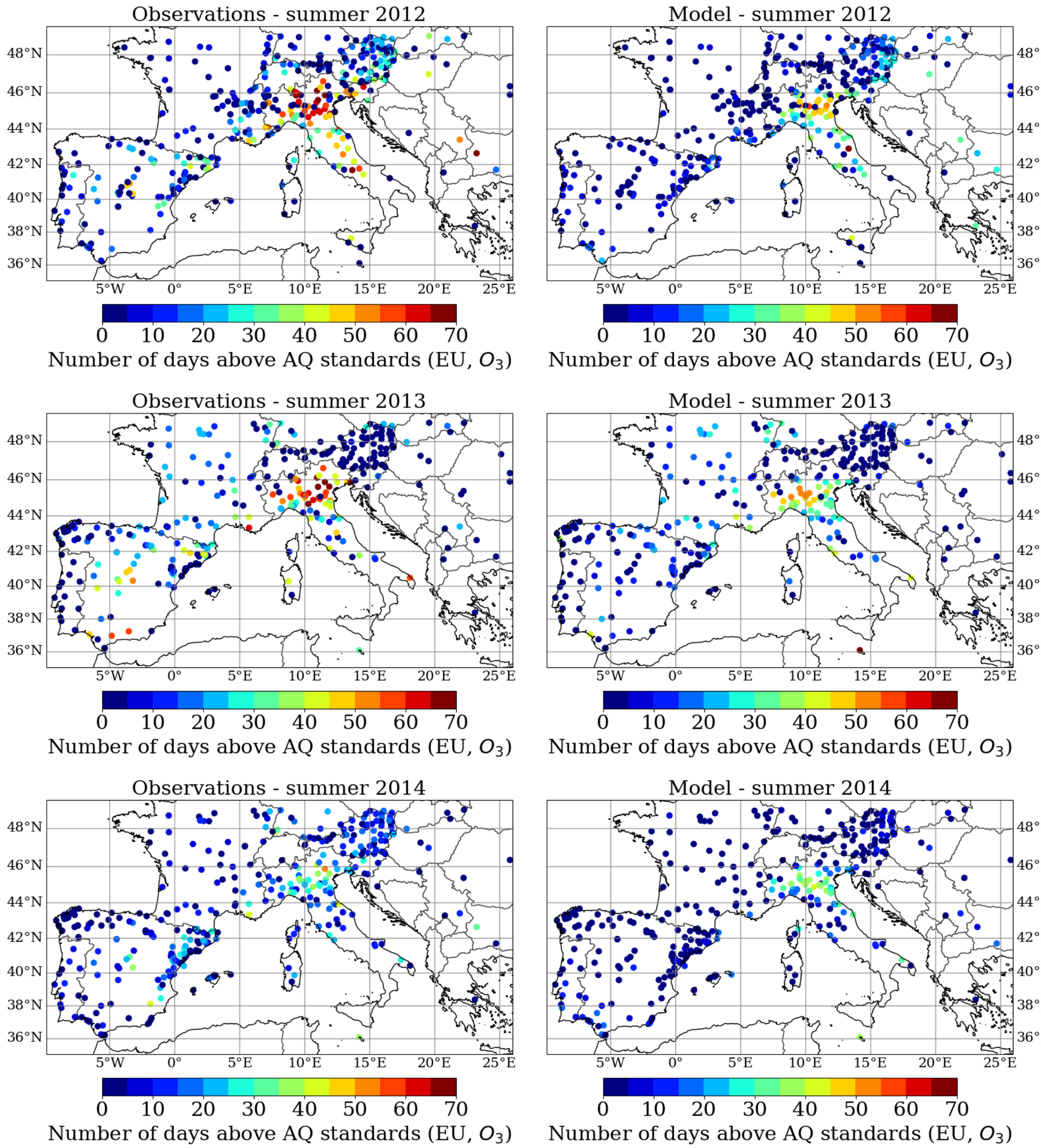

Figure 6.12: Number of days above the air quality threshold value from the European Union for surface $O_3$ (maximum daily 8 hour mean of 120 $\mu g/m^3$) over the summer 2012, 2013 and 2014 (JJA, 92 days in total). EEA observations (left column) are compared to CHIMERE ("all-emiss-dep") simulations (righ column).

Table 6.4 presents the distribution characteristics of stations with at least one day above the EU standard during summer period. On average over 2000-2016, this concerns 54% of

EEA stations over the Western Mediterranean. The average number of exceedance days per station is 27 (almost a third of the summer period). Summer 2012 is above the 2000-2016 average, with 61% of stations affected and 28 days on average per station. For the same year, co-located values from CHIMERE simulations ("all-emiss-dep" experiment) are lower: 57% of stations and 18 days on average.
Over all summers between 2000 and 2016, 34% of the exceeding days occurred during heatwaves (with a mean exceeding value of $24\mu g/m^3$) and 27% during droughts ($+18\mu g/m^3$). The number of days decreases by 13% if we consider only the isolated droughts (14%, $+15\mu g/m^3$). Summer 2012 was affected by exceptional droughts and heatwaves, resulting in high $O_3$ pollution. Around 80% of days above the EU threshold occurred during heatwaves or droughts for both observations and simulations.

Table 6.4: Average percentage of stations with at least one exceedance day (first row) regarding EU standard during summer (JJA). Considering only those stations, the second row shows the average number of exceeding days per station and the lower rows the average distribution of days above the EU standard in function of extreme weather events. The mean exceedance concentration is indicated in parenthesis.

| | EEA (2000-2016) | EEA (2012) | CHIMERE (2012) |
|---|---|---|---|
| Average fraction of stations (over all): | 54% | 61% | 57% |
| Average number of exc. days / station: | 27 days | 28 days | 18 days |
| | | | |
| Average distribution of exc. days: | | | |
| Normal conditions | 52% ($+17\mu g/m^3$) | 20% ($+15\mu g/m^3$) | 21% ($+15\mu g/m^3$) |
| Heatwaves or droughts | 48% ($+22\mu g/m^3$) | 80% ($+18\mu g/m^3$) | 79% ($+17\mu g/m^3$) |
| Heatwaves | 34% ($+24\mu g/m^3$) | 58% ($+20\mu g/m^3$) | 65% ($+18\mu g/m^3$) |
| Isolated heatwaves | 21% ($+24\mu g/m^3$) | 16% ($+21\mu g/m^3$) | 18% ($+16\mu g/m^3$) |
| Droughts | 27% ($+18\mu g/m^3$) | 64% ($+18\mu g/m^3$) | 61% ($+17\mu g/m^3$) |
| Isolated droughts | 14% ($+15\mu g/m^3$) | 22% ($+14\mu g/m^3$) | 14% ($+15\mu g/m^3$) |

## 6.5 Conclusions

The overall aim of this study was to quantify the variation of surface $O_3$ over the Southwestern Europe during agricultural droughts, combined or not with heatwaves. Therefore, we analyzed both $BVOCs$ emissions and $O_3$ dry deposition velocity during these extreme events, based on the available observations and regional CTM simulations (CHIMERE model).
Agricultural droughts and heatwaves were identified based on the coupled WRF-ORCHIDEE regional model (RegIPSL) using the percentile limit anomalies (PLA) on 2m temperature and soil moisture. During the period 2000-2016, 59% of summer drought days were not accompanied by heatwaves (isolated droughts). For the summers 2012-2014, analyzed more specifically in this study, the 2m temperature is on average 5.5% lower during isolated droughts compared to all droughts, the shortwave radiation is 13.5% lower and the cloud fraction is 42% higher. As a result, the variations of $BVOC$ emissions, $O_3$ dry deposition velocity but also surface $O_3$ are substantially different if the drought considered is accompanied by a heatwave.
Based on a cluster approach using the PLA indicator, heatwaves show the highest increase of $C_5H_8$ emission rate, +33% on average compared to normal conditions. On the opposite, isolated droughts present a decrease of -16% (non-significant difference) when a soil moisture parameter is included. Those simulated variations are in agreement with the $HCHO$ observations from the OMI instrument that were used as a quantitative proxy of $BVOC$ emissions, despite important discrepancies between them regarding the absolute values. In addition to the soil moisture factor suggested by the MEGAN model which is mainly based on the wilting point ($\gamma_{SM}$), we propose an innovative activity factor based on a soil water stress function ($\gamma_{SWS}$) simulated by a land surface and vegetation model (ORCHIDEE). The latter induces a larger reduction of $C_5H_8$ emissions, but with more homogeneous patterns that follow the drought indicator. Therefore, we adjusted this factor with a function fitted from experimental measurements ($\gamma_{SWSfit}$). By comparing the simulated surface concentration of $C_5H_8$ with observations at a measurement site, this approach shows promising results.
We simulated a mean significant decrease of $O_3$ dry deposition of about 25% during both droughts and heatwaves. The stomatal conductance, as lower level of resistance for dry deposition of gases, mainly decreases due to the the leaf-to-air vapour pressure deficit factor ($f_{VPD}$), temperature factor ($f_t$), soil wetness factor ($f_{SW}$) but also the biomass variation (LAI).
The overall increase of $C_5H_8$ emissions and decrease of $O_3$ dry deposition during droughts and heatwaves lead to an accumulation of $O_3$. This has been confirmed by the EEA observations analyzed over 14 summers (2000-2016). On average, surface $O_3$ is larger by $+18\mu g/m^3$ in daily maximum during heatwaves and by $+9\mu g/m^3$ during droughts, compared to normal conditions. Isolated droughts being characterized by reduced $O_3$ precursor emissions and re-

duced $O_3$ dry deposition, those effects could compensate each other with a slight dominance of the latter one, leading to a slight but non-significant increase of observed $O_3$ concentration ($+4\mu g/m^3$). Furthermore, we simulated favourable weather conditions for photochemistry (warm and sunny) during isolated droughts.

Finally, almost half of summer days (2000-2016 period) exceeding the EU standard of $O_3$ for air quality in Southwestern Europe occurred during droughts or heatwaves. However, this percentage can increase (up to 80%) for exceptionally dry and hot summers, like in 2012. Only 14% of the exceedance days occurred during isolated droughts.

The implementation of dynamical effects of droughts in the MEGAN - CHIMERE model contributes to a better representation of biosphere-atmosphere interactions. However, comparisons between simulated and observed surface $O_3$ still show large discrepancies. Important uncertainties appear to be related to $BVOC$ emissions, especially about the land cover classification, to $NO_x$ concentrations for which CHIMERE presents limited performance scores of validation, and finally to meteorological conditions (e.g. temperature and PBL height). Such uncertainties need to be addressed to improve the simulation of $O_3$ during the summer, and especially over the Southwestern Europe.

In conclusion, we provide in this paper a detailed analysis of the drought and heatwave effects on biosphere-troposphere interactions controlling surface $O_3$ concentration. Heatwaves, and droughts in a lower extent, induce a significant increase of the surface $O_3$. Soil dryness and biomass decrease, as specific effects of droughts, are key factors for the variations of $C_5H_8$ emissions and $O_3$ dry deposition over the Southwestern Europe. We emphasize the need for a more dynamical representation of interactions between vegetation, hydrology, meteorology and atmospheric chemistry in models in order to improve the simulation of summer $O_3$.

## 6.6 General conclusion

The draft of the article ends here. Including droughts and heatwaves identified in Chapter 4 as well as the impact study conducted in Chapter 5, this last chapter of results reaches the final topic of this thesis, answering to the following question: "How do surface $O_3$ concentrations, and more specifically $O_3$ peaks, vary due to vegetation under abiotic stresses ?".
Combining multi-annual observations ($HCHO$ column and surface $O_3$) with CTM simulations, I have shown that droughts and heatwaves as a whole can significantly increase surface $O_3$ concentration, until exceeding threshold values. However, there is still no consensus in the scientific community on the specific effects of agricultural droughts, since the soil water content is a variable difficult to assess accurately and large uncertainties remain on how plants react to soil dryness. Nevertheless, the set of simulation experiments presented in this chapter highlights the soil dryness as a critical factor (to a larger extent than biomass decrease) for the computation of BVOC emissions and $O_3$ dry deposition. Agricultural drought effects on surface $O_3$ appear to be the most important during simultaneous droughts and heatwaves.

# Chapter 7

# Conclusions and perspectives

**Contents**

## 7.1 Conclusions

The objective of this thesis was to analyze the interactions between land surface and the troposphere during droughts and heatwaves and more specifically, to assess the impact of such extreme weather events on the biomass, fire activity and ground-level ozone pollution in the Western Mediterranean. This work was mainly based on 3D modeling at regional scale, supported by different data sets of observations (both satellite and in-situ).

The main conclusions are provided for the three research questions introduced in Section 1.5. Figure 7.1 sums up the different effects studied throughout this thesis. Each effect is represented as an arrow and will be summarized in the following.

### Suitable methods for the identification of heatwaves, meteorological and agricultural droughts

Different methods were applied using the land surface-atmosphere coupled model RegIPSL to identify extreme events in the Euro-Mediterranean region over the time period 1979-2016: the SPEI for meteorological droughts and the percentile limit anomalies on the 2m temperature ($PLA_{T2m}$) for heatwaves and on the soil dryness ($PLA_{SD}$) for agricultural droughts (see Chap. 4). Their spatio-temporal distribution was described, highlighting the most frequently and intensely affected areas (e.g. Western France, Western Iberian Peninsula, Northern Italy and the Pannonian Plain).

In spite of a general good agreement between SPEI and $PLA_{SD}$, some discrepancies were found over (semi-)arid regions (e.g. Southern Spain) due to the limits of the SPEI to assess accurately inter-annual variability of soil moisture (almost permanently low) in such areas. Nevertheless, this discussion could be complemented with soil moisture observations at both surface and root zone soil layers using in-situ measurements and satellite products like, for instance, the NASA's Soil Moisture Active Passive mission (Colliander et al., 2021).

Another major feature highlighted in this work concerns the interactions and co-variability of droughts and heatwaves in the Mediterranean. This was made possible by the coupled RegIPSL model allowing the development of the soil moisture-temperature feedback (Stéfanon et al., 2014). We computed a +19% increase of heatwave intensity during agricultural droughts (Fig. 7.1).

Most studies in the literature focus on either heatwaves or droughts, with low representation of agricultural droughts. This work allowed to provide a three dimensional database of agricultural droughts and heatwaves covering the Euro-Mediterranean region at daily time step and 20km resolution. This product (freely available here `https://thredds-x.ipsl.fr/thredds/catalog/HyMeX/medcordex/data/Droughts_Heatwaves_1979_2016/catalog.html`) was used in this thesis to better assess processes involved in wildfire activity, vegetation growth and ground-level ozone concentration. However, this product may be relevant for different applications like in forestry or agroecology, especially since water scarcity is projected to become even more problematic in line with climate change (Cos et al., 2021).

### Detailed impact analysis on wildfire activity and biomass

The impact on fire characteristics and biomass (see Chap. 5) was analyzed by combining simulated droughts and heatwaves with satellite observations of wildfires and vegetation from the MODIS instruement.

Due to water stress, plants decrease their photosynthetic activity resulting in biomass decrease (-10% LAI on average compared to a normal summer). Extreme hot temperatures, like during summer 2003 in Central Europe, can affect the metabolism of plants leading to biomass decrease as well (-4% LAI on average). On the opposite, spring and summer heatwaves of lower intensity appear to be associated with positive anomalies, especially in the Northern Mediterranean.

The analysis was complemented with the simulated LAI from RegIPSL providing two major findings. Firstly, the spatial variability of biomass variation can be explained by the response to water stress as a function of vegetation type (in addition to the relief). Secondly, the biomass reduction can be overestimated in some DGVMs like ORCHIDEE due to a lack of integrated human factors (e.g. irrigated areas). The inclusion of human activities which is ongoing in ORCHIDEE, is recommended for future studies about agricultural droughts.

Hot, dry and windy weather conditions are favourable to wildfires. Their effects can be cumulative. The enhancement of the wildfire activity during simultaneous droughts and heatwaves is quantified by a burned area and a fire intensity 2.1 and 2.9 times larger, respectively (compared to wildfires during normal conditions) (Fig. 7.1). Furthermore, the $PLA_{SD,T}$ indicator has shown good predictive capability for intense fires, unlike the Fire Weather Index (FWI). The poor correlation of the FWI with the burned area has already been highlighted (e.g. Dimitrakopoulos et al., 2011; Chelli et al., 2015).

Performing a correlation analysis with the CDI, this thesis contributes to the scientific discussion about the key role of droughts in the dynamics of fires, regarding the "fuel dryness" and "fuel availability" effect (e.g. Turco et al., 2017; Gannon and Steinberg, 2021). According to our results, the inter-annual variation in fire activity over the Western Mediterranean is mainly driven by weather conditions rather than fuel load.

### Integrated analysis of drought and heatwave effects on canopy-troposphere exchanges influencing surface ozone

Finally, this thesis ends with a detailed analysis of the drought and heatwave effects on the biosphere-troposphere interactions controlling surface $O_3$ variation and its pollution peaks (see Chap. 6).

Combining the PLA indicator and surface $O_3$ observations (AQ e-Reporting), almost half of summer days exceeding the EU standard of $O_3$ for air quality in Southwestern Europe occurred during droughts or heatwaves, on average for the time period 2000-2016. However, this percentage can increase (up to 80%) for exceptionally dry and hot summers, like in 2012. Only 14% of the exceedance days occurred during isolated droughts (summers 2000-2016). These findings confirm that special attention must be paid by public health agencies to these events, especially heatwaves, in order to propose appropriate air quality mitigation and adaptation strategies.

A series of sensitivity analysis with integration of new dynamical variables (soil dryness and biomass) in MEGAN-CHIMERE allowed to quantify the effect of droughts and heatwaves on $C_5H_8$ emissions, $O_3$ dry deposition and $O_3$ concentration. Considering all types of heatwaves and droughts, the overall effect is a ground-level $O_3$ increase (e.g. +7% and +3% respectively in daily mean), due to an $O_3$ precursor emissions enhancement and $O_3$ dry deposition decrease (Fig. 7.1). Although the specific effects of biomass decrease and soil dryness are critical for $BVOC$ emissions and $O_3$ dry deposition, their isolated effects on surface $O_3$ remain low in Southwestern Europe.

Summer $O_3$ peaks in the Mediterranean remain difficult to simulate. In addition to the meteorological effects, accurate simulation of $VOCs$ and $NO_X$ is crucial. For $VOC$ concentrations, the role of biogenic emissions and its high uncertainties are established. The comparison between simulated and observed surface $NO_2$ also showed very high uncertainties which are at least partly related to the emission database used. Finally, important uncertainties are linked to the different land cover classes and phenological parameters of vegetation used in the $BVOC$ emissions in MEGAN model and the scheme of gas dry deposition in CHIMERE. In spite of the large uncertainties characterizing both observations and models, this thesis contributes to the current development in the scientific community aiming at integrating dynamical interactions between biosphere, meteorology and atmospheric chemistry.

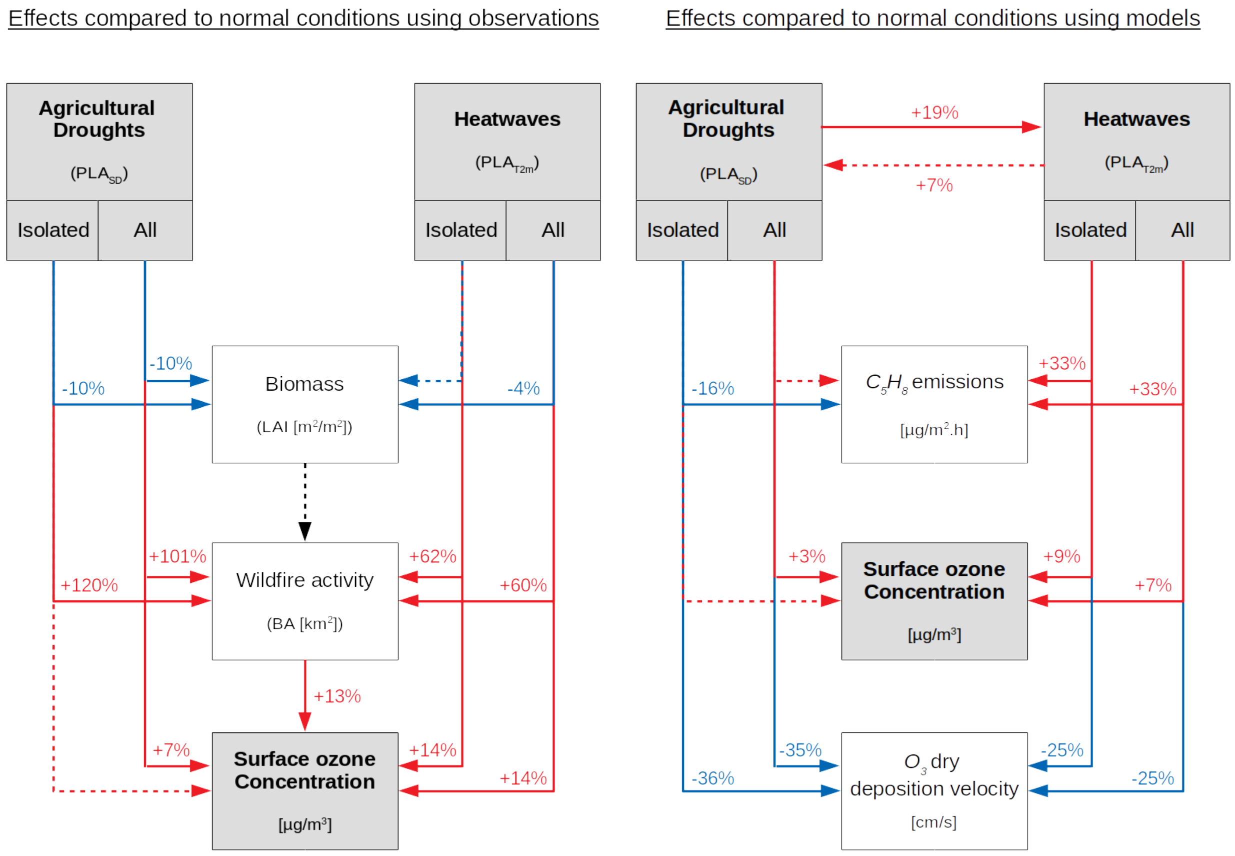

Figure 7.1: Summary of the mean effects quantified during this thesis between agricultural droughts, heatwaves and surface ozone based on observations (left panel) and regional models (right panel). Blue (red) arrows indicate an increasing (decreasing) effect. The black arrow means that no dominant signal was detected from the analyses. The estimated percentage is an average based on the cluster method of extreme weather events ($PLA$ indicator). Dashed arrows indicate that the difference between droughts/heatwaves and the normal conditions (neither drought nor heatwave) is statistically non-significant. The estimated effects from regional modeling (right panel) come from the MEGAN-CHIMERE simulations integrating heatwave and droughts effects for both biogenic emissions and gas dry deposition ("all-emiss-dep" experiment, see Chap. 6) over the summers 2012, 2013 and 2014.

## 7.2 Perspectives

The study of interactions between the biosphere and the atmosphere is a very active field and many processes need to be better understood and quantified, like for the calculation of natural emissions, the dry deposition schemes or the interactions between gas phase and particulate phase. In this section, I chose to focus on three main questions resulting from either limitations encountered during this thesis or prioritization choice.

### $O_3$ pollution induced by biomass burning emissions

The performed analysis showed that wildfire activity is significantly larger during droughts and heatwaves (see Chap. 5). Large amount of $O_3$ precursors emitted during biomass burning can contribute to $O_3$ pollution peaks (e.g. Hodnebrog et al., 2012).

Wildfire emissions are computed over the summer period 2012-2014 using the APIFLAME model. On daily average, $CO$ emissions are 13 times larger for fires occuring during combined heatwave and drought days (compared to normal days). Based on the performed simulations in this thesis, Figure 7.2 shows timeseries of observed (AQ e-Reporting) and simulated (CHIMERE) surface $O_3$ over Northern Portugal during the intense wildfire episodes of summer 2013 (enhanced by heatwaves), including simulations without biogenic and fire emissions respectively. Even if the simulated contribution of fire emissions to $O_3$ formation occurs generally for short periods of time (several days), it can exceed the contribution of biogenic emissions by reaching for instance 40% of almost $200\mu g/m^3$ in daily maximum (contribution map available in Appendix B: Fig. B.22). Moreover, measurements of $O_3$ from EEA stations colocated with observed fires (in ~20×20 km grid cells) present daily mean concentration 13% higher (+ $9\mu g/m^3$) than in absence of fires (Fig. 7.1). These days are, of course, combined with other factors favouring ozone pollution (e.g. high temperature).

It would be therefore interesting to pursue this work by simulating with CHIMERE multiple case studies to answer the following research question: how do intensified wildfires by droughts and heatwaves modify $O_3$ concentration? However, the use of EEA stations as main observations involves a strong dependency on the network distribution and the data availability. I would recommend to focus on the largest events and compare simulations with some satellite products.

Furthermore, the alteration of post-fire vegetation would represent another interesting topic to explore. Based on the same research material used in this thesis (observed LAI and fire characteristics, MEGAN model), the vegetation recovery and biogenic emissions evolution at short- and long-term could be studied, including fire-vegetation feedbacks (e.g. Tepley et al., 2018).

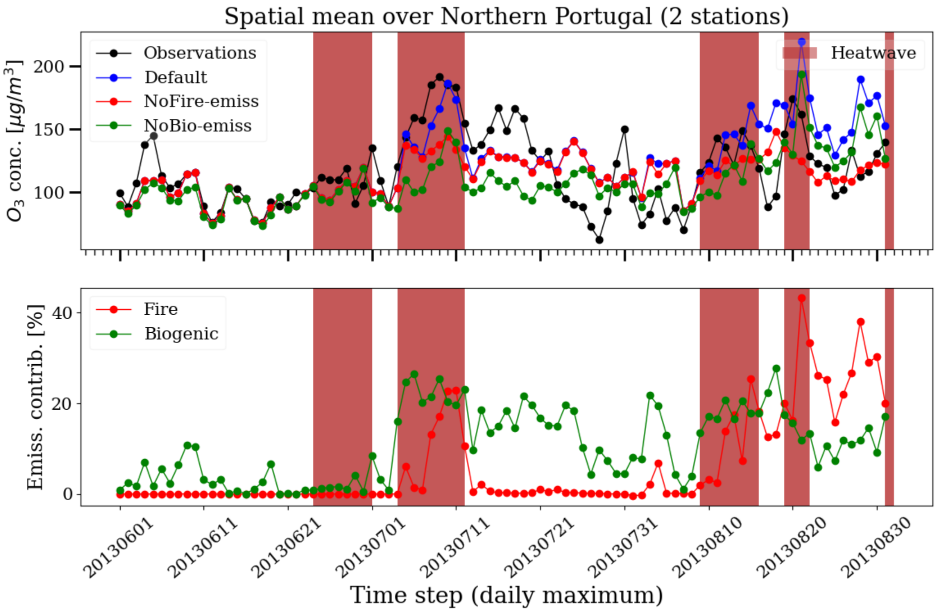

Figure 7.2: Daily maximum $O_3$ concentration [$\mu g/m^3$] during summer 2012, spatially averaged over the Northern Portugal (-10°E:-7°E, 41°N:42°N) for EEA observations and different CHIMERE simulations, including the absence of fire and biogenic emissions ("NoFire-emiss" and "NoBio-emiss" respectively). The red bands indicate heatwave events.

### Sensitivity of particulate matter concentration to droughts and heatwaves

Another interesting perspective to explore based on this work concerns the $PM$ pollution variations during droughts and heatwaves. Both fire and biogenic emissions are composed of primary aerosols that also contribute to the formation of secondary aerosols, increasing therefore $PM$ concentration in the atmosphere (e.g. Couvidat et al., 2018; Majdi et al., 2019). Performing the same cluster analysis as in Chapter 6, measured $PM_{10}$ concentrations (AQ e-Reporting, summers 2000-2016) are on average significantly larger by 24% ($+8\mu g/m^3$ in daily mean and $+14\mu g/m^3$ in daily maximum) for both heatwaves and droughts (Fig. 7.3). Wang et al. (2017) find an averaged increase of 17% for surface $PM_{2.5}$ concentration during droughts over the United States, highlighting the increasing wildfire, biogenic and dust emissions as well as the absence of wet deposition as dominant processes.

However, we have demonstrated in this thesis that intense isolated droughts can lead to a reduction of $C_5H_8$ emissions (acting as precursor of SOA) compared to normal days. For instance, the MEGAN-CHIMERE "$\gamma_{SWS}$-emiss" simulation induces an averaged 5% decrease of surface $PM_{10}$ concentration over the summer 2012 (map of relative difference in Appendix B: Fig. B.23). It would be interesting to further investigate the sensitivity of $PM$ concentration

to biogenic and fire emissions during droughts and heatwaves. A scientific article about this topic that will be submitted to a peer-reviewed journal, is in preparation (Appendix C).
In addition to those processes, heatwaves and droughts could lead to dust uplift. Intense droughts in semi-arid regions can induce biomass loss through high plant mortality, tending towards bare soil and contributing to land degradation (e.g. Nicholson et al., 1998; Vicente-Serrano et al., 2015). Through soil erosion, dust uplift can occur. The use of soil moisture (from WRF-Noah) for mineral dust emissions is integrated in CHIMERE (Menut et al., 2021) following the Fécan et al. (1999) parametrization. This consists of a variation of the threshold friction velocity used to determine if erosion occurs or not.
However, there are still large uncertainties about the involved physical mechanisms in dust emissions, highlighting a need of experimental campaigns. Furthermore, the observations of $PM$ concentration induced by dust emissions in the Mediterranean can be complicated due to frequent Saharan dust transport (e.g. Paz et al., 2013).

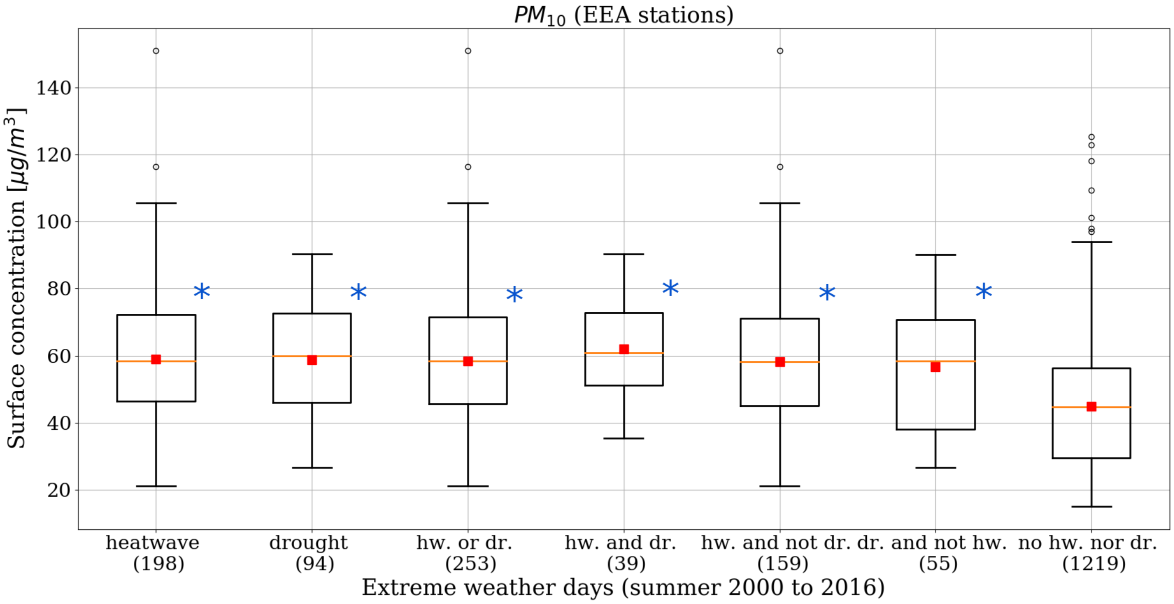

Figure 7.3: Daily maximum observed $PM_{10}$ concentration [$\mu g/m^3$] over Southwestern Europe, clustered by identified extreme weather events (based on $PLA_{T2m}$ and $PLA_{SD}$ indicators from RegIPSL). The number of extreme days is shown in parentheses. The analyzed period covers the summers between 2000 and 2016, with a total of 1472 available days.

### Towards the integration of atmospheric chemistry, weather and canopy interactions in coupled models

Finally, a complete coupling between a land surface vegetation (e.g. ORCHIDEE), meteorological (e.g. WRF) and chemistry transport model (e.g. CHIMERE) representing interactions between atmospheric chemistry, land surface hydrology and vegetation activity would allow a better representation of drought and heatwave effects. Long-term effects on biochemical cycles triggered by extreme weather events could be simulated to study some feedbacks currently discussed in the scientific literature like, for instance, the ozone-vegetation feedback (e.g. Anav et al., 2011; Zhou et al., 2018; Gong et al., 2020). The $O_3$ accumulation at surface level due to stomatal uptake decrease during droughts and heatwaves (as shown in Chap. 6) is able to damage plant due to its oxidizing power and so reduce the active leaf area for dry deposition, resulting in a net $O_3$ increase. In addition, impact of aerosol deposition on land ecosystems could be studied (e.g. Mahowald et al., 2017).

In such coupling perspective and on the basis of the results found in this thesis, I would point out two aspects to solve in priority. Firstly, it concerns an accurate discretization of the land cover classes, and more specifically an adapted parameterization of the PFTs to the concerned biome. Secondly, it is about the homogenization of land cover and vegetation data sets for both biogenic emissions and dry deposition. It would allow to improve dynamic interactions, but especially to avoid phenological shift between two types of surface-troposphere exchanges that occur through the same component, the vegetation.

On a longer term, the development at IPSL of a fully coupled regional plateform (RegIPSL) including a CTM will allow more consistent analysis.

# Bibliography

Abd-Elmabod, S. K., Muñoz-Rojas, M., Jordán, A., Anaya-Romero, M., Phillips, J. D., Jones, L., Zhang, Z., Pereira, P., Fleskens, L., van der Ploeg, M., and de la Rosa, D. Climate change impacts on agricultural suitability and yield reduction in a Mediterranean region. *Geoderma*, 374:114453, September 2020. ISSN 00167061. doi: 10.1016/j.geoderma.2020.114453. URL https://linkinghub.elsevier.com/retrieve/pii/S0016706119318026.

Abramowitz, M., Stegun, I. A., and Romer, R. *Handbook of mathematical functions with formulas, graphs, and mathematical tables*, volume 55. United states of america government printing office edition, 1965.

Alfaro, S. C. and Gomes, L. Modeling mineral aerosol production by wind erosion: Emission intensities and aerosol size distributions in source areas. *Journal of Geophysical Research: Atmospheres*, 106(D16):18075–18084, August 2001. ISSN 01480227. doi: 10.1029/2000JD900339. URL http://doi.wiley.com/10.1029/2000JD900339.

Amante, C. and Eakins, B. ETOPO1 arc-minute global relief model: procedures, data sources and analysis. Technical report NESDIS NGDC-24, NOAA, Boulder, Colorado, 2009.

Anand, J. S., Anav, A., Vitale, M., Peano, D., Unger, N., Yue, X., Parker, R. J., and Boesch, H. Ozone-induced gross primary productivity reductions over European forests inferred from satellite observations. preprint, Biogeochemistry: Land, May 2021. URL https://bg.copernicus.org/preprints/bg-2021-125/.

Anastasiou, E., Doignon, Y., Karkanis, D., Léger, J. F., Parant, A., and Sahraoui, S. E. Tendances et perspectives démographiques en Méditerranée. *Plan Bleu, UN Environment/MAP Regional Activity Centre*, Cahier 21:130, 2021. URL https://planbleu.org/wp-content/uploads/2020/10/PLAN-BLEU-CAHIER-21-Tendances-demographiques-en-Mediterranee.pdf.

Anav, A., Menut, L., Khvorostyanov, D., and Viovy, N. Impact of tropospheric ozone on the Euro-Mediterranean vegetation. *Global Change Biology*, 17(7):2342–2359, July 2011. ISSN

13541013. doi: 10.1111/j.1365-2486.2010.02387.x. URL https://onlinelibrary.wiley.com/doi/10.1111/j.1365-2486.2010.02387.x.

Atkinson, R. Atmospheric chemistry of VOCs and NOx. *Atmospheric Environment*, page 39, 2000.

Bastin, S., Chiriaco, M., and Drobinski, P. Control of radiation and evaporation on temperature variability in a WRF regional climate simulation: comparison with colocated long term ground based observations near Paris. *Climate dynamics*, 51(3):985–1003, 2018. URL https://doi.org/10.1007/s00382-016-2974-1. Publisher: Springer.

Baumbach, L., Siegmund, J. F., Mittermeier, M., and Donner, R. V. Impacts of temperature extremes on European vegetation during the growing season. *Journal of Geophysical Research: Biogeosciences*, 14(21):4891–4903, 2017. URL https://doi.org/10.5194/bg-14-4891-2017.

Beer, T. The interaction of wind and fire. *Boundary-Layer Meteorology*, 54(3):287–308, 1991. Publisher: Springer.

Bian, H. and Prather, M. J. Fast-J2: Accurate Simulation of Stratospheric Photolysis in Global Chemical Models. page 16, 2002. URL https://link.springer.com/content/pdf/10.1023/A:1014980619462.pdf.

Bigi, A., Ghermandi, G., and Harrison, R. M. Analysis of the air pollution climate at a background site in the Po valley. *J. Environ. Monit.*, 14(2):552–563, 2012. ISSN 1464-0325, 1464-0333. doi: 10.1039/C1EM10728C. URL http://xlink.rsc.org/?DOI=C1EM10728C.

Bittelli, M. Measuring Soil Water Content: A Review. *HortTechnology*, 21(3):293–300, June 2011. ISSN 1063-0198, 1943-7714. doi: 10.21273/HORTTECH.21.3.293. URL https://journals.ashs.org/view/journals/horttech/21/3/article-p293.xml.

Bladé, I., Liebmann, B., Fortuny, D., and van Oldenborgh, G. J. Observed and simulated impacts of the summer NAO in Europe: implications for projected drying in the Mediterranean region. *Climate dynamics*, 39(3-4):709–727, 2012. URL https://doi.org/10.1007/s00382-011-1195-x. Publisher: Springer.

Bonn, B., Magh, R.-K., Rombach, J., and Kreuzwieser, J. Biogenic isoprenoid emissions under drought stress: different responses for isoprene and terpenes. *Biogeosciences*, 16 (23):4627–4645, December 2019. ISSN 1726-4189. doi: 10.5194/bg-16-4627-2019. URL https://bg.copernicus.org/articles/16/4627/2019/.

Bowman, D. M., Balch, J. K., Artaxo, P., Bond, W. J., Carlson, J. M., Cochrane, M. A., D'Antonio, C. M., DeFries, R. S., Doyle, J. C., Harrison, S. P., and others. Fire in the Earth system. *science*, 324(5926):481–484, 2009. URL `https://doi.org/10.1126/science.1163886`. Publisher: American Association for the Advancement of Science.

Boynard, A., Beekmann, M., Foret, G., Ung, A., Szopa, S., Schmechtig, C., and Coman, A. An ensemble assessment of regional ozone model uncertainty with an explicit error representation. *Atmospheric Environment*, 45(3):784–793, January 2011. ISSN 13522310. doi: 10.1016/j.atmosenv.2010.08.006. URL `https://linkinghub.elsevier.com/retrieve/pii/S135223101000659X`.

Caldararu, S., Purves, D., Palmer, P., and others. Phenology as a strategy for carbon optimality: a global model. *Journal of Geophysical Research: Biogeosciences*, 11(3):763–778, 2014. URL `https://doi.org/10.5194/bg-11-763-2014`.

Cao, J., Situ, S., Hao, Y., Xie, S., and Li, L. Enhanced summertime ozone and SOA from biogenic volatile organic compound (BVOC) emissions due to vegetation biomass variability during 1981–2018 in China. preprint, Gases/Atmospheric Modelling/Troposphere/Chemistry (chemical composition and reactions), September 2021. URL `https://acp.copernicus.org/preprints/acp-2021-675/`.

Carter, W. P. Development of the SAPRC-07 chemical mechanism. *Atmospheric Environment*, 44(40):5324–5335, December 2010. ISSN 13522310. doi: 10.1016/j.atmosenv.2010.01.026. URL `https://linkinghub.elsevier.com/retrieve/pii/S1352231010000646`.

Cassou, C., Terray, L., and Phillips, A. S. Tropical Atlantic Influence on European Heat Waves. *Journal of Climate*, 18(15):2805–2811, August 2005. ISSN 1520-0442, 0894-8755. doi: 10.1175/JCLI3506.1. URL `http://journals.ametsoc.org/doi/10.1175/JCLI3506.1`.

Chakroun, H., Mouillot, F., Nasr, Z., Nouri, M., Ennajah, A., and Ourcival, J. Performance of LAI-MODIS and the influence on drought simulation in a Mediterranean forest. *Ecohydrology*, 7(3):1014–1028, 2014. URL `https://doi.org/10.1002/eco.1426`. Publisher: Wiley Online Library.

Chakroun, M., Bastin, S., Chiriaco, M., and Chepfer, H. Characterization of vertical cloud variability over Europe using spatial lidar observations and regional simulation. *Climate dynamics*, 51(3):813–835, 2018. URL `https://doi.org/10.1007/s00382-016-3037-3`. Publisher: Springer.

Chance, K. OMI/Aura Formaldehyde (HCHO) Total Column Daily L3 Weighted Mean Global 0.1deg Lat/Lon Grid V003, 2019. URL `10.5067/Aura/OMI/DATA3010`.

Chang, K.-L., Petropavlovskikh, I., Cooper, O. R., Schultz, M. G., and Wang, T. Regional trend analysis of surface ozone observations from monitoring networks in eastern North America, Europe and East Asia. *Elementa: Science of the Anthropocene*, 5:50, January 2017. ISSN 2325-1026. doi: 10.1525/elementa.243. URL https://online.ucpress.edu/elementa/article/doi/10.1525/elementa.243/112464/Regional-trend-analysis-of-surface-ozone.

Chelli, S., Maponi, P., Campetella, G., Monteverde, P., Foglia, M., Paris, E., Lolis, A., and Panagopoulos, T. Adaptation of the Canadian Fire Weather Index to Mediterranean forests. *Natural Hazards*, 75(2):1795–1810, January 2015. ISSN 0921-030X, 1573-0840. doi: 10.1007/s11069-014-1397-8. URL http://link.springer.com/10.1007/s11069-014-1397-8.

Chen, F. and Dudhia, J. Coupling an Advanced Land Surface–Hydrology Model with the Penn State–NCAR MM5 Modeling System. Part I: Model Implementation and Sensitivity. *Monthly Weather Review*, 129(4):569–585, April 2001. ISSN 0027-0644, 1520-0493. doi: 10.1175/1520-0493(2001)129<0569:CAALSH>2.0.CO;2. URL http://journals.ametsoc.org/doi/10.1175/1520-0493(2001)129<0569:CAALSH>2.0.CO;2.

Cheng, S., Huang, J., Ji, F., and Lin, L. Uncertainties of soil moisture in historical simulations and future projections. *Journal of Geophysical Research: Atmospheres*, 122(4):2239–2253, February 2017. ISSN 2169-897X, 2169-8996. doi: 10.1002/2016JD025871. URL https://onlinelibrary.wiley.com/doi/abs/10.1002/2016JD025871.

Cherif, S., Doblas-Miranda, E., Lionello, P., Borrego, C., Giorgi, F., Iglesias, A., Jebari, S., Mahmoudi, E., Moriondo, M., Pringault, O., Rilov, G., Somot, S., Tsikliras, A., Vila, M., and Zittis, G. Drivers of change. In *Climate and Environmental Change in the Mediterranean Basin – Current Situation and Risks for the Future*, pages 59–180. Marseille, France, first mediterranean assessment report [cramer w, guiot j, marini k (eds.)] union for the mediterranean, plan bleu, unep/map edition, 2020.

Chin, M., Ginoux, P., Kinne, S., Torres, O., Holben, B. N., Duncan, B. N., Martin, R. V., Logan, J. A., Higurashi, A., and Nakajima, T. Tropospheric Aerosol Optical Thickness from the GOCART Model and Comparisons with Satellite and Sun Photometer Measurements. *Journal of the Atmospheric Sciences*, 59(3):461–483, February 2002. ISSN 0022-4928, 1520-0469. doi: 10.1175/1520-0469(2002)059<0461:TAOTFT>2.0.CO;2. URL http://journals.ametsoc.org/doi/10.1175/1520-0469(2002)059<0461:TAOTFT>2.0.CO;2.

Clifton, O. E., Paulot, F., Fiore, A. M., Horowitz, L. W., Correa, G., Baublitz, C. B., Fares, S., Goded, I., Goldstein, A. H., Gruening, C., Hogg, A. J., Loubet, B., Mammarella, I., Munger, J. W., Neil, L., Stella, P., Uddling, J., Vesala, T., and Weng, E. Influence of Dynamic Ozone Dry Deposition on Ozone Pollution. *Journal of Geophysical Research: Atmospheres*, 125(8), April 2020. ISSN 2169-897X, 2169-8996. doi: 10.1029/2020JD032398. URL `https://onlinelibrary.wiley.com/doi/abs/10.1029/2020JD032398`.

Colliander, A., Reichle, R., Crow, W., Cosh, M. H., Chen, F., Chan, S. K., Das, N. N., Bindlish, R., Chaubell, M. J., Kim, S., Liu, Q., Oneill, P. E., Dunbar, S., Dang, L. B., Kimball, J. S., Jackson, T. J., Aljassar, H. K., Asanuma, J., Bhattacharya, B. K., Berg, A., Bosch, D. D., Bourgeau-Chavez, L. L., Caldwell, T., Calvet, J.-C., Collins, C. H., Jensen, K. H., Livingston, S., Lopez-Baeza, E., Martinez-Fernandez, J., Mcnairn, H., Moghaddam, M., Montzka, C., Notarnicola, C., Pellarin, T., Pfeil, I., Pulliainen, J., Ramos, J., Seyfried, M., Starks, P., Su, B., Van der Velde, R., Zeng, Y., Thibeault, M., Vreugdenhil, M., Walker, J. P., Zribi, M., Entekhabi, D., and Yueh, S. H. Validation of Soil Moisture Data Products from the NASA SMAP Mission. *IEEE Journal of Selected Topics in Applied Earth Observations and Remote Sensing*, pages 1–1, 2021. ISSN 1939-1404, 2151-1535. doi: 10.1109/JSTARS.2021.3124743. URL `https://ieeexplore.ieee.org/document/9599364/`.

Cook, B. I., Anchukaitis, K. J., Touchan, R., Meko, D. M., and Cook, E. R. Spatiotemporal drought variability in the Mediterranean over the last 900 years. *Journal of Geophysical Research: Atmospheres*, 121(5):2060–2074, March 2016. ISSN 2169-897X, 2169-8996. doi: 10.1002/2015JD023929. URL `https://onlinelibrary.wiley.com/doi/10.1002/2015JD023929`.

Cornes, R. C., van der Schrier, G., van den Besselaar, E. J., and Jones, P. D. An ensemble version of the E-OBS temperature and precipitation data sets. *Journal of Geophysical Research: Atmospheres*, 123(17):9391–9409, 2018. URL `https://doi.org/10.1029/2017JD028200`. Publisher: Wiley Online Library.

Cos, J., Doblas-Reyes, F., Jury, M., Marcos, R., Bretonnière, P.-A., and Samsó, M. The Mediterranean climate change hotspot in the CMIP5 and CMIP6 projections. preprint, Earth system change: climate scenarios, July 2021. URL `https://esd.copernicus.org/preprints/esd-2021-65/`.

Couvidat, F., Bessagnet, B., Garcia-Vivanco, M., Real, E., Menut, L., and Colette, A. Development of an inorganic and organic aerosol model (CHIMERE 2017&lt;i&gt;$\beta$&lt;/i&gt; v1.0): seasonal and spatial evaluation over Europe. *Geoscientific Model Development*, 11(1):165–194, January 2018. ISSN 1991-9603. doi: 10.5194/gmd-11-165-2018. URL `https://gmd.copernicus.org/articles/11/165/2018/`.

Craig, A., Valcke, S., and Coquart, L. Development and performance of a new version of the

OASIS coupler, OASIS3-MCT_3. 0. *Geoscientific Model Development*, 10(9), 2017. URL https://doi.org/10.5194/gmd-10-3297-2017,2017.

Curci, G., Palmer, P. I., Kurosu, T. P., Chance, K., and Visconti, G. Estimating European volatile organic compound emissions using satellite observations of formaldehyde from the Ozone Monitoring Instrument. *Atmospheric Chemistry and Physics*, 10(23):11501–11517, December 2010. ISSN 1680-7324. doi: 10.5194/acp-10-11501-2010. URL https://acp.copernicus.org/articles/10/11501/2010/.

De Andrés, J. M., Borge, R., de la Paz, D., Lumbreras, J., and Rodríguez, E. Implementation of a module for risk of ozone impacts assessment to vegetation in the Integrated Assessment Modelling system for the Iberian Peninsula. Evaluation for wheat and Holm oak. *Environmental Pollution*, 165:25–37, June 2012. ISSN 02697491. doi: 10.1016/j.envpol.2012.01.048. URL https://linkinghub.elsevier.com/retrieve/pii/S0269749112000784.

De Rosnay, P. and Polcher, J. Modelling root water uptake in a complex land surface scheme coupled to a GCM. *Hydrology and Earth System Sciences*, 2:239–255, 1998. URL https://hess.copernicus.org/articles/2/239/1998/.

De Rosnay, P., Polcher, J., Bruen, M., and Laval, K. Impact of a physically based soil water flow and soil-plant interaction representation for modeling large-scale land surface processes. *Journal of Geophysical Research: Atmospheres*, 107(D11):ACL–3, 2002. URL https://doi.org/10.1029/2001JD000634. Publisher: Wiley Online Library.

Demarty, J., Chevallier, F., Friend, A., Viovy, N., Piao, S., and Ciais, P. Assimilation of global MODIS leaf area index retrievals within a terrestrial biosphere model. *Geophysical research letters*, 34(15), 2007. URL https://doi:10.1029/2007GL030014. Publisher: Wiley Online Library.

Demetillo, M. A. G., Anderson, J. F., Geddes, J. A., Yang, X., Najacht, E. Y., Herrera, S. A., Kabasares, K. M., Kotsakis, A. E., Lerdau, M. T., and Pusede, S. E. Observing Severe Drought Influences on Ozone Air Pollution in California. *Environmental Science & Technology*, 53(9):4695–4706, May 2019. ISSN 0013-936X, 1520-5851. doi: 10.1021/acs.est.8b04852. URL https://pubs.acs.org/doi/10.1021/acs.est.8b04852.

Derognat, C. Effect of biogenic volatile organic compound emissions on tropospheric chemistry during the Atmospheric Pollution Over the Paris Area (ESQUIF) campaign in the Ile-de-France region. *Journal of Geophysical Research*, 108(D17):8560, 2003. ISSN 0148-0227. doi: 10.1029/2001JD001421. URL http://doi.wiley.com/10.1029/2001JD001421.

Di Luca, A., Flaounas, E., Drobinski, P., and Brossier, C. L. The atmospheric component of the Mediterranean Sea water budget in a WRF multi-physics ensemble and observations. *Climate dynamics*, 43(9-10):2349–2375, 2014. URL `https://doi.org/10.1007/s00382-014-2058-z`. Publisher: Springer.

Dimitrakopoulos, A. P., Bemmerzouk, A. M., and Mitsopoulos, I. D. Evaluation of the Canadian fire weather index system in an eastern Mediterranean environment. *Meteorological Applications*, 18(1):83–93, March 2011. ISSN 13504827. doi: 10.1002/met.214. URL `https://onlinelibrary.wiley.com/doi/10.1002/met.214`.

Dowdy, A., Mills, G. A., , F., Klara, Bureau of Meteorology, and CSIRO. *Australian fire weather as represented by the McArthur Forest Fire Danger Index and the Canadian Forest Fire Weather Index.* Centre for australian weather and climate research edition, 2009. ISBN 978-1-921605-18-5. URL `https://nla.gov.au/nla.obj-2968722661`. OCLC: 1268354673.

Drobinski, P., Anav, A., Brossier, C. L., Samson, G., Stéfanon, M., Bastin, S., Baklouti, M., Béranger, K., Beuvier, J., Bourdallé-Badie, R., and others. Model of the Regional Coupled Earth system (MORCE): Application to process and climate studies in vulnerable regions. *Environmental Modelling & Software*, 35:1–18, 2012. URL `https://doi.org/10.1016/j.envsoft.2012.01.017`. Publisher: Elsevier.

Drobinski, P., Bastin, S., Arsouze, T., Béranger, K., Flaounas, E., and Stéfanon, M. Northwestern Mediterranean sea-breeze circulation in a regional climate system model. *Climate Dynamics*, 51(3):1077–1093, August 2018. ISSN 0930-7575, 1432-0894. doi: 10.1007/s00382-017-3595-z. URL `http://link.springer.com/10.1007/s00382-017-3595-z`.

Drobinski, P., Da Silva, N., Bastin, S., Mailler, S., Muller, C., Ahrens, B., Christensen, O. B., and Lionello, P. How warmer and drier will the Mediterranean region be at the end of the twenty-first century? *Regional Environmental Change*, 20(3):78, September 2020. ISSN 1436-3798, 1436-378X. doi: 10.1007/s10113-020-01659-w. URL `https://link.springer.com/10.1007/s10113-020-01659-w`.

Duane, A. and Brotons, L. Synoptic weather conditions and changing fire regimes in a Mediterranean environment. *Agricultural and Forest Meteorology*, 253:190–202, 2018. URL `https://doi.org/10.1016/j.agrformet.2018.02.014`. Publisher: Elsevier.

EEA. Air quality in Europe — 2020 report, 2020. URL `https://www.actu-environnement.com/media/pdf/36559.pdfa`. European Environment Agency.

Ek, M. B., Mitchell, K. E., Lin, Y., Rogers, E., Grunmann, P., Koren, V., Gayno, G., and Tarpley, J. D. Implementation of Noah land surface model advances in the National Centers for Environmental Prediction operational mesoscale Eta model. *Journal of Geophysical Research: Atmospheres*, 108(D22):2002JD003296, November 2003. ISSN 0148-0227, 2156-2202. doi: 10.1029/2002JD003296. URL `https://onlinelibrary.wiley.com/doi/abs/10.1029/2002JD003296`.

Emberson, L., Simpson, D., Tuovinen, J.-P., Ashmore, M., and Cambridge, H. *Towards a model of ozone deposition and stomatal uptake over Europe*. Number Research Note No. 42. Norwegian Meteorological Institute, emep/msc-w edition, 2000.

Emmerson, K. M., Palmer, P. I., Thatcher, M., Haverd, V., and Guenther, A. B. Sensitivity of isoprene emissions to drought over south-eastern Australia: Integrating models and satellite observations of soil moisture. *Atmospheric Environment*, 209:112–124, July 2019. ISSN 13522310. doi: 10.1016/j.atmosenv.2019.04.038. URL `https://linkinghub.elsevier.com/retrieve/pii/S1352231019302535`.

Erisman, J. W., Van Pul, A., and Wyers, P. Parametrization of surface resistance for the quantification of atmospheric deposition of acidifying pollutants and ozone. *Atmospheric Environment*, 28(16):2595–2607, September 1994. ISSN 13522310. doi: 10.1016/1352-2310(94)90433-2. URL `https://linkinghub.elsevier.com/retrieve/pii/1352231094904332`.

ESA. ESA CCI Land Cover time-series v2.0.7 (1992 - 2015). Report, European Space Agency - Climate Change Initiative, 2017. URL `https://maps.elie.ucl.ac.be/CCI/viewer/`.

Fang, H., Liang, S., and Hoogenboom, G. Integration of MODIS LAI and vegetation index products with the CSM–CERES–Maize model for corn yield estimation. *International Journal of Remote Sensing*, 32(4):1039–1065, 2011. URL `https://doi.org/10.1080/01431160903505310`. Publisher: Taylor & Francis.

Fécan, F., Marticonera, B., and Bergametti, G. Soil-derived dust emissions from semiarid lands: 1. parametrization of the soil moisture effect on the threshold wind friction velocities. *Annales Geophysicae*, (17):149–157, 1999.

Feng, Z., Yuan, X., Fares, S., Loreto, F., Li, P., Hoshika, Y., and Paoletti, E. Isoprene is more affected by climate drivers than onoterpenes: A meta-analytic review on plant isoprenoid emissions. *Pland, Cell & Environment*, 42(6):1939–1949, 2019. doi: https://doi.org/10.1111/pce.13535. URL `https://doi.org/10.1111/pce.13535`.

Fischer, E. M., Seneviratne, S. I., Lüthi, D., and Schär, C. Contribution of land-atmosphere coupling to recent European summer heat waves. *Geophysical Research Letters*, 34(6), 2007. URL `https://doi.org/10.1029/2006GL029068`. Publisher: Wiley Online Library.

Friedl, M. A., Sulla-Menashe, D., Tan, B., Schneider, A., Ramankutty, N., Sibley, A., and Huang, X. MODIS Collection 5 global land cover: Algorithm refinements and characterization of new datasets. *Remote sensing of Environment*, 114(1):168–182, 2010. URL `https://doi.org/10.1016/j.rse.2009.08.016`. Publisher: Elsevier.

Gannon, C. S. and Steinberg, N. C. A global assessment of wildfire potential under climate change utilizing Keetch-Byram drought index and land cover classifications. *Environmental Research Communications*, 3(3):035002, March 2021. ISSN 2515-7620. doi: 10.1088/2515-7620/abd836. URL `https://iopscience.iop.org/article/10.1088/2515-7620/abd836`.

García-Vila, M., Lorite, I., Soriano, M., and Fereres, E. Management trends and responses to water scarcity in an irrigation scheme of Southern Spain. *Agricultural Water Management*, 95(4):458–468, April 2008. ISSN 03783774. doi: 10.1016/j.agwat.2007.11.009. URL `https://linkinghub.elsevier.com/retrieve/pii/S0378377407002958`.

Garrigues, S., Olioso, A., Carrer, D., Decharme, B., Calvet, J.-C., Martin, E., Moulin, S., and Marloie, O. Impact of climate, vegetation, soil and crop management variables on multi-year ISBA-A-gs simulations of evapotranspiration over a Mediterranean crop site. *Geoscientific Model Development*, 8(10):3033–3053, October 2015. ISSN 1991-9603. doi: 10.5194/gmd-8-3033-2015. URL `https://gmd.copernicus.org/articles/8/3033/2015/`.

Gaubert, B., Coman, A., Foret, G., Meleux, F., Ung, A., Rouil, L., Ionescu, A., Candau, Y., and Beekmann, M. Regional scale ozone data assimilation using an ensemble Kalman filter and the CHIMERE chemical transport model. *Geoscientific Model Development*, 7(1):283–302, February 2014. ISSN 1991-9603. doi: 10.5194/gmd-7-283-2014. URL `https://gmd.copernicus.org/articles/7/283/2014/`.

Genard-Zielinski, A.-C., Boissard, C., Ormeño, E., Lathière, J., Reiter, I. M., Wortham, H., Orts, J.-P., Temime-Roussel, B., Guenet, B., Bartsch, S., Gauquelin, T., and Fernandez, C. Seasonal variations of Quercus pubescens isoprene emissions from an in natura forest under drought stress and sensitivity to future climate change in the Mediterranean area. *Biogeosciences*, 15(15):4711–4730, August 2018. ISSN 1726-4189. doi: 10.5194/bg-15-4711-2018. URL `https://bg.copernicus.org/articles/15/4711/2018/`.

Giannaros, T. M., Kotroni, V., and Lagouvardos, K. Climatology and trend analysis (1987–2016) of fire weather in the Euro Mediterranean. *International Journal of Climatology*, 41:E491–E508, 2021. doi: 10.1002/joc.6701. URL `https://onlinelibrary.wiley.com/doi/10.1002/joc.6701`.

Giglio, L., Randerson, J., Van der Werf, G., Kasibhatla, P., Collatz, G., Morton, D., and DeFries, R. Assessing variability and long-term trends in burned area by merging multiple satellite fire products. *Journal of Geophysical Research: Biogeosciences*, 7(3):1171–1186, 2010. URL https://doi.org/10.5194/bg-7-1171-2010.

Giglio, L., Boschetti, L., Roy, D. P., Humber, M. L., and Justice, C. O. The Collection 6 MODIS burned area mapping algorithm and product. *Remote Sensing of Environment*, 217: 72 – 85, 2018. ISSN 0034-4257. URL https://doi.org/10.1016/j.rse.2018.08.005.

Giglio, L., Csiszar, I., and Justice, C. O. Global distribution and seasonality of active fires as observed with the Terra and Aqua Moderate Resolution Imaging Spectroradiometer (MODIS) sensors. *Journal of Geophysical Research: Biogeosciences*, 111(G2), 2006. URL https://doi.org/10.1029/2005JG000142. Publisher: Wiley Online Library.

Gong, C., Lei, Y., Ma, Y., Yue, X., and Liao, H. Ozone–vegetation feedback through dry deposition and isoprene emissions in a global chemistry–carbon–climate model. *Atmospheric Chemistry and Physics*, 20(6):3841–3857, March 2020. ISSN 1680-7324. doi: 10.5194/acp-20-3841-2020. URL https://acp.copernicus.org/articles/20/3841/2020/.

González Abad, G., Liu, X., Chance, K., Wang, H., Kurosu, T. P., and Suleiman, R. Updated Smithsonian Astrophysical Observatory Ozone Monitoring Instrument (SAO OMI) formaldehyde retrieval. *Atmospheric Measurement Techniques*, 8(1):19–32, January 2015. ISSN 1867-8548. doi: 10.5194/amt-8-19-2015. URL https://amt.copernicus.org/articles/8/19/2015/.

Gouveia, C. M., Bistinas, I., Liberato, M. L., Bastos, A., Koutsias, N., and Trigo, R. The outstanding synergy between drought, heatwaves and fuel on the 2007 Southern Greece exceptional fire season. *Agricultural and forest meteorology*, 218:135–145, 2016. URL https://doi.org/10.1016/j.agrformet.2015.11.023. Publisher: Elsevier.

Gouveia, C., Trigo, R., Beguería, S., and Vicente-Serrano, S. M. Drought impacts on vegetation activity in the Mediterranean region: An assessment using remote sensing data and multi-scale drought indicators. *Global and Planetary Change*, 151:15–27, 2017. URL https://doi.org/10.1016/j.gloplacha.2016.06.011. Publisher: Elsevier.

Greve, P., Warrach-Sagi, K., and Wulfmeyer, V. Evaluating Soil Water Content in a WRF-Noah Downscaling Experiment. *Journal of Applied Meteorology and Climatology*, 52(10):2312–2327, October 2013. ISSN 1558-8424, 1558-8432. doi: 10.1175/JAMC-D-12-0239.1. URL https://journals.ametsoc.org/view/journals/apme/52/10/jamc-d-12-0239.1.xml.

Grulke, N. E. and Heath, R. L. Ozone effects on plants in natural ecosystems. *Plant Biology*, 22(S1):12–37, January 2020. ISSN 1435-8603, 1438-8677. doi: 10.1111/plb.12971. URL `https://onlinelibrary.wiley.com/doi/10.1111/plb.12971`.

Guenther, A., Karl, T., Harley, P., Wiedinmyer, C., Palmer, P. I., and Geron, C. Estimates of global terrestrial isoprene emissions using MEGAN (Model of Emissions of Gases and Aerosols from Nature). *Atmos. Chem. Phys.*, page 31, 2006.

Guenther, A. B., Jiang, X., Heald, C. L., Sakulyanontvittaya, T., Duhl, T., Emmons, L. K., and Wang, X. The Model of Emissions of Gases and Aerosols from Nature version 2.1 (MEGAN2.1): an extended and updated framework for modeling biogenic emissions. *Geoscientific Model Development*, 5(6):1471–1492, November 2012. ISSN 1991-9603. doi: 10.5194/gmd-5-1471-2012. URL `https://gmd.copernicus.org/articles/5/1471/2012/`.

Guenther, A. B., Monson, R. K., and Fall, R. Isoprene and monoterpene emission rate variability: Observations with eucalyptus and emission rate algorithm development. *Journal of Geophysical Research*, 96(D6):10799, 1991. ISSN 0148-0227. doi: 10.1029/91JD00960. URL `http://doi.wiley.com/10.1029/91JD00960`.

Guenther, A. B., Zimmerman, P. R., Harley, P. C., Monson, R. K., and Fall, R. Isoprene and monoterpene emission rate variability: Model evaluations and sensitivity analyses. *Journal of Geophysical Research*, 98(D7):12609, 1993. ISSN 0148-0227. doi: 10.1029/93JD00527. URL `http://doi.wiley.com/10.1029/93JD00527`.

Guion, A., Turquety, S., Polcher, J., Pennel, R., Bastin, S., and Arsouze, T. Droughts and heatwaves in the Western Mediterranean: impact on vegetation and wildfires using the coupled WRF-ORCHIDEE regional model (RegIPSL). *Climate Dynamics*, September 2021. ISSN 0930-7575, 1432-0894. doi: 10.1007/s00382-021-05938-y. URL `https://link.springer.com/10.1007/s00382-021-05938-y`.

Guiot, J. and Cramer, W. Climate change: The 2015 Paris Agreement thresholds and Mediterranean basin ecosystems. *Science*, 354(6311):465–468, 2016. URL `https://doi.org/10.1126/science.aah5015`. Publisher: American Association for the Advancement of Science.

Harmanny, K. S. and Malek, Ž. Adaptations in irrigated agriculture in the Mediterranean region: an overview and spatial analysis of implemented strategies. *Regional environmental change*, 19(5):1401–1416, 2019. URL `https://doi.org/10.1007/s10113-019-01494-8`. Publisher: Springer.

Harris, I., Jones, P., Osborn, T., and Lister, D. Updated high-resolution grids of monthly climatic observations - the CRU TS3.10. *International Journal of Climatology*, 34(3):623–642, March 2014. ISSN 08998418. doi: 10.1002/joc.3711. URL `https://onlinelibrary.wiley.com/doi/10.1002/joc.3711`.

Harris, I., Osborn, T. J., Jones, P., and Lister, D. Version 4 of the CRU TS monthly high-resolution gridded multivariate climate dataset. *Scientific Data*, 7(1):109, December 2020. ISSN 2052-4463. doi: 10.1038/s41597-020-0453-3. URL `http://www.nature.com/articles/s41597-020-0453-3`.

Hauglustaine, D. A., Hourdin, F., Jourdain, L., Filiberti, M.-A., Walters, S., Lamarque, J.-F., and Holland, E. A. Interactive chemistry in the Laboratoire de Météorologie Dynamique general circulation model: Description and background tropospheric chemistry evaluation. *Journal of Geophysical Research: Atmospheres*, 109(D4):n/a–n/a, February 2004. ISSN 01480227. doi: 10.1029/2003JD003957. URL `http://doi.wiley.com/10.1029/2003JD003957`.

Hauglustaine, D. A., Balkanski, Y., and Schulz, M. A global model simulation of present and future nitrate aerosols and their direct radiative forcing of climate. preprint, Aerosols/Atmospheric Modelling/Troposphere/Chemistry (chemical composition and reactions), March 2014. URL `https://acp.copernicus.org/preprints/14/6863/2014/acpd-14-6863-2014.pdf`.

Haworth, M., Catola, S., Marino, G., Brunetti, C., Michelozzi, M., Riggi, E., Avola, G., Cosentino, S. L., Loreto, F., and Centritto, M. Moderate Drought Stress Induces Increased Foliar Dimethylsulphoniopropionate (DMSP) Concentration and Isoprene Emission in Two Contrasting Ecotypes of Arundo donax. *Frontiers in Plant Science*, 8:1016, June 2017. ISSN 1664-462X. doi: 10.3389/fpls.2017.01016. URL `http://journal.frontiersin.org/article/10.3389/fpls.2017.01016/full`.

Haylock, M., Hofstra, N., Tank, A. K., Klok, E., Jones, P., and New, M. A European daily high-resolution gridded data set of surface temperature and precipitation for 1950–2006. *Journal of Geophysical Research: Atmospheres*, 113(D20), 2008. URL `https://doi.org/10.1029/2008JD010201`. Publisher: Wiley Online Library.

Heald, C. L., Wilkinson, M. J., Monson, R. K., Alo, C. A., Wang, G., and Guenther, A. Response of isoprene emission to ambient CO $_2$ changes and implications for global budgets. *Global Change Biology*, 15(5):1127–1140, May 2009. ISSN 13541013, 13652486. doi: 10.1111/j.1365-2486.2008.01802.x. URL `https://onlinelibrary.wiley.com/doi/10.1111/j.1365-2486.2008.01802.x`.

Hernandez, C., Drobinski, P., and Turquety, S. How much does weather control fire size and intensity in the Mediterranean region? *Annales Geophysicae*, 33(7):931–939, July 2015. URL https://doi.org/10.5194/angeo-33-931-2015. Publisher: European Geosciences Union.

Hertig, E., Russo, A., and Trigo, R. M. Heat and Ozone Pollution Waves in Central and South Europe—Characteristics, Weather Types, and Association with Mortality. *Atmosphere*, 11 (12):1271, November 2020. ISSN 2073-4433. doi: 10.3390/atmos11121271. URL https://www.mdpi.com/2073-4433/11/12/1271.

Herwehe, J. A., Alapaty, K., Spero, T. L., and Nolte, C. G. Increasing the credibility of regional climate simulations by introducing subgrid-scale cloud-radiation interactions. *Journal of Geophysical Research: Atmospheres*, 119(9):5317–5330, 2014. URL https://doi.org/10.1002/2014JD021504. Publisher: Wiley Online Library.

Hodnebrog, Ø., Solberg, S., Stordal, F., Svendby, T. M., Simpson, D., Gauss, M., Hilboll, A., Pfister, G. G., Turquety, S., Richter, A., Burrows, J. P., and Denier van der Gon, H. A. C. Impact of forest fires, biogenic emissions and high temperatures on the elevated Eastern Mediterranean ozone levels during the hot summer of 2007. *Atmospheric Chemistry and Physics*, 12(18):8727–8750, September 2012. ISSN 1680-7324. doi: 10.5194/acp-12-8727-2012. URL https://acp.copernicus.org/articles/12/8727/2012/.

Hoerling, M., Eischeid, J., Perlwitz, J., Quan, X., Zhang, T., and Pegion, P. On the Increased Frequency of Mediterranean Drought. *Journal of Climate*, 25(6):2146–2161, March 2012. ISSN 0894-8755, 1520-0442. doi: 10.1175/JCLI-D-11-00296.1. URL http://journals.ametsoc.org/doi/10.1175/JCLI-D-11-00296.1.

Hofstra, N., Haylock, M., New, M., and Jones, P. D. Testing E-OBS European high-resolution gridded data set of daily precipitation and surface temperature. *Journal of Geophysical Research: Atmospheres*, 114(D21), 2009. URL https://doi.org/10.1029/2009JD011799. Publisher: Wiley Online Library.

Hong, S.-Y., Dudhia, J., and Chen, S.-H. A revised approach to ice microphysical processes for the bulk parameterization of clouds and precipitation. *Monthly weather review*, 132(1): 103–120, 2004. URL https://doi.org/10.1175/1520-0493(2004)132<0103:ARATIM>2.0.CO;2.

Hourdin, F., Musat, I., Bony, S., Braconnot, P., Codron, F., Dufresne, J.-L., Fairhead, L., Filiberti, M.-A., Friedlingstein, P., Grandpeix, J.-Y., Krinner, G., LeVan, P., Li, Z.-X., and Lott, F. The LMDZ4 general circulation model: climate performance and sensitivity to parametrized physics with emphasis on tropical convection. *Climate Dynamics*, 27(7-8):

787–813, October 2006. ISSN 0930-7575, 1432-0894. doi: 10.1007/s00382-006-0158-0. URL http://link.springer.com/10.1007/s00382-006-0158-0.

Hu, L., Jacob, D. J., Liu, X., Zhang, Y., Zhang, L., Kim, P. S., Sulprizio, M. P., and Yantosca, R. M. Global budget of tropospheric ozone: Evaluating recent model advances with satellite (OMI), aircraft (IAGOS), and ozonesonde observations. *Atmospheric Environment*, 167: 323–334, October 2017. ISSN 13522310. doi: 10.1016/j.atmosenv.2017.08.036. URL https://linkinghub.elsevier.com/retrieve/pii/S1352231017305484.

Iacono, M. J., Delamere, J. S., Mlawer, E. J., Shephard, M. W., Clough, S. A., and Collins, W. D. Radiative forcing by long-lived greenhouse gases: Calculations with the AER radiative transfer models. *Journal of Geophysical Research: Atmospheres*, 113(D13), 2008. URL https://doi.org/10.1029/2008JD009944. Publisher: Wiley Online Library.

Im, U., Brandt, J., Geels, C., Hansen, K. M., Christensen, J. H., Andersen, M. S., Solazzo, E., Kioutsioukis, I., Alyuz, U., Balzarini, A., Baro, R., Bellasio, R., Bianconi, R., Bieser, J., Colette, A., Curci, G., Farrow, A., Flemming, J., Fraser, A., Jimenez-Guerrero, P., Kitwiroon, N., Liang, C.-K., Nopmongcol, U., Pirovano, G., Pozzoli, L., Prank, M., Rose, R., Sokhi, R., Tuccella, P., Unal, A., Vivanco, M. G., West, J., Yarwood, G., Hogrefe, C., and Galmarini, S. Assessment and economic valuation of air pollution impacts on human health over Europe and the United States as calculated by a multi-model ensemble in the framework of AQMEII3. *Atmospheric Chemistry and Physics*, 18(8):5967–5989, April 2018. ISSN 1680-7324. doi: 10.5194/acp-18-5967-2018. URL https://acp.copernicus.org/articles/18/5967/2018/.

Ioannidis, E., Lolis, C., Papadimas, C., Hatzianastassiou, N., and Bartzokas, A. On the intra-annual variation of cloudiness over the Mediterranean region. *Atmospheric Research*, 208: 246–256, 2018. URL https://doi.org/10.1016/j.atmosres.2017.08.021. Publisher: Elsevier.

IPCC. Climate Change 2021: The Physical Science Basis. Contribution of Working Group I to the Sixth Assessment Report of the Intergovernmental Panel on Climate Change, 2021. Intergovernmental Panel on Climate Change.

Jacob, D. J. *Introduction to atmospheric chemistry*. Princeton university press. edition, 1999.

Jaén, C., Udina, M., and Bech, J. Analysis of two heat wave driven ozone episodes in Barcelona and surrounding region: Meteorological and photochemical modeling. *Atmospheric Environment*, 246:118037, February 2021. ISSN 13522310. doi: 10.1016/j.atmosenv.2020.118037. URL https://linkinghub.elsevier.com/retrieve/pii/S135223102030769X.

Jansa, A., Homar, V., Romero, R., Alonso, S., Guijarro, J. A., and Ramis, C. Extension of summer climatic conditions into spring in the Western Mediterranean area. *International Journal of Climatology*, 37(4):1938–1950, March 2017. ISSN 08998418. doi: 10.1002/joc.4824. URL `https://onlinelibrary.wiley.com/doi/10.1002/joc.4824`.

Janssens-Maenhout, G., Crippa, M., Guizzardi, D., Dentener, F., Muntean, M., Pouliot, G., Keating, T., Zhang, Q., Kurokawa, J., Wankmüller, R., Denier van der Gon, H., Kuenen, J. J. P., Klimont, Z., Frost, G., Darras, S., Koffi, B., and Li, M. HTAP_v2.2: a mosaic of regional and global emission grid maps for 2008 and 2010 to study hemispheric transport of air pollution. *Atmospheric Chemistry and Physics*, 15(19):11411–11432, October 2015. ISSN 1680-7324. doi: 10.5194/acp-15-11411-2015. URL `https://acp.copernicus.org/articles/15/11411/2015/`.

Jenkin, M. E. and Clemitshaw, K. C. Ozone and other secondary photochemical pollutants: chemical processes governing their formation in the planetary boundary layer. *Atmospheric Environment*, 34(16):2499–2527, January 2000. ISSN 13522310. doi: 10.1016/S1352-2310(99)00478-1. URL `https://linkinghub.elsevier.com/retrieve/pii/S1352231099004781`.

Jerrett, M., Burnett, R. T., Pope, C. A., Ito, K., Thurston, G., Krewski, D., Shi, Y., Calle, E., and Thun, M. Long-Term Ozone Exposure and Mortality. *New England Journal of Medicine*, 360(11):1085–1095, March 2009. ISSN 0028-4793, 1533-4406. doi: 10.1056/NEJMoa0803894. URL `http://www.nejm.org/doi/abs/10.1056/NEJMoa0803894`.

Jiang, X., Guenther, A., Potosnak, M., Geron, C., Seco, R., Karl, T., Kim, S., Gu, L., and Pallardy, S. Isoprene emission response to drought and the impact on global atmospheric chemistry. *Atmospheric Environment*, 183:69–83, June 2018. ISSN 13522310. doi: 10.1016/j.atmosenv.2018.01.026. URL `https://linkinghub.elsevier.com/retrieve/pii/S1352231018300402`.

Jones, P. D., Jonsson, T., and Wheeler, D. Extension to the North Atlantic Oscillation using early instrumental pressure observations from Gibraltar and south-west Iceland. *International Journal of Climatology: A Journal of the Royal Meteorological Society*, 17(13):1433–1450, 1997. URL `https://doi.org/10.1002/(SICI)1097-0088(19971115)17:13<1433::AID-JOC203>3.0.CO;2-P`. Publisher: Wiley Online Library.

Kain, J. S. The Kain–Fritsch convective parameterization: an update. *Journal of applied meteorology*, 43(1):170–181, 2004. URL `https://doi.org/10.1175/1520-0450(2004)043<0170:TKCPAU>2.0.CO;2`.

Katragkou, E., García Díez, M., Vautard, R., Sobolowski, S. P., Zanis, P., Alexandri, G., Cardoso, R. M., Colette, A., Fernández Fernández, J., Gobiet, A., and others. Regional climate hindcast simulations within EURO-CORDEX: evaluation of a WRF multi-physics ensemble. *Geoscientific Model Development*, 8:603–618, 2015. URL `https://doi.org/10.5194/gmd-8-603-2015`. Publisher: Copernicus GmbH.

Kaufman, Y. J., Justice, C. O., Flynn, L. P., Kendall, J. D., Prins, E. M., Giglio, L., Ward, D. E., Menzel, W. P., and Setzer, A. W. Potential global fire monitoring from EOS-MODIS. *Journal of Geophysical Research: Atmospheres*, 103(D24):32215–32238, December 1998. ISSN 01480227. doi: 10.1029/98JD01644. URL `http://doi.wiley.com/10.1029/98JD01644`.

Kavassalis, S. C. and Murphy, J. G. Understanding ozone-meteorology correlations: A role for dry deposition: Ozone-Meteorology Correlations: Dry Dep. *Geophysical Research Letters*, 44(6):2922–2931, March 2017. ISSN 00948276. doi: 10.1002/2016GL071791. URL `http://doi.wiley.com/10.1002/2016GL071791`.

Kelley, C., Ting, M., Seager, R., and Kushnir, Y. Mediterranean precipitation climatology, seasonal cycle, and trend as simulated by CMIP5. *Geophysical Research Letters*, 39(21): n/a–n/a, November 2012. ISSN 00948276. doi: 10.1029/2012GL053416. URL `http://doi.wiley.com/10.1029/2012GL053416`.

Khodayar, S., Sehlinger, A., Feldmann, H., and Kottmeier, C. Sensitivity of soil moisture initialization for decadal predictions under different regional climatic conditions in Europe. *International Journal of Climatology*, 35(8):1899–1915, June 2015. ISSN 08998418. doi: 10.1002/joc.4096. URL `https://onlinelibrary.wiley.com/doi/10.1002/joc.4096`.

Knyazikhin, Y., Martonchik, J., Myneni, R. B., Diner, D., and Running, S. W. Synergistic algorithm for estimating vegetation canopy leaf area index and fraction of absorbed photosynthetically active radiation from MODIS and MISR data. *Journal of Geophysical Research: Atmospheres*, 103(D24):32257–32275, 1998. URL `https://doi.org/10.1029/98JD02462`. Publisher: Wiley Online Library.

Koppmann, R. *Volatile Organic Compounds in the Atmosphere*. Blackwell Publishing Ltd, Germany, john wiley & sons edition, 2008. URL `https://onlinelibrary.wiley.com/doi/book/10.1002/9780470988657`.

Krinner, G., Viovy, N., de Noblet-Ducoudré, N., Ogée, J., Polcher, J., Friedlingstein, P., Ciais, P., Sitch, S., and Prentice, I. C. A dynamic global vegetation model for studies of the coupled atmosphere-biosphere system. *Global Biogeochemical Cycles*, 19(1), March

2005. ISSN 08866236. doi: 10.1029/2003GB002199. URL http://doi.wiley.com/10.1029/2003GB002199.

Lamsal, L. N., Martin, R. V., van Donkelaar, A., Steinbacher, M., Celarier, E. A., Bucsela, E., Dunlea, E. J., and Pinto, J. P. Ground-level nitrogen dioxide concentrations inferred from the satellite-borne Ozone Monitoring Instrument. *Journal of Geophysical Research*, 113(D16):D16308, August 2008. ISSN 0148-0227. doi: 10.1029/2007JD009235. URL http://doi.wiley.com/10.1029/2007JD009235.

Lantz, A. T., Allman, J., Weraduwage, S. M., and Sharkey, T. D. Isoprene: New insights into the control of emission and mediation of stress tolerance by gene expression. *Plant, Cell & Environment*, 42(10), 2019. doi: https://doi.org/10.1111/pce.13629. URL https://onlinelibrary.wiley.com/doi/abs/10.1111/pce.13629?casa_token=YdX0Dd-nDXkAAAAA:ncSMJPlMoKA8tV9k03BSlWg3CfII8k8bjIccSl_sazWQ67Ir8qsJpOZGhbsCetOPxJceA-eX-hGEhc_D.

Lattuati, M. *Lattuati, M. (1997). Contribution à l'étude du bilan de l'ozone troposphérique à l'interface de l'Europe et de l'Atlantique Nord: modélisation lagrangienne et mesures en altitude.* These de sciences, Université Paris 6, Paris, 1997.

Levelt, P., van den Oord, G., Dobber, M., Malkki, A., Huib Visser, Johan de Vries, Stammes, P., Lundell, J., and Saari, H. The ozone monitoring instrument. *IEEE Transactions on Geoscience and Remote Sensing*, 44(5):1093–1101, May 2006. ISSN 0196-2892. doi: 10.1109/TGRS.2006.872333. URL http://ieeexplore.ieee.org/document/1624590/.

Levelt, P. F., Joiner, J., Tamminen, J., Veefkind, J. P., Bhartia, P. K., Stein Zweers, D. C., Duncan, B. N., Streets, D. G., Eskes, H., van der A, R., McLinden, C., Fioletov, V., Carn, S., de Laat, J., DeLand, M., Marchenko, S., McPeters, R., Ziemke, J., Fu, D., Liu, X., Pickering, K., Apituley, A., González Abad, G., Arola, A., Boersma, F., Chan Miller, C., Chance, K., de Graaf, M., Hakkarainen, J., Hassinen, S., Ialongo, I., Kleipool, Q., Krotkov, N., Li, C., Lamsal, L., Newman, P., Nowlan, C., Suleiman, R., Tilstra, L. G., Torres, O., Wang, H., and Wargan, K. The Ozone Monitoring Instrument: overview of 14 years in space. *Atmospheric Chemistry and Physics*, 18(8):5699–5745, April 2018. ISSN 1680-7324. doi: 10.5194/acp-18-5699-2018. URL https://acp.copernicus.org/articles/18/5699/2018/.

Lhotka, O. and Kyselý, J. Characterizing joint effects of spatial extent, temperature magnitude and duration of heat waves and cold spells over Central Europe. *International Journal of Climatology*, 35(7):1232–1244, June 2015. ISSN 08998418. doi: 10.1002/joc.4050. URL https://onlinelibrary.wiley.com/doi/10.1002/joc.4050.

Lin, M., Horowitz, L., Xie, Y., Paulot, F., Malyshev, S., Shevliakova, E., Finco, A., Gerosa, G., Kubistin, D., and Pilegaard, K. Vegetation feedbacks during drought exacerbate ozone air pollution extremes in Europe. *Nature Climate Change*, 10(444-451), 2020. doi: https://doi.org/10.1038/s41558-020-0743-y.

Lionello, P., Malanotte-Rizzoli, P., Boscolo, R., Alpert, P., Artale, V., Li, L., Luterbacher, J., May, W., Trigo, R., Tsimplis, M., Ulbrich, U., and Xoplaki, E. The Mediterranean climate: An overview of the main characteristics and issues. In *Developments in Earth and Environmental Sciences*, volume 4, pages 1–26. Elsevier, 2006. ISBN 978-0-444-52170-5. doi: 10.1016/S1571-9197(06)80003-0. URL `https://linkinghub.elsevier.com/retrieve/pii/S1571919706800030`.

Liss, P. S. and Mervilat, L. Air-Sea Gas Exchange Rates: Introduction and Synthesis. *Springer Netherlands, Dordrecht*, pages 113–127, 1986. URL `https://doi.org/10.1007/978-94-009-4738-2_5`.

Liu, X., He, B., Guo, L., Huang, L., and Chen, D. Similarities and Differences in the Mechanisms Causing the European Summer Heatwaves in 2003, 2010, and 2018. *Earth's Future*, 8(4), April 2020. ISSN 2328-4277, 2328-4277. doi: 10.1029/2019EF001386. URL `https://onlinelibrary.wiley.com/doi/abs/10.1029/2019EF001386`.

Loveland, T. R. and Belward, A. S. The IGBP-DIS global 1km land cover data set, DISCover: First results. *International Journal of Remote Sensing*, 18:3289–3295, 1997. doi: https://doi.org/10.1080/014311697217099.

Lu, X., Zhang, L., and Shen, L. Meteorology and Climate Influences on Tropospheric Ozone: a Review of Natural Sources, Chemistry, and Transport Patterns. *Current Pollution Reports*, 5(4):238–260, December 2019. ISSN 2198-6592. doi: 10.1007/s40726-019-00118-3. URL `http://link.springer.com/10.1007/s40726-019-00118-3`.

Mahowald, N. M., Scanza, R., Brahney, J., Goodale, C. L., Hess, P. G., Moore, J. K., and Neff, J. Aerosol Deposition Impacts on Land and Ocean Carbon Cycles. *Current Climate Change Reports*, 3(1):16–31, March 2017. ISSN 2198-6061. doi: 10.1007/s40641-017-0056-z. URL `http://link.springer.com/10.1007/s40641-017-0056-z`.

Maignan, F., Bréon, F.-M., Chevallier, F., Viovy, N., Ciais, P., Garrec, C., Trules, J., and Mancip, M. Evaluation of a Global Vegetation Model using time series of satellite vegetation indices. *Geoscientific Model Development*, 4(4):1103–1114, December 2011. ISSN 1991-9603. doi: 10.5194/gmd-4-1103-2011. URL `https://gmd.copernicus.org/articles/4/1103/2011/`.

Mailler, S., Menut, L., Khvorostyanov, D., Valari, M., Couvidat, F., Siour, G., Turquety, S., Briant, R., Tuccella, P., Bessagnet, B., Colette, A., Létinois, L., Markakis, K., and Meleux, F. CHIMERE-2017: from urban to hemispheric chemistry-transport modeling. *Geoscientific Model Development*, 10(6):2397–2423, June 2017. ISSN 1991-9603. doi: 10.5194/gmd-10-2397-2017. URL `https://gmd.copernicus.org/articles/10/2397/2017/`.

Majdi, M., Sartelet, K., Lanzafame, G. M., Couvidat, F., Kim, Y., Chrit, M., and Turquety, S. Precursors and formation of secondary organic aerosols from wildfires in the Euro-Mediterranean region. *Atmospheric Chemistry and Physics*, 19(8):5543–5569, April 2019. ISSN 1680-7324. doi: 10.5194/acp-19-5543-2019. URL `https://acp.copernicus.org/articles/19/5543/2019/`.

Marticorena, B. and Bergametti, G. Modeling the atmospheric dust cycle: 1. Design of a soil-derived dust emission scheme. *Journal of Geophysical Research*, 100(D8):16415, 1995. ISSN 0148-0227. doi: 10.1029/95JD00690. URL `http://doi.wiley.com/10.1029/95JD00690`.

McKee, T. B., Doesken, N. J., Kleist, J., and others. The relationship of drought frequency and duration to time scales. In *Proceedings of the 8th Conference on Applied Climatology*, volume 17, pages 179–183. American Meteorological Society Boston, MA, 1993. Issue: 22.

Menut, L., Bessagnet, B., Khvorostyanov, D., Beekmann, M., Blond, N., Colette, A., Coll, I., Curci, G., Foret, G., Hodzic, A., Mailler, S., Meleux, F., Monge, J.-L., Pison, I., Siour, G., Turquety, S., Valari, M., Vautard, R., and Vivanco, M. G. CHIMERE 2013: a model for regional atmospheric composition modelling. *Geoscientific Model Development*, 6(4):981–1028, July 2013. ISSN 1991-9603. doi: 10.5194/gmd-6-981-2013. URL `https://gmd.copernicus.org/articles/6/981/2013/`.

Menut, L., Bessagnet, B., Briant, R., Cholakian, A., Couvidat, F., Mailler, S., Pennel, R., Siour, G., Tuccella, P., Turquety, S., and Valari, M. The CHIMERE v2020r1 online chemistry-transport model. preprint, Atmospheric sciences, April 2021. URL `https://gmd.copernicus.org/preprints/gmd-2021-96/`.

Mertens, M., Kerkweg, A., Grewe, V., Jöckel, P., and Sausen, R. Attributing ozone and its precursors to land transport emissions in Europe and Germany. *Atmospheric Chemistry and Physics*, 20(13):7843–7873, July 2020. ISSN 1680-7324. doi: 10.5194/acp-20-7843-2020. URL `https://acp.copernicus.org/articles/20/7843/2020/`.

Messina, P., Lathière, J., Sindelarova, K., Vuichard, N., Granier, C., Ghattas, J., Cozic, A., and Hauglustaine, D. A. Global biogenic volatile organic compound emissions in the ORCHIDEE and MEGAN models and sensitivity to key parameters. *Atmospheric Chem-*

*istry and Physics*, 16(22):14169–14202, November 2016. ISSN 1680-7324. doi: 10.5194/acp-16-14169-2016. URL `https://acp.copernicus.org/articles/16/14169/2016/`.

Millet, D. B., Jacob, D. J., Turquety, S., Hudman, R. C., Wu, S., Fried, A., Walega, J., Heikes, B. G., Blake, D. R., Singh, H. B., Anderson, B. E., and Clarke, A. D. Formaldehyde distribution over North America: Implications for satellite retrievals of formaldehyde columns and isoprene emission. *Journal of Geophysical Research*, 111(D24):D24S02, 2006. ISSN 0148-0227. doi: 10.1029/2005JD006853. URL `http://doi.wiley.com/10.1029/2005JD006853`.

Millet, D. B., Jacob, D. J., Boersma, K. F., Fu, T.-M., Kurosu, T. P., Chance, K., Heald, C. L., and Guenther, A. Spatial distribution of isoprene emissions from North America derived from formaldehyde column measurements by the OMI satellite sensor. *Journal of Geophysical Research*, 113(D2):D02307, January 2008. ISSN 0148-0227. doi: 10.1029/2007JD008950. URL `http://doi.wiley.com/10.1029/2007JD008950`.

Moatti, J.-P., Thiébault, S., and eds. *The Mediterranean region under climate change: a scientific update*. IRD éditions, Marseille, 2018. ISBN 978-2-7099-2219-7.

Molina, M. O., Sánchez, E., and Gutiérrez, C. Future heat waves over the Mediterranean from an Euro-CORDEX regional climate model ensemble. *Scientific Reports*, 10(1):8801, December 2020. ISSN 2045-2322. doi: 10.1038/s41598-020-65663-0. URL `http://www.nature.com/articles/s41598-020-65663-0`.

Monahan, E. In The Role of Air-Sea Exchange in Geochemical Cyclong, chap. The ocean as a source of atmospheric particles. *Kluwer Academic Publishers, Dordrecht, Holland*, pages 129–163, 1986.

Moriondo, M., Good, P., Durao, R., Bindi, M., Giannakopoulos, C., and Corte-Real, J. Potential impact of climate change on fire risk in the Mediterranean area. *Climate Research*, 31:85–95, June 2006. ISSN 0936-577X, 1616-1572. doi: 10.3354/cr031085. URL `http://www.int-res.com/abstracts/cr/v31/n1/p85-95/`.

Müller, J.-F., Stavrakou, T., Wallens, S., De Smedt, I., Van Roozendael, M., Potosnak, M. J., Rinne, J., Munger, B., Goldstein, A., and Guenther, A. B. Global isoprene emissions estimated using MEGAN, ECMWF analyses and a detailed canopy environment model. *Atmos. Chem. Phys.*, 8:1329–1341, 2008. URL `https://acp.copernicus.org/articles/8/1329/2008/`.

Myneni, R., Knyazikhin, Y., and Park, T. MOD15A2H MODIS/terra leaf area index/FPAR 8-day L4 global 500 m SIN grid V006. *NASA EOSDIS Land Processes DAAC*, 2015. URL `https://modis.gsfc.nasa.gov/data/dataprod/mod15.php`.

Nakanishi, M. and Niino, H. Development of an improved turbulence closure model for the atmospheric boundary layer. *Journal of the Meteorological Society of Japan. Ser. II*, 87(5): 895–912, 2009. URL `https://doi.org/10.2151/jmsj.87.895`. Publisher: Meteorological Society of Japan.

Nicholson, S. E., Tucker, C. J., and Ba, M. B. Desertification, Drought, and Surface Vegetation: An Example from the West African Sahe. *Bulletin of the American Meteorological Society*, 79(5):815–830, 1998. doi: https://doi.org/10.1175/1520-0477(1998)079<0815:DDASVA>2.0.CO;2. URL `https://journals.ametsoc.org/view/journals/bams/79/5/1520-0477_1998_079_0815_ddasva_2_0_co_2.xml`.

NRC. *Rethinking the ozone problem in urban and regional air pollution*. National academies press edition, 1992. National Research Council.

Nuvolone, D., Petri, D., and Voller, F. The effects of ozone on human heatlh. *Environ Sci Pollut Res*, pages 8074–8088, 2018. URL `https://doi.org/10.1007/s11356-017-9239-3`. Section: 25.

Omrani, H., Drobinski, P., and Dubos, T. Using nudging to improve global-regional dynamic consistency in limited-area climate modeling: What should we nudge? *Climate Dynamics*, 44(5-6):1627–1644, 2015. URL `https://doi.org/10.1007/s00382-014-2453-5`. Publisher: Springer.

Otero, N., Jurado, O., Butler, T., and Rust, H. W. The impact of atmospheric blocking on the compounding effect of ozone pollution and temperature: A copula-based approach. preprint, Aerosols/Atmospheric Modelling/Troposphere/Chemistry (chemical composition and reactions), April 2021. URL `https://acp.copernicus.org/preprints/acp-2021-297/`.

Palmer, W. C. *Meteorological drought*. Washington, DC, us department of commerce, weather bureau edition, 1965.

Panthou, G., Vrac, M., Drobinski, P., Bastin, S., and Li, L. Impact of model resolution and Mediterranean sea coupling on hydrometeorological extremes in RCMs in the frame of HyMeX and MED-CORDEX. *Climate Dynamics*, 51:915–932, 2018. URL `https://doi.org/10.1007/s00382-016-3374-2`.

Park, S. and Bretherton, C. S. The University of Washington shallow convection and moist turbulence schemes and their impact on climate simulations with the Community Atmosphere Model. *Journal of Climate*, 22(12):3449–3469, 2009. URL `https://doi.org/10.1175/2008JCLI2557.1`.

Parrish, D. D., Derwent, R. G., and Staehelin, J. Long-term changes in northern mid-latitude tropospheric ozone concentrations: Synthesis of two recent analyses. *Atmospheric Environment*, 248:118227, March 2021. ISSN 13522310. doi: 10.1016/j.atmosenv.2021.118227. URL `https://linkinghub.elsevier.com/retrieve/pii/S1352231021000455`.

Paz, D. d. l., Vedrenne, M., Borge, R., Lumbreras, J., Manuel de Andrés, J., Pérez, J., Rodríguez, E., Karanasiou, A., Moreno, T., Boldo, E., and Linares, C. Modelling Saharan dust transport into the Mediterranean basin with CMAQ. *Atmospheric Environment*, 70: 337–350, May 2013. ISSN 13522310. doi: 10.1016/j.atmosenv.2013.01.013. URL `https://linkinghub.elsevier.com/retrieve/pii/S1352231013000265`.

Perkins-Kirkpatrick, S. E. and Gibson, P. B. Changes in regional heatwave characteristics as a function of increasing global temperature. *Scientific Reports*, 7(1):12256, December 2017. ISSN 2045-2322. doi: 10.1038/s41598-017-12520-2. URL `http://www.nature.com/articles/s41598-017-12520-2`.

Pfeifroth, U., Sanchez-Lorenzo, A., Manara, V., Trentmann, J., and Hollmann, R. Trends and variability of surface solar radiation in Europe based on surface-and satellite-based data records. *Journal of Geophysical Research: Atmospheres*, 123(3):1735–1754, 2018. URL `https://doi.org/10.1002/2017JD027418`. Publisher: Wiley Online Library.

Philandras, C. M., Nastos, P. T., Kapsomenakis, J., Douvis, K. C., Tselioudis, G., and Zerefos, C. S. Long term precipitation trends and variability within the Mediterranean region. *Natural Hazards and Earth System Sciences*, 11(12):3235–3250, December 2011. ISSN 1684-9981. doi: 10.5194/nhess-11-3235-2011. URL `https://nhess.copernicus.org/articles/11/3235/2011/`.

Polcher, J., McAvaney, B., Viterbo, P., Gaertner, M.-A., Hahmann, A., Mahfouf, J.-F., Noilhan, J., Phillips, T., Pitman, A., Schlosser, C., and others. A proposal for a general interface between land surface schemes and general circulation models. *Global and Planetary Change*, 19(1-4):261–276, 1998. URL `https://doi.org/10.1016/S0921-8181(98)00052-6`. Publisher: Elsevier.

Porter, W. C. and Heald, C. L. The mechanisms and meteorological drivers of the summertime ozone–temperature relationship. *Atmospheric Chemistry and Physics*, 19(21): 13367–13381, October 2019. ISSN 1680-7324. doi: 10.5194/acp-19-13367-2019. URL `https://acp.copernicus.org/articles/19/13367/2019/`.

Potosnak, M. J., LeStourgeon, L., Pallardy, S. G., Hosman, K. P., Gu, L., Karl, T., Geron, C., and Guenther, A. B. Observed and modeled ecosystem isoprene fluxes from an oak-dominated temperate forest and the influence of drought stress. *Atmospheric Environment*, 84:314–322, February 2014. ISSN 13522310. doi: 10.1016/j.atmosenv.2013.11.055. URL https://linkinghub.elsevier.com/retrieve/pii/S1352231013009059.

Raymond, F., Ullmann, A., Camberlin, P., Drobinski, P., and Smith, C. C. Extreme dry spell detection and climatology over the Mediterranean Basin during the wet season. *Geophysical Research Letters*, 43(13):7196–7204, July 2016. ISSN 00948276. doi: 10.1002/2016GL069758. URL http://doi.wiley.com/10.1002/2016GL069758.

Raymond, F., Ullmann, A., and Camberlin, P. Très longs épisodes secs hivernaux dans le bassin méditerranéen : variabilité spatio-temporelle et impact sur la production céréalière en Espagne. *Cybergeo*, June 2018a. ISSN 1278-3366. doi: 10.4000/cybergeo.29156. URL http://journals.openedition.org/cybergeo/29156.

Raymond, F., Ullmann, A., Camberlin, P., Oueslati, B., and Drobinski, P. Atmospheric conditions and weather regimes associated with extreme winter dry spells over the Mediterranean basin. *Climate dynamics*, 50(11-12):4437–4453, 2018b. URL https://doi.org/10.1007/s00382-017-3884-6. Publisher: Springer.

Richards, N. A. D., Arnold, S. R., Chipperfield, M. P., Miles, G., Rap, A., Siddans, R., Monks, S. A., and Hollaway, M. J. The Mediterranean summertime ozone maximum: global emission sensitivities and radiative impacts. *Atmospheric Chemistry and Physics*, 13(5):2331–2345, March 2013. ISSN 1680-7324. doi: 10.5194/acp-13-2331-2013. URL https://acp.copernicus.org/articles/13/2331/2013/.

Rivoire, P., Tramblay, Y., Neppel, L., Hertig, E., and Vicente-Serrano, S. M. Impact of the dry-day definition on Mediterranean extreme dry-spell analysis. *Natural Hazards and Earth System Sciences*, 19(8):1629–1638, August 2019. ISSN 1684-9981. doi: 10.5194/nhess-19-1629-2019. URL https://nhess.copernicus.org/articles/19/1629/2019/.

Russo, S., Sillmann, J., and Fischer, E. M. Top ten European heatwaves since 1950 and their occurrence in the coming decades. *Environmental Research Letters*, 10(12):124003, December 2015. ISSN 1748-9326. doi: 10.1088/1748-9326/10/12/124003. URL https://iopscience.iop.org/article/10.1088/1748-9326/10/12/124003.

Ruti, P. M., Somot, S., Giorgi, F., Dubois, C., Flaounas, E., Obermann, A., Dell'Aquila, A., Pisacane, G., Harzallah, A., Lombardi, E., Ahrens, B., Akhtar, N., Alias, A., Arsouze, T., Aznar, R., Bastin, S., Bartholy, J., Béranger, K., Beuvier, J., Bouffies-Cloché, S., Brauch, J., Cabos, W., Calmanti, S., Calvet, J.-C., Carillo, A., Conte, D., Coppola, E., Djurdjevic, V., Drobinski, P., Elizalde-Arellano, A., Gaertner, M., Galàn, P., Gallardo, C., Gualdi, S., Goncalves, M., Jorba, O., Jordà, G., L'Heveder, B., Lebeaupin-Brossier, C., Li, L., Liguori, G., Lionello, P., Maciàs, D., Nabat, P., Önol, B., Raikovic, B., Ramage, K., Sevault, F., Sannino, G., Struglia, M. V., Sanna, A., Torma, C., and Vervatis, V. Med-CORDEX Initiative for Mediterranean Climate Studies. *Bulletin of the American Meteorological Society*, 97 (7):1187–1208, July 2016. ISSN 0003-0007, 1520-0477. doi: 10.1175/BAMS-D-14-00176.1. URL https://journals.ametsoc.org/doi/10.1175/BAMS-D-14-00176.1.

Ryder, J., Polcher, J., Peylin, P., Ottlé, C., Chen, Y., van Gorsel, E., Haverd, V., McGrath, M. J., Naudts, K., Otto, J., Valade, A., and Luyssaert, S. A multi-layer land surface energy budget model for implicit coupling with global atmospheric simulations. *Geoscientific Model Development*, 9(1):223–245, January 2016. ISSN 1991-9603. doi: 10.5194/gmd-9-223-2016. URL https://gmd.copernicus.org/articles/9/223/2016/.

Safieddine, S., Boynard, A., Coheur, P.-F., Hurtmans, D., Pfister, G., Quennehen, B., Thomas, J. L., Raut, J.-C., Law, K. S., Klimont, Z., Hadji-Lazaro, J., George, M., and Clerbaux, C. Summertime tropospheric ozone assessment over the Mediterranean region using the thermal infrared IASI/MetOp sounder and the WRF-Chem model. *Atmospheric Chemistry and Physics*, 14(18):10119–10131, September 2014. ISSN 1680-7324. doi: 10.5194/acp-14-10119-2014. URL https://acp.copernicus.org/articles/14/10119/2014/.

San-Miguel-Ayanz, J., Schulte, E., Schmuck, G., Camia, A., Strobl, P., Liberta, G., Giovando, C., Boca, R., Sedano, F., Kempeneers, P., and others. Comprehensive monitoring of wildfires in Europe: the European forest fire information system (EFFIS). In *Approaches to managing disaster-Assessing hazards, emergencies and disaster impacts*. IntechOpen, 2012. URL https://doi.org/10.5772/28441.

San-Miguel-Ayanz, J., Moreno, J. M., and Camia, A. Analysis of large fires in European Mediterranean landscapes: Lessons learned and perspectives. *Forest Ecology and Management*, 294:11–22, April 2013. ISSN 03781127. doi: 10.1016/j.foreco.2012.10.050. URL https://linkinghub.elsevier.com/retrieve/pii/S0378112712006561.

Sarris, D., Christopoulou, A., Angelonidi, E., Koutsias, N., Fulé, P. Z., and Arianoutsou, M. Increasing extremes of heat and drought associated with recent severe wildfires in southern Greece. *Regional environmental change*, 14(3):1257–1268, 2014. URL https://doi.org/10.1007/s10113-013-0568-6. Publisher: Springer.

Saunier, A., Ormeño, E., Boissard, C., Wortham, H., Temime-Roussel, B., Lecareux, C., Armengaud, A., and Fernandez, C. Effect of mid-term drought on Quercus pubescens BVOCs' emission seasonality and their dependency on light and/or temperature. *Atmospheric Chemistry and Physics*, 17(12):7555–7566, June 2017. ISSN 1680-7324. doi: 10.5194/acp-17-7555-2017. URL https://acp.copernicus.org/articles/17/7555/2017/.

Sharkey, T. D., Singsaas, E. L., Lerdau, M. T., and Geron, C. D. Weather effects on isoprene emission capacity and applications in emissions algorithms. *Ecological Applications*, 9(4): 1132–1137, 2000. ISSN 1051-0761. URL `https://esajournals.onlinelibrary.wiley.com/doi/abs/10.1890/1051-0761%281999%29009%5B1132%3AWEOIEC%5D2.0.CO%3B2`.

Sicard, P., De Marco, A., Troussier, F., Renou, C., Vas, N., and Paoletti, E. Decrease in surface ozone concentrations at Mediterranean remote sites and increase in the cities. *Atmospheric Environment*, 79:705–715, November 2013. ISSN 13522310. doi: 10.1016/j.atmosenv.2013.07.042. URL `https://linkinghub.elsevier.com/retrieve/pii/S1352231013005712`.

Simpson, D., Fagerli, H., Jonson, J. E., Tsyro, S., Wind, P., and Tuovien, J. P. Transboundary Acidification, Eutrophication and Ground Level Ozone in Europe. Part I: Unified EMEP Model Description. Technical report, Norwegian Meteorological Institute, 2003.

Simpson, D., Benedictow, A., Berge, H., Bergström, R., Emberson, L. D., Fagerli, H., Flechard, C. R., Hayman, G. D., Gauss, M., Jonson, J. E., Jenkin, M. E., Nyíri, A., Richter, C., Semeena, V. S., Tsyro, S., Tuovinen, J.-P., Valdebenito, Á., and Wind, P. The EMEP MSC-W chemical transport model – technical description. *Atmospheric Chemistry and Physics*, 12(16):7825–7865, August 2012. ISSN 1680-7324. doi: 10.5194/acp-12-7825-2012. URL `https://acp.copernicus.org/articles/12/7825/2012/`.

Singh, V. P., Guo, H., and Yu, F. X. Parameter estimation for 3-parameter log-logistic distribution (LLD3) by Pome. *Stochastic Hydrology and Hydraulics*, 7(3):163–177, September 1993. ISSN 0931-1955, 1436-3259. doi: 10.1007/BF01585596. URL `http://link.springer.com/10.1007/BF01585596`.

Skamarock, W. C., Klemp, J. B., Dudhia, J., Gill, D. O., Barker, D. M., Wang, W., and Powers, J. G. A description of the Advanced Research WRF version 3. NCAR/TN-475+STR. Technical report, University Corporation for Atmospheric Research, 2008. URL `http://dx.doi.org/10.5065/D68S4MVH`.

Skamarock, W. C., Klemp, J. B., Dudhia, J., Gill, D. O., Liu, Z., Berner, J., Wang, W., Powers, J. G., Duda, M. G., Barker, D. M., and Huang, X.-Y. A Description of the Advanced Research WRF Model Version 4. Technical report, University Corporation for Atmospheric Research, 2019.

Spinoni, J., Naumann, G., Vogt, J. V., and Barbosa, P. The biggest drought events in Europe from 1950 to 2012. *Journal of Hydrology: Regional Studies*, 3:509–524, March 2015. ISSN 22145818. doi: 10.1016/j.ejrh.2015.01.001. URL `https://linkinghub.elsevier.com/retrieve/pii/S2214581815000026`.

Spinoni, J., Vogt, J. V., Naumann, G., Barbosa, P., and Dosio, A. Will drought events become more frequent and severe in Europe? *International Journal of Climatology*, 38(4):1718–1736, March 2018. ISSN 08998418. doi: 10.1002/joc.5291. URL `https://onlinelibrary.wiley.com/doi/10.1002/joc.5291`.

Sprintsin, M., Karnieli, A., Berliner, P., Rotenberg, E., Yakir, D., and Cohen, S. Evaluating the performance of the MODIS Leaf Area Index (LAI) product over a Mediterranean dryland planted forest. *International journal of Remote sensing*, 30(19):5061–5069, 2009. URL `https://doi.org/10.1080/01431160903032885`. Publisher: Taylor & Francis.

Stéfanon, M., D'Andrea, F., and Drobinski, P. Heatwave classification over Europe and the Mediterranean region. *Environmental Research Letters*, 7(1):014023, March 2012a. ISSN 1748-9326. doi: 10.1088/1748-9326/7/1/014023. URL `https://iopscience.iop.org/article/10.1088/1748-9326/7/1/014023`.

Stéfanon, M., Drobinski, P., D'Andrea, F., and Noblet-Ducoudré, N. Effects of interactive vegetation phenology on the 2003 summer heat waves. *Journal of Geophysical Research: Atmospheres*, 117(D24), 2012b. URL `https://doi.org/10.1029/2012JD018187`. Publisher: Wiley Online Library.

Stéfanon, M., Drobinski, P., D'Andrea, F., Lebeaupin-Brossier, C., and Bastin, S. Soil moisture-temperature feedbacks at meso-scale during summer heat waves over Western Europe. *Climate Dynamics*, 42(5-6):1309–1324, March 2014. ISSN 0930-7575, 1432-0894. doi: 10.1007/s00382-013-1794-9. URL `http://link.springer.com/10.1007/s00382-013-1794-9`.

Stegehuis, A. I., Vautard, R., Ciais, P., Teuling, A. J., Jung, M., and Yiou, P. Summer temperatures in Europe and land heat fluxes in observation-based data and regional climate model simulations. *Climate dynamics*, 41(2):455–477, 2013. URL `https://doi.org/10.1007/s00382-012-1559-x`. Publisher: Springer.

Strode, S. A., Ziemke, J. R., Oman, L. D., Lamsal, L. N., Olsen, M. A., and Liu, J. Global changes in the diurnal cycle of surface ozone. *Atmospheric Environment*, 199:323–333, February 2019. ISSN 13522310. doi: 10.1016/j.atmosenv.2018.11.028. URL `https://linkinghub.elsevier.com/retrieve/pii/S1352231018308008`.

Svoboda, M. D. and Fuchs, B. A. *Handbook of drought indicators and indices.* Geneva, world meteorological organization and global water partnership edition, 2016. ISBN 978-92-63-11173-9. OCLC: 958433349.

Tai, A. P. K., Martin, M. V., and Heald, C. L. Threat to future global food security from climate change and ozone air pollution. *Nature Climate Change*, 4(9):817–821, September

2014. ISSN 1758-678X, 1758-6798. doi: 10.1038/nclimate2317. URL `http://www.nature.com/articles/nclimate2317`.

Tepley, A. J., Thomann, E., Veblen, T. T., Perry, G. L. W., Holz, A., Paritsis, J., Kitzberger, T., and Anderson-Teixeira, K. J. Influences of fire–vegetation feedbacks and post-fire recovery rates on forest landscape vulnerability to altered fire regimes. *Journal of Ecology*, 106(5):1925–1940, September 2018. ISSN 0022-0477, 1365-2745. doi: 10.1111/1365-2745.12950. URL `https://onlinelibrary.wiley.com/doi/10.1111/1365-2745.12950`.

Thornthwaite, C. W. An Approach toward a Rational Classification of Climate. *Geographical Review*, 38(1):55–94, 1948. URL `https://www.jstor.org/stable/210739?seq=1#metadata_info_tab_contents`.

Thunis, P., Pernigotti, D., and Gerboles, M. Model quality objectives based on measurement uncertainty. Part I: Ozone. *Atmospheric Environment*, 79:861–868, November 2013. ISSN 13522310. doi: 10.1016/j.atmosenv.2013.05.018. URL `https://linkinghub.elsevier.com/retrieve/pii/S1352231013003610`.

Tramblay, Y., Koutroulis, A., Samaniego, L., Vicente-Serrano, S. M., Volaire, F., Boone, A., Le Page, M., Llasat, M. C., Albergel, C., Burak, S., Cailleret, M., Kalin, K. C., Davi, H., Dupuy, J.-L., Greve, P., Grillakis, M., Hanich, L., Jarlan, L., Martin-StPaul, N., Martínez-Vilalta, J., Mouillot, F., Pulido-Velazquez, D., Quintana-Seguí, P., Renard, D., Turco, M., Türkeş, M., Trigo, R., Vidal, J.-P., Vilagrosa, A., Zribi, M., and Polcher, J. Challenges for drought assessment in the Mediterranean region under future climate scenarios. *Earth-Science Reviews*, 210:103348, November 2020. ISSN 00128252. doi: 10.1016/j.earscirev.2020.103348. URL `https://linkinghub.elsevier.com/retrieve/pii/S0012825220303949`.

Trigo, R. M., Pozo-Vázquez, D., Osborn, T. J., Castro-Díez, Y., Gámiz-Fortis, S., and Esteban-Parra, M. J. North Atlantic Oscillation influence on precipitation, river flow and water resources in the Iberian Peninsula. *International Journal of Climatology*, 24(8):925–944, 2004. URL `https://doi.org/10.1002/joc.1048`. Publisher: Wiley Online Library.

Turco, M., Bedia, J., Di Liberto, F., Fiorucci, P., von Hardenberg, J., Koutsias, N., Llasat, M.-C., Xystrakis, F., and Provenzale, A. Decreasing fires in Mediterranean Europe. *PLOS one*, 11(3):e0150663, 2016. URL `https://doi.org/10.1371/journal.pone.0150663`. Publisher: Public Library of Science.

Turco, M., von Hardenberg, J., AghaKouchak, A., Llasat, M. C., Provenzale, A., and Trigo, R. M. On the key role of droughts in the dynamics of summer fires in Mediterranean Europe.

*Scientific reports*, 7(1):81, 2017. URL https://doi.org/10.1038/s41598-017-00116-9. Publisher: Nature Publishing Group.

Turco, M., Herrera, S., Tourigny, E., Chuvieco, E., and Provenzale, A. A comparison of remotely-sensed and inventory datasets for burned area in Mediterranean Europe. *International Journal of Applied Earth Observation and Geoinformation*, 82:101887, 2019. URL https://doi.org/10.1016/j.jag.2019.05.020. Publisher: Elsevier.

Turner, J. and Lawson, B. Weather in the Canadian forest fire danger rating system. A user guide to national standards and practices. Information Report BC-X-177, Fisheries and Environment Canada, Canadian Forest Service, Victoria, BC, 1978. URL https://cfs.nrcan.gc.ca/publications?id=1843.

Turquety, S., Menut, L., Bessagnet, B., Anav, A., Viovy, N., Maignan, F., and Wooster, M. APIFLAME v1.0: high-resolution fire emission model and application to the Euro-Mediterranean region. *Geoscientific Model Development*, 7(2):587–612, April 2014. ISSN 1991-9603. doi: 10.5194/gmd-7-587-2014. URL https://gmd.copernicus.org/articles/7/587/2014/.

Turquety, S., Menut, L., Siour, G., Mailler, S., Hadji-Lazaro, J., George, M., Clerbaux, C., Hurtmans, D., and Coheur, P.-F. APIFLAME v2.0 biomass burning emissions model: impact of refined input parameters on atmospheric concentration in Portugal in summer 2016. *Geoscientific Model Development*, 13(7):2981–3009, July 2020. ISSN 1991-9603. doi: 10.5194/gmd-13-2981-2020. URL https://gmd.copernicus.org/articles/13/2981/2020/.

Van Dingenen, R., Dentener, F. J., Raes, F., Krol, M. C., Emberson, L., and Cofala, J. The global impact of ozone on agricultural crop yields under current and future air quality legislation. *Atmospheric Environment*, 43(3):604–618, January 2009. ISSN 13522310. doi: 10.1016/j.atmosenv.2008.10.033. URL https://linkinghub.elsevier.com/retrieve/pii/S1352231008009424.

Van Leer, B. Towards the ultimate conservative difference scheme. IV. A new approach to numerical convection. *Journal of Computational Physics*, 23(3):276–299, March 1977. ISSN 00219991. doi: 10.1016/0021-9991(77)90095-X. URL https://linkinghub.elsevier.com/retrieve/pii/002199917790095X.

Van Loon, A. F., Stahl, K., Di Baldassarre, G., Clark, J., Rangecroft, S., Wanders, N., Gleeson, T., Van Dijk, A. I. J. M., Tallaksen, L. M., Hannaford, J., Uijlenhoet, R., Teuling, A. J., Hannah, D. M., Sheffield, J., Svoboda, M., Verbeiren, B., Wagener, T., and

Van Lanen, H. A. J. Drought in a human-modified world: reframing drought definitions,understanding, and analysis approaches. *Hydrology and Earth System Sciences*, 20 (9):3631–3650, September 2016. ISSN 1607-7938. doi: 10.5194/hess-20-3631-2016. URL `https://hess.copernicus.org/articles/20/3631/2016/`.

Van Wagner, C. and Pickett, T. Equations and FORTRAN Program for the Canadian Forest Fire Weather Index System. Forestry Technical Report 33, Canadian Forestry Service, Petawawa National Forestry Institute, Chalk River, Ontario, 1985. URL `https://scf.rncan.gc.ca/publications?id=19973&lang=fr_CA`.

Vandentorren, S., Bretin, P., Zeghnoun, A., Mandereau-Bruno, L., Croisier, A., Cochet, C., Ribéron, J., Siberan, I., Declercq, B., and Ledrans, M. August 2003 Heat Wave in France: Risk Factors for Death of Elderly People Living at Home. *European Journal of Public Health*, 16(6):583–591, December 2006. ISSN 1464-360X, 1101-1262. doi: 10.1093/eurpub/ckl063. URL `http://academic.oup.com/eurpub/article/16/6/583/587693/August-2003-Heat-Wave-in-France-Risk-Factors-for`.

Vautard, R., Honore, C., Beekmann, M., and Rouil, L. Simulation of ozone during the August 2003 heat wave and emission control scenarios. *Atmospheric Environment*, 39 (16):2957–2967, May 2005. ISSN 13522310. doi: 10.1016/j.atmosenv.2005.01.039. URL `https://linkinghub.elsevier.com/retrieve/pii/S1352231005000889`.

Vautard, R., Yiou, P., D'Andrea, F., de Noblet, N., Viovy, N., Cassou, C., Polcher, J., Ciais, P., Kageyama, M., and Fan, Y. Summertime European heat and drought waves induced by wintertime Mediterranean rainfall deficit. *Geophysical Research Letters*, 34(7):L07711, April 2007. ISSN 0094-8276. doi: 10.1029/2006GL028001. URL `http://doi.wiley.com/10.1029/2006GL028001`.

Vautard, R., van Aalst, M., Boucher, O., Drouin, A., Haustein, K., Kreienkamp, F., van Oldenborgh, G. J., Otto, F. E. L., Ribes, A., Robin, Y., Schneider, M., Soubeyroux, J.-M., Stott, P., Seneviratne, S. I., Vogel, M. M., and Wehner, M. Human contribution to the record-breaking June and July 2019 heatwaves in Western Europe. *Environmental Research Letters*, 15(9):094077, September 2020. ISSN 1748-9326. doi: 10.1088/1748-9326/aba3d4. URL `https://iopscience.iop.org/article/10.1088/1748-9326/aba3d4`.

Vicente-Serrano, S., Cabello, D., Tomás-Burguera, M., Martín-Hernández, N., Beguería, S., Azorin-Molina, C., and Kenawy, A. Drought Variability and Land Degradation in Semiarid Regions: Assessment Using Remote Sensing Data and Drought Indices (1982–2011). *Remote Sensing*, 7(4):4391–4423, April 2015. ISSN 2072-4292. doi: 10.3390/rs70404391. URL `http://www.mdpi.com/2072-4292/7/4/4391`.

Vicente-Serrano, S. M. Evaluating the impact of drought using remote sensing in a Mediterranean, semi-arid region. *Natural Hazards*, 40(1):173–208, 2007. URL `https://doi.org/10.1007/s11069-006-0009-7`. Publisher: Springer.

Vicente-Serrano, S. M., Beguería, S., and López-Moreno, J. I. A Multiscalar Drought Index Sensitive to Global Warming: The Standardized Precipitation Evapotranspiration Index. *Journal of Climate*, 23(7):1696–1718, April 2010. ISSN 1520-0442, 0894-8755. doi: 10.1175/2009JCLI2909.1. URL `http://journals.ametsoc.org/doi/10.1175/2009JCLI2909.1`.

Vicente-Serrano, S. M., Beguería, S., Lorenzo-Lacruz, J., Camarero, J. J., López-Moreno, J. I., Azorin-Molina, C., Revuelto, J., Morán-Tejeda, E., and Sanchez-Lorenzo, A. Performance of Drought Indices for Ecological, Agricultural, and Hydrological Applications. *Earth Interactions*, 16(10):1–27, September 2012. ISSN 1087-3562. doi: 10.1175/2012EI000434.1. URL `https://journals.ametsoc.org/doi/10.1175/2012EI000434.1`.

Vicente-Serrano, S. M., Gouveia, C., Camarero, J. J., Beguería, S., Trigo, R., López-Moreno, J. I., Azorín-Molina, C., Pasho, E., Lorenzo-Lacruz, J., Revuelto, J., and others. Response of vegetation to drought time-scales across global land biomes. *Proceedings of the National Academy of Sciences*, 110(1):52–57, 2013. URL `https://doi.org/10.1073/pnas.1207068110`. Publisher: National Acad Sciences.

Wang, P., Liu, Y., Dai, J., Fu, X., Wang, X., Guenther, A., and Wang, T. Isoprene Emissions Response to Drought and the Impacts on Ozone and SOA in China. *Journal of Geophysical Research: Atmospheres*, 126(10), May 2021a. ISSN 2169-897X, 2169-8996. doi: 10.1029/2020JD033263. URL `https://onlinelibrary.wiley.com/doi/10.1029/2020JD033263`.

Wang, Y., Tan, X., Huang, L., Wang, Q., Li, H., Zhang, H., Zhang, K., Liu, Z., Traore, D., Yaluk, E., Fu, J. S., and Li, L. The impact of biogenic emissions on ozone formation in the Yangtze River Delta region based on MEGANv3.1. *Air Quality, Atmosphere & Health*, 14(5):763–774, May 2021b. ISSN 1873-9318, 1873-9326. doi: 10.1007/s11869-021-00977-0. URL `https://link.springer.com/10.1007/s11869-021-00977-0`.

Wang, Y., Xie, Y., Dong, W., Ming, Y., Wang, J., and Shen, L. Adverse effects of increasing drought on air quality via natural processes. *Atmospheric Chemistry and Physics*, 17(20):12827–12843, October 2017. ISSN 1680-7324. doi: 10.5194/acp-17-12827-2017. URL `https://acp.copernicus.org/articles/17/12827/2017/`.

Wells, N., Goddard, S., and Hayes, M. J. A Self-Calibrating Palmer Drought Severity Index. *Journal of Climate*, 17:17, 2004.

Wesely, M. Parameterization of surface resistances to gaseous dry deposition in regional-scale numerical models. *Atmospheric Environment*, 41:52–63, 1989. ISSN 13522310. doi: 10.

1016/j.atmosenv.2007.10.058. URL `https://linkinghub.elsevier.com/retrieve/pii/S1352231007009740`.

Xoplaki, E., González-Rouco, J. F., Luterbacher, J., and Wanner, H. Wet season Mediterranean precipitation variability: influence of large-scale dynamics and trends. *Climate Dynamics*, 23(1):63–78, August 2004. ISSN 0930-7575, 1432-0894. doi: 10.1007/s00382-004-0422-0. URL `http://link.springer.com/10.1007/s00382-004-0422-0`.

Yengoh, G. T., Dent, D., Olsson, L., Tengberg, A. E., and Tucker, C. *Use of the Normalized Difference Vegetation Index (NDVI) to assess Land degradation at multiple scales: current status, future trends, and practical considerations.* Springer edition, 2015. URL `https://link.springer.com/book/10.1007/978-3-319-24112-8`.

Yuan, H., Dai, Y., Xiao, Z., Ji, D., and Shangguan, W. Reprocessing the MODIS Leaf Area Index products for land surface and climate modelling. *Remote Sensing of Environment*, 115(5):1171–1187, May 2011. ISSN 00344257. doi: 10.1016/j.rse.2011.01.001. URL `https://linkinghub.elsevier.com/retrieve/pii/S0034425711000149`.

Zampieri, M., D'Andrea, F., Vautard, R., Ciais, P., de Noblet-Ducoudré, N., and Yiou, P. Hot European summers and the role of soil moisture in the propagation of Mediterranean drought. *Journal of Climate*, 22(18):4747–4758, 2009. URL `https://doi.org/10.1175/2009JCLI2568.1`.

Zampieri, M., Ceglar, A., Dentener, F., and Toreti, A. Wheat yield loss attributable to heat waves, drought and water excess at the global, national and subnational scales. *Environmental Research Letters*, 12(6):064008, 2017. URL `https://doi.org/10.1088/1748-9326/aa723b`. Publisher: IOP Publishing.

Zhou, S. S., Tai, A. P. K., Sun, S., Sadiq, M., Heald, C. L., and Geddes, J. A. Coupling between surface ozone and leaf area index in a chemical transport model: strength of feedback and implications for ozone air quality and vegetation health. *Atmospheric Chemistry and Physics*, 18(19):14133–14148, October 2018. ISSN 1680-7324. doi: 10.5194/acp-18-14133-2018. URL `https://acp.copernicus.org/articles/18/14133/2018/`.

Zhu, L., Jacob, D. J., Kim, P. S., Fisher, J. A., Yu, K., Travis, K. R., Mickley, L. J., Yantosca, R. M., Sulprizio, M. P., De Smedt, I., González Abad, G., Chance, K., Li, C., Ferrare, R., Fried, A., Hair, J. W., Hanisco, T. F., Richter, D., Jo Scarino, A., Walega, J., Weibring, P., and Wolfe, G. M. Observing atmospheric formaldehyde (HCHO) from space: validation andintercomparison of six retrievals from four satellites (OMI, GOME2A, GOME2B,OMPS) with SEAC&lt;sup&gt;4&lt;/sup&gt;RS aircraft observations over the southeast US. *Atmospheric Chemistry and Physics*, 16(21):13477–13490, November 2016.

ISSN 1680-7324. doi: 10.5194/acp-16-13477-2016. URL https://acp.copernicus.org/articles/16/13477/2016/.

Zhu, L., Mickley, L. J., Jacob, D. J., Marais, E. A., Sheng, J., Hu, L., Abad, G. G., and Chance, K. Long-term (2005-2014) trends in formaldehyde (HCHO) columns across North America as seen by the OMI satellite instrument: Evidence of changing emissions of volatile organic compounds: HCHO Trend Across North America. *Geophysical Research Letters*, 44(13):7079–7086, July 2017. ISSN 00948276. doi: 10.1002/2017GL073859. URL http://doi.wiley.com/10.1002/2017GL073859.

# Appendices

# Appendix A

# Science outreach paper about air pollution from wildfires

This article was written as part of a mission of science outreach within the Geosciences Unit of the Palais de la Découverte (Universcience). The target audience covers high school students and interested adults. The present version is a pre-print. The Découverte journal n°345 including the printed version of the article can be found here : `https://www.palais-decouverte.fr/fr/lascienceestla/revue-decouverte/n-435-octobre-decembre-2021/articles/#item-grid-121854`

# Les feux de végétation. Quelle empreinte dans l'atmosphère ?

Antoine Guion

L'été 2021 a été sévèrement touché par les feux de végétation, que ce soit en Méditerranée ou en Californie. Largement relayées dans les médias, personne n'a pu passer à côté de ces images impressionnantes de panaches de fumée s'élevant de plus en plus haut dans le ciel. Face à ce phénomène, une multitude de questions viennent dès lors attiser notre curiosité. Jusqu'où ces panaches de fumée sont-ils transportés ? Ont-ils un effet sur la composition de l'atmosphère ? Peuvent-ils polluer l'air respiré à 100 kilomètres du lieu de l'incendie ?

## Introduction

Le feu de végétation est un phénomène mondial, touchant tous types de milieux naturels. Il peut être de cause naturelle ou humaine (volontaire ou accidentelle). Les émissions qui lui sont liées modifient la chimie de l'atmosphère et peuvent mener à des niveaux de pollution élevés. Ces effets font partie des sujets d'étude de nombreux laboratoires scientifiques. L'ère moderne offre à disposition de la recherche scientifique des outils d'observation et de modélisation jusqu'à présent inégalés. Cependant, de nombreuses incertitudes et méconnaissances persistent, notamment quant à la quantification de l'impact des émissions de feux sur la santé humaine.

Afin de mieux comprendre le phénomène et la difficulté du sujet à étudier, retraçons les différentes étapes d'un panache de fumée, de son émission à la surface du sol jusqu'à sa diffusion dans l'air environnant.

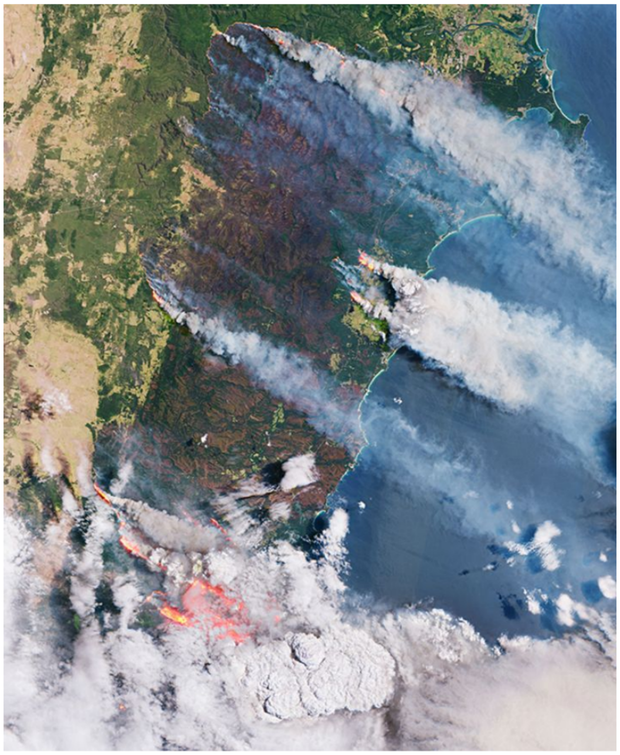

Figure 1: Feux de végétation le long de la côte est de l'Australie et transport de panaches de fumée. Image satellite prise le 31 décembre 2019. © European Union, Copernicus Sentinel-2 imagery.

## Cocktail de composés injectés dans l'atmosphère

Un feu de végétation est le résultat d'une réaction de combustion durant laquelle la matière végétale (biomasse) agit comme combustible et le dioxygène ($O_2$) comme comburant. La troisième condition nécessaire à son déclenchement est la présence d'une énergie d'activation, comme par exemple une cigarette ou un éclair.

Le feu est caractérisé par l'émission de chaleur, de lumière mais également de fumée (fig. 1 et 2). Une large variété de matières particulaires (aérosols) et de gaz composent les panaches de fumée. Ces derniers sont majoritairement injectés dans la troposphère, c'est-à-dire au sein de la couche inférieure de l'atmosphère dont la hauteur varie entre 9 kilomètres (aux pôles) et 17 kilomètres (à l'équateur). A l'échelle mondiale, il a été estimé que 90% des incendies de végétation injectent leurs émissions en dessous de 3 kilomètres d'altitude. Seuls les incendies les plus intenses et avec des conditions météorologiques spécifiques sont capables d'envoyer leur fumée dans la stratosphère, il s'agit de la couche atmosphérique qui se situe au-dessus de la troposphère et dont la limite supérieure atteint environ 50 kilomètres d'altitude.

Parmi les différents gaz émis lors d'un feu de végétation, les gaz à effet de serre se distinguent des gaz polluants. Alors que les gaz à effet de serre tels que le dioxyde de carbone ($CO_2$), ont un impact sur le climat, ils ne sont pas répertoriés comme étant néfastes pour la santé humaine. Les gaz polluants les plus émis par les feux sont le monoxyde de carbone ($CO$), les composés organiques volatiles ($COV$) et les oxydes d'azote (monoxyde et dioxyde d'azote - $NO$ et $NO_2$ regroupés sous l'abréviation $NO_x$). Ils sont tous définis comme des polluants primaires, c'est-à-dire issus directement d'une source d'émission. Ils se différencient des polluants secondaires, résultant d'une réaction chimique avec un polluant primaire. Par exemple, l'ozone ($O_3$) est produit par photolyse (décomposition chimique par la lumière) dans la troposphère à partir du $CO$, des $COV$ ou encore des $NO_x$. Il ne faut pas le confondre avec l'ozone stratosphérique (présent dans la stratosphère) dont l'origine et les effets sont complètement différents. Ce dernier nous protège par exemple du rayonnement ultraviolet (UV) du Soleil.

Les aérosols émis par les feux de végétation sont de composition et taille très variables. Ils sont définis comme des particules de matière solide ou liquide en suspension dans l'atmosphère. Ce sont par exemple des cendres, du carbone suie, du carbone organique, de la poussière minérale, et même des gouttelettes d'eau. Tout comme les gaz polluants, les aérosols peuvent être secondaires. Dans le domaine des sciences de l'atmosphère, ils sont classifiés en fonction de leur taille (fig. 3). Ainsi, les particules fines PM2,5 regroupent tous les aérosols dont le diamètre est inférieur à 2,5 micromètres ($1\mu\text{m} = 10^{-6}m$). Les particules grossières sont comprises entre 2,5 et 10$\mu$m de diamètre. Cependant, l'appellation PM10 regroupe tous les aérosols inférieurs à 10$\mu$m, ce qui inclut également les PM2,5. Les nouvelles recherches en la matière s'intéressent de plus en plus aux particules ultrafines (PM0,1).

Bien que la majorité des incendies émettent les composés présentés ci-avant, la constitution exacte des émissions est propre à chaque incendie. Elle dépend largement du type de végétation brûlée (composition chimique et humidité du combustible) ainsi que des conditions de combustion (complète ou incomplète). D'après une étude portant sur les feux de végétation à l'échelle mondiale entre 2003 et 2008, 340 téragrammes

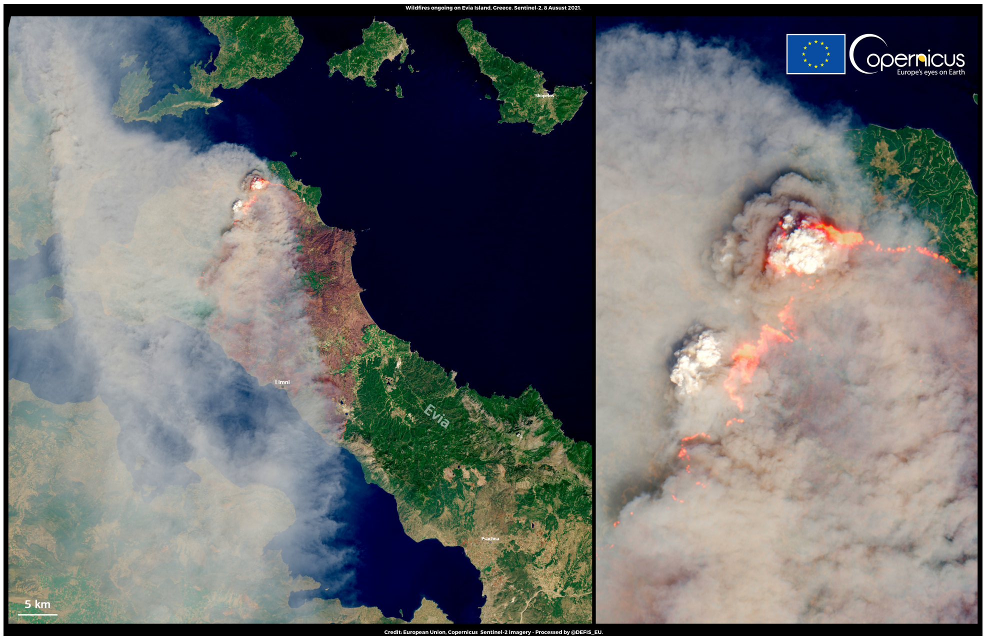

Credit: European Union, Copernicus Sentinel-2 imagery - Processed by @DEFIS_EU.

Figure 2: Image satellite capturant un incendie en cours sur l'île d'Evia, en Grèce, le 8 août 2021. La partie gauche de l'image montre le transport des panaches de fumée en direction du sud-ouest. Celle de droite est un agrandissement du front de flamme. © European Union, Copernicus Sentinel-2 imagery.

($1\text{Tg} = 10^{12}g$), soit 340 000 000 tonnes, de $CO$, 9,5Tg de $NO_x$ et 29,5Tg de PM2,5 seraient émis annuellement. Toutefois, les méthodes d'estimation des émissions sont assez complexes et présentent parfois un degré d'incertitude non-négligeable.

## Voyage à durée variable dans l'atmosphère

Une fois le panache de fumée injecté dans l'atmosphère, celui-là entame un voyage qui ne sera pas de tout repos. En effet, les gaz et aérosols qui le composent, sont transportés et dispersés par les mouvements de l'atmosphère (fig. 1 et 2), mais sont également susceptibles de réagir avec d'autres espèces, voire même de se déposer à la surface de la Terre.

Parlons d'abord du transport d'un panache de fumée dans l'atmosphère, et ce, quelle que soit sa composition chimique. Pour une meilleure compréhension, son déplacement peut être divisé en deux axes : l'un vertical et l'autre horizontal. Le transport vertical, qu'il soit ascendant ou descendant, est principalement déterminé par la stabilité de l'atmosphère. Ainsi, le transport vertical est favorisé dans la zone des trois premiers kilomètres de l'atmosphère. Il s'agit de la couche limite atmosphérique (CLA). Elle est définie comme la couche mélangée par convection suite au rayonnement solaire réémis à la surface de la Terre. L'échelle de temps caractéristique du mélange des gaz polluants et des aérosols au sein de la CLA est d'à peine un à deux jours. Pour ce qui est du reste de la troposphère, le transport vertical prend un peu plus de temps, à savoir un mois, étant donné que les masses d'air y sont plus stables. Toutefois,

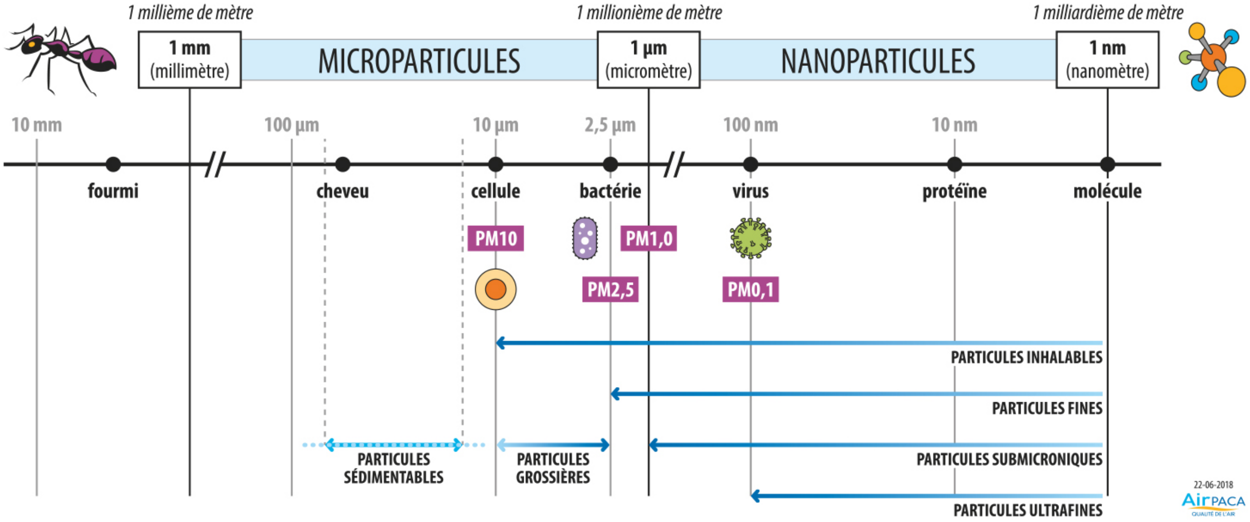

Figure 3: Comparaison des tailles des différentes particules en suspension. © AtmoSud.

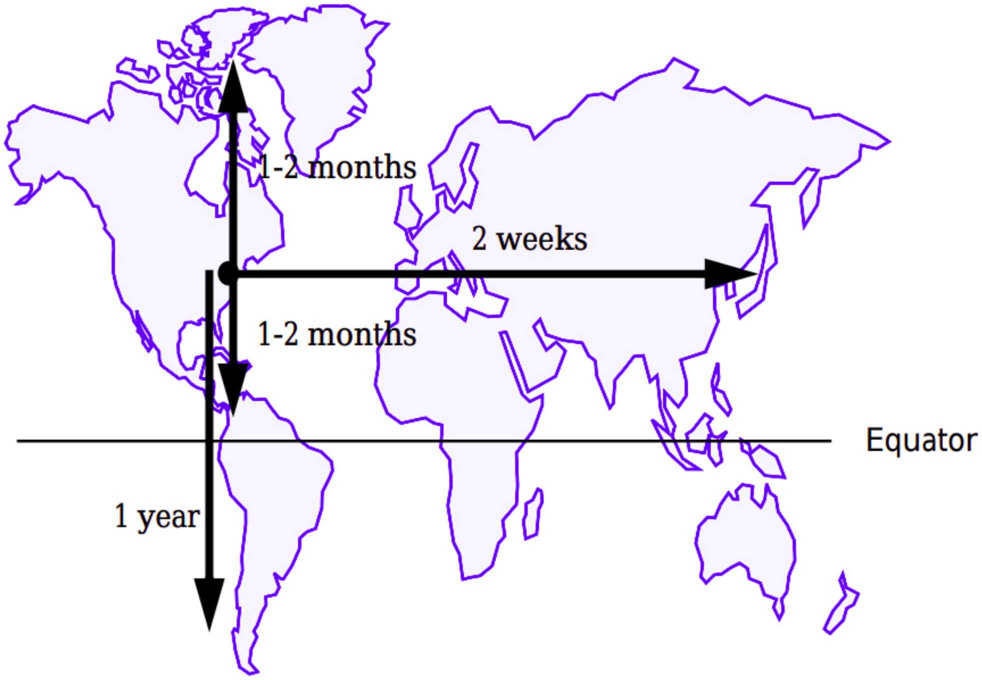

Figure 4: Echelles de temps caractéristiques du transport horizontal des masses d'air. © D. J. Jacobs.

la chaleur dégagée par les flammes peut accélérer le transport vertical par convection.

En ce qui concerne le transport horizontal, il est à la fois déterminé par les vents régionaux et par la circulation générale de l'atmosphère qui elle se fait à l'échelle de la planète. Ces vents régionaux sont appelés «vents géostrophiques». Ils résultent d'un équilibre entre la force de Coriolis (causée par la rotation de la Terre) et la force du gradient de pression atmosphérique (causée par une différence de pression entre une zone d'anticyclone et de dépression). La circulation générale de l'atmosphère est quant à elle dirigée par le rayonnement solaire qui varie en intensité selon la latitude sur Terre. La combinaison de ces processus complexes induit des échelles de temps caractéristiques du transport horizontal très variables, surtout selon la direction (fig. 4). Ainsi, une masse d'air contenant des polluants pourrait mettre plus de un an pour passer de l'hémisphère nord à l'hémisphère sud, alors qu'elle pourrait traverser la totalité de la Terre d'est en ouest en un mois. En juillet 2015, un incendie s'étant déclaré dans la province de Manitoba, au Canada, a émis un panache de fumée à forte concentration en $CO$ (environ 230 microgrammes par mètre cube - $1\mu g/m^3 = 10^{-6} g/m^3$). Celui-là a été transporté par un courant d'altitude (courants-jets) d'ouest en est. Il a été traqué par satellite et détecté à peine une semaine plus tard au niveau de Francfort, en Allemagne.

Le transport par les mouvements atmosphériques est donc déterminant pour expliquer le sens et la direction de propagation des fumées d'incendie. Néanmoins, il faut prendre en compte le fait que chaque composé a un temps de vie dans l'atmosphère bien spécifique. De ce fait, l'étendue spatiale des gaz polluants ou aérosols dépend avant tout de leur durée de résidence dans l'atmosphère. Celle-là est régulée, entre autres, par leur réactivité chimique. La composition chimique ainsi que les propriétés physiques des composés peuvent varier durant leur transport. Les $NO_x$ et l'$O_3$ sont par exemple plus réactifs que les aérosols et le $CO$. Le temps de résidence du $NO_x$ est de quelques jours contre quelques mois pour le $CO$. Ce dernier est donc le gaz polluant avec le plus fort potentiel d'impact sur les populations éloignées de plusieurs centaines de kilomètres.

Les gaz et aérosols peuvent également quitter l'atmosphère par un processus de déposition. On parle de déposition humide lorsque les composés sont ramenés au sol par la pluie (lessivage). La déposition sèche, quant à elle, s'effectue indépendamment des précipitations lorsqu'une parcelle d'air rencontre une surface. Certains gaz et aérosols sont absorbés par le sol ou les plantes.

## Normes de concentration à ne pas dépasser

De par le transport atmosphérique, des concentrations élevées en polluants issus des incendies peuvent se retrouver dans l'air environnant de zones habitées. Afin de pouvoir évaluer au mieux l'ampleur de la pollution causée par un feu, il faut l'isoler de la pollution déjà présente non-attribuable à l'événement considéré (appelée pollution de fond). Par exemple, plusieurs stations de surveillance mises en place par l'association AtmoSud ont mesuré le 22 juillet 2009 des pics de pollution au PM10 dans les rues de Marseille, entre 200 et $300\mu g/m^3$ alors que le niveau de fond variait entre 20 et $80\mu g/m^3$. La raison: un incendie de végétation de plus de 1200 hectares au sud-est de Marseille, dont les rafales de vent ont

Table 1: Réglementation européenne d'après la directive n° 2008/50/CE concernant la qualité de l'air ambiant et un air pur pour l'Europe. Les concentrations limites sont en moyenne sur la période considérée sauf pour l'$O_3$ où il s'agit du maximum journalier.

| Polluant | Concentration limite | | |
|---|---|---|---|
| | Par an | Par jour | Par heure |
| $O_3$ | - | 120 $\mu g/m^3$ (moyennée sur 8 heures) | - |
| $NO_2$ | 40 $\mu g/m^3$ | - | 200 $\mu g/m^3$ |
| $CO$ | - | - | 10 $mg/m^3$ |
| $PM10$ | 40 $\mu g/m^3$ | - | 50 $\mu g/m^3$ |
| $PM2,5$ | 25 $\mu g/m^3$ | - | - |

transporté les fumées jusqu'au centre-ville. Des pics de pollution ont pu être mesurés pendant un peu plus de 24 heures.

Une fois la concentration des différents polluants estimée, la qualité de l'air peut être évaluée comme étant bonne ou mauvaise. En effet, le concept de qualité de l'air se traduit par des normes de concentration à ne pas dépasser pour chaque polluant. Sur la base d'études toxicologiques, une organisation ou un gouvernement peut fixer les limites de concentration audelà desquelles l'air est jugé nocif pour l'être humain. Ainsi, les normes de concentration peuvent être différentes selon l'origine de la réglementation. Il existe des normes à ne pas dépasser au niveau européen (Agence Européenne pour l'Environnement) (tab. 1) mais aussi national (Code français de l'environnement par exemple). L'Organisation Mondiale de la Santé (OMS) a publié également des valeurs indicatives. Même si elles ne font pas l'objet d'un contrôle permanent et obligatoire, elles sont plus strictes, c'est-à-dire avec des concentrations limites plus basses. Les normes de qualité de l'air sont généralement variables selon les temps d'exposition. Ainsi, des maximums journaliers traduisent une exposition aiguë, alors que les moyennes annuelles et le nombre de jours de dépassement concernent les expositions chroniques.

## Effets néfastes sur la santé

L'inhalation de fumée peut avoir des effets néfastes sur la santé humaine. Les symptômes vont de l'irritation des yeux et voies respiratoires à des maladies respiratoires chroniques (telles que l'asthme) et la diminution des fonctions pulmonaires. Pour les personnes les plus vulnérables, la pollution atmosphérique peut mener à une mort prématurée pour cause de dysfonctionnements respiratoires et/ou cardiovasculaires.

Les effets sont variés et peuvent être sensiblement différents selon le gaz polluant. Par exemple, le $CO$ se propageant dans le système sanguin à partir des poumons, il peut limiter la distribution de l'oxygène aux organes et tissus du corps. L'$O_3$ est un oxydant très réactif; à forte concentration, il est capable de détériorer les tissus des poumons. En ce qui concerne les matières

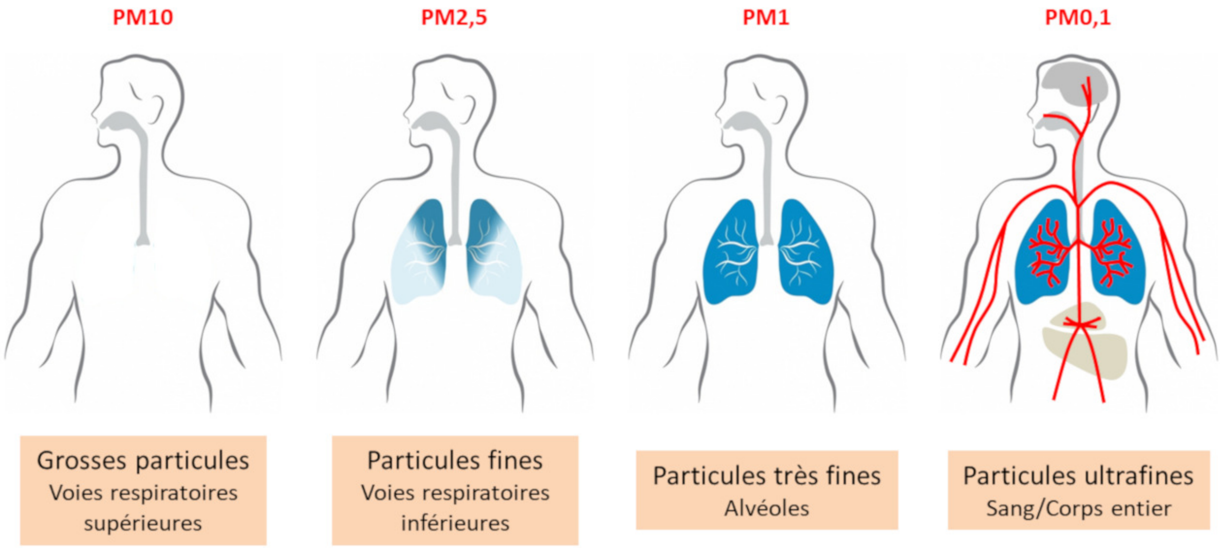

Figure 5: Pénétration des particules dans le système respiratoire en fonction de leur taille. © Encyclopédie de l'Environnement.

particulaires (PM), une fois inhalées, elles peuvent pénétrer plus ou moins profondément dans l'organisme en fonction de leur taille (fig. 5). Les PM2,5 peuvent parvenir jusqu'aux bronches et bronchioles, tandis que les PM0,1 étant plus petites que les globules rouges, peuvent s'introduire dans le système sanguin. En plus des incidences mentionnées ci-avant, les particules fines pourraient altérer le système immunitaire et empêcher l'excrétion de corps étrangers, tels que le pollen ou les bactéries, des poumons.

Les études épidémiologiques associant les polluants atmosphériques à la santé des populations sont réalisées pour la plupart en condition de pollution urbaine. Il existe encore trop peu d'études sur la mesure des impacts spécifiques de la pollution par les feux de végétation. Cependant, une relation causale entre les épisodes d'incendie et l'augmentation de la fréquentation des services de santé (admission aux urgences et hospitalisation) a été mise en évidence à plusieurs reprises. D'après une étude scientifique, les incendies de 2015 à Palangkaraya, en Indonésie, auraient entraîné le développement d'infections respiratoires chez 500 000 personnes. Se concentrant principalement sur les effets des PM et de l'$O_3$, une autre étude réalisée à l'échelle mondiale estime à 339 000 le nombre annuel moyen de décès causés par les feux de végétation.

Afin d'obtenir une estimation correcte des risques sanitaires liés aux fumées de feux de végétation, il faut prendre en compte la vulnérabilité de la population. En effet, les impacts sanitaires mentionnés ci-avant sont plutôt limités chez les adultes en bonne santé qui peuvent récupérer rapidement. En revanche, les personnes déjà atteintes de maladies respiratoires ou cardiovasculaires peuvent connaître des symptômes chroniques accrus (inflammation prononcée des voies respiratoires ou attaque cardiaque plus risquée). Les personnes âgées (mécanismes de défense respiratoire diminués), les enfants (poumons en développement) ainsi que les fumeurs (voies respiratoires déjà endommagées) font partie des populations dites «sensibles» à la pollution atmosphérique. Enfin, le lieu et la durée d'exposition sont également des facteurs importants à prendre en compte. Les fumées d'incendie atteignant les villes s'ajoutent à la pollution urbaine de fond, qui peut déjà être considérable (liée en partie à la circulation routière et au chauffage des habitations), menant à un effet d'accumulation. L'exposition chronique à la pollution, y compris à de plus faibles concentrations, pourrait être plus néfaste pour la santé humaine que des expositions aiguës mais ponctuelles. Cependant, encore trop peu d'études renseignent sur les effets d'une exposition à long terme.

## Conclusions

En conclusion, la pollution atmosphérique engendrée par les incendies de végétation est un problème majeur, aussi bien sur le plan environnemental que sanitaire. Concernant certains incendies, l'effet sur la qualité de l'air engendre plus de victimes humaines que les flammes elles-mêmes. Ce phénomène est d'autant plus inquiétant qu'il s'inscrit dans un contexte de réchauffement climatique, où le risque météorologique des incendies ne fait qu'augmenter.

Sur la base des avancées réalisées dans le domaine de la chimie atmosphérique au cours des dernières décennies, nous pouvons espérer raisonnablement une amélioration quant à l'estimation des gaz polluants et aérosols du point de vue de leur distribution, quantité et composition. Néanmoins, il serait plus que bénéfique d'augmenter le nombre d'études interdisciplinaires associant spécialistes de l'atmosphère, épidémiologistes et toxicologues, concernant plus particulièrement les feux de végétation.

## Références

Jacob, D. J. Introduction to Atmospheric Chemistry. *Princeton University Press*, 1999, `https://acmg.seas.harvard.edu/education/introduction-atmospheric-chemistry`.

Réa, G. Impact des feux de végétation sur la pollution particulaire en région Euro-Méditerranéenne et en Australie. *Thèse de doctorat, Interfaces continentales, environnement. Université Pierre et Marie Curie - Paris VI*, 2015, `https://tel.archives-ouvertes.fr/tel-01490374/`.

Turquety, S., Menut, L., Siour, G., Mailler, S., Hadji-Lazaro., J., George, M., Clerbaux, C., Hurtmans, D. & Coheur, P. F. APIFLAME v2.0 biomass burning emissions model: impact of refined input parameters on atmospheric concentration in Portugal in summer 2016. *Geoscientific Model Development, vol. 13, no 7, p. 2981-3009*, 2020, `https://gmd.copernicus.org/articles/13/2981/2020/`.

Voulgarakis, A & Field, R. D. Fire Influences on Atmospheric Composition, Air Quality and Climate. *Current Pollution Reports, vol. 1, no. 2, p. 70-81*, 2015, `https://link.springer.com/article/10.1007/s40726-015-0007-z`.

### Informations sur l'auteur

En dernière année de doctorat au Laboratoire de Météorologie Dynamique (Sorbonne Université), je réalise une thèse sur l'impact des sécheresses et vagues de chaleur sur la pollution à l'ozone dans l'Ouest Méditerranéen.

Cet article a été rédigé dans le cadre d'une mission de diffusion scientifique au sein de l'Unité Géosciences du Palais de la Découverte.

Le public cible couvre les lycéens et adultes intéressés.

La présente version est une pré-impression. La revue Découverte n°435 incluant la version imprimée de l'article se trouve à l'adresse suivante : https://www.palais-decouverte.fr/fr/lascienceestla/revue-decouverte/n-435-octobre-decembre-2021/.

# Appendix B

# Supplementary material

## Regional modeling

Table B.1: MEGAN2.1 biogenic emission classes and emission factors ($\mu g/m^2.h$) for each of the Plant Functional Types (Guenther et al., 2012). Species and PFTs are partly represented, selecting the ones relevant for this thesis. "Temp." is for temperate, "B" for broadleaf, "N" for needleleaf, "E" for evergeen and "S" for summergreen.

| | TempNE Tree | TempBE Tree | TempBS Tree | TempBE Shrub | TempBS Shrub | C3 Grass | Crop |
|---|---|---|---|---|---|---|---|
| Isoprene | 600 | 10 000 | 10 000 | 2000 | 4000 | 800 | 1 |
| Myrcene | 70 | 30 | 30 | 30 | 50 | 0.3 | 0.3 |
| Sabinene | 70 | 50 | 50 | 50 | 70 | 0.7 | 0.7 |
| Limonene | 100 | 80 | 80 | 60 | 100 | 0.7 | 0.7 |
| $\beta$-Pinene | 300 | 130 | 130 | 100 | 150 | 1.5 | 1.5 |
| $\alpha$-Pinene | 500 | 400 | 400 | 200 | 300 | 2 | 2 |
| Methanol | 900 | 900 | 900 | 900 | 900 | 500 | 900 |
| Bidirectional VOC | 500 | 500 | 500 | 500 | 500 | 80 | 80 |
| Stress VOC | 300 | 300 | 300 | 300 | 300 | 300 | 300 |

Table B.2: Parameters of biogenic species used in MEGAN model. Table inspired from Guenther et al. (2012). "TDF" is for Temperature Dependent Fraction and "LDF" Light Dependent Fraction". "$C_{eo}$" and "$C_{t1}$" are empirically determined coefficients for the calculation of $\gamma_T$. "$A_{new}$", "$A_{gro}$", "$A_{mat}$" and "$A_{old}$" are empirical coefficients, that describe the relative emission rates for new, growing, mature, and senescing leaves, respectively. "$\rho$" is the production/loss term within canopy.

| Coumpound class | TDF | LDF | $C_{eo}$ | $C_{t1}$ | $A_{new}$ | $A_{gro}$ | $A_{mat}$ | $A_{old}$ | $\rho$ |
|---|---|---|---|---|---|---|---|---|---|
| Isoprene | 0.13 | 1.0 | 2.0 | 95. | 0.05 | 0.6 | 1.0 | 0.9 | 1.0 |
| $\alpha$-Pinene | 0.1 | 0.6 | 1.83 | 80. | 2.0 | 1.8 | 1.0 | 1.05 | 1.0 |
| $\beta$-Pinene | 0.1 | 0.2 | 1.83 | 80. | 2.0 | 1.8 | 1.0 | 1.05 | 1.0 |
| Limonene | 0.1 | 0.2 | 1.83 | 80. | 2.0 | 1.8 | 1.0 | 1.05 | 1.0 |
| t-$\beta$-Ocimene | 0.1 | 0.8 | 1.83 | 80. | 2.0 | 1.8 | 1.0 | 1.05 | 1.0 |
| 3-Carene | 0.1 | 0.2 | 1.83 | 80. | 2.0 | 1.8 | 1.0 | 1.05 | 1.0 |
| Sabinene | 0.1 | 0.6 | 1.83 | 80. | 2.0 | 1.8 | 1.0 | 1.05 | 1.0 |
| Myrcene | 0.1 | 0.6 | 1.83 | 80. | 2.0 | 1.8 | 1.0 | 1.05 | 1.0 |
| NO | 0.1 | 0.0 | 1.83 | 80. | 1.0 | 1.0 | 1.0 | 1.0 | 1.0 |
| Other monoterpenes | 0.1 | 0.4 | 1.83 | 80. | 2.0 | 1.8 | 1.0 | 1.05 | 1.0 |
| $\alpha$-Farnesene | 0.17 | 0.5 | 2.37 | 130. | 0.4 | 0.6 | 1.0 | 0.95 | 1.0 |
| $\beta$-Caryophyllene | 0.17 | 0.5 | 2.37 | 130. | 0.4 | 0.6 | 1.0 | 0.95 | 1.0 |
| Other sesquiterpenes | 0.17 | 0.5 | 2.37 | 130. | 0.4 | 0.6 | 1.0 | 0.95 | 1.0 |
| 232-MBO | 0.13 | 1.0 | 2.0 | 95. | 0.05 | 0.6 | 1.0 | 0.9 | 1.0 |
| Methanol | 0.08 | 0.8 | 1.6 | 60. | 3.5 | 3.0 | 1.0 | 1.2 | 1.0 |
| Acetone | 0.1 | 0.2 | 1.83 | 80. | 1.0 | 1.0 | 1.0 | 1.0 | 1.0 |
| CO | 0.08 | 1.0 | 1.6 | 60. | 1.0 | 1.0 | 1.0 | 1.0 | 1.0 |
| Bidirectional VOC | 0.13 | 0.8 | 2.0 | 95. | 1.0 | 1.0 | 1.0 | 1.0 | 1.0 |
| Stress VOC | 0.1 | 0.8 | 1.83 | 80. | 1.0 | 1.0 | 1.0 | 1.0 | 1.0 |
| Other VOC | 0.1 | 0.2 | 1.83 | 80. | 1.0 | 1.0 | 1.0 | 1.0 | 1.0 |

Table B.3: Aggregation matrix used to convert MEGAN species to CHIMERE species. Abbreviation "monot." is for monoterpenes, "sesq." for sesquiterpenes and "bid." for bidirectional.

| MEGAN species | C5H8 | APINEN | BPINEN | LIMONE | TERPEN | OCIMEN | HUMULE | NO | CO | CH3OH | C2H4 | CH3CHO | CH3COE | MEMALD |
|---|---|---|---|---|---|---|---|---|---|---|---|---|---|---|
| Isoprene | 1 | 0 | 0 | 0 | 0 | 0 | 0 | 0 | 0 | 0 | 0 | 0 | 0 | 0 |
| $\alpha$-Pinene | 0 | 1 | 0 | 0 | 0 | 0 | 0 | 0 | 0 | 0 | 0 | 0 | 0 | 0 |
| $\beta$-Pinene | 0 | 0 | 1 | 0 | 0 | 0 | 0 | 0 | 0 | 0 | 0 | 0 | 0 | 0 |
| Limonene | 0 | 0 | 0 | 1 | 0 | 0 | 0 | 0 | 0 | 0 | 0 | 0 | 0 | 0 |
| t-$\beta$-Ocimene | 0 | 0 | 0 | 0 | 0 | 1 | 0 | 0 | 0 | 0 | 0 | 0 | 0 | 0 |
| 3-Carene | 0 | 0 | 1 | 0 | 0 | 0 | 0 | 0 | 0 | 0 | 0 | 0 | 0 | 0 |
| Sabinene | 0 | 1 | 0 | 0 | 0 | 0 | 0 | 0 | 0 | 0 | 0 | 0 | 0 | 0 |
| Myrcene | 0 | 0 | 0 | 0 | 0 | 1 | 0 | 0 | 0 | 0 | 0 | 0 | 0 | 0 |
| NO | 0 | 0 | 0 | 0 | 0 | 0 | 0 | 1 | 0 | 0 | 0 | 0 | 0 | 0 |
| Other monot. | 0 | 1 | 0 | 0 | 0 | 0 | 0 | 0 | 0 | 0 | 0 | 0 | 0 | 0 |
| $\alpha$-Farnesene | 0 | 0 | 0 | 0 | 0 | 0 | 1 | 0 | 0 | 0 | 0 | 0 | 0 | 0 |
| $\beta$-Caryophyllene | 0 | 0 | 0 | 0 | 0 | 0 | 1 | 0 | 0 | 0 | 0 | 0 | 0 | 0 |
| Other sesq. | 0 | 0 | 0 | 0 | 0 | 0 | 1 | 0 | 0 | 0 | 0 | 0 | 0 | 0 |
| 232-MBO | 0 | 0 | 0 | 0 | 0 | 0 | 0 | 0 | 0 | 0 | 0 | 0 | 0 | 1 |
| Methanol | 0 | 0 | 0 | 0 | 0 | 0 | 0 | 0 | 0 | 1 | 0 | 0 | 0 | 0 |
| Acetone | 0 | 0 | 0 | 0 | 0 | 0 | 0 | 0 | 0 | 0 | 0 | 0 | 1 | 0 |
| CO | 0 | 0 | 0 | 0 | 0 | 0 | 0 | 0 | 1 | 0 | 0 | 0 | 0 | 0 |
| Bid. VOC | 0 | 0 | 0 | 0 | 0 | 0 | 0 | 0 | 0 | 0 | 0 | 1 | 0 | 0 |
| Stress VOC | 0 | 0 | 0 | 0 | 0 | 0 | 0 | 0 | 0 | 0 | 1 | 0 | 0 | 0 |
| Other VOC | 0 | 0 | 0 | 0 | 0 | 0 | 0 | 0 | 0 | 0 | 0 | 0 | 1 | 0 |

# Observations

Table B.4: Aggregation matrix used to convert MODIS MCD12 (IBGC) land cover classes (rows) to ORCHIDEE PFTs (columns). The result of the coefficients is normalized. Abbreviation "need." is for needleleaf and "broad." for broadleaf.

| | Bare soil | TrBE | TrBR | TempNE | TempBE | TempBS | BoNE | BoBS | BoNS | C3G | C4G | C3A | C4A |
|---|---|---|---|---|---|---|---|---|---|---|---|---|---|
| Evergreen need. forests | 0 | 1 | 1 | 1 | 1 | 1 | 1 | 1 | 1 | 0 | 0 | 0 | 0 |
| Evergreen broad. forests | 0 | 1 | 1 | 1 | 1 | 1 | 1 | 1 | 1 | 0 | 0 | 0 | 0 |
| Deciduous need. forests | 0 | 1 | 1 | 1 | 1 | 1 | 1 | 1 | 1 | 0 | 0 | 0 | 0 |
| Deciduous broad. forests | 0 | 1 | 1 | 1 | 1 | 1 | 1 | 1 | 1 | 0 | 0 | 0 | 0 |
| Mixed forests | 0 | 1 | 1 | 1 | 1 | 1 | 1 | 1 | 1 | 0 | 0 | 0 | 0 |
| Closed shrublands | 0 | 1 | 1 | 1 | 1 | 1 | 1 | 1 | 1 | 1 | 1 | 0 | 0 |
| Open shrublands | 0 | 0.2 | 0.2 | 0.2 | 0.2 | 0.2 | 0.2 | 0.2 | 0.2 | 1 | 1 | 0 | 0 |
| Woody savannas | 0 | 0.3 | 0.3 | 0.3 | 0.3 | 0.3 | 0.3 | 0.3 | 0.3 | 1 | 1 | 0 | 0 |
| Savannas | 0 | 0 | 0 | 0 | 0 | 0 | 0 | 0 | 0 | 1 | 1 | 0.1 | 0.1 |
| Grasslands | 0 | 0 | 0 | 0 | 0 | 0 | 0 | 0 | 0 | 1 | 1 | 1 | 1 |
| Permanent wetlands | 0 | 1 | 1 | 0.3 | 0.3 | 0.3 | 1 | 1 | 1 | 0.5 | 0.5 | 0 | 0 |
| Croplands | 0 | 0 | 0 | 0 | 0 | 0 | 0 | 0 | 0 | 1 | 1 | 1 | 1 |
| Built-up land | 0 | 0 | 0 | 0 | 0 | 0 | 0 | 0 | 0 | 0 | 0 | 0 | 0 |
| Croplands, mosaics | 0 | 0.5 | 0.5 | 0.5 | 0.5 | 0.5 | 0.5 | 0.5 | 0.5 | 1 | 1 | 1 | 1 |
| Snow and ice | 0 | 0 | 0 | 0 | 0 | 0 | 0 | 0 | 0 | 0 | 0 | 0 | 0 |
| Barren, sparsely vegetated | 1 | 0 | 0 | 0 | 0 | 0 | 0 | 0 | 0 | 0 | 0 | 0 | 0 |

## Droughts and heatwaves

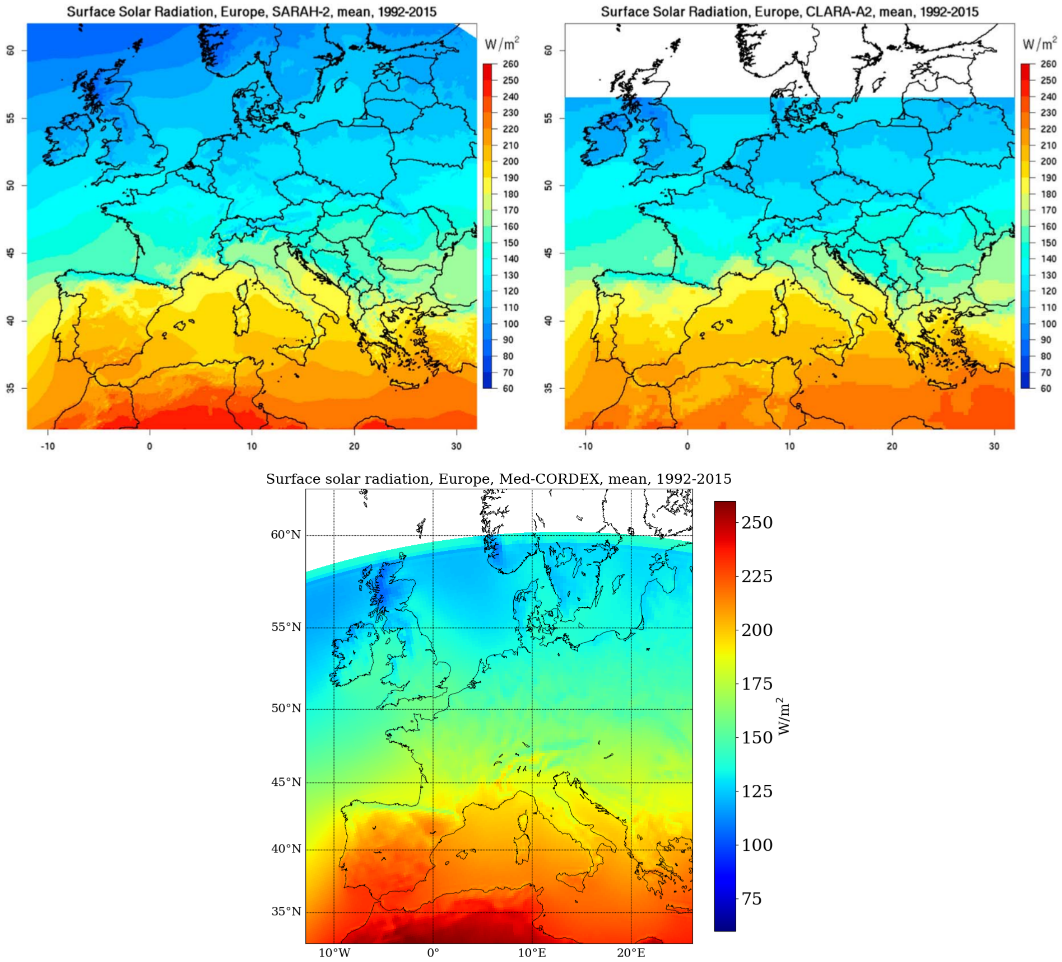

Surface Solar Radiation, Europe, SARAH-2, mean, 1992-2015

Surface Solar Radiation, Europe, CLARA-A2, mean, 1992-2015

Surface solar radiation, Europe, Med-CORDEX, mean, 1992-2015

Figure B.1: Upper panel: surface solar radiation from the two satellite-based climate data sets SARAH-2 and CLARA-A2 (Pfeifroth et al., 2018). Lower panel: surface solar radiation from the Med-CORDEX simulation performed by the RegIPSL model. The limits of the colour scale are the same as for the upper panel.

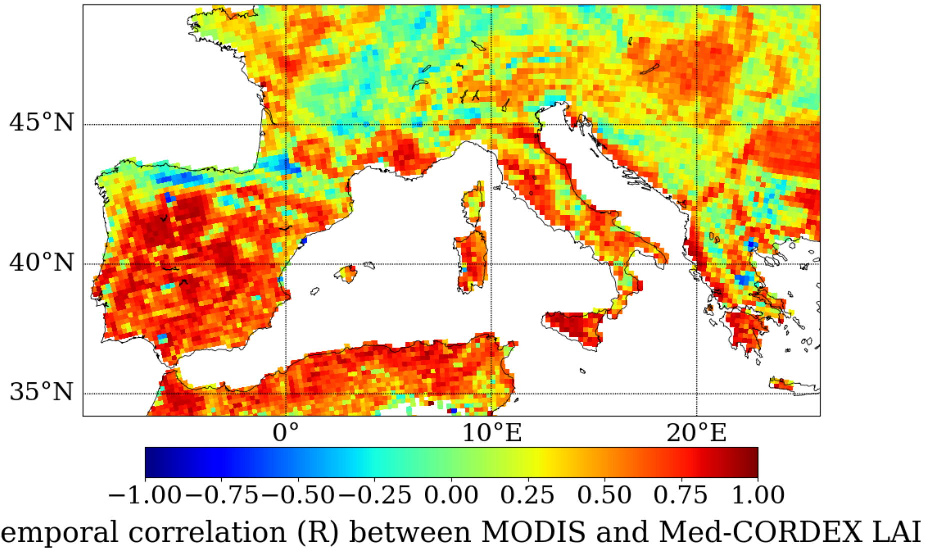

Figure B.2: Spatial distribution of the temporal correlation (R) between the LAI from Med-CORDEX and MODIS for summers days between 2003 and 2016.

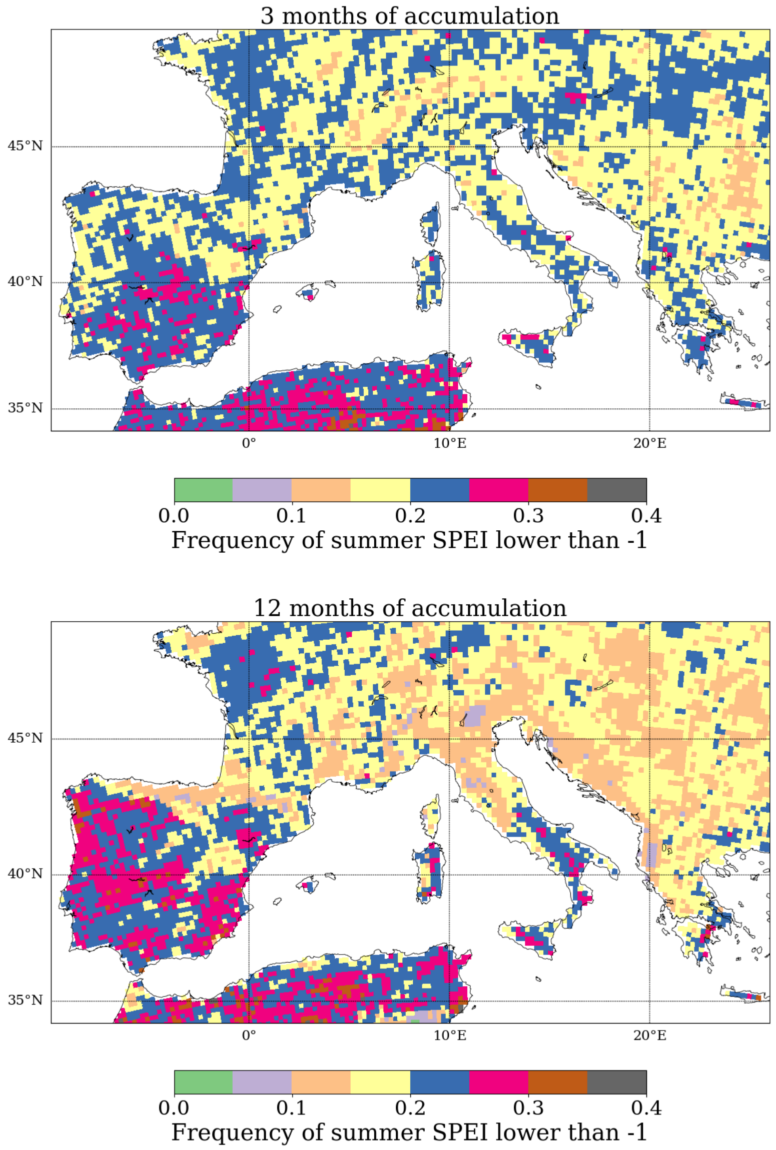

Figure B.3: Spatial distribution of frequency of summer SPEI lower than -1 computed with 3 (top) and 12 (bottom) months of accumulation period. The frequency is expressed over the total number of summer months along the simulation period, namely 114 months.

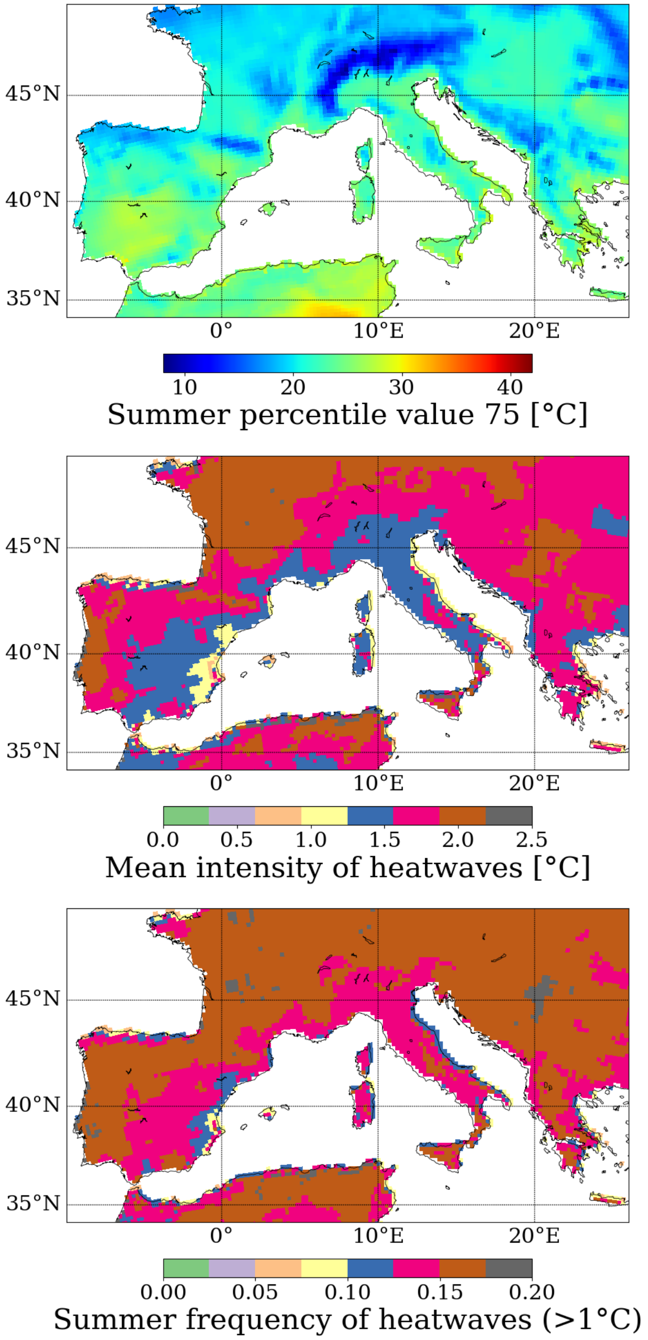

Figure B.4: Heatwaves detection based on the PLA method using the 2m above surface temperature from the E-OBS data set. The first row shows the value of the percentile 75, the second one the mean intensity of heatwaves and the third one the frequency of intense events.

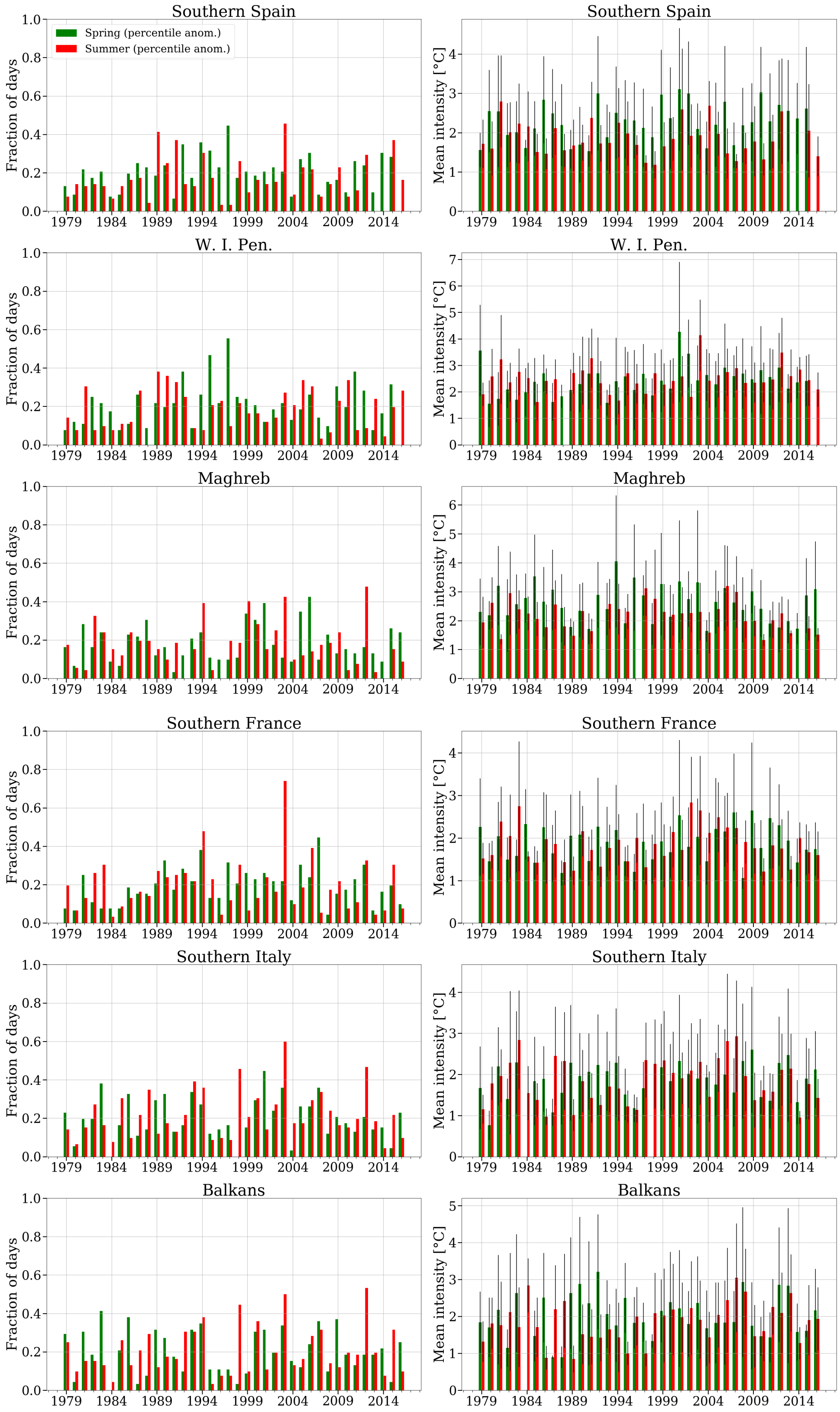

Figure B.5: Temporal variation of spring (MAM) and summer (JJA) heatwaves for the sub-regions defined in Figure 4.10, using the $PLA_{T2m}$ method (on 2m temperature). Left column: fraction of days affected. Right column: mean $PLA_{T2m}$ and its standard deviation (error bars).

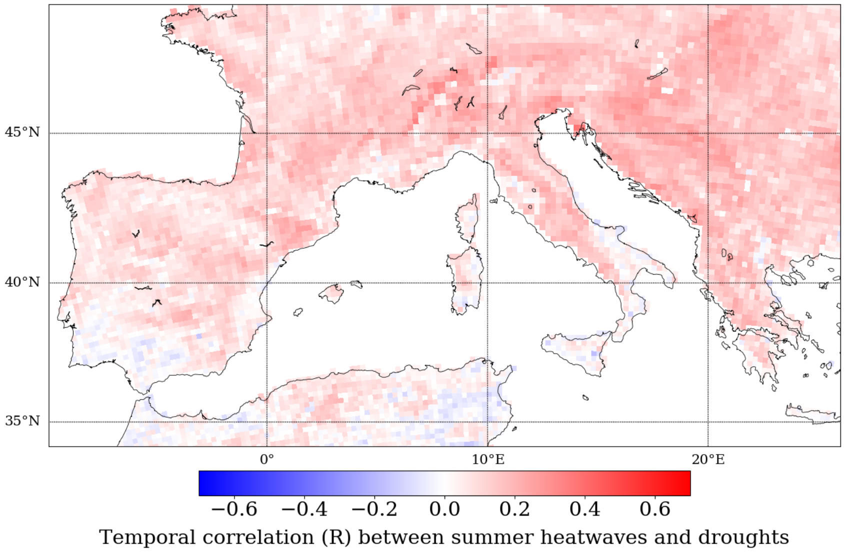

Figure B.6: Spatial distribution of the temporal correlation (R) between the summer droughts ($PLA_{SD}$) and heatwaves ($PLA_{T2m}$). A filter of significant correlation has been applied (Spearman test with p-value $< 0.1$).

## Effects on the biosphere

Table B.5: Mean ΔLAI in absolute and relative values between the reference cold summer (2014) and hot summers (2003, 2009, 2011 and 2016) at the Western Mediterranean scale for the Med-CORDEX simulation (weighted sum of PFTs) and MODIS observations. ΔLAI is computed only for heatwave days. The percentage of hot days and simultaneous dry days for the considered summer is given in the fourth and fifth column. Only years with at least 10% of summer hot days are kept. The dominant PFT affected is given in the last column.

| | ΔLAI obs. ($m^2/m^2$) | ΔLAI sim. ($m^2/m^2$) | Hot days (%) | Simult. dry days (%) | Dominant PFT |
|---|---|---|---|---|---|
| Balkans 2003 | -0.28 (-11%) | -0.09 (-5%) | 30 | 29 | C3 agriculture |
| 2009 | 0.09 (4%) | 0.03 (1%) | 11 | 3 | C3 agriculture |
| 2011 | -0.05 (-1%) | -0.12 (-3%) | 13 | 8 | C3 agriculture |
| Maghreb 2003 | -0.05 (-11%) | -0.01 (-2%) | 27 | 4 | bare soil / C3 agr. |
| 2009 | -0.01 (-1%) | -0.01 (-1%) | 16 | 0 | bare soil / C3 agr. |
| W. I. Pen. 2003 | -0.10 (-7%) | -0.01 (-1%) | 16 | 2 | C3 agriculture |
| 2009 | -0.10 (-10%) | -0.11 (-9%) | 11 | 6 | C3 agriculture |
| 2016 | 0.02 (2%) | -0.01 (-1%) | 16 | 2 | C3 grass |
| S. France 2003 | -0.20 (-12%) | -0.19 (-12%) | 18 | 8 | C3 agriculture |
| S. Italy 2003 | -0.22 (-13%) | -0.24 (-15%) | 19 | 8 | C3 grass |
| S. Spain 2003 | -0.01 (-2%) | 0.11 (14%) | 36 | 12 | C3 grass |
| 2009 | -0.02 (-3%) | 0.01 (1%) | 23 | 10 | C3 grass |
| 2011 | 0.07 (11%) | 0.13 (17%) | 38 | 8 | C3 grass |
| 2016 | 0.01 (1%) | 0.03 (4%) | 18 | 8 | C3 grass |
| W. Medit. 2003 | -0.13 (-9%) | -0.08 (-6%) | 25 | 10 | C3 grass |
| 2009 | -0.04 (-3%) | -0.04 (-3%) | 12 | 3 | C3 grass |
| 2016 | 0.02 (3%) | -0.03 (-2%) | 10 | 3 | C3 grass |

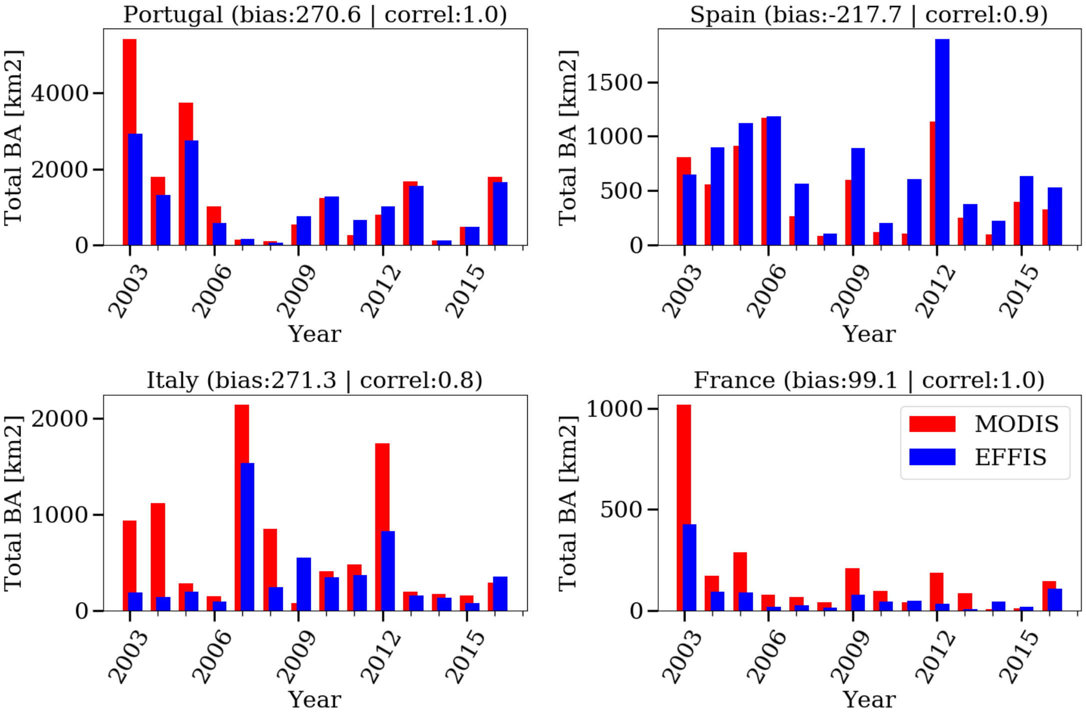

Figure B.7: Total burned area (2003-2016) from EFFIS (blue) and MODIS (red) over several countries of the Western Mediterranean. The mean annual bias (MODIS-EFFIS in $km^2$) as well as the temporal correlation (R) are indicated in the title of each sub-plot.

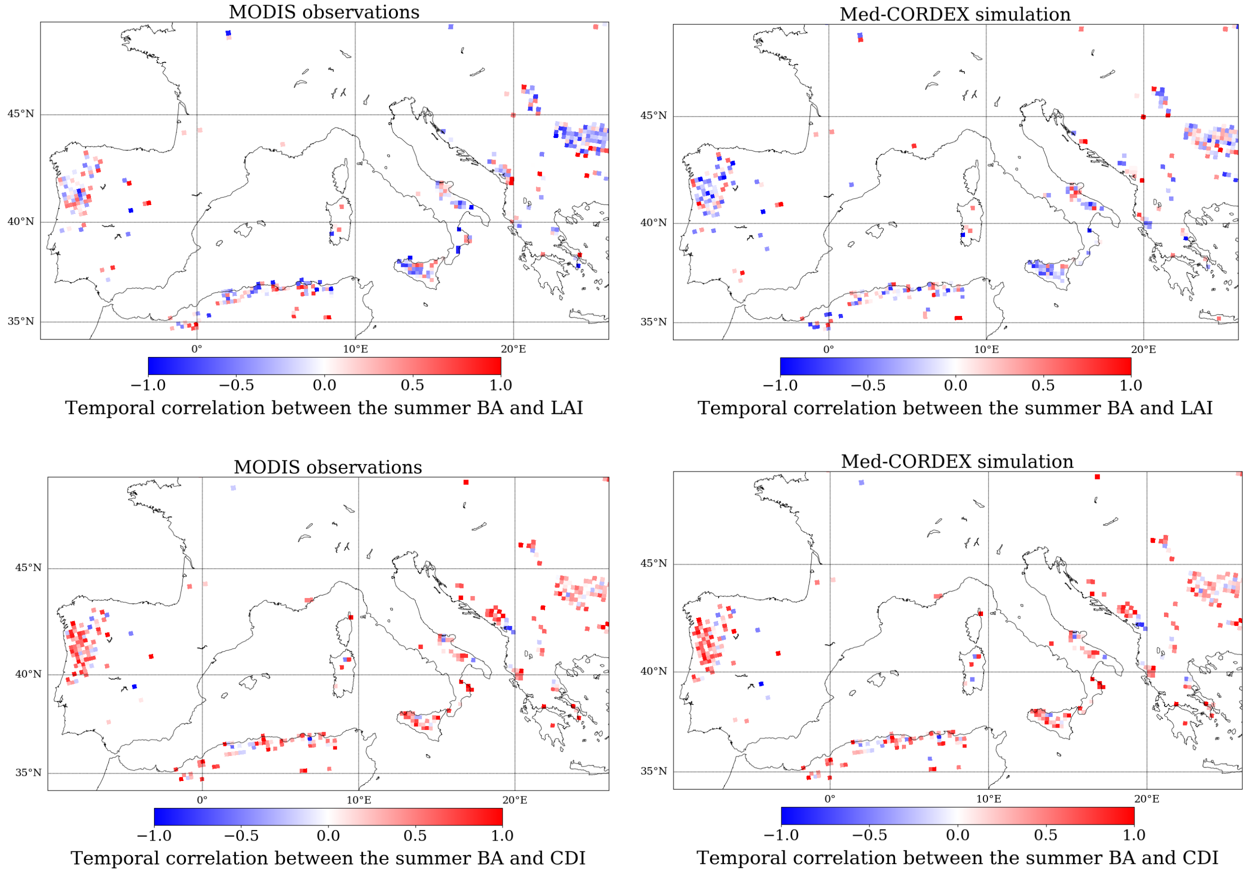

Figure B.8: Spatial distribution of temporal correlation (R) between summer Burned Area (BA) and Leaf Area Index (LAI) from MODIS (upper left panel) and from Med-CORDEX (upper right panel) for areas of high fire activity (pixels with at least 1km$^2$ of burned area for minimum 3 summers over 2003-2016). Same criteria of correlation are applied between FRP and CDI from MODIS (lower left panel) and from Med-CORDEX (lower right panel). Number of hot days (NHD) used for CDI is from Med-CORDEX ($PLA_{T2m}$) in both configurations. Only significant correlation (Spearman test with p-value $< 0.1$) are shown.

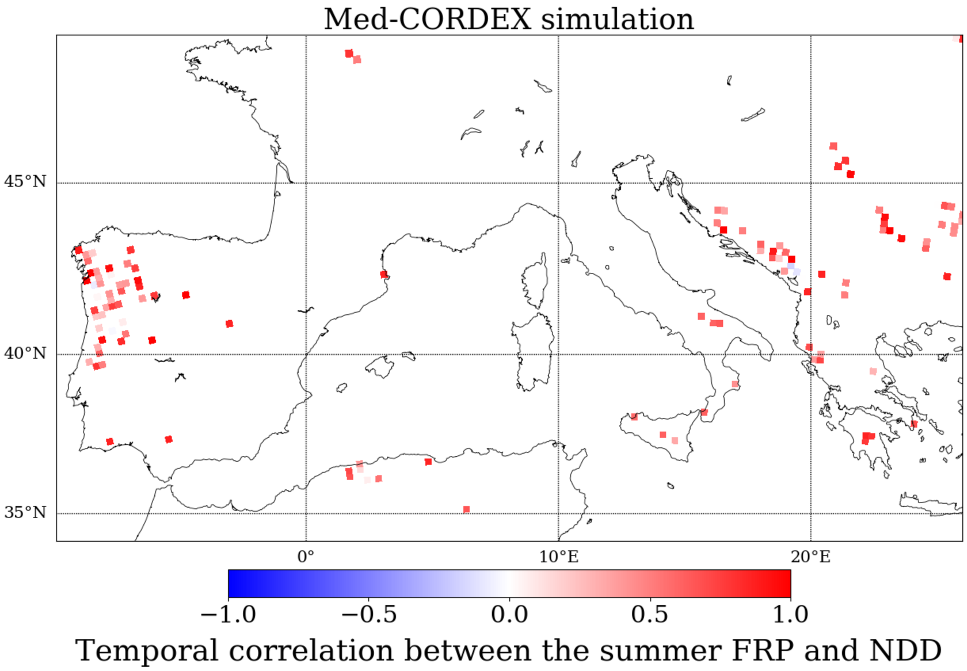

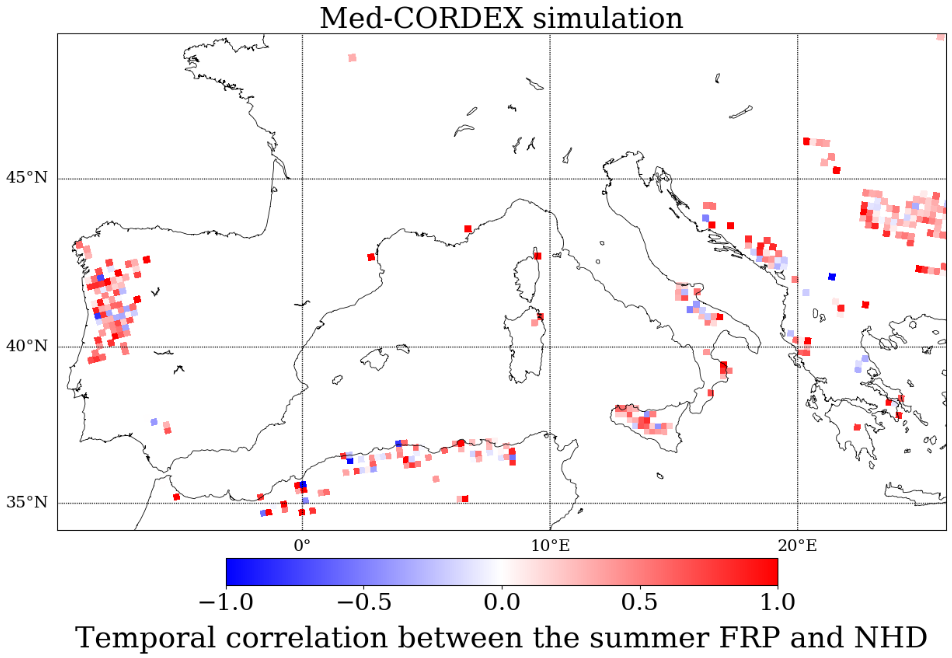

Figure B.9: Spatial distribution of temporal correlation (R) between summer Fire Radiative Power (FRP) and Number of Dry Days (upper panel) for areas of high fire activity (pixels with at least 1km$^2$ of burned area for a minimum of 3 summers over 2003-2016). Only significant correlation (Spearman test with p-value $< 0.1$) are shown. The same for the correlation of the Number of Hot Days (lower panel).

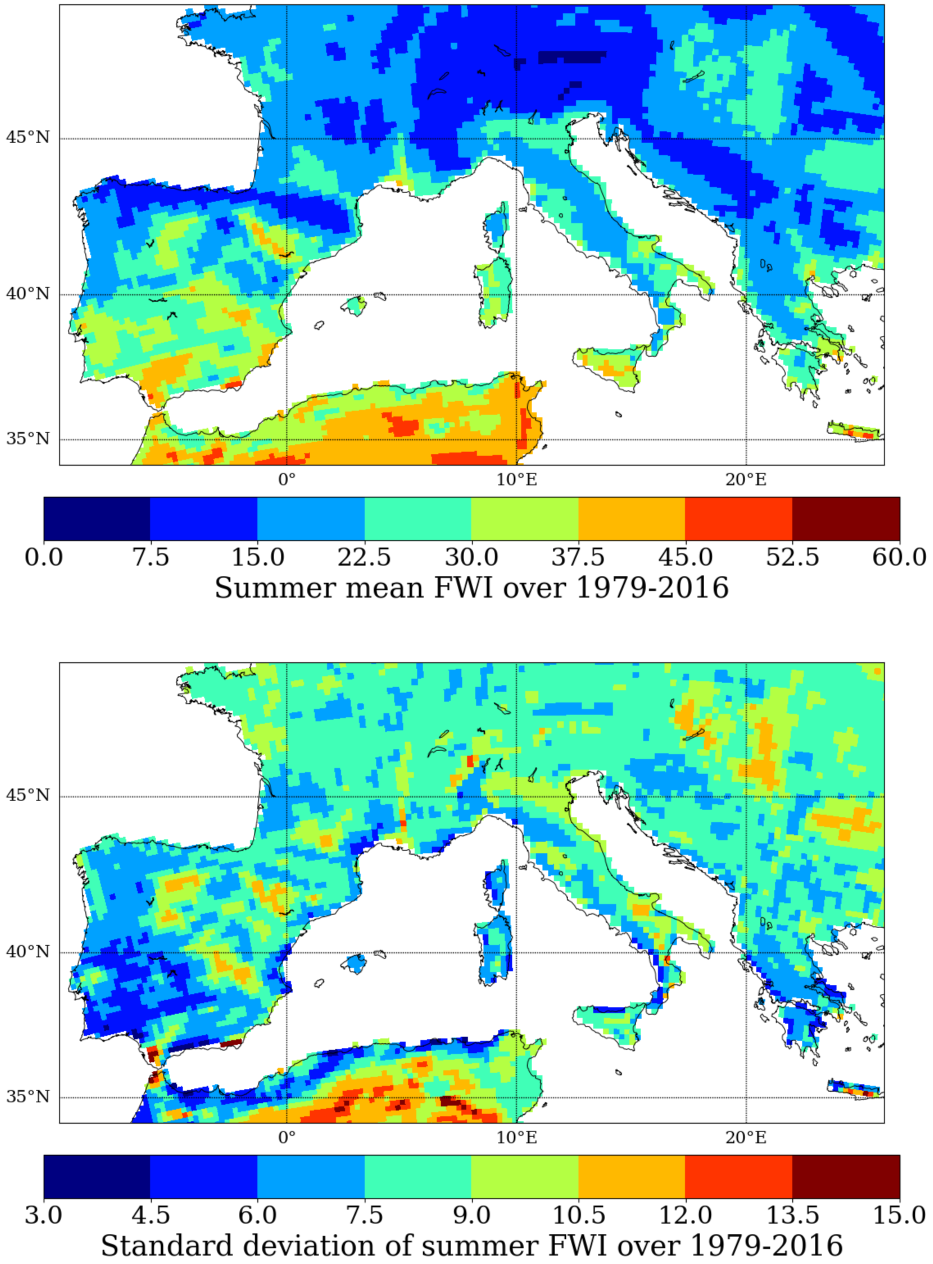

Figure B.10: Mean (upper panel) and standard deviation (lower panel) of FWI over summers 1979-2016.

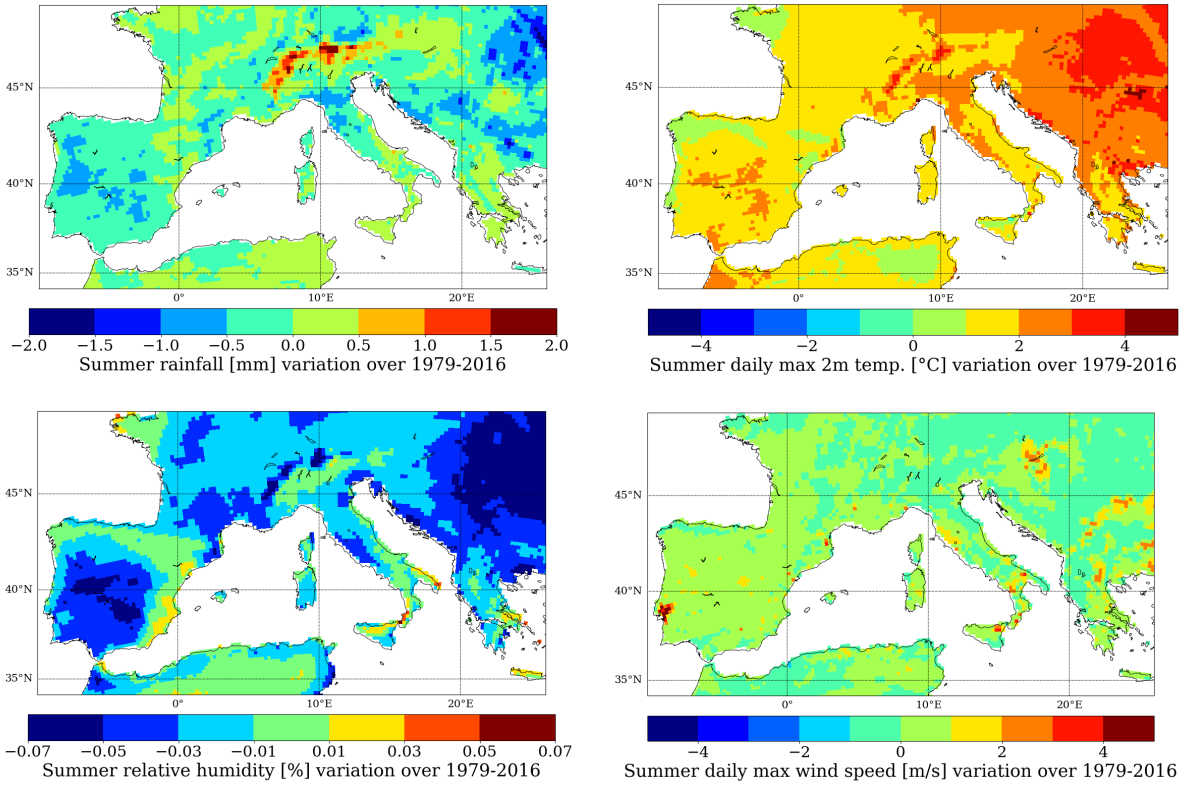

Figure B.11: Spatial distribution of the summer variation for daily total rainfall (top left), maximum 2m temperature (top right), mean relative humidity (bottom left) and maximum wind speed (bottom left), over the period 1979-2016 with a daily timestep.

## Surface ozone pollution

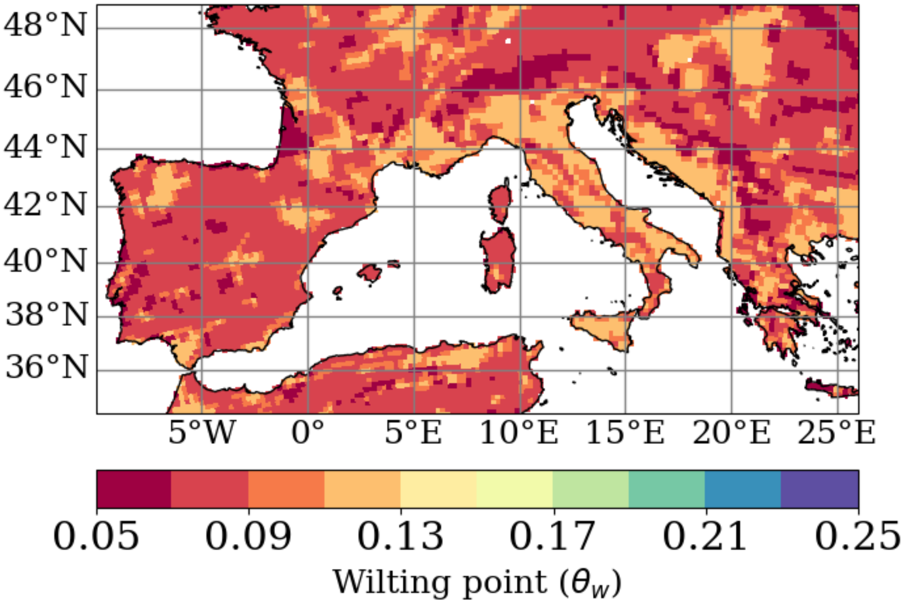

Figure B.12: Wilting point parameter $[m^3/m^3]$ from Chen and Dudhia (2001) gridded over the Med-CORDEX domain with the USGS soil types.

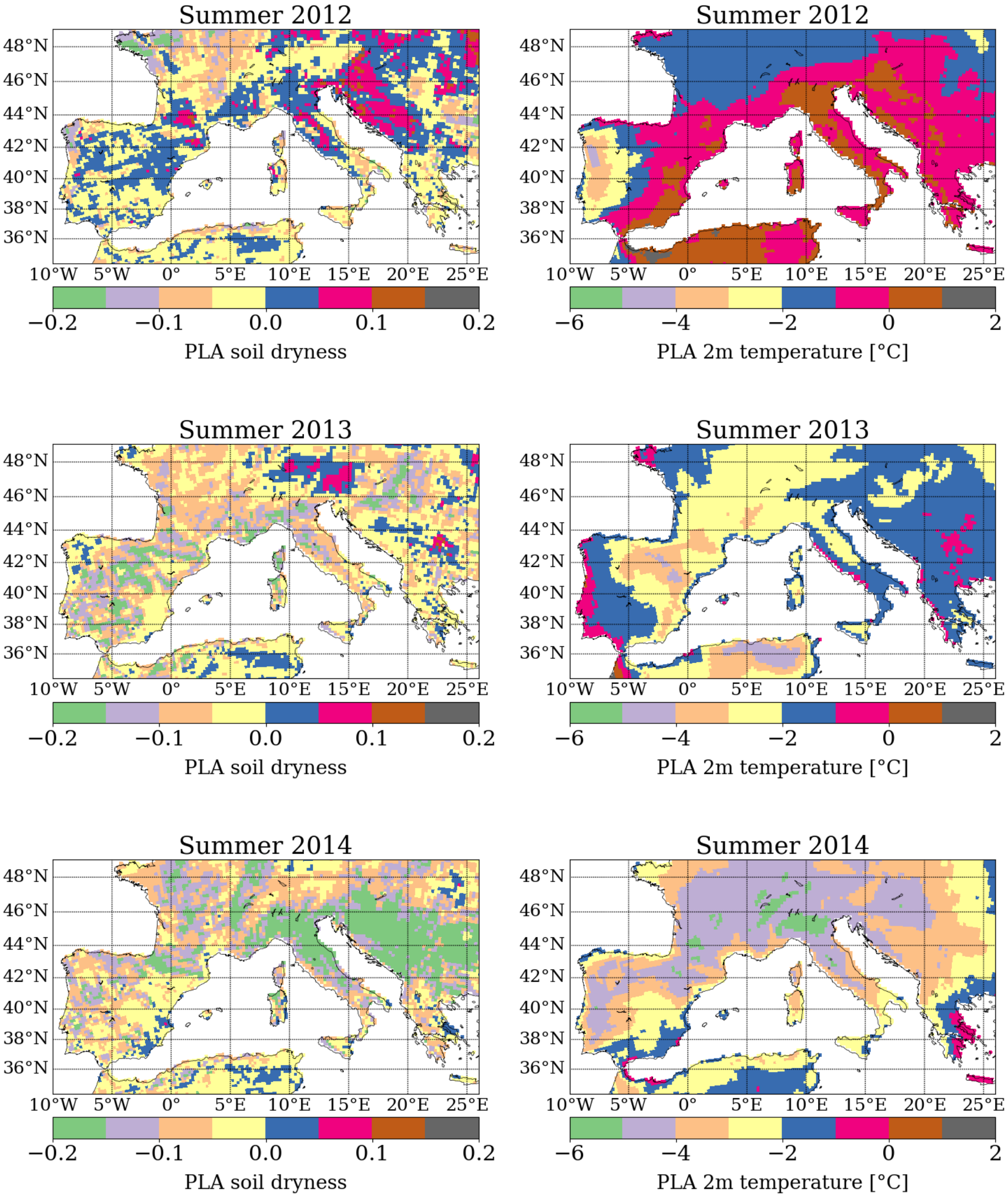

Figure B.13: Summer mean (JJA) drought ($PLA_{SD}$) and heatwave indicators ($PLA_{T2m}$) for 2012, 2013 and 2014.

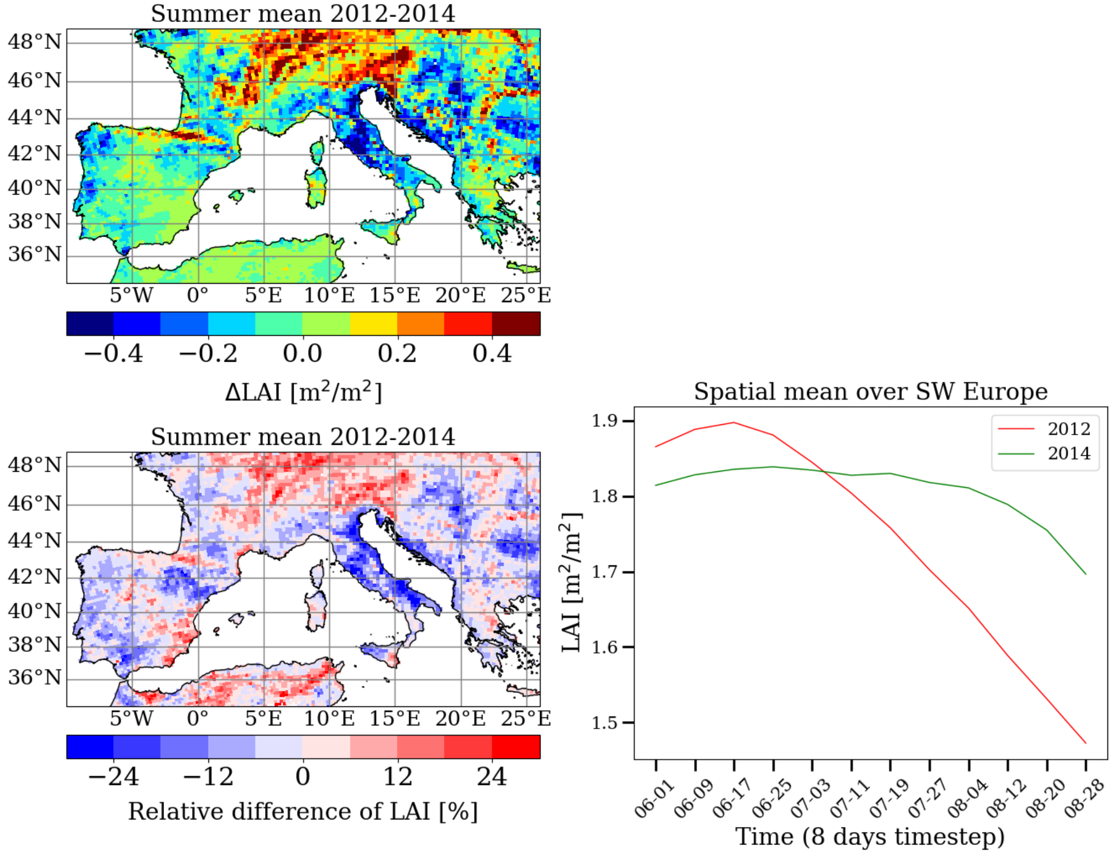

Figure B.14: Mean ΔLAI $[m^2/m^2]$ between summer (JJA) 2012 and 2014 (upper left), relative difference of LAI (lower left) and time series of LAI spatially averaged over the Southwestern Europe (lower right).

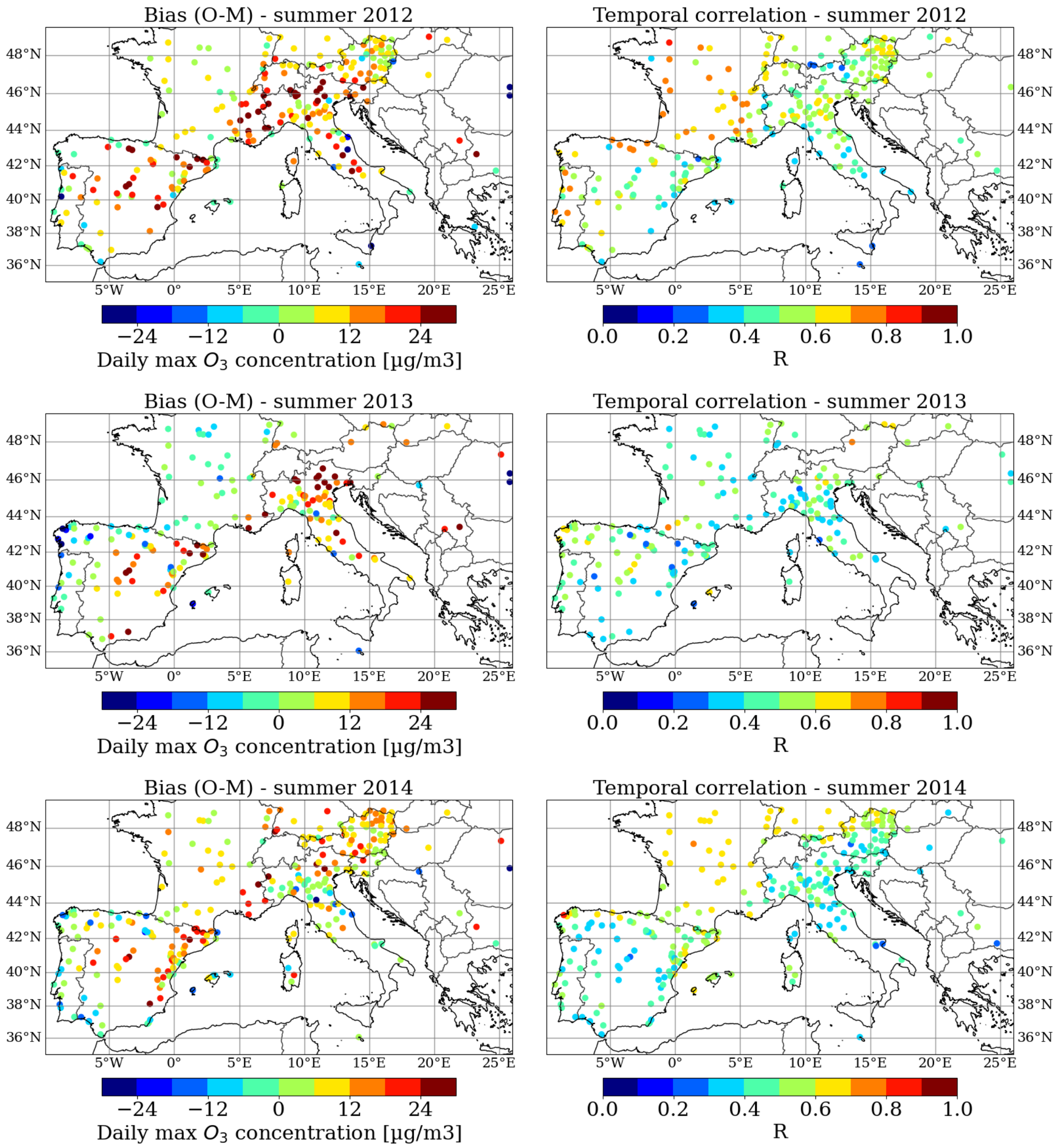

Figure B.15: Validation scores of the daily maximum surface $O_3$ [$\mu g/m^3$] for summer (JJA) 2012, 2013 and 2014 ("Reference" simulations), with the European surface network observations AQ e-Reporting. Left column: mean bias. Right column: temporal correlation (R pearson).

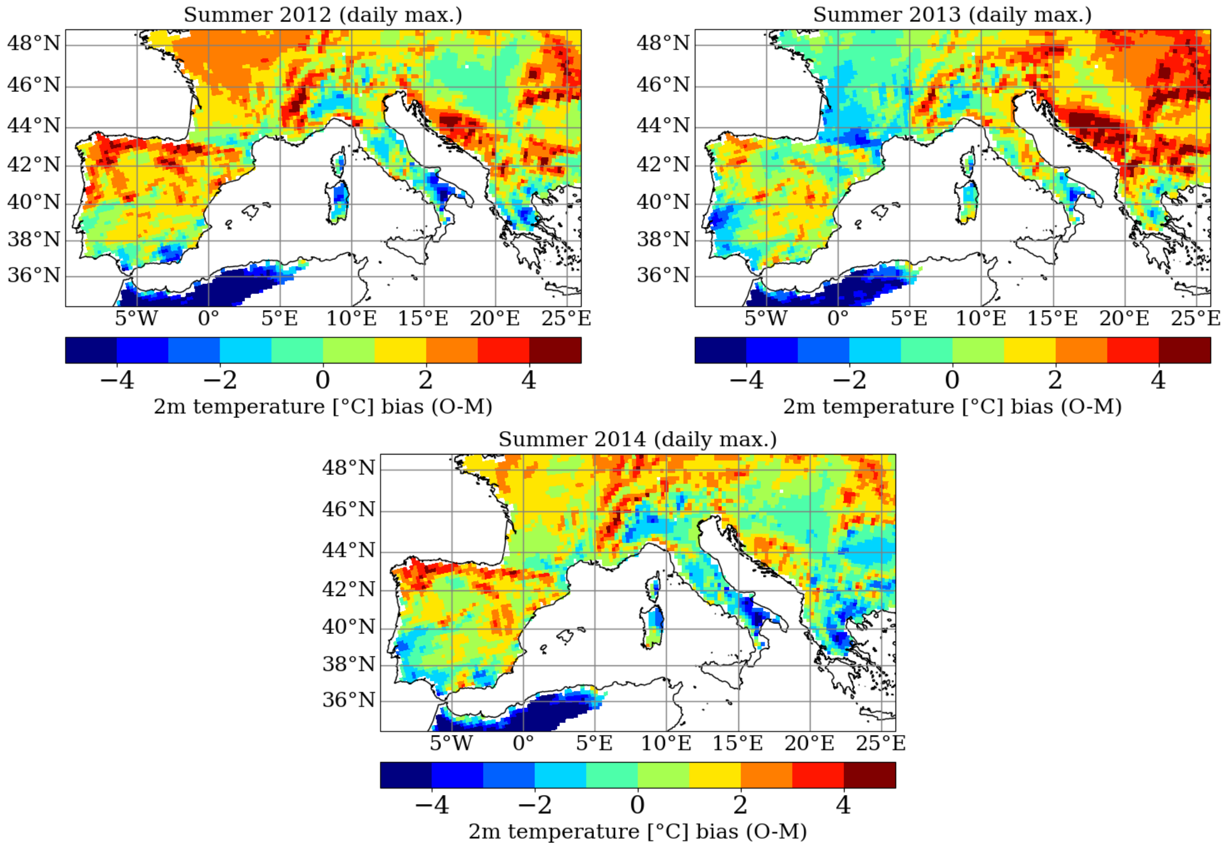

Summer 2012 (daily max.)

Summer 2013 (daily max.)

Summer 2014 (daily max.)

Figure B.16: Summer mean bias (JJA) of the daily maximum 2m temperature between observations (E-OBS) and simulations (CHIMERE) for 2012, 2013 and 2014.

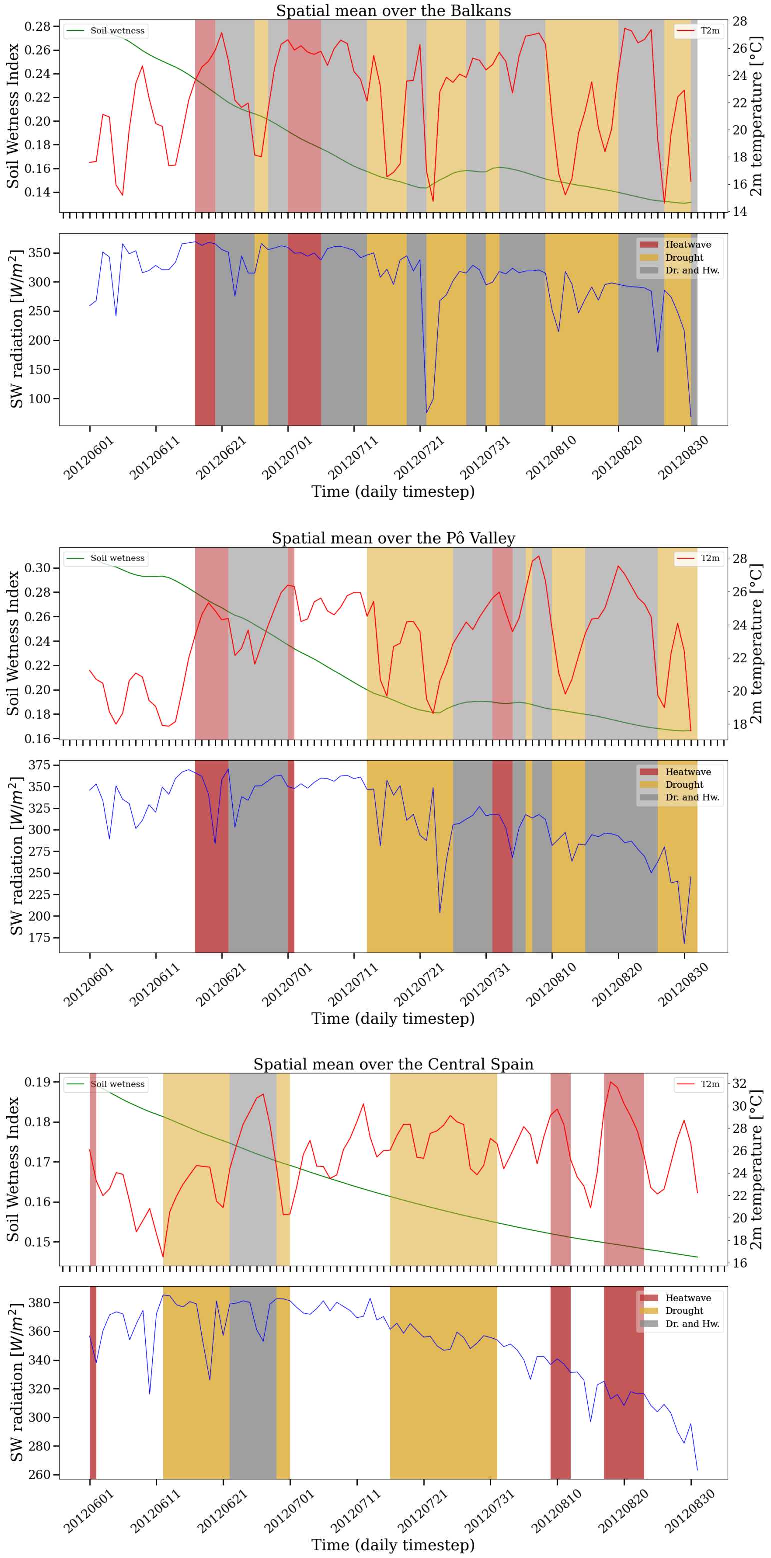

Figure B.17: Daily mean 2m temperature, shortwave radiation and soil wetness simulated by the WRF model during summer 2012 over the Balkans (upper panel), Pô Valley (middle) and Central Spain (lower).

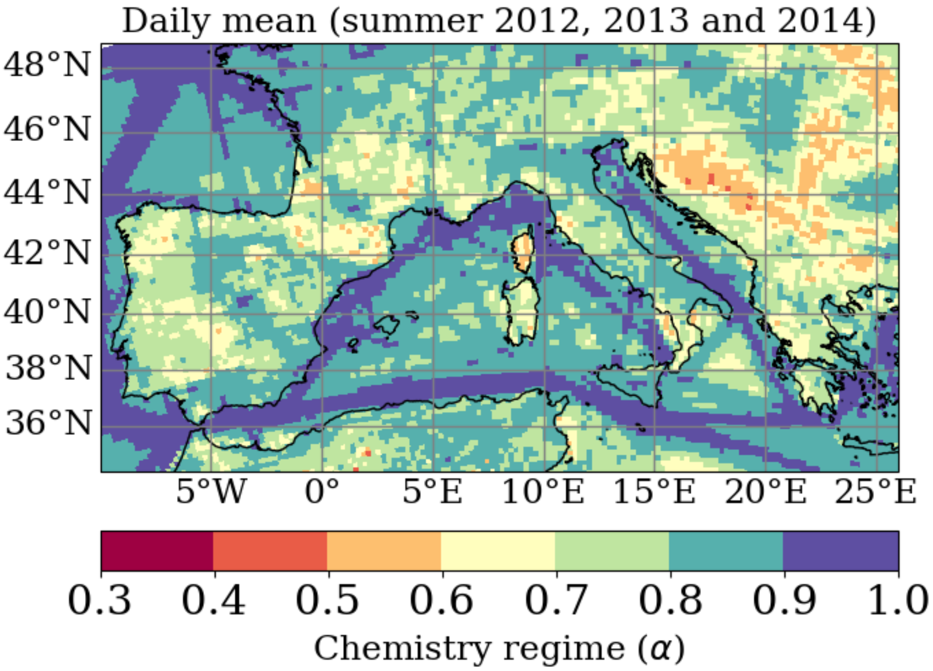

Figure B.18: Daily mean chemistry regime parameter [$\alpha$] averaged over the summer 2012, 2013 and 2014 ("Reference" simulations). $\alpha$ indicates the areas of low-$NO_x$ regime (low $\alpha$) and high-$NO_x$ regime (high $\alpha$). More information about the calculation method is provided on the online documentation (`https://www.lmd.polytechnique.fr/chimere/`).

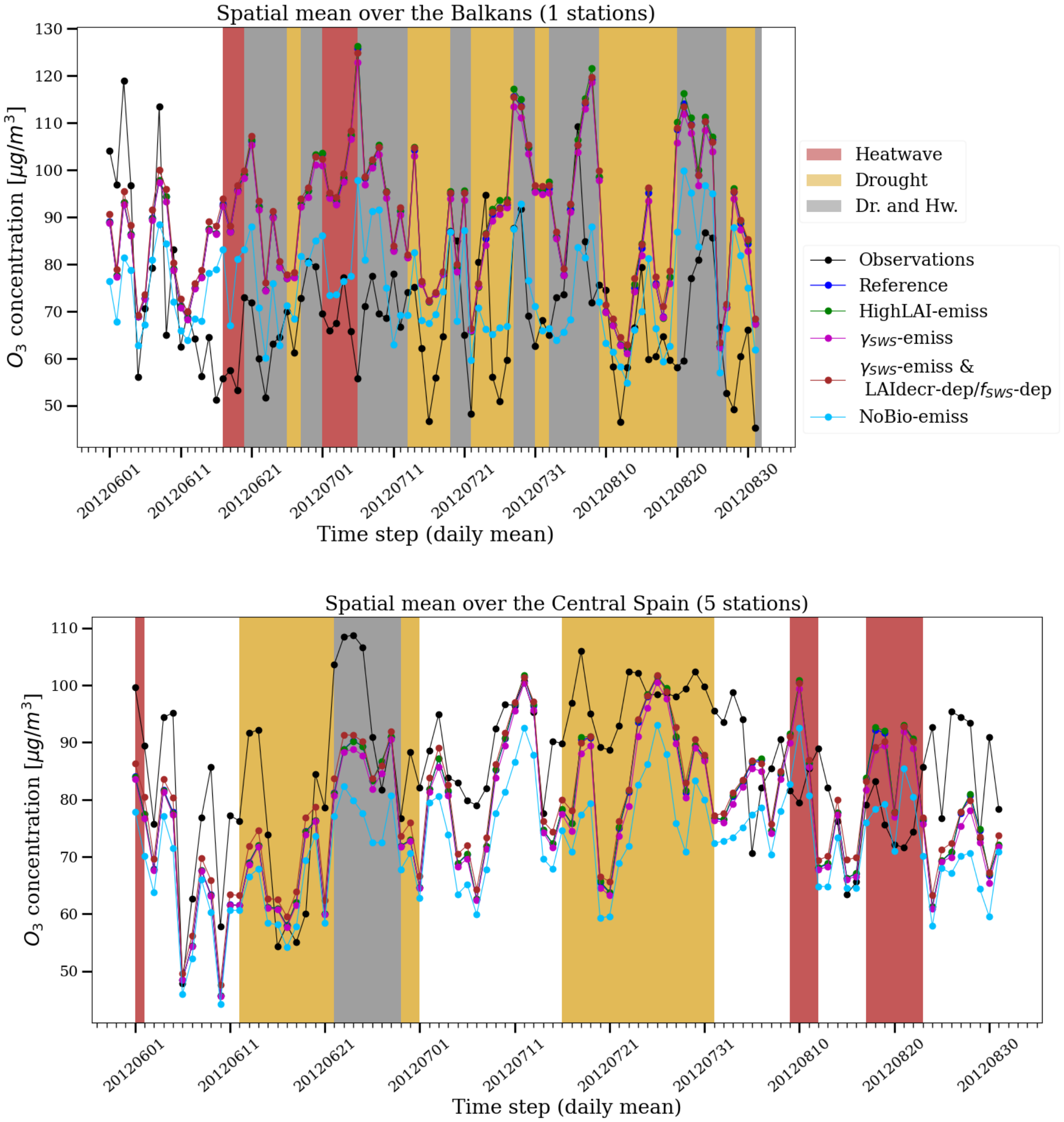

Figure B.19: Daily mean $O_3$ surface concentration [$\mu g/m^3$] during summer 2012, spatially averaged over the Balkans (upper panel) and Central Spain (lower panel) from the EEA observations and the different CHIMERE experiments.

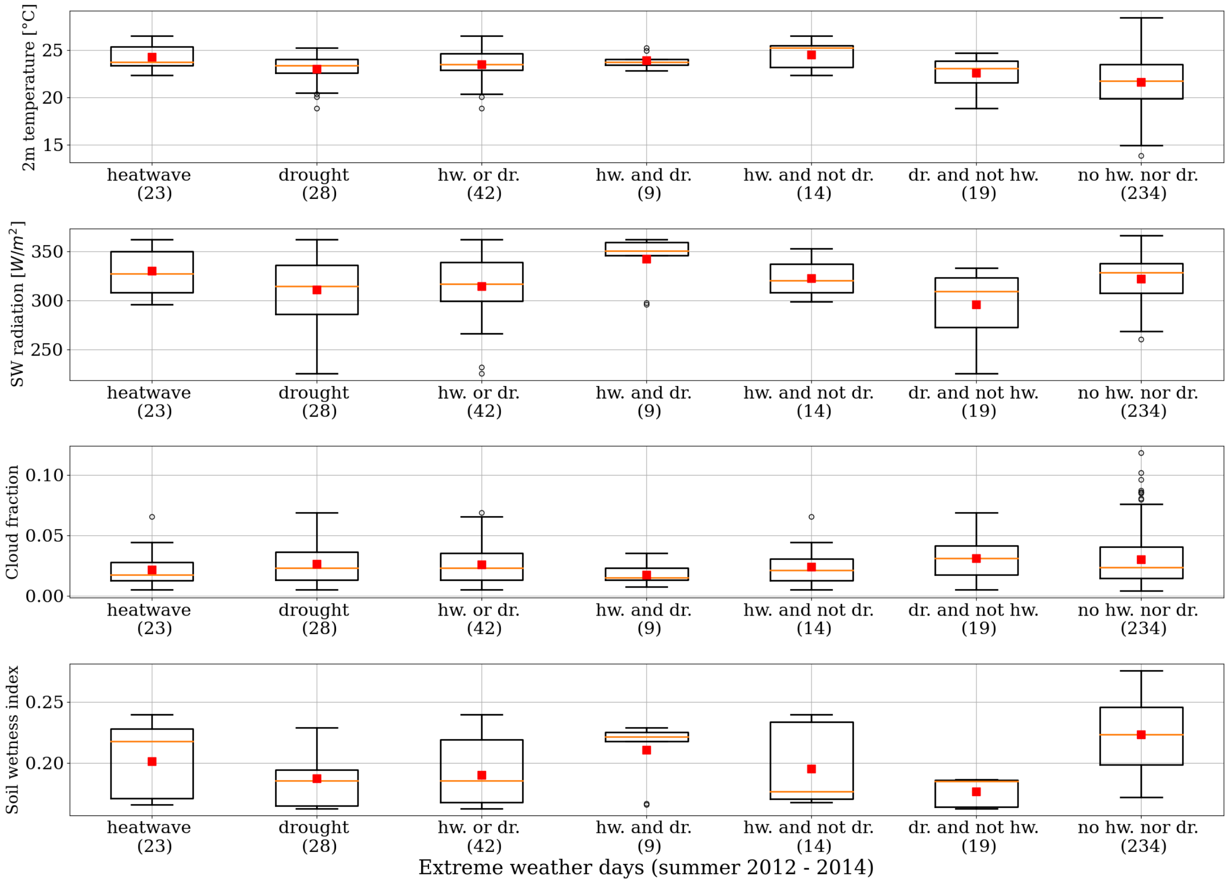

Figure B.20: Simulated weather conditions (2m temperature, shortwave radiation, cloud fraction and soil wetness) by the WRF model over the Southwestern Europe, clustered by identified extreme weather events (from the RegIPSL model). The number of days is in parentheses. The analyzed period is summer 2012, 2013 and 2014, covering a total number of 276 days.

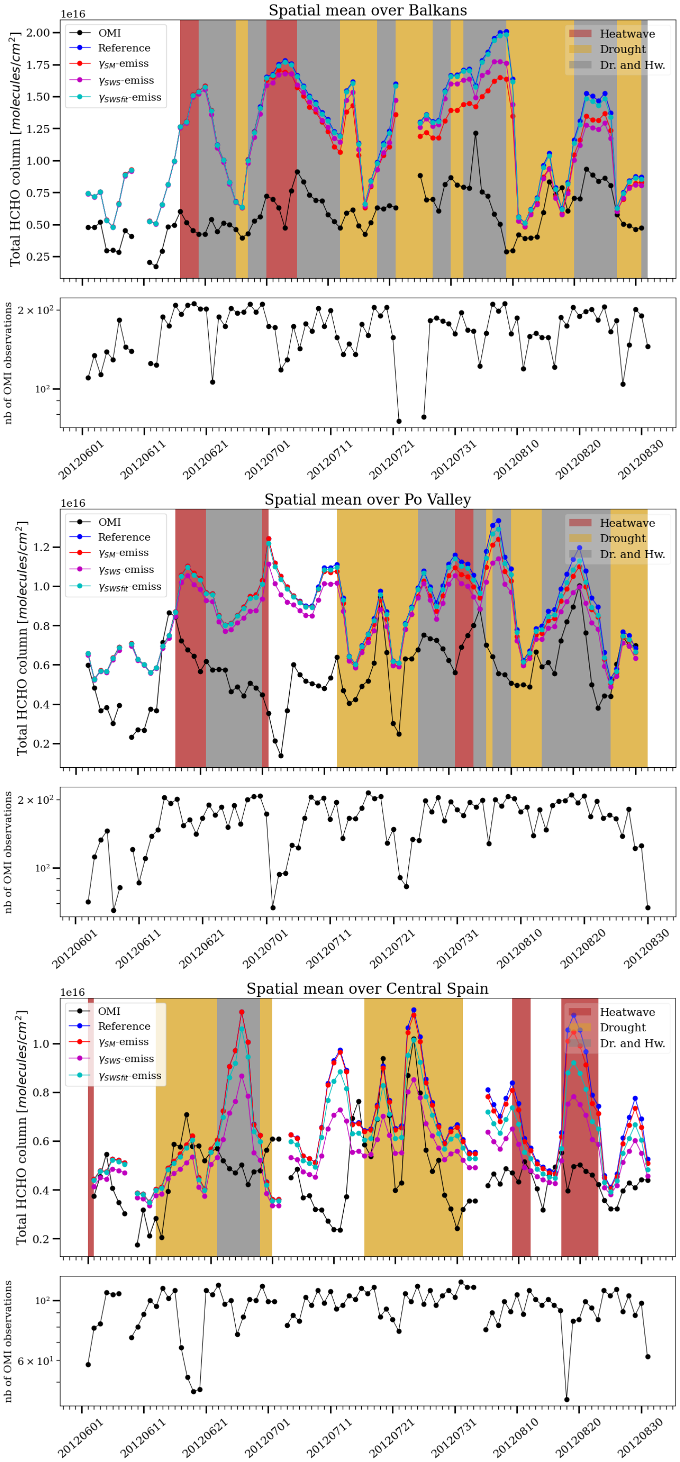

Figure B.21: Daily HCHO total column [$molecules/cm^2$] during summer 2012 observed by OMI and simulated by CHIMERE, averaged over the Balkans (upper panel), Pô Valley (middle panel) and Central Spain (lower panel). A moving average window of 3 days is applied on observations and only days with at least 30% of data over the spatial cover are kept. The number of observations (OMI pixels) is indicated below each panel.

## Conclusions and perspectives

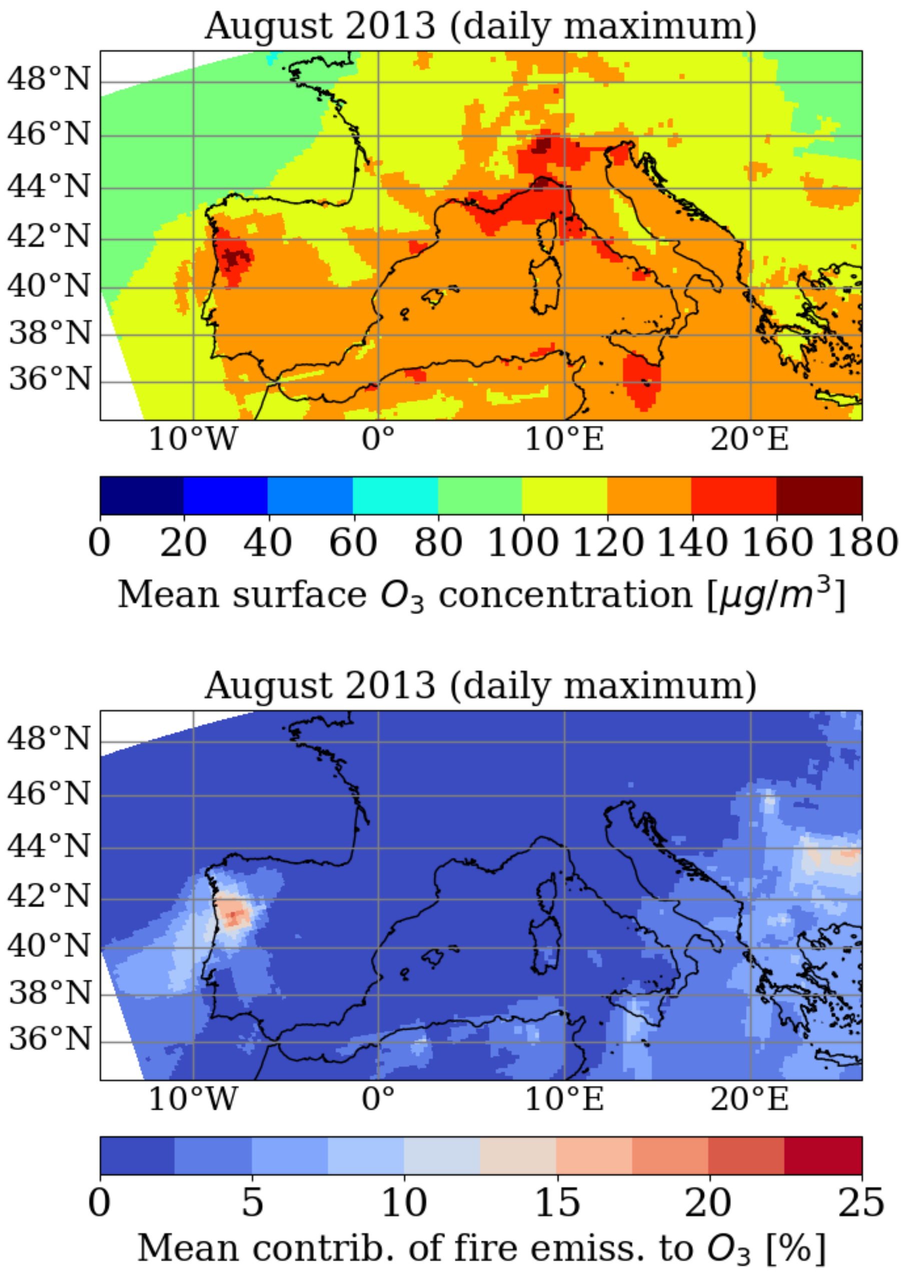

Figure B.22: August mean surface $O_3$ (daily maximum) simulated by CHIMERE ("Reference" simulation) for 2013 (upper panel). Based on the "NoFire-emiss" simulation, lower panel presents the mean contribution of fire emissions to $O_3$ concentration.

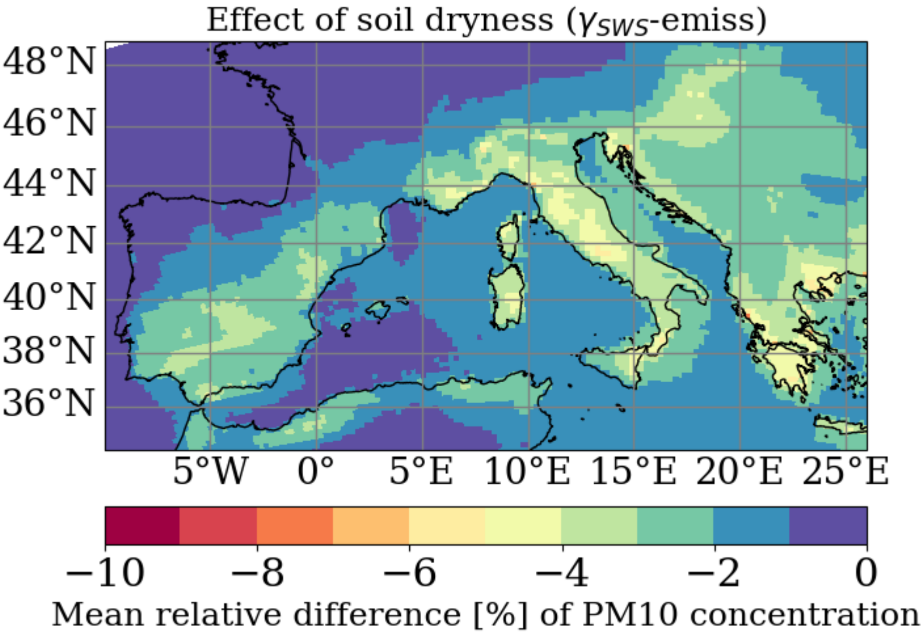

Figure B.23: Summer mean (JA) relative difference [%] of surface $PM_{10}$ concentration due to soil dryness based on RegIPSL ("$\gamma_{SWS}$-emiss" simulation), computed from the "Reference" simulation.

# Appendix C

# Communications related to this PhD thesis

## Scientific papers:

- **Guion, A.**, Turquety, S., Cholakian, A., and Polcher, J. Sensitivity of surface particulate matter concentrations to drought effects, in preparation, 2022.
- **Guion, A.**, Turquety, S., Cholakian, A., Ehret, A., Polcher, J., and Lathière, J. Variation of canopy-troposphere interactions during droughts and heatwaves, impact on surface ozone over Southwestern Europe. *Atmospheric Chemistry and Physics*, in review, 2022.
- **Guion, A.**, Turquety, S., Polcher, J., Pennel, R., Bastin, S., and Arsouze, T. Droughts and heatwaves in the Western Mediterranean: impact on vegetation and wildfires using the coupled WRF-ORCHIDEE regional model (RegIPSL). *Climate Dynamics*, 2021, `https://doi.org/10.1007/s00382-021-05938-y`.

## Science outreach paper:

- **Guion, A.** Les feux de végétation. Quelle empreinte dans l'atmosphère ? *Découverte, Universcience, Paris, France*, 2021.

## International conferences:

- **Guion, A.**, Turquety, S., Cholakian, A., Ehret, A., Polcher, J., and Lathière, J. Impact of droughts and heatwaves on surface ozone over Southwestern Europe. *EGU General Assembly Conference*, 2022.

- **Guion, A.**, Turquety, S., Polcher, J., and Cholakian, A. Observed and simulated effects of droughts and heatwaves on ozone concentration in Southern Europe. *16th IGAC Scientific Conference*, 2021.
- **Guion, A.**, Turquety, S., Polcher, J., Pennel, R., and Fita, L. Identification of droughts and heatwaves in the Western Mediterranean, variability and impacts on vegetation and wildfires using the coupled ORCHIDEE-WRF regional model. *EGU General Assembly Conference*, 2020.

## Invited seminar:

- **Guion, A.**, Turquety, S., Polcher, J., Pennel, R., and Fita, L. Identification of droughts and heatwaves in the Western Mediterranean, variability and impacts on vegetation and wildfires. *DCAO/CIMA, Universidad de Buenos Aires*, 2019.

# List of Figures and Tables

# List of Figures

# List of Tables